HAL
open science

New experiment for understanding the physical mechanisms of ultrafast laser-induced electron emission from novel metallic nanotips

Mina Bionta

To cite this version:

Mina Bionta. New experiment for understanding the physical mechanisms of ultrafast laser-induced electron emission from novel metallic nanotips. Physics [physics]. Université Paul Sabatier - Toulouse III, 2015. English. NNT : 2015TOU30220 . tel-01281828v2

HAL Id: tel-01281828

https://theses.hal.science/tel-01281828v2

Submitted on 18 Apr 2016

HAL is a multi-disciplinary open access archive for the deposit and dissemination of scientific research documents, whether they are published or not. The documents may come from teaching and research institutions in France or abroad, or from public or private research centers.

L'archive ouverte pluridisciplinaire **HAL**, est destinée au dépôt et à la diffusion de documents scientifiques de niveau recherche, publiés ou non, émanant des établissements d'enseignement et de recherche français ou étrangers, des laboratoires publics ou privés.

Université de Toulouse

THÈSE

En vue de l'obtention du

DOCTORAT DE L'UNIVERSITÉ DE TOULOUSE

Délivré par l'Université Toulouse III – Paul Sabatier
Discipline ou spécialité: Physique

New experiment for understanding the physical mechanisms of ultrafast laser-induced electron emission from novel metallic nanotips

---

Présentée et soutenue par
Mina R. BIONTA

15 September 2015

JURY

Mme	Béatrice CHATEL	Directrice de recherche, CNRS, LCAR, Toulouse	Directrice de Thèse
M.	Benoît CHALOPIN	Maître de conferences, LCAR, Université Paul Sabatier Toulouse III	Co-directeur de Thèse
M.me	Natalia DEL FATTI	Professeur, Université Lyon I, ILM, Lyon	Rapporteur
M.	Eric CONSTANT	Directeur de recherche, CNRS, CELIA, Bordeaux	Rapporteur
M.	Jesse GROENEN	Professeur, CEMES, Université Paul Sabatier Toulouse III	Président du Jury
M.	Hamed MERDJI	Chercheur, CEA, IRAMIS - LIDYL, Saclay	Examiner

École doctorale: Sciences de la Matière (SDM)
Unité de recherche: Laboratoire Collisions Agrégats Réactivité (LCAR IRSAMC UMR5589)
Directrice de Thèse: Béatrice CHATEL
Co-directeur de Thèse: Benoît CHALOPIN

UNIVERSITÉ TOULOUSE III PAUL SABATIER

Université de Toulouse

Ph.D. Thesis

New experiment for understanding the physical mechanisms of ultrafast laser-induced electron emission from novel metallic nanotips

presented by:
Mina R. BIONTA

A thesis submitted to the
Graduate School Sciences de la Matière (SDM) of the
Université Toulouse III – Paul Sabatier
in partial fulfillment of the requirements for the degree of
Doctor of Philosophy (Ph.D.) of the Université de Toulouse

Toulouse, France. 15 September 2015

JURY

Mme	Béatrice CHATEL	Directrice de recherche, CNRS, LCAR, Toulouse	Advisor
M.	Benoît CHALOPIN	Maître de conferences, Université Paul Sabatier Toulouse III, LCAR, Toulouse	Co-advisor
Mme	Natalia DEL FATTI	Professeur, Université Lyon I, ILM, Lyon	Reviewer
M.	Eric CONSTANT	Directeur de recherche, CNRS, CELIA, Bordeaux	Reviewer
M.	Jesse GROENEN	Professeur, Université Paul Sabatier Toulouse III, CEMES, Toulouse	Jury President
M	Hamed MERDJI	Chercheur, CEA, IRAMIS - LIDYL, Saclay	Examiner

Graduate School: Sciences de la Matière (SDM)
Research laboratory: Laboratoire Collisions Agrégats Réactivité (LCAR IRSAMC UMR5589)
Supervisor: Béatrice CHATEL
Co-supervisor: Benoît CHALOPIN

© 2015 by **Mina R. BIONTA**

New experiment for understanding the physical mechanisms of ultrafast laser-induced electron emission from novel metallic nanotips

Ph.D. thesis, 15 September 2015
Supervisor: Béatrice CHATEL
Co-Supervisor: Benoît CHALOPIN
Reviewers: Natalia DEL FATTI and Eric CONSTANT
Examiners: Jesse GROENEN and Hamed MERDJI

Université Toulouse III – Paul Sabatier
Sciences de la Matière (SDM)
Laboratoire Collisions Agrégats Réactivité (LCAR IRSAMC UMR5589)
118 Rue de Narbonne – 31062 Toulouse – France

To my parents

Stories are light. Light is precious in a world so dark. Begin at the beginning. Tell Gregory a story. Make some light.

– Kate DiCamillo,
The Tale of Despereaux

Acknowledgments

First and foremost I would like to thank my advisors Béatrice and Benoît. Their continual guidance has been amazing and could not be better. This includes not only in terms of scientific help and direction, but also with helping me with my cross-continental + trans-Atlantic move and dealing with all the little (and big!) nuances that are the difference between French and American culture and administration. By the end I was thinking of you as my surrogate French parents.

I'd also like to thank the rest of our group: Elsa, Stéphane, Laurent, Julien and Sébastien. Without you certainly our experiments would not have been able to run so smoothly and I wouldn't have been able to get such great data. I'd especially like to thank Sébastien. Thanks for doing a post-doc in England and coming to LCLS for a beam time. Without you I'd never have found such a great Ph.D. and would probably still be looking for the perfect project.

I'd also like to thank our collaboration with CEMES, especially Aurélien for teaching me how to make tips and answering my many questions about materials, and everyone else in the group with whom I interacted with a lot: Florent, Ludvig, Robin. And of course there was our other collaboration with GPM in Rouen: Ivan, Jonathan, Angela, Bernard. A great thanks for your kindness and hospitality and sharing of ideas, and a huge thanks to Ivan for making my silver tips! And a special thank you to Jean-Philippe and Patrick from the I^2M group at LCAR for help with the construction and design of the spectrometer as well.

There's the rest of the researchers at LCAR: Chris, Jacques, Sébastien, Jean-Marc, David, Juliette, Alex, Valérie, Matthias. Thank you so much for always being so friendly towards me and for welcoming me into your little community. And a big thanks to Sylvie and Christine for helping me figure out the endless French paperwork and solving any administration problem I may have had!

I'd like to thank my core German contingency: Peter, Sarah, Philipp and my office-mate David,. Thanks for integrating with me and all those adventures by the Garonne and getting Lebanese Sandwiches. Not to mention teasing GinTonic and endless balcony sessions. I'd also like to thank the Foreign kids (mostly) from my first year: Arun, Ayhan (and for taking me to Ikea!), Marina, Wes, Alex. I would not have been able to find all the culinary deliciousness of Toulouse without you guys and our Sunday dinners. The "Spanish" kids: Patricia and Ori-

ana. All our explorations of Toulouse and the area. Bar hopping, Café Populaire, Montpellier, finding cheap places to go shopping! And of course all the other (effective) PhD students: Maummar and Claudia, Aéla, Simon, François, Florian, Isabelle, Etienne, Boris, Julien, Annaël, Medha, Lionel, Guillaume, Morane (invitée non-scientifique), Romain, Chiara, Citlali. Seriously guys! I finished! I'm not kidding you! I'm glad you got over your fear of the scary foreign new girl to accept me as one of your own. All those nights at Dubliners, I will remember them fondly. I now have to find myself a new "Irish" bar now! It won't be easy.

There are a few non-IRSAMC related folks to mention. First I'd like to thank my econ friends: Adrian, Jakob, Shenkar, Shagun, Rodrigo. Thanks for speaking English with me, and providing some refreshing non-scientific conversation and points of view. I'd also like to thank the Saarbrücken kids: Daniel, Per, Pierre-Luc, Louise Anne, Bruno. Thanks for putting up with me and my frequent visits. You're welcome to come stay with us in Montréal at any time! Caitlin and Jen, your continued presence over the internet provided a reassuring connection to home. Even if you both weren't physically located at "home". Caitlin your understanding of #french problems was comforting that I wasn't the only one with these issues. And Jen, your simultaneous #expatproblems with mine were a great help when feeling like everything was too different and I would never survive.

I'd like to thank my parents. Thank you for supporting me all these years in my academic (and non) endeavors. Thank you for allowing me to take risks and pursue my dreams of physics, even when it seemed like I might be lost. Thank you for letting your only daughter move to France and finish her Ph.D. Thank you.

I never would have thought that a summer school in a tiny town in Germany on not-quite my field would lead to such an important connection. Luke, since the moment I met you, your continual support and guidance has been unwavering. Your constant love and encouragement has kept me focused and on the right path to finish. Without you I would not have been able to finish (even though you claim otherwise). I am lucky to have you.

Finally, to all those that are mentioned here, and those that are not (sorry I forgot you) a huge thank you. Your support has shaped me into the woman (doctor!) I am today.

Merci beaucoup!

Abstract

This thesis concerns the interaction of a sharp nanotip with an ultrashort laser pulse for the observation of emission of photoelectrons. An electron can be emitted from a sharp nanotip system by many different mechanisms. Each mechanism gives a unique signature that can be identified by the photoelectron energy spectrum.

We developed a new experiment to observe and identify these emission mechanisms. This consists of a flexible laser system (including the development of a high repetition rate, variable repetition rate noncollinear optical parametric amplifier (NOPA)), ultra high vacuum chamber, electron detector (electron spectrometer with 2D resolution), nanopositioning of a sharp nanotip in the focus of the laser, and fabrication of these nanotip samples in a variety of materials (in collaboration with CEMES (Toulouse) and GPM (Rouen)).

We observed the emission of photoelectrons from various nanotips based on different materials: tungsten, silver, and a new type of carbon-based nanotip formed around a single carbon nanotube. We confirm the observation of above threshold photoemission (ATP) peaks from a tungsten nanotip. We detected the first laser induced electron emission from a carbon cone based on a single carbon nanotube. We observed a plateau in the electron spectra from a silver nanotip, the signature of electron recollision and rescattering in the tip. Various studies were performed in function of the voltage applied, repetition rate of the laser, laser polarization, energy and wavelength of the laser in order to understand these phenomena. From spectral features we were able to extract information about the system such as the enhancement factor of the laser electric field near the nanotip and the probability of above threshold photon absorption. Comparisons of the various spectra observed allowed us to spectrally identify the mechanisms for photoemission for tip based systems.

Résumé

Cette thèse étudie l'interaction de nanopointes avec des impulsions laser ultracourtes pour observer l'émission photo-assistée d'électrons. Plusieurs mécanismes physiques entrent en jeu, chacun ayant une signature unique identifiable dans le spectre d'énergie des électrons.

Nous avons développé une nouvelle expérience pour observer et identifier ces mécanismes d'émission. Ceci inclut le développement complet d'un système laser flexible (notamment un amplificateur optique non colinéaire (NOPA) haute cadence), une chambre ultra-vide avec détecteur d'électrons (mesure de spectre d'électrons et carte 2D de l'émission) et un dispositif de nanopositionnement de la pointe dans le foyer du laser, et enfin la fabrication et caractérisation de pointes diverses (en collaboration avec les laboratoires CEMES (Toulouse) et GPM (Rouen)).

Nous avons observé l'émission photo-induite d'électrons à partir de nanopointes de différents matériaux (tungstène, argent, et une nouvelle pointe formée autour d'un nanotube de carbone unique). Nous avons confirmé l'observation de pics ATP (signature de la photoémission au dessus du seuil) sur une pointe de tungstène. Nous avons détecté la première émission induite par laser à partir de nanocône de carbone unique. Enfin, nous avons observé un plateau dans le spectre d'énergie des électrons d'une pointe d'argent, signature de la recollision et rediffusion des électrons sur la pointe. Pour identifier et caractériser ces mécanismes, des études variées ont été faites en fonction de la tension appliquée sur la pointe, du taux de répétition du laser, de sa polarisation, de sa puissance et de sa longueur d'onde. En étudiant la forme du spectre des photoélectrons, nous avons pu extraire des informations sur l'interaction : le facteur d'amplification du champ laser proche de la nanopointe et la probabilité d'absorption d'un photon au dessus du seuil.

Contents

List of Figures **xxii**

List of Tables **xxiii**

Introduction **1**

1 Theory of electron emission mechanisms **5**

1.1 Generalities of the system **5**

1.1.1 Electron potential at a metal/vacuum interface 6

1.1.2 Description of an ultrashort laser pulse 8

1.1.3 Observables 10

1.1.4 Space charge effects 10

1.2 Mechanisms of electron emission **10**

1.2.1 Thermonic emission 11

1.2.2 Cold field emission 12

1.2.3 Thermally enhanced field emission 13

1.3 Other mechanisms: emission processes induced by a laser field **14**

1.3.1 Photofield emission 14

1.3.2 Intense laser induced emission processes 14

1.3.3 Electron recollision and rescattering 18

1.4 Peculiarities arising from a nanotip geometry **20**

1.4.1 Geometric field enhancement 20

1.4.2 Optical field enhancement 21

1.4.3 Facet emission 22

1.4.4 Electron propagation in the vicinity of a nanotip 23

1.5 Summary **24**

2 Optical setup and development of a NOPA **27**

2.1 Optical setup **27**

2.1.1 The laser system 28

2.1.2 Oscillator 28

2.1.3 Regenerative Amplifier: 28

2.1.4 1030 nm fiber laser 29

2.2 Laser characterization diagnostics **30**

2.2.1 Spot Size Characterization . . . 30
2.2.2 Pulse duration and phase . . . 32
2.2.3 Peak Intensity . . . 33
2.3 Noncollinear Optical Parametric Amplifier (NOPA) . . . 33
2.3.1 Optical parametric amplification . . . 34
2.3.2 NOPA overview . . . 36
2.3.3 NOPA setup . . . 37
2.3.4 Characterization of the NOPA output . . . 38
2.4 Summary . . . 43

3 Experimental setup and methods 47
3.1 Nanotip fabrication and characterization . . . 48
3.1.1 Tungsten tips . . . 48
3.1.2 Carbon Cone nanoTips (CCnT) . . . 52
3.1.3 Silver Tips . . . 54
3.2 Vacuum chamber . . . 56
3.3 Tip holder and manipulator . . . 58
3.3.1 Holder for tungsten based tips . . . 59
3.3.2 Holder for silver tips . . . 59
3.3.3 Laser focus and intensity on the tip . . . 59
3.3.4 Anode . . . 61
3.3.5 Voltage applied to the tip, V_{tip} . . . 62
3.4 Evolution of the setup . . . 62
3.5 Electron emission and detection: the electron spectrometer . . . 62
3.6 Alignment Procedure . . . 67
3.6.1 Laser Alignment . . . 67
3.6.2 Spectrometer Alignment . . . 69
3.7 Summary . . . 69

4 Results from tungsten nanotips 71
4.1 *In-situ* tip characterization . . . 71
4.1.1 Fowler-Nordheim plots . . . 71
4.1.2 Field emission microscopy . . . 73
4.2 Thermal damage studies . . . 74
4.3 Laser induced emission . . . 76
4.3.1 Laser polarization dependence . . . 76
4.3.2 Laser power dependence . . . 78
4.3.3 Two pulse interferometry . . . 80
4.3.4 Photoelectron spectra . . . 81
4.4 Above Threshold Photoemission . . . 82
4.5 Summary . . . 84

5 Carbon Cone nanoTips (CCnT) 85
5.1 Description of a Carbon Cone nanoTip (CCnT) . . . 85
5.2 CCnT characterization . . . 87
5.2.1 Scanning electron microscopy . . . 87
5.2.2 Fowler-Nordheim plots . . . 88
5.2.3 Field emission microscopy . . . 89
5.3 First CCnT results . . . 90

5.4 Thermal damage studies **91**
5.5 Laser emission **93**
5.5.1 Polarization studies 93
5.5.2 Laser induced spectra 93
5.6 Perspectives on laser-induced CCnT emission **94**
5.7 Summary **95**

6 Silver nanotip results **97**
6.1 Why silver? **97**
6.2 *In-situ* tip characterization **98**
6.2.1 Scanning electron microscopy 98
6.2.2 Field emission microscopy 99
6.2.3 Fowler-Nordheim plots 100
6.3 High repetition rate laser induced emission results **101**
6.3.1 First Ag nanotip results 101
6.3.2 Second Ag tip results 102
6.4 Low repetition rate emission results **104**
6.4.1 Non kinetically resolved electron results at 1 kHz 104
6.4.2 Kinetically resolved analysis at 1 kHz 106
6.5 Preliminary 400 nm results **112**
6.6 Summary **114**

7 Re-examining emission mechanisms using spectral shape **117**
7.1 ATP peaks: probability of free-free transitions **117**
7.2 Spectral shape **119**
7.2.1 Different shapes for different mechanisms 119
7.2.2 Comparisons of photoemission spectra 120
7.2.3 Spectral simulations 122
7.3 Summary **123**

Conclusion and Perspectives **125**

A List of Symbols and Abbreviations **129**

B Thermal studies on W **131**

C Thermal studies on CCnTs **139**
C.1 First tests: on-axis spherical focusing mirror **139**
C.2 Second tests: off-axis parabolic focusing mirror **141**

D Résumé en français **143**
D.1 Théorie des mécanismes d'émission d'électrons **145**
D.2 Dispositifs optiques et développement d'un NOPA **147**
D.3 Dispositif expérimental **150**
D.4 Résultats avec une nanopointe de tungstène **151**
D.5 Résultats avec un nanocône de carbone **155**
D.6 Résultats avec une nanopointe d'argent **158**
D.7 Re-examen des mécanismes d'émission en utilisant la forme spectrale . . **161**

References **165**

List of Figures

1.1 Schematic of the laser-tip interaction 5
1.2 Cold field emission 7
1.3 Schottky effect 8
1.4 Thermonic emission 11
1.5 Thermally enhanced field emission 13
1.6 Photofield emission 14
1.7 Photofield emission spectrum 15
1.8 Strong-field emission 16
1.9 ATP peaks in Cu 17
1.10 ATI spectrum with plateau in Xe 19
1.11 3 step model of recollision 19
1.12 Optical field enhancement 21
1.13 W facet emission 22
1.14 Electron Quiver Motion 24
1.15 Emission mechanisms 24

2.1 Kerr lens modelocking principle 28
2.2 Laser beamline schematic 29
2.3 Knife edge for OAP 31
2.4 LX SPIDER 32
2.5 Schematic of DFG 34
2.6 DFG vector schematic 35
2.7 NOPA phase matching curves 36
2.8 NOPA schematic and photo 37
2.9 WLC spctra for different repetition rates 39
2.10 NOPA chirp correction 40
2.11 NOPA spectrum for different repetition rates 40
2.12 NOPA spectra 41
2.13 NOPA energy measurements for different repetition rates 42
2.14 NOPA gain 42
2.15 Prism compressor schematic 43
2.16 NOPA autocorrelation for 750 nm 44

3.1 Schematic of the experimental setup 47
3.2 Tip base schematic 48

3.3 SEM of tip micro-welding 49
3.4 Electrochemical chemical etching setup 50
3.5 SEM of tip micro-welding 50
3.6 Failed etch of W tip 51
3.7 CCnT 52
3.8 TEM of CCnT 53
3.9 CCnT mounting process 54
3.10 SEM of mounted CCnT 55
3.11 SEM of tip microwelding 55
3.12 Chamber schematic 57
3.13 Photo of chamber geometry 58
3.14 Photo and schematic of the tip manipulating ensemble 59
3.15 Photos of the tip holders 60
3.16 Focusing mirror geometries 60
3.17 Photo of the anode 61
3.18 Photo and schematic of the electron spectrometer 63
3.19 MCP signal amplifier 64
3.20 Derivation of the spectrum 64
3.21 Static spectrum 65
3.22 Electron energies from angled tips 66
3.23 Projection of electron trajectories 67
3.24 On-axis spherical mirror focus alignment 68
3.25 OAP alignment 68
3.26 Experimental setup schematic 70

4.1 Fowler-Nordheim plots for W 72
4.2 SEM of FN-ed tips 73
4.3 FEM of tungsten tips 74
4.4 SEM of B1 before and after 75
4.5 SEM of C2 before and after 76
4.6 W polarization dependence 77
4.7 Misaligned tip polarization dependence 77
4.8 Derivation of the power law exponent 78
4.9 PCW power law 79
4.10 Michelson interferometer schematic 80
4.11 Electron emission for two interfering pulses 80
4.12 W(310) photoelectron spectrum 81
4.13 W spectra for increasing laser intensity 82
4.14 ATP power law for peaks 83

5.1 TEM and profile of interior of CCnT 86
5.2 SEM of CCnT 86
5.3 SEM of CCnT 87
5.4 FN for CCnT 88
5.5 FEM of CCnT 89
5.6 Spectra from unknown source 90
5.7 Destroyed CCnT 91
5.8 Damaged CCnT 91
5.9 First CCnT thermal tests 92

5.10 Second CCnT thermal tests 93
5.11 CCnT polarization dependence 94
5.12 Spectrum from CCnT 95

6.1 First Ag tip in chamber 98
6.2 First Ag after laser irradiation 99
6.3 Second Ag tip in chamber 99
6.4 FEM of PC Ag tip 100
6.5 Ag FN plot 101
6.6 First silver tip polarization scans 102
6.7 First silver tip spectra 102
6.8 Ag tip MHz polarization scans 103
6.9 Ag tip MHz spectra 103
6.10 kHz polarization curve for Ag 105
6.11 Power law exponent for Ag 106
6.12 kHz uncorrected spectra for Ag 106
6.13 kHz Fermi corrected spectra for Ag 109
6.14 Cutoff linear fit 110
6.15 Ag spectra corrected Fermi 111
6.16 Ag spectrum for 400 nm and 800 nm 113
6.17 Fermi corrected spectra for 400 nm and 800 Nm 114

7.1 Probability of photon absorption, $\mathscr{P}_1$ 118
7.2 $\mathscr{P}_1$ vs Intensity 118
7.3 Schematic of spectral shapes 119
7.4 Spectral comparisons 121

B.1 W comb 132
B.2 Alignment of W comb in laser 132
B.3 Tip A1 133
B.4 Tip A2 133
B.5 Tip A4 133
B.6 Tip A5 134
B.7 Tip A6 134
B.8 Tip A7 134
B.9 Tip B1 135
B.10 Tip B2 135
B.11 Tip B3 135
B.12 Tip B4 136
B.13 Tip B5 136
B.14 Tip B6 136
B.15 Tip B7 137
B.16 Tip B8 137
B.17 Tip C1 137
B.18 Tip C2 138

C.1 Tip 1, thermal test 1 139
C.2 Tip 2, thermal test 1 140
C.3 Tip 3, thermal test 1 140

C.4 Tip 4, thermal test 1 140
C.5 Tip 1, thermal test 2 141
C.6 Tip 2, thermal test 2 141
C.7 Tip 3, thermal test 2 142
C.8 Tip 4, thermal test 2 142

D.1 Mécanismes d'émission 146
D.2 Dispositif optique 148
D.3 Dispositif expérimental 151
D.4 Dépendance en polarisation pour une pointe de W 152
D.5 Spectre des photoélectrons d'une pointe de W(310) 153
D.6 Pics d'ATP 154
D.7 CCnT endommagée 156
D.8 Spectre d'un CCnT 157
D.9 Spectre au MHz pour une nanopointe d'Ag 158
D.10 Spectre au kHz pour une nanopointe d'Ag 159
D.11 Linéarité de l'énergie de coupure 160
D.12 Comparaison des spectres 163

List of Tables

1.1 Cold field emission thresholds 21

2.1 WLC characterization 39
2.2 NOPA Fourier limit 41
2.3 Laser characteristics summary 45

4.1 Fowler-Nordheim calculations 73

6.1 Calculated Keldysh 107
6.2 U_p from peak shifting 108
6.3 Measured cutoff 109
6.4 Corrected cutoff and enhancement 110
6.5 Adiabaticity parameter 111
6.6 Calculated effective $\mathscr{E}_0$ 112
6.7 U_p from peak shifting 113
6.8 Measured cutoff at 400 nm 114

7.1 Probability of photon absorption, $\mathscr{P}_1$ 119

B.1 W thermal tests 131

C.1 CCnT on-axis spherical mirror thermal tests 139
C.2 CCnT OAP thermal tests 141

D.1 Résumé des caractéristiques du laser 149
D.2 Énergie de coupure corrigé et amplification 161

Introduction

Electron emission from materials is a fundamental physical problem of great interest. Understanding the mechanisms behind the emission of an electron is a foundation for material properties as well as for particular physical processes. The emission of electrons from a material induced by light, the photoelectric effect [Einstein05], has historically been of interest to study due to its potential applications. With the advent of lasers, laser-assisted emission from metallic surfaces has been systematically studied [Lee73, Venus83]. This has led to the study of physics interactions of light and matter and the resulting phenomena. Potential applications include electron sources for microscopy, accelerators and free electron lasers.

At high enough laser intensity, the electric field of the laser is strong enough to control the motion of an emitted electron. This means the field of the laser can drive the electron back to the parent material to be rescattered and absorb more energy from the laser acceleration. We call this the strong field regime. In atomic and molecular systems, the interaction of electrons with strong laser fields approaching or exceeding the interatomic field strength gives rise to interesting phenomena such as above threshold ionization (ATI)[1] [Agostini79], attosecond streaking [Itatani02], the generation of attosecond electron wave packets for tomographic imaging of molecular orbitals [Itatani04] or high harmonic generation (HHG)[2] [Burnett77, McPherson87, Ferray88, L'Huillier93]. These phenomena have been extensively studied in atoms and molecules [Joachain12] as well as in solid-state nanostructures such as dielectric nanospheres [Zherebtsov11], or gold nanoparticles [Schertz12] and surfaces such as in photocathodes.

One such source of strong-field investigations can be in sharp nanotips. These have the benefit of the natural optical field enhancement that arise from their sharp geometric shapes. This means that the optical field is amplified simply due the shape of the sample, and thus do not have to be as high to reach strong field regimes. Sharp nanotips can be used as a source of ultrashort electron pulses with high spatial and temporal coherence for use in matter wave ex-

[1] ATI: the emission of an electron with more energy than what is needed to remove it from the system (the ionization potential)

[2] HHG: the recollision of a laser accelerated electron with its parent ion leading to the emission of a photon corresponding to a high harmonic of the fundamental photon from the laser

periments [Barwick08]. This has direct applications for femtosecond imaging and as ultrafast electron diffraction sources.

My thesis is concerned with the physical mechanisms behind photoelectron emission induced by an ultrafast laser from a sharp nanotip. This is a new scientific direction for my group involving the complete development of a new experimental setup and apparatus. Prior to my arrival, the research of our group has been involved with the experimental development of coherent control schemes using tailored ultrashort pulses [Monmayrant10] on various systems from atoms to molecules and quantum dots, including scattered media [McCabe11]. This expertise in laser development and control techniques adds parameters with which we can use to investigate photoelectron emission mechanisms. I worked to incorporate these techniques to our new experimental setup for precise studies of the light-matter interaction at a sharp nanotip.

Sharp nanotips have a long history of usage as field emitters [Gomer61]. Emission from surfaces, atoms and molecules has long been studied [Wood97, Joachain12, Agostini79, Luan89, Kupersztych01]. Metals require a large electric field application to promote electric field emission, and the usage of nanotips exploits their sharp shape to naturally enhance the applied field. Emission from a nanotip is determined by a variety of parameters. The tip radius and applied voltage determine the applied field seen by the system [Gomer61]. Changing the tip material changes the corresponding work function and therefore how much energy the system must acquire to overcome it. Some materials have a plasmonic response, or surface resonance, that may be excited when irradiated by specific laser wavelengths.

Laser induced field emission experiments on sharp nanotips to study strong field physics are a recent domain, with experiments first performed in 2006 [Hommelhoff06b] by the Kasevich group at Stanford, and independently in 2007 [Ropers07] by the Ropers group. Nanotips act a bridge between the atomic and condensed states creating a unique regime for studying light-matter interactions. Electron emission has been investigated on nanotips made of tungsten [Hommelhoff06b, Barwick07] and gold [Ropers07, Park12] and HfC [Kealhofer12]. Strong field phenomena were studied by investigating kinetically resolved electron spectrum. Multiphoton photoemission and in particular above threshold photoemission has been observed in many experiments [Barwick07, Ropers07, Schenk10, Krüger11, Krüger12a, Park12]. A spectral plateau – a signature of optical field emission and rescattering – was observed by [Krüger11, Krüger12b]. Other evidence for optical field emission has been found based on deviations from the multiphoton intensity scaling of the emitted photocurrent [Bormann10]. Beyond these signatures of strong-field phenomena, no high harmonic generation has been demonstrated yet. Moreover a comment has been published recently in Nature [Sivis12] to contest the observation by Kim *et al.* [Kim08] of nanostructure-enhanced HHG. Until now, only second and third harmonics have been observed on a nanotip in a different excitation geometry configuration [Bouhelier03].

The strong field steering of the electron motion was observed and characterized for gold nanotips. In this case, the strong field of the laser suppresses the natural quiver motion of the

electrons promoting the acceleration of the electrons away from the tip [Herink12], and leading to the narrowing of the kinetic energy spectrum of the emitted electrons [Park12].

Combining a strong applied electric field and a weak laser intensity can lead to tunneling effects, photofield emission. These were identified by comparing the emitted current from tips with and without laser illumination [Hommelhoff06b]. It was also identified in the electron energy spectra by the asymetrical shape of the field emission and the sharp edges around the energies of one-photon and two-photon absorptions [Yanagisawa11].

Spatially resolved electron emission also known as field emission microscopy (FEM) is used to study the crystallographic dependency of emission [Yanagisawa09, Yanagisawa10]. These studies show the suppression of emission on the side relative to the laser irradiation. Polarization dependent studies show field enhancement is maximized, and therefore emission is most efficient for polarizations parallel to the axis of the tip [Yanagisawa09, Barwick07]. Thermal effects have been carefully studied in the case of hafnium carbide tip [Kealhofer12] and aluminum [Houard11].

Numerical investigations into the enhancement have been studied for a variety of materials and using several different methods. These include dyadic numerical approaches [Arbouet12] and finite element modeling [Thomas13, Kealhofer12]. Aside from investigating a variety of materials, such as tungsten [Thomas13, Arbouet12], gold [Arbouet12] and HfC [Kealhofer12], other considerations such as the tip geometries [Thomas14] have been modeled.

The applications of electrons emitted from a sharp nanotip are many. The emitted electrons have an ultrashort temporal duration [Hommelhoff06b, Barwick07] with a high spatial and temporal coherence, measured by the brightness of the source. This means that they are ideal for use as an ultrafast electron diffraction source [Baum13]. Up until now, existing time-resolved electron microscopy [Aidelsburger10, Sciaini11, Zewail10] is based on photocathodes where electron emission is a photoelectric process on a large area (i.e. associated with low brightness). Therefore there is a demand for high-brightness and ultra-fast electron sources [Arbouet12] that would also be attractive for free electron lasers [Ganter08]. This has been realized with the recent creation of ultrafast tip enhanced microscopy techniques as a pulsed electron gun [Gulde14, Quinonez13, Yang10]. The bunches that are emitted can be accelerated [Breuer13] and can be optimized for use in Free Electron Lasers [Hoffrogge14] unlike those from the customary copper surface cathodes used in these facilities [Emma10].

This research aims to combine existing electron spectroscopy techniques and laser development expertise with novel tip materials to understand and identify various emission mechanisms. Our new experimental setup expands upon existing electron spectroscopy experiments by adding coherent control elements in combination with novel nanotip materials. Our collaboration with the Nanomaterials group at the Centre d'Élaboration de Matériaux et d'Etudes Structurales (CEMES) allows us access to a carbon based nanotip. The carbon cone nanotip (CCnT) [Houdellier12] is formed with a central single carbon nanotube surrounded by concentric graphene sheets. Also investigated are silver nanotips [Sasaki13, Zhang11], which allow us to probe regimes of emission and enhancement factors that are different than that of conventional tungsten field emitters. By changing the various parameters of the experiments—laser

factors, applied voltage, tip composition, etc.—we are able to explore the different regimes of electron emission.

This thesis is organized as follows:

Chapter 1 introduces the generalities to our system and the variables with which we can adjust. I also discuss physical mechanisms behind electron emission from a surface and the particularities that arise from a sharp nanotip geometry.
Chapter 2 describes the laser system used in the experiment including the development of a NOPA system of variable repetition rate and wavelength.
Chapter 3 gives an overview of the experimental techniques and setup used in our investigations. This includes nanotip sample preparation as well as construction of the sample manipulators and a field retarding electron spectrometer.
Chapter 4 describes results obtained from a tungsten nanotip. These provide a baseline with which we can compare our new experimental setup and results to existing experiments. This includes description of emission with and without a laser as well as systematic studies on thermal effects of the system.
Chapter 5 describes results obtained on a new type of nanotip based on concentric graphene sheets surrounding a central carbon nanotube (CCnT). This includes spatially resolved measurements and the first laser induced photoelectron spectra taken from a carbon nanotube based nanotip.
Chapter 6 presents results from a silver nanotip. By lowering the repetition rate of the laser, we observe strong field effects in the resulting electron spectra. From this we can measure the effective optical field enhancement from the silver.
Chapter 7 compares all the emitted spectrum from all the various parameters that are changed (laser intensity, laser repetition rate, tip material, etc.) and shows how the dominant emission mechanism can change.

1

Theory of electron emission mechanisms

In this chapter, I describe the physical processes and theory for electron emission from a sharp metallic nanotip system. Emission is induced by several parameters, such as: temperature, applied static electric field, or laser illumination. Electron emission has been studied towards fundamental understanding of electron processes. It has been used as a source for electron microscopy revealing unprecedented spatial resolution for material studies [Gomer61]. I will first discuss emission from the general case of a metal surface, and detail the effects induced by laser illumination. I will then discuss the particularities arising from an ultrasharp nanotip geometry. Before explaining the different processes, I will describe the system and its environment.

1.1 Generalities of the system

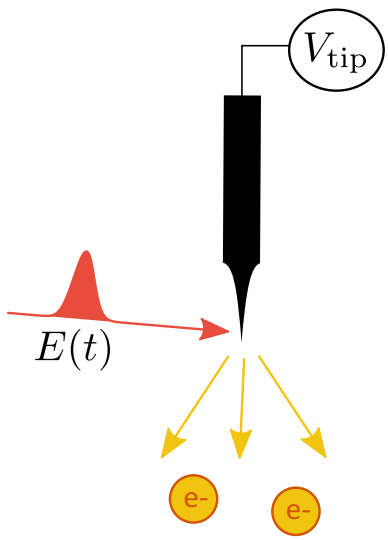

Figure 1.1 – Schematic showing the interaction of the nanotip in the laser field, with the controllable variables.

In this thesis we study electron emission induced by the interaction of a laser pulse and a metallic nanotip (Fig. 1.1). We will look at the emission mechanisms induced by the local

temperature of the system (T [K]), the static electric field (F [V/m]), which is linked to the applied tip bias (V_{tip} [V]) and nanotip size by the relation $F = \beta V_{\text{tip}}$ [Gomer61], with β [m^{-1}] taking into account the tip geometry and the electric field of the laser $\mathscr{E}$.

In this section I will introduce the system and the variables we use to describe it.

1.1.1 Electron potential at a metal/vacuum interface

The energy states of the electrons in a metallic system can be described according to the Fermi-Dirac distribution. This distribution is given by

$$f(E,T) = \frac{1}{1+\exp\left(\frac{E-\mu}{k_b T}\right)}, \tag{1.1}$$

where T is the electron temperature, k_B is the Boltzman constant, and μ is the Fermi energy. The Fermi energy is the maximum energy an electron can have in a metal when the system is at $T = 0$ K. This equation refers to the number of electrons for a given energy E, where $E = E_\perp + E_\parallel$. $E_\perp$ is the normal part of the kinetic energy and $E_\parallel$ is the transverse. For our system, what matters is the component that is normal to the surface, which is found by integrating over the transverse components of the electron energy. Using the Sommerfeld model of free electrons inside a metal, we get the electronic distribution

$$D(E_\perp,T)\mathrm{d}E_\perp = \frac{4\pi m_e k_B T}{h^3}\ln\left(1+\exp\left(\frac{\mu - E_\perp}{k_B T}\right)\right)\mathrm{d}E_\perp, \tag{1.2}$$

where m_e is the mass of an electron and h is the Planck constant.

Potential seen by an electron:
Let's consider the potential barrier $U(x)$ seen by an electron at the metal-vacuum interface at postition $x = 0$, with metal filling the region of space for $x < 0$ and vacuum for $x > 0$ (Fig 1.2).

The unmodified barrier seen by an electron, for $x > 0$, is given by

$$U(x) = \mu + \phi, \tag{1.3}$$

where μ is the Fermi energy and ϕ is the work function of the metal. The work function is the minimum amount of energy needed to remove an electron from a metallic system. This is equivalent to the minimum ionization energy required to remove an electron from an atom or molecule. If the electronic states are full up to the Fermi energy, then an electron requires an additional ϕ amount of energy to be removed from the metal. The work function depends on the material and its orientation (such as the different facets of a crystalline structure) as well as the surface state (adsorbed molecules and cleanliness).

In a metal, due to its good conductance, $U(x) = 0$ for $x < 0$. When we apply an electric field, the potential barrier becomes

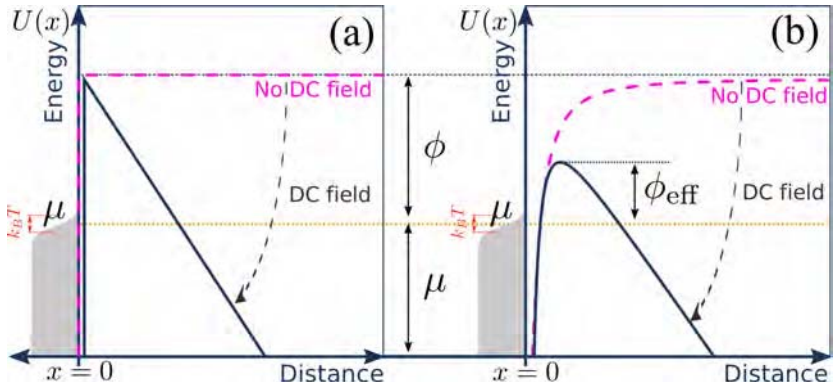

Figure 1.2 – Potential barrier seen by an electron. μ is the Fermi Energy, and ϕ is the work function of the material. (a) The unmodified potential barrier is shown in the dashed pink line, with the modified potential after an electric field is applied, shown with the solid blue line. (b) The same potential barriers as in (a), but after correcting for the image potential. The reduced effective work function is shown and given by ϕ_{eff}.

$$U(x) = \mu + \phi - eFx, \tag{1.4}$$

where e is the electric charge and F is the applied electric field. This applied field modifies the potential such that an electron can quantum mechanically tunnel through it. The potential barrier before and after an applied electric field can be seen in Fig. 1.2 (a).

As the electron leaves the system, the potential of Eq. 1.4 continues to be modified. The conduction electrons left in the surface of the metal shift to form an image potential or image correction to shield the interior of the metal from the field of the free electron. Adding the classical image potential for an electron a distance x from a conducting plane yields

$$U(x) = \mu + \phi - eFx - \frac{e^2}{16\pi\varepsilon_0 x}. \tag{1.5}$$

With the inclusion of the image potential and applied electric field, the height of the potential barrier is now less than the work function of the material. This reduction of the barrier is called the **Schottky effect** [Schottky23]. The effective work function is now

$$\phi_{\text{eff}} = \phi - \sqrt{\frac{e^3 F}{4\pi\varepsilon_0}}. \tag{1.6}$$

The inclusion of the image potential and the reduction of the work function is illustrated in Fig. 1.2 (b).

The reduction of the work function for single crystal tungsten (310), $\phi = 4.35$ eV can be seen in Fig. 1.3. From this plot, we can see that to have a reduction of 1 eV, we must apply a voltage of 6.9×10^8 eV.

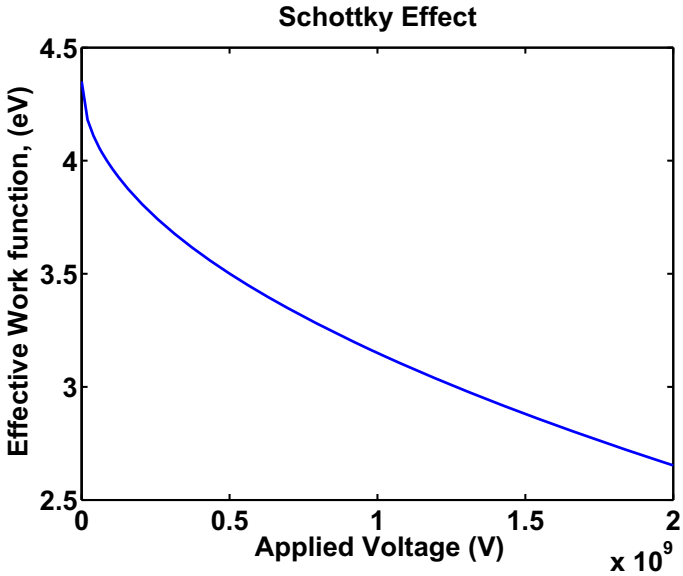

Figure 1.3 – This shows effective work function from the Schottky effect as a function of the applied DC electric field to the system.

1.1.2 Description of an ultrashort laser pulse

The laser light is described as an electric field which is the solution of Maxwell's equations. The complex electric field of an ultrashort laser pulse can be written as

$$\boldsymbol{\mathcal{E}}(t) = A(t)\mathrm{e}^{i(\omega_0 t + \Phi(t))}\boldsymbol{\varepsilon}, \tag{1.7}$$

where $A(t)$ is the temporal envelope of the pulse, ω_0 is the frequency of the light, $\Phi(t)$ is the temporal phase, and $\boldsymbol{\varepsilon}$ is the laser polarization. For a Gaussian envelope, the real part of the electric field becomes

$$\Re\left(\mathscr{E}(t)\right) = \frac{1}{2}\mathscr{E}_0 \exp\left(-2\ln 2\frac{t^2}{\Delta t^2}\right)\cdot\cos\left(\omega_0 t + \Phi(t)\right), \tag{1.8}$$

where $\mathscr{E}_0$ is the amplitude of the field and Δt is the pulse duration at full width at half maximum (fwhm) of the intensity.

The temporal structure of an ultrashort pulse is easier to define in frequency space as the Fourier transform of electric field

$$\widetilde{\mathscr{E}}(\omega) = \widetilde{A}(\omega)\mathrm{e}^{i\varphi(\omega)}, \tag{1.9}$$

where $\varphi(\omega)$ is the spectral phase of the pulse and $\widetilde{A}(\omega)$ is the spectral envelope. The spectral phase can be expanded as a Taylor Expansion:

$$\varphi(\omega) = \varphi(\omega_0) + \varphi'(\omega_0)(\omega-\omega_0) + \frac{1}{2}\varphi''(\omega_0)(\omega-\omega_0)^2 + \frac{1}{6}\varphi'''(\omega_0)(\omega-\omega_0)^3\ldots, \tag{1.10}$$

in which φ describes the phase within the pulse envelope width of the carrier oscillation phase, carrier envelope phase (CEP); the first order φ' describes the relative delay of the pulse; the second order φ'' is the group delay dispersion (GDD) or chirp; the third order φ''' is the third order dispersion (TOD).

The easiest way to conceptualize the temporal chirp of a pulse is to think about the relative arrival time of the different frequency components of a pulse at a certain point in space. For a pulse with a GDD of 0 (assuming all other dispersion orders are also 0), the frequency components all arrive at the same time and the pulse duration is the minimum achievable as determined by the time-bandwidth product. Since the speed of light in a material is dependent on the wavelength of the light, as the pulse passes through a dispersive material the different frequency components slow down respectively, thus arrive at our point in space at different times, stretching out the pulse duration. A positively chirped pulse is one in which the lower energy components (redder end of the spectrum) arrive before the higher energy components (bluer end of the spectrum) and as such, with negatively chirped pulses the higher energy components arrive first.

The relationship between the pulse duration and the spectral bandwidth can be given by the energy-time uncertainty (recall the energy relation: $E = \hbar\omega$):

$$\Delta\omega\Delta t \geqslant 2\pi K, \tag{1.11}$$

where $\Delta\omega$ is the frequency bandwidth fwhm and K is a constant that depends on the pulse envelope shape. For Gaussian pulses $K = 2\ln 2$. This inequality defines a relationship between the spectral bandwidth and minimum achievable pulse duration, i.e. the shorter the pulse duration, the larger the spectral width and is known as the time-bandwidth product. As such, the minimum pulse duration achievable, or Fourier transform or bandwidth limited pulse, is given by:

$$\Delta t = \frac{2\pi K}{\Delta\omega} = K\frac{\lambda_0^2}{c\Delta\lambda}, \tag{1.12}$$

where λ_0 is the central wavelength of the pulse, $\Delta\lambda$ is the wavelength bandwidth at fwhm, and c is the speed of light in a vacuum with $c = \frac{1}{2\pi}\lambda\omega$. Since fundamentally the relationship is between energy and time, a higher energy overall allows for shorter pulses, and thus less bandwidth is required to have equivalent pulse durations for pulses with a shorter central wavelength.

In practice we measure the mean power of a laser. Given a repetition rate R of the laser, the average power is

$$P_{\text{mean}} = E \times R, \tag{1.13}$$

where E is the pulse energy.

In our experimental setup we measure the spectrum, and pulse duration, energy per pulse, mean power. The peak power of the laser pulse depends on the pulse duration, Δt, of the pulse and is given by

$$P_{\text{peak}} = \frac{E}{\Delta t} = \frac{P_{\text{mean}}}{R\Delta t}. \tag{1.14}$$

With the spot size of the laser $(\Delta x)^2$, we can also calculate the peak intensity.

$$I_{\text{peak}} = \frac{P_{\text{peak}}}{(\Delta x)^2}. \tag{1.15}$$

The cycle averaged intensity of the laser (I) is given by

$$I = \frac{1}{2} c \varepsilon_0 \mathscr{E}_0^2, \tag{1.16}$$

where ε_0 is the permittivity of free space. From this we can calculate the amplitude of the electric field of the laser $\mathscr{E}_0$.

1.1.3 Observables

We are interested in the electron emission mechanisms. The physical quantities that can be measured are:

- emitted current
- energy distribution of emitted electrons
- spatial distribution of emitted electrons
- temporal aspects (however this is not discussed in this thesis)

1.1.4 Space charge effects

Space charge effects occur when more than one electron is emitted at the same time and are then repelled from each other by Couloumb repulsion. The number of electrons emitted and detected depends on many factors including the applied voltage and the laser intensity as well as the geometrical constraints of the spectrometer and detector. For our experiment and the theory presented in the rest of this chapter, we consider that there are no space charge effects.

1.2 Mechanisms of electron emission

The emission of electrons from the surface of a condensed phase (generally a metallic surface) into another phase (generally a vacuum) due to a high externally applied electric field is called field emission [Good Jr56, Gomer61]. This means that when a high enough direct current (DC) electric field is applied to the system, electrons can quantum mechanically tunnel through the metal/vacuum interface. This interface forms a potential barrier through with electrons must either tunnel through, or acquire enough energy to escape from the system. Field emission was first observed and described by R.W. Wood in 1897 [Wood97], in which Wood describes a

cathode discharge. W. Schottky, in 1923, described the mechanisms behind field emission, and a connection between the applied field and a reduction in the height of the potential barrier (the Schottky effect, Sec. 1.1.1) [Schottky23]. The emission current rate was described by Fowler and Nordheim in 1928 [Fowler28] (Sec. 1.2.2). In the 1930s, E. W. Müller started using field emission to study the surface properties of materials from nanotip based experiments [Müller36]. From these experiments was developed the technique of exploiting the nanometer sized termination from nanotip emitters to obtain high fields. This paved the path towards field emission microscopy (FEM), scanning electron microscopy (SEM), and other techniques [Gomer61].

1.2.1 Thermonic emission

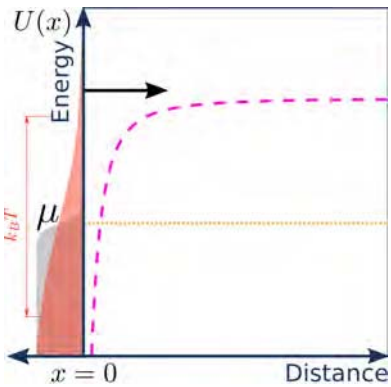

Figure 1.4 – This shows the thermonic emission process where the system is heated enough that some of the excited electrons have enough energy to overcome the work function and classically escape. Note there is no externally applied DC field.

As the system heats up, the Fermi-Dirac distribution changes with temperature until a portion of the electrons have sufficient energy to escape the work function. This is called thermonic emission. This process is governed by the Richardson-Dushman equation [Murphy56, Herring49]

$$J = A\eta T^2 \exp\left(\frac{-\phi}{k_b T}\right), \tag{1.17}$$

where J is the emitted current density, ϕ is the material work function, η is a material dependent pre-factor and A is the Richardson constant defined as

$$A = \frac{4\pi m_e k_b^2 e}{h^3}, \tag{1.18}$$

where m_e is the mass of an electron, e is the charge of an electron and h is the Planck constant. Note that in thermonic emission, there is no need for an externally applied electric field. Instead, the system is heated enough such that some of the excited electrons have sufficient energy to overcome the work function and classically escape from the metal [Lee73] as seen in Fig. 1.4. The emission is governed by electrons whose energies are on the tail end of the

Fermi-Dirac distribution and have energies greater than that of the barrier height. This means that k_bT must be on the order of ϕ. For single crystal W(310), with $\phi = 4.35$ eV, this corresponds to a temperature of 5×10^4 K. This is historically the first emission which has been observed experimentally, but we did not observe this process in our experiment as it requires a very high temperature.

1.2.2 Cold field emission

Cold field emission is found to be extremely useful in electron microscopy as its spectrum is spectrally coherent and yields a very narrow energy bandwidth [Gomer61, Murphy56]. The theory present below describes field emission from a metal surface. Application of the nanotip geometry is presented in Sec. 1.4.1.

A strongly applied electric field will create a finite potential barrier through which an electron may quantum mechanically tunnel. In this case, calculations are made with an assumption that the temperature is 0 K. This is called cold field emission. In cold field emission we apply a large voltage to the system resulting in a large electric field, typically on the order of ∼1–10 GV/m. This enables electron tunneling emission.

Considering a Fermi-Dirac electron distribution, an electron has a probability $\mathscr{P}_\perp$ to tunnel through the potential barrier, the current density is given by $J = \int_E \mathscr{P}_\perp \cdot D(E_\perp, T)\mathrm{d}E_\perp$, where $D(E_\perp, T)\mathrm{d}E_\perp$ is the electron distribution given by Eq. 1.2.

The Fowler-Nordheim (FN) equation [Fowler28, Hommelhoff06b, Gomer61] describes the emission current density from the system for an applied field, F, at 0 K

$$J \propto \frac{e^3F^2}{4\pi h\phi} \cdot \exp\left(-\frac{4\sqrt{2m_e}\phi^{3/2}}{3\hbar eF}v(w)\right) \propto F^2 \cdot \exp\left(-\frac{\alpha}{F}\right), \tag{1.19}$$

with

$$\alpha = \frac{4\sqrt{2m_e}}{3\hbar eF}v(w) \cdot \phi^{3/2}, \tag{1.20}$$

and J is the current density of the emission, e is the electron charge, ϕ is the work function, m_e is the electron mass, $\hbar$ is the reduced Planck constant and $v(w)$ is a slowly varying function, the Nordheim function [Murphy56, Hommelhoff06b, Gomer61], that takes into account the image force of the tunneling electron (from the Schottky effect), with w, the Nordheim parameter given by $w = e^{3/2}\sqrt{F/4\pi\varepsilon_0}/\phi$ [Murphy56, Hommelhoff06b]. The function can be determined by an iterative method described in [Gomer61]. The parameter w is simply the ratio between the effective work function from the Schottky effect to the work function. At a low applied field, there is minimal image force and $v(w) = 1$. The Nordheim function is valued between $0.4 < v(w) < 0.8$ [Hommelhoff06b] and can be determined by an iterative method described in [Gomer61]. $v(w)$ depends on the material and geometry of the tip. For our tungsten tips, we use $v(w) = 0.6$ [Hommelhoff06b].

The FN equation relates the evolution of the current density to F. Since F is proportional to the applied tip bias, V_{tip}, by a constant relating to the tip radius and material. The effects of a nanotip geometry are explained in more detail in Sec. 1.4.1. Experimentally we can plot $\ln\left(J/V_{\text{tip}}^2\right)$ as a function of $1/V_{\text{tip}}$ to determine the tip radius. This is discussed more in Sec. 4.1.1.

1.2.3 Thermally enhanced field emission

Cold field emission is dominated by tunneling of electrons near the Fermi level of the system. Likewise, thermonic emission is governed by electrons whose energies are on the tail end of the Fermi-Dirac distribution and have energies greater than that of the barrier height. In between these two processes is the regime of thermally enhanced field emission, where the electrons are thermally excited, in our case, by laser light, but not enough to overcome the barrier and instead are emitted via tunneling. This emission is caused by laser heating and for our purposes is called thermally enhanced field emission. This is demonstrated in Fig. 1.5.

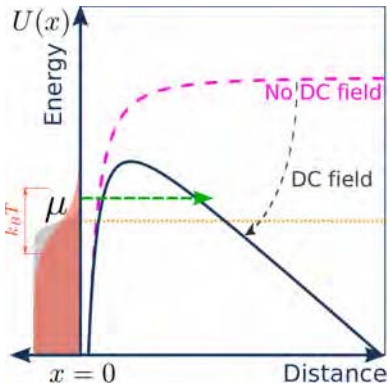

Figure 1.5 – This shows thermally enhanced field emission in which the electron gas within the metal tip is heated to assist in the quantum mechanical tunneling of some of the highly excited electrons when an electric field is applied to the system.

The electron gas is strongly heated to extremely high temperatures via excitation of the electrons within the metal tip, but not enough to overcome the potential barrier [Murphy56, Lee73, Kealhofer12]. For example, laser light can heat the electron gas to temperatures on the order of 1000–2000 K [Krüger13], which is not enough to overcome the barrier. Here, temperature does not refer to the temperature of the metal itself, rather to the temperature of the electron gas. With the absorption of heat by the electron gas, the electrons can transiently occupy higher energy states than the Fermi level and thus can be emitted from the tip via quantum tunneling if a strong electric field is applied to the system, as opposed to absorption of enough energy to overcome the potential barrier as in thermonic emission, Sec. 1.2.1. The heating effects of the system by the laser depend on many parameters such as laser intensity, repetition rate, wavelength, and material properties and is found to be highly non-linear [Kealhofer12].

1.3 Other mechanisms: emission processes induced by a laser field

Since the invention of lasers, laser-assisted electron emission from metallic surfaces has been extensively studied [Lee73, Venus83]. This translates to the emission of electrons via the absorption of energy quanta, or photons, of light and is analogous to the photoelectric effect [Einstein05]. Using continuous wave (cw) lasers, the process of photofield emission (Sec. 1.3.1) was identified [Lee73, Venus83], in which energy from a laser is absorbed by the system to promote an electron to a higher energy state and aid in tunneling. With the advent of ultrafast laser systems, the laser intensity can be greatly increased, and other emission processes begin to dominate, namely above threshold photoemission and eventually optical induced electron tunneling.

1.3.1 Photofield emission

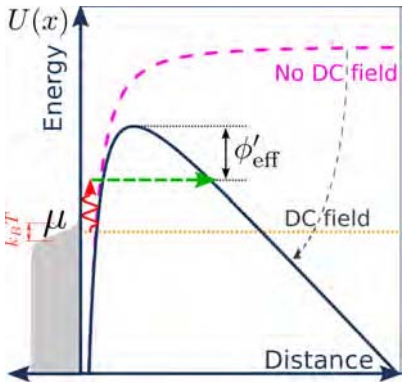

Figure 1.6 – The system absorbs 1 photon, exciting the electrons, causing them to see an effective barrier of $\phi'_{\text{eff}} = \phi_{\text{schottky}} - n\hbar\omega$ promoting tunneling.

In photofield emission the system absorbs less photons than are needed to overcome the barrier. With an externally applied electric field, a penetrable barrier is formed through which electrons can tunnel as seen in Fig. 1.6. The emission rate can be described by the Fowler-Nordheim equation (Eq. 1.19), with the work function replaced by the effective barrier height $\phi'_{\text{eff}} = \phi_{\text{schottky}} - n\hbar\omega$, where ϕ_{schottky} is the effective work function described by the Schottky reduction in Sec. 1.1.1 and n is the number of photons absorbed with $n\hbar\omega < \phi$.

Photofield emission can be identified by comparing the emitted current from tips with and without laser illumination [Hommelhoff06b]. Assuming the tip radius does not change, the effective work function can be deduced from the FN equation. Photofield emission can also be identified in the electron energy spectra by the asymetrical shape of the field emission and the sharp edges around the energies of one-photon and two-photon absorptions [Yanagisawa11]. These one and two photon edges and asymetrical spectra can be seen in Fig. 1.7.

1.3.2 Intense laser induced emission processes

By increasing the laser intensity, the absorption of many photons is more likely, and it is therefore possible for the system to absorb more photons than necessary for the electron to

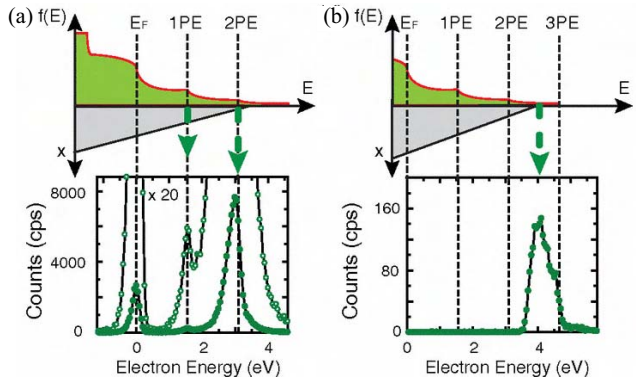

Figure 1.7 – This shows experimental and schematic spectrum showing the edges corresponding to one and two absorbed photons. The experimental conditions for (a) are V_{tip} = -2300 V and the laser power is 50 mW and for (b) V_{tip} = -500 V with a laser power of 50 mW. Here, the top panels show the energy schematic of the Fermi-Dirac distribution of the electrons within the system show in green. The abscissa axis is the distance where $y = 0$ is the metal/vacuum interface and the ordinate axis is the energy. Sharp edges are seen in the distributions corresponding to 1 and 2 photon absorptions, which in turn are seen as sharp peaks in the energy spectrum below. Reprinted figure with permission from H. Yanagisawa *et al.* Phys. Rev. Lett. **108**(8) 087602, 2011. © (2011) by the American Physical Society. [Yanagisawa11].

overcome the potential barrier defined by the work function. This leads to the absorption of more photons and to the emission of electrons with larger energies at high laser intensities. This absorption pushes the electron up into the continuum to an energy of $n\hbar\omega$, where n is the number of photons absorbed and ω is the angular frequency of the photon. The rate of emission of an electron is correlated to the number of photons absorbs as:

$$J(I) \propto I^n, \tag{1.21}$$

and is in agreement with the lowest order of perturbation theory (LOPT) [Joachain12].

At high laser intensity, the laser can no longer be considered from the photon picture. For a small portion of the optical cycle, the laser field acts as a strong DC field, creating a penetrable barrier through which electrons can tunnel. This process is called optical field emission or optically induced tunneling.

Keldysh Theory:

Keldysh introduced a theory providing a link between multiphoton emission and optically induced tunneling [Keldysh65]. We call the regime described by this theory as the Keldysh regime. The Keldysh parameter γ distinguishes between these two regimes; when $\gamma \gg 1$ the system is in the multiphoton regime and when $\gamma \ll 1$ the system is in the optical tunneling regime. In the multiphoton regime, the laser is regarded as a small disturbance to the system and from which the interaction can be considered from the photon point-of-view. In this case, the system can absorb discrete amounts of photon energy until the electrons have enough energy to overcome the potential barrier as seen in Fig. 1.8 (a). By contrast, in the optical tunneling regime, the potential barrier is strongly modulated by the laser field and a tunnelable barrier is formed for a fraction of the optical cycle as seen in Fig. 1.8 (b). For the Keldysh the-

ory to be applicable, the photon energy from the laser must be smaller than the work function of the metal, or ionization potential for an atom.

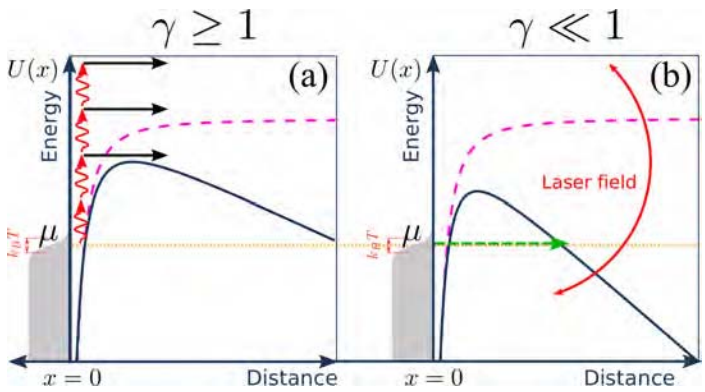

Figure 1.8 – (a) multiphoton regime, $\gamma \gg 1$ (b) tunneling regime, $\gamma \ll 1$

The Keldysh parameter is given by

$$\gamma = \sqrt{\frac{\phi}{2U_\mathrm{p}}}, \tag{1.22}$$

where ϕ is the work function of the material and U_p is the ponderomotive energy. The ponderomotive energy is the cycle-averaged quiver energy, or mean kinetic free energy, of an electron oscillating in the electromagnetic field of a laser light field. U_p is given by

$$U_\mathrm{p} = \frac{e^2 \mathscr{E}_0^2}{4 m_e \omega^2}, \tag{1.23}$$

where e is the electron charge, m_e is the electron mass and $\mathscr{E}_0$ is the peak electric field of the laser with frequency ω. Recalling the cycle-averaged laser intensity from Eq. 1.16, the ponderomotive energy becomes

$$U_\mathrm{p} = \frac{e^2}{2\varepsilon_0 m_e} \times \frac{I}{\omega^2} \propto I\lambda^2. \tag{1.24}$$

From this relation we can see that the tunneling regime (i.e. large U_p) can be reached by either increasing the laser intensity or decreasing its frequency. Emission from this regime is called optical field emission.

The general rate of photoemission [Keldysh65, Bunkin65, Tóth91], $J(\gamma)$, derived from the sum of all the contributions of photoemission from different multiphoton orders, can then be given as

$$J(\gamma) \propto \exp\left(-\frac{2\phi}{\hbar\omega}\left(\left(1+\frac{1}{2\gamma^2}\right)\operatorname{asinh}(\gamma) - \frac{1}{2\gamma}\sqrt{1+\gamma^2}\right)\right). \tag{1.25}$$

This relation is applicable for all γ. The full derivation is found in [Bunkin65].

It is useful to express Eq. 1.25 in the limiting cases where $\gamma \gg 1$ and $\gamma \ll 1$.

Above Threshold Photoemission:
In the case where $\gamma \geqslant 1$, the case with small field amplitude, or large frequency, the system can be thought of in the photon point of view. We have $\operatorname{asinh}(\gamma) \approx \ln(2\gamma)$ giving

$$J(\gamma) \propto \exp\left(-\frac{2\phi}{\hbar\omega}\ln(2\gamma)\right) \propto \left(\frac{1}{2\gamma}\right)^{2\frac{\phi}{\hbar\omega}} \propto \mathscr{E}_0^{2\frac{\phi}{\hbar\omega}}. \tag{1.26}$$

Recall from Eq. 1.16 that the intensity of the laser scales as $\mathscr{E}_0^2$ of the laser field. This means that the photocurrent is proportional to $I^{n_{\min}}$ with $n_{\min} = \phi/\hbar\omega$, approximately the minimum number of photons needed to overcome the potential barrier of the system. We can think of the energy absorption of the system from the photon point of view.

The system absorbs n photons, increasing the energy by $n\hbar\omega$. This pushes a portion of the Fermi-Dirac distribution above the potential barrier for emission as seen in Fig. 1.8 (a). Eqs. 1.21 and 1.26 indicate that the majority of electron emission comes from the absorption of $n_{\min}$ photons. This is enough energy for the electron to escape the potential and be detected with an energy of $\phi - n_{\min}\hbar\omega$. A free electron cannot absorb a photon, so no electrons with higher energy should be detected. If $\gamma \geqslant 1$, there is a high enough probability that the system absorbs more than $n_{\min}$ photons, before an electron is emitted. This is because the laser field is strong enough that even while the electron has adequate energy to escape the potential, it remains within the barrier and can absorb additional photons. These cases where $n > n_{\min}$ are called Above Threshold Photoemission (ATP) for solids and Above Threshold Ionization (ATI) for atoms. (The cases of $n < n_{\min}$ are thermally enhanced and photofield emission. These are discussed above in Secs. 1.2.3, 1.3.1) This phenomenon was first observed in the atomic case in 1979 by Agostini *et al.* in xenon [Agostini79] and for the metallic case in 1989 by Luan *et al.* in copper [Luan89]. Luan *et al.* irradiated a copper surface with 1064 nm (1.16 eV) laser light with an intensity of 5×10^8 W cm^{-2}. They saw characteristic peaks in the emitted photoelectron spectrum (Fig.1.9) separated by the photon energy of the laser, and corresponding to ATP.

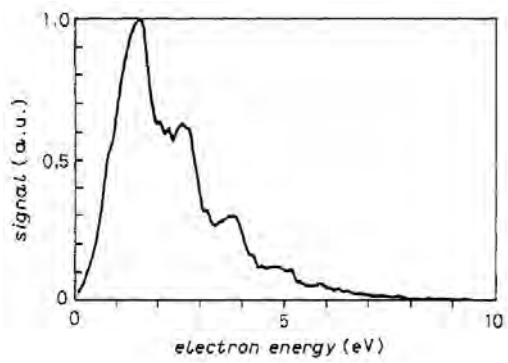

Figure 1.9 – This shows the first observation of ATP peaks by Luan *et al.* in 1989. A copper surface was irradiated with linearly polarized 1064 nm (1.16 eV) laser light with an intensity of 5×10^8 W cm^{-2}. Note the peaks are separated by the photon energy of the incident light. Reprinted with permission from S. Luan *et al.*, "Electron Emission from Polycrystalline Copper Surfaces by Multi-Photon Absorption" Europhys. Lett., **9**(5) 489 (1989) `http://iopscience.iop.org/0295-5075/9/5/014` [Luan89].

Due to the discrete nature of energy absorption by the system, the kinetic energy spectrum of the emitted electrons has peaks with energies $E^{(n)} = n\hbar\omega - \phi_{\text{eff}}$, where $n \geqslant n_{\text{min}}$ is the number of photons absorbed. The peaks may be spread out as the initial states of the electrons involved may be at or below the Fermi level.

As the intensity of the laser increases and γ moves towards 1, changes in the emitted spectra are observed. Most noticeably, at sufficient intensity, the suppression of the lowest-order multiphoton peak is observed. This phenomenon is known as channel closing and is due to the AC Stark effect [Schenk10]. Due to the presence of the laser field, the potential barrier is effectively increased. If the shifted potential barrier exceeds the energy of a given photon order, then the corresponding peak will be suppressed [Muller83, Muller88, Mulser93].

Optical Field Emission:
The transition to the optical tunneling regime is when $\gamma \ll 1$. In this regime, for a fraction of the laser cycle, the laser field forms a penetrable barrier through which electrons can escape via tunneling, not unlike the emission process in cold field emission Sec. 1.2.2 with a high applied external electric field.

In this case we see that $\text{asinh}(\gamma) \approx \gamma - \frac{\gamma^3}{6}$ which gives

$$J(\gamma) \propto \exp\left(-\frac{2\phi}{\hbar\omega} \times \frac{2}{3}\gamma\right) \propto \exp\left(-\frac{4\sqrt{2m_e}\phi^{3/2}}{3e\hbar\mathscr{E}_0}\right). \tag{1.27}$$

This rate is, indeed, equivalent to the tunneling rates for electron emission in static electric field as seen in Eq. 1.19 [Fowler28] and shifts away from the photon picture of $J \propto I^n$ (Eq. 1.26) [Tóth91, Bormann10]. The optical tunneling regime is therefore considered a quasi-static regime, where for a small fraction of the optical cycle the system acts as a large field as been applied to the system. This is analogous to laser-induced ionization in atomic systems.

1.3.3 Electron recollision and rescattering

After an electron has been photoemitted, with a high enough applied electric field from the laser, the laser will drive the potential barrier and possibly steer the motion of the photoelectron back to the system. When the electric field of the laser changes sign, the electron will be accelerated towards the system and can recollide with the system itself. This recollision can lead to several phenomenon, specifically high harmonic generation (HHG) [Burnett77, McPherson87, Ferray88, L'Huillier93] and electron rescattering [Paulus94b]. HHG refers to the recombination of these electrons leading to high-energy photon emission. Rescattering is the fully elastic scattering of a photoelectron with the system itself leading to high-energy electron emission. In this thesis, we are only concerned with electrons and rescattering effects.

The electron spectrum from the rescattering process can be broken up into distinct sections depending on the mechanism behind the emission. The low energy part of the spectrum is dominated by direct electron emission and not from rescattering. The count rate in this region follows the exponential decay superimposed with ATP peaks as observed in multiphotonic

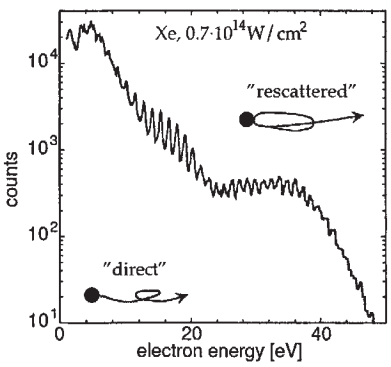

Figure 1.10 – This shows the photoelectron spectrum for rescattered electrons from Xe at a wavelength of 800 nm and intensity 0.7×10^{14} W cm^{-2}. The low energy part of the spectrum is dominated by direct electron emission while the higher energy shows the characteristic plateau of electron recollision with a cutoff of 39 eV. Figure reproduced from [Paulus04] © The Royal Swedish Academy of Sciences. Reproduced by permission of IOP Publishing. All rights reserved.

emission. At sufficiently high energies, the electron count rate does not change with increasing energy. This is called the plateau. The plateau was first observed by Paulus *et al.* in 1994 [Paulus94b, Paulus94a]. A typical ATI plateau (in xenon) can be seen in Fig. 1.10. Eventually at even higher energies, the count rate begins to diminish again. This point is known as the cut-off. The plateau and cut-off form the regions where electron rescattering occurs. The maximum instantaneous kinetic energy an incoming electron can have at the time of recollision is $3.17U_p$ [Corkum93], and the maximum final energy an electron can gain through rescattering is $10U_p$ [Paulus94a]. This is known as the cutoff energy. The cutoff can be identified experimentally by the cutoff in the spectrum, or energy where the count rate begins to drop off after the plateau.

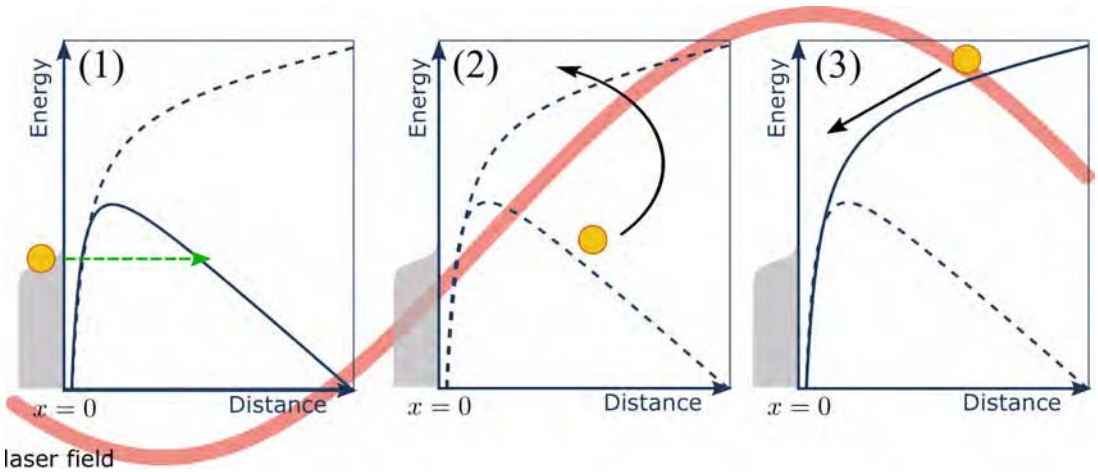

Figure 1.11 – The three step model of electron recollision and rescattering (1) The **photoemission** of an electron via optical field emission. (2) The **propagation** of the photoelectron away from the system and its acceleration back towards the parent system as the laser field (red curve) changes sign. (3) The **recollision** of the photoelectron with the parent system.

Three Step Model:

The rescattering process can be easily envisioned using the Three Step Model (TSM), formulated by Paul Corkum in 1993 [Corkum93]. The three steps are given as:

1. **Photoemission** of an electron generally via tunneling in optical field emission
2. **Propagation** of the photoelectron away from system and then acceleration back towards the system as the field changes sign
3. **Recollision** of the photoelectron with the parent system. Many physical phenomena are possible at this stage such as recombination and reabsorption with the parent system itself, however we are only concerned with recollision and rescattering of the photoelectron with the parent system in this thesis

By applying Eq. 1.23 to Eq. 1.22, we can rewrite the Keldysh parameter as the ratio of two frequencies

$$\gamma = \frac{\omega}{\omega_{\mathrm{t}}}, \tag{1.28}$$

where ω is the optical driving frequency of the laser and ω_{t} is a characteristic tunneling frequency given by $\omega_{\mathrm{t}} = eE_0/\sqrt{2m_e\phi}$ [Herink12]. The parameter can be thought of as an adiabaticity parameter to define the different photoemission regimes. As discussed in above the resulting electron movement in the driving field, and energy cutoff, scale with the ponderomotive energy, U_{p} (Eq. 1.23), forming the first two steps of the three step model.

1.4 Peculiarities arising from a nanotip geometry

The laser emission phenomenon described thus far hold true for atomic systems and metallic surfaces [Joachain12], however we must take into account that in this thesis, investigations are on photoemission from nanotip systems. As such, the geometry of these systems must be taken into account when considering the applied DC field as well as optical field from the laser.

1.4.1 Geometric field enhancement

To achieve cold field emission by applying reasonable voltages, etched field emission nanotips are generally used, which have a half-sphere termination on a nanometer size. This is due to the accumulation of charge within the surface apex of the tip, called the lightning rod effect. For tips, the field at the end of the apex is given by

$$F = \beta V_{\mathrm{tip}}, \tag{1.29}$$

where V_{tip} is the applied voltage, and β is related to the tip radius r with $\beta = 1/kr$, with k being a dimensionless factor depending on the shape of the tip and the extraction geometry typically on the order of $k \sim 5$ near the apex [Gomer61]. β can be thought of as the field amplification factor and can reach factors varying from 10^6 to 10^7 m^{-1} from tip to tip. Thus, the high fields needed to achieve emission can be enhanced geometrically by the sharpness of the tips.

In nanotip systems, since the natural field enhancement is geometrical, the sharper the tip, the lower the voltage needed to reach observable emission. The minimum voltage needed to observe emission is called the emission threshold. For our typical systems, the voltages needed to reach this regime are given in the Table 1.1.

Table 1.1 – This table lists typical samples placed in our system along with their work functions [Mendenhall37, Haynes12, Houdellier12] and typical detectable emission thresholds for our experiment.

Tip Material	ϕ	Average r	Average V_{tip}	β	Applied F
Polycrystalline W	4.5 eV	250 nm	750 V	4×10^6 m^{-1}	3 GV/m
Single Crystal W(310)	4.35 eV	30 nm	200 V	20×10^6 m^{-1}	4 GV/m
Polycrystalline Ag	4.26 eV	50 nm	800 V	4×10^6 m^{-1}	3.2 GV/m
CCnT	5 eV	5 nm	300 V	40×10^6 m^{-1}	12 GV/m

1.4.2 Optical field enhancement

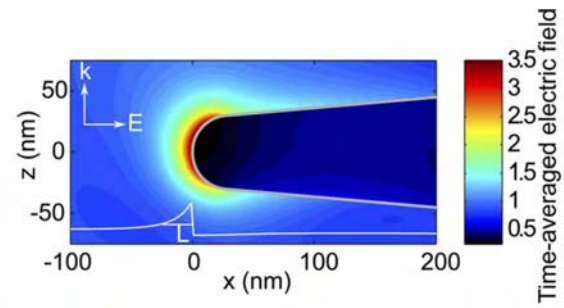

Figure 1.12 – This shows a finite element modeling of the optical field enhancement in the vicinity of a sharp tungsten nanotip with radius $r = 30$ nm. The color indicates the ratio of the field to that of the incident light ($\lambda = 800$ nm, polarization parallel to the tip axis). Enhancements up to 3.4 are seen in close proximity to the tip. The enhancement (white curve) quickly decays in free space. Adapted with permission from S. Thomas *et al.*, Nano Lett. **13**(10) 4790. © (2013) American Chemical Society. [Thomas13].

Optical fields from a laser are strongly affected by nanoobjects. In particular, optical near fields are excited when the wavelength of the light is greater than the size of the object. A strong localization of the fields occurs near sharp structures and edges. Typically our nanotips are on the order of ∼10-100 nm in diameter, much smaller than the commonly used 800 nm wavelength of the laser light.

There are three main reasons for the optical field enhancement [Thomas13]:

1. A **geometric field enhancement** caused by the dielectric constant discontinuity at the metal/vacuum interface. This leads to an accumulation of charge just under the surface which creates a strong local field due to the small structure size of the nanoobject. This is analogous to the electrostatic lightning rod effect and to the geometric field enhancement for static fields described in Sec. 1.4.1.

2. **Antenna resonance** occurs in structures of size an odd multiple of half the wavelength [Thomas13, Krüger13].

3. **Plasmonic effects** in plasmonic materials such as silver or gold create a surface or plasmon resonance when the optical frequency is close to the resonance frequency of the plasmon [Sasaki13, Stockman11]. These resonances are highly material, shape and wavelength dependent.

This means that the typical laser intensities needed to reach the strong-field regime are greatly reduced due to optical field enhancement and the need for an amplified laser chain is much less.

The optical field enhancement in the vicinity of a sharp tungsten nanotip, with radius $r =$ 30 nm can be calculated using finite element modeling. This is seen in Fig. 1.12 (calculation performed by [Thomas13]). The tip is illuminated with a laser pulse of wavelength 800 nm and polarization parallel to the tip axis. From this we that the optical field of the laser is enhance up to 3.4 in close proximity of the tip. This enhancement exponentially decays away in free space. Inside the tip, the metal is nearly field free.

The optical field enhancement depends on the both the geometry of the tip and its material. Gold and Silver have plasmonic resonances in the visible domain, which lead to higher field enhancement [Arbouet12]. The radius of the tip and the opening angle also greatly influence the field enhancement. A smaller radius tip has higher enhancement, as discussed above, but the dependence of the angle is not straightforward. In [Thomas14], Thomas (group of P. Hommelhoff) calculated that there is an optimal angle for which the field enhancement is highest. For tungsten, this is a half opening angle of 30°; for gold it is 15°.

1.4.3 Facet emission

The metallic nature of tip means that the atoms in the tip are oriented in a crystalline structure. Each crystal orientation has a slightly different work function [Mendenhall37, Haynes12], and thus electron emission is easier or harder from a particular orientation. In an etched nanotip, this corresponds to each side, or facet, having a different crystal orientation. Etching a nanotip from a single crystal oriented wire ensures the location of each facet orientation with respect to the detector.

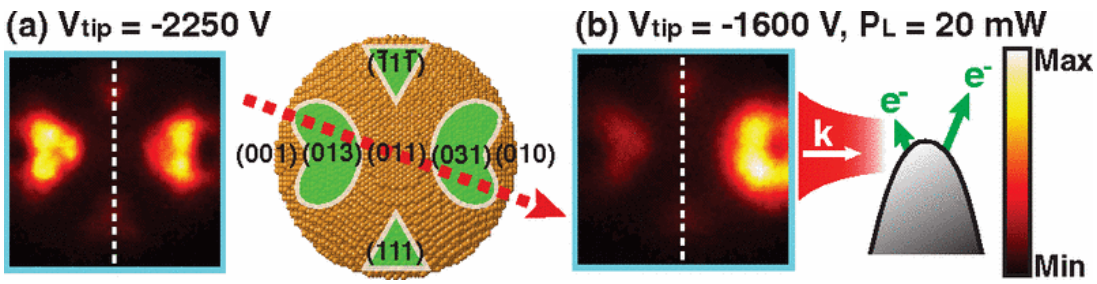

Figure 1.13 – (a) This shows emission sites from a (011) oriented W nanotip illustrating that the (310) facet has the most intense electron emission. The schematic shows the crystal facet orientations of the nanotip. (b) This shows the emission patterns with laser irradiation. The schematic shows the side view of the laser-induced field-emission geometry. Reprinted figure with permission from H. Yanagisawa *et al.* Phys. Rev. Lett. **103**(25) 257603, 2009. © (2009) by the American Physical Society. [Yanagisawa09]

In tungsten, the (310) orientation has the lowest work function [Mendenhall37]. In Fig. 1.13 (a), Yanagisawa *et al.* [Yanagisawa09, Yanagisawa10] show that the most intense electron emission comes from the (310) oriented facets. When illuminated by a laser (Fig.1.13 (b)), the emission pattern becomes strongly asymmetrical. Here the most intense emission is opposite the exposed side relative to the laser incidence. As the (310) orientation yields the brightest electron emission, we chose to etch our tungsten nanotips out of single crystal tungsten oriented in the (310) direction such that the bright emission site is oriented towards the detector.

1.4.4 Electron propagation in the vicinity of a nanotip

Let us consider an electron after it has left the system, traveling in the electric field of a laser in the vicinity of the sharp nanotip. Due to the sub-wavelength size of nanostructures, and in particular our nanotips, the optical fields interacting with, and around these structures vary greatly (Sec. 1.4.2) such that the resulting electron dynamics may be quite unexpected [Herink12].

Herink *et al.* (group of C. Ropers) [Herink12] investigated the cutoff energy of electrons from a gold nanotip as a function of laser wavelength (and by consequence U_p). Recall the ponderomotive energy, is the cycle-averaged quiver energy of an electron in an electric field. The quiver motion, or excursion, is the amplitude of a free electron in the electric field of a laser [Joachain12]. This motion is given by

$$l_\mathrm{q} = \frac{e\mathscr{E}_0}{m_e\omega^2}. \tag{1.30}$$

At longer wavelengths, Herink *et al.* observed the convergence of the cutoff energies. This is because the quiver motion of the emitted electrons extends beyond the decay length of the optical field ($\sim 1/4$ the tip radius) [Herink12]. We can now define a new adiabaticity parameter, δ, relating the (1/e)-decay length $l_{\mathscr{E}_0}$ of the optical field to the quiver amplitude as

$$\delta = \frac{l_{\mathscr{E}_0}}{l_\mathrm{q}} = \frac{l_{\mathscr{E}_0} m_e\omega^2}{e\mathscr{E}_0}. \tag{1.31}$$

While the Keldysh parameter describe the emission process of the electron from the system (step 1 in the TSM), δ describes the propagation and acceleration of the electron once emitted from the system (step 2 in the TSM) [Herink12]. For $\delta \gg 1$, the quiver regime, the electron oscillates in a nearly homogeneous field for multiple optical cycles, as described for "normal" electron propagation. For $\delta \ll 1$, the sub-cycle regime, the electron rapidly escapes the tip-enhanced field in a time much shorter than an optical cycle as seen in Fig. 1.14.

This effect is corroborated by Park *et al.* (group of C. Lienau) [Park12] who observed a pronounced acceleration of electrons within the field gradient of their nanotip for long wavelengths. They found that in the sub-cycle $\delta \ll 1$ regime, angle-dependent kinetic energy spectra revealed a narrowing of the emission cone for fast emission, ascribed to the fast escape of the electrons from the modified field. This is attributed field-induced steering of these sub-cycle electrons, as opposed to the divergent quiver motion of the $\delta \gg 1$ regime. The results of

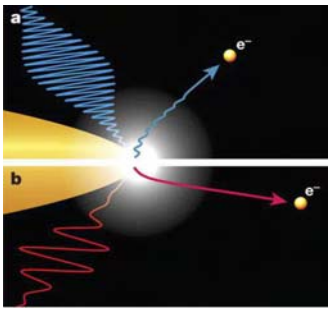

Figure 1.14 – This shows the electron trajectories for photoelectrons in a strong light field for (a) short wavelengths and (b) long wavelengths. The white region is the characteristic decay length of the optical cycle. Adapted by permission from Macmillan Publishers Ltd: Nature **483**(7388) 190. Copyright (2012) [Herink12].

Park *et al.* indicate that in the sub-cycle regime, both the kinetic energy distribution and the electron emission direction (i.e. propagation direction) are influenced by the modified laser field.

1.5 Summary

The focus of this chapter was to present the physical mechanisms behind electron emission from sharp nanotips. These emission processes are summarized graphically in Fig. 1.15. From changing the parameters applied to our system (applied voltage V_{tip}, laser intensity I and photon energy $\hbar\omega$, and nanotip material and radius r) we can change the dominant emission process that we observe.

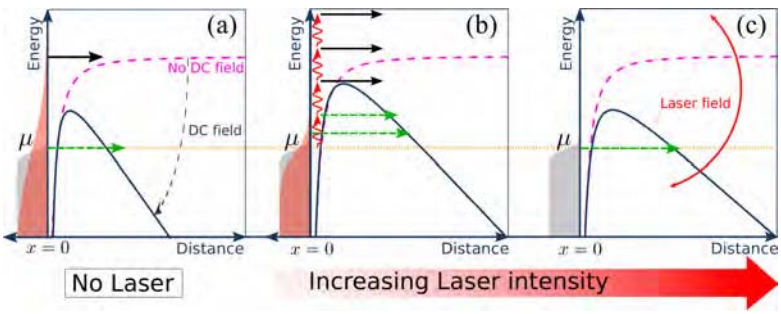

Figure 1.15 – Schematic showing the mechanisms behind laser induced electron emission from a system. The Fermi energy level, μ, and distribution is shown in gray, with the redistribution of the energies due to thermal effects shown in red. The metal/vacuum interface is located at $x = 0$. (a) This shows cold field tunneling (green dashed arrow) and thermal emission (black arrow) that take place without laser illumination. (b) This shows emission processes for low laser illumination. The laser pulses can be thought of from the photon point of view. If a sufficient number of photons are absorbed, an electron can escape over the potential barrier (black arrows), if not an electron can be emitted via assisted tunneling by absorption of a photon or thermal absorption of the energy of a photon (green dashed arrows). (c) At high laser intensities, the laser field modifies the potential barrier itself and electrons can emit via optical tunneling.

There are three main mechanisms behind electron emission from a nanotip, depending on the field applied and the laser intensity induced on the system. Fig. 1.15 shows these emission mechanisms. The Fermi energy distribution is shown in gray, with the Fermi level, μ, marked

by a yellow line to aid the eye. The redistribution of the Fermi energies due to thermal effects is shown in red. The metal/vacuum interface is located at $x = 0$. With no laser, the system can be heated up such that the electrons can obtain enough energy to overcome the potential barrier (black arrow), or by applying a sufficient external electric field, the barrier is modified such that the electron can quantum mechanically tunnel through (green dashed arrow) as seen in Fig. 1.15 (a). In Fig. 1.15 (b), the laser pulses can be thought of from the photon point-of-view. Here the laser has moderate intensity and a low to moderate external field can be applied to the system. If a sufficient number of photons are absorbed, an electron can escape over the potential barrier (black arrow). If not, an electron can be emitted via assisted tunneling by absorption of a photon or thermal absorption of the energy of a photon (green dashed arrows). At sufficiently high enough laser intensities, the laser field itself modifies the potential barrier allowing it to be penetrable via tunneling (Fig. 1.15 (c)).

For the rest of the manuscript, I focus mainly on laser induced phenomena and use the cold field emission (Fig. 1.15 (a), green dashed arrow) only to determine the static local field and provide a baseline for emission. During my research I observed thermally enhanced field emission in carbon and silver based tips (Fig. 1.15 (b), green dashed arrow). Above threshold emission was seen in all the samples we studied, tungsten, silver and potentially carbon; however, ATP peaks were only observed in tungsten tips (Fig. 1.15 (b), black arrows). Optical tunneling and rescattering effects were seen in silver tip emission, (Fig. 1.15 (c)).

2

Optical setup and development of a NOPA

The colours red, blue and green are real. The colour yellow is a mystical experience shared by everybody.

– Tom Stoppard,
Rosencrantz & Guildenstern are Dead

To investigate the emission of electrons from a nanotip induced by a laser field, there are certain requirements that must be met by the system. We need a short pulse duration to avoid thermal effects created by the laser as well as the high peak power associated with such short pulses. We also would like a high repetition rate to have the best signal to noise ratio possible. As such, the laser system went through much evolution. In general, the system is very versatile involving many different elements from a commercially available laser amplification chain to home made laser development. The first setup uses the traditional ultrafast laser amplification chain, an Ti:sapphire femtosecond oscillator at 62 MHz with the ability to be amplified in energy via a regenerative amplifier at 1 kHz. The next generation laser source is a variable repetition rate (from single shot to 2 MHz) infrared (IR) fiber laser with a non-collinear optical parametric amplifying (NOPA) stage, which allows us the opportunity to keep the duration short and both vary the repetition rate of the laser as well as the wavelength.

In this chapter I will first detail the conventional Ti:sapphire laser system and amplification chain that was used for the results in this thesis. I describe the laser characterization that is needed to interpret the data. Finally I discuss the NOPA development required to further clarify and augment our conclusions.

2.1 Optical setup

In this section I explain the optical setup of the experiment that was used in the research I present in this thesis. I describe the Ti:sapphire laser system and amplification chain as well as the diagnostics and characterization necessary for understanding the physics of the interaction.

2.1.1 The laser system

A standard commercial Ti:sapphire femtosecond oscillator, Femtolaser[1] femtosource synergy, is the primary laser source for high repetition rate experiments. The oscillator has a repetition rate of 62 MHz, with a central wavelength of 800 nm and spectral bandwidth of about 70 nm full width at half maximum (fwhm) corresponding to a a pulse duration of ∼20 fs. The total available mean power at the output of the oscillator is ∼360 mW which corresponds to a pulse energy of 5.8 nJ. The output of the oscillator can then be either sent to the experiment, or amplified via a regenerative amplifier.

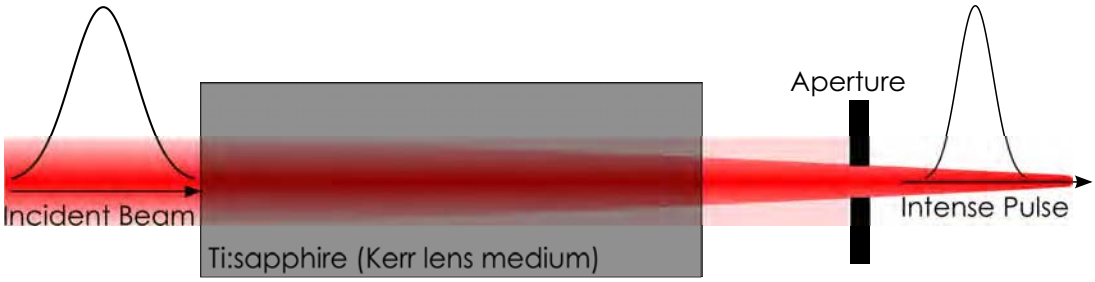

Figure 2.1 – schematic of the Kerr lens modelocking principle

The laser system is based on the output of a Kerr lens modelocked (KLM) titanium-sapphire (Ti:sapphire) oscillator whose pulses can be amplified in a chirped pulse amplification (CPA) system [Träger07, Brabec92]. The gain medium is a titanium doped sapphire (Ti:sapphire) crystal generally used for ultrafast systems due to its high absorption in the visible wavelengths and broad gain bandwidth around 800 nm ($\Delta\lambda \approx 200$ nm) [Moulton86] (Fig. 2.1).

2.1.2 Oscillator

The output of the oscillator is a meticulously controlled parameter of the experiment (Fig. 2.2 (a)). The pulse energy, polarization, duration and chirp are carefully monitored and regulated throughout the experiment. The inherent chirp of the oscillator as well as any additional chirp from optical materials and the input window of the experimental chamber are measured with a SPIDER (described in Sec. 2.2) and pre-compensated for with chirped mirror pairs. The power is carefully regulated with a half wave plate and thin film polarizer (TFP) throttle with an extinction ratio of ∼200:1. The polarization of the beam is additionally cleaned with another TFP pair and then selected with a half-wave plate before being delivered to the experimental setup. In order to minimize chirp and maintain the short pulse duration all reflective optics are used when possible (mirrors, reflective focusing elements, etc.), and when not, the thinnest possible (TFP, 0 order broadband (femtolaser) half-wave plate, etc.).

2.1.3 Regenerative Amplifier:

Alternatively, the output of the oscillator can be sent for amplification through a regenerative amplifier (regen) (Fig. 2.2 (b)). A regen works similarly to a laser cavity [Barty96, Wynne94],

[1] http://www.femtolasers.com/

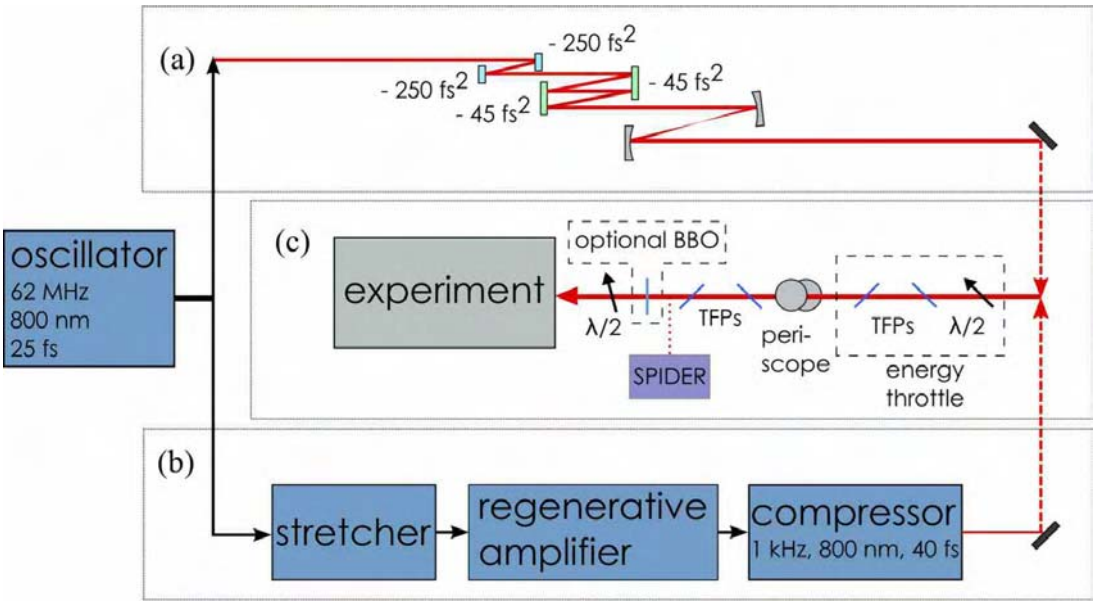

Figure 2.2 – (a) The direct output of the oscillator can be carefully controlled and shown onto the experiment (b) or can be amplified in energy and reduced in repetition rate. (c) The careful control of polarization and energy deposited onto the tip is crucial for the experiment. An optional nonlinear crystal can be inserted into the beamline to frequency double the light. TFP: thin film polarizer, SPIDER: pulse characterizer described in Sec. 2.2

with one pulse injected into the cavity and then extracted after amplification. For the amplification stage, the few femtosecond pulses generated from the oscillator are stretched temporally to a few hundreds of picoseconds before amplified and then compressed back to few femtosecond pulses. The low energy, stretched pulse, is injected into the cavity using a Pockels cell. The pulse makes several round trips through the gain medium (generally Ti:sapphire) and then switched out via another Pockels cell. The high energy pulse is then recompressed back to its Fourier limited duration. This allows us to have pulses with energy on the order of 350 μJ, with a repetition rate of 1 kHz, and pulses around 40 fs, with a Fourier limit of 35 fs. While only a few nJ of energy are required for electron emission from a nanotip, the higher energy pulses allow for more pulse manipulation such as pulse shaping and wavelength conversion. The relatively low repetition rate allows the investigation of potential thermal effects put on the system due to moderate mean power deposition.

2.1.4 1030 nm fiber laser

The acquisition of a Tangerine fiber laser system from Amplitude Systems[1] provides an expansion from the well-developed Ti:Sapphire laser system. A unique property of this fiber laser system is its variable repetition rate. The output has the same peak power and pulse characteristics, with an adjustable repetition rate from single shot up to 2 MHz and pulse duration of 300 fs. This is of interest to us since we wish to investigate the thermal properties of the electron emission using a large range of repetition rates. Since the output of the laser has a

[1] http://www.amplitude-systemes.com/tangerine-fiber-lasers.html

central wavelength of 1030 nm, and a pulse duration of 300 fs, a NOPA stage is built to allow for short pulses and flexibility in wavelength. The NOPA is described in Sec. 2.3

2.2 Laser characterization diagnostics

The correct characterization of the laser pulses is vital to understanding its effects on the system. As the processes are often intensity dependent, this means that careful measuring of the laser spot size, pulse duration and pulse energy that are needed to evaluate the laser intensity (in W cm^{-2}) that illuminate the nanotips.

2.2.1 Spot Size Characterization

For a Gaussian beam, the $1/\mathrm{e}^2$ radius (where e is Euler's number) of the intensity, w, for a beam of wavelength λ is given as function of beam propagation, x, where

$$w(x) = w_0\sqrt{\left(1+\frac{x^2}{x_R^2}\right)}, \tag{2.1}$$

and x_R is the Rayleigh range given by

$$x_R = \frac{\pi w_0^2}{\lambda}, \tag{2.2}$$

and is defined as the positions where $w(x) < \sqrt{2}w_0$. The beam is narrowest at position $z = 0$ and this position is called the beam waist and has a size of w_0. For a focus of length f, w_0 can be found by

$$2w_0 = \left(\frac{4\lambda}{\pi}\right)\left(\frac{f}{D}\right), \tag{2.3}$$

where D is the diameter illuminated on the lens, in other words, the collimated $1/e^2$ diameter of the laser beam before focusing. The derivation of this relation can be found in Ref. [Saleh07].

The beam is never a perfect Gaussian, nor is it perfectly focused, so measuring the beam diameter is necessary. The easiest method of spot size measurement is to directly focus the laser onto a beam profiling charge-coupled device (CCD) camera and to measure the spot size from the image produced. However, the geometrical constraints of our optical setup due to the focusing elements – on-axis spherical mirror and off-axis parabolas (OAP) – and small focal length do not allow us to characterize the focus spot size with a beam profiler. Instead we turn to other means of spot size measurement, such as a knife edge measurement.

In a knife edge measurement, the intensity of the beam is measured as a function of the position of the translation of a sharp edge (a knife or razor blade) as it passes through the beam. If the edge passes through the focus, a 1-dimensional measurement of the focus spot size is recorded.

The same measurement for the edge rotated 90 degrees gives the second dimension of the spot and tells us the asymmetry of the spot.

The intensity can be fit to the error function (See Fig. 2.3)

$$I(x) = \frac{1}{2} I_{\max} \left(1 - \operatorname{erf}\left(\frac{\sqrt{2}x}{w(x)} \right) \right), \tag{2.4}$$

where x is the coordinate of translation of the edge and $I_{\max}$ is the maximum intensity (when the beam is not blocked). From this, the beam size can be calculated.

The actual measurement of the spot size can be a bit difficult. Due to the small focal length of the spherical and off axis parabola mirrors we used, the geometry for making a knife edge measurement can be tricky and confining. The on-axis focusing of the spherical mirror adds another element of difficulty. For the on-axis measurement, the mirror is tilted so that the focus is astigmatic in one dimension. The non-astigmatic dimension is measured, and the process is repeated for the other dimension.

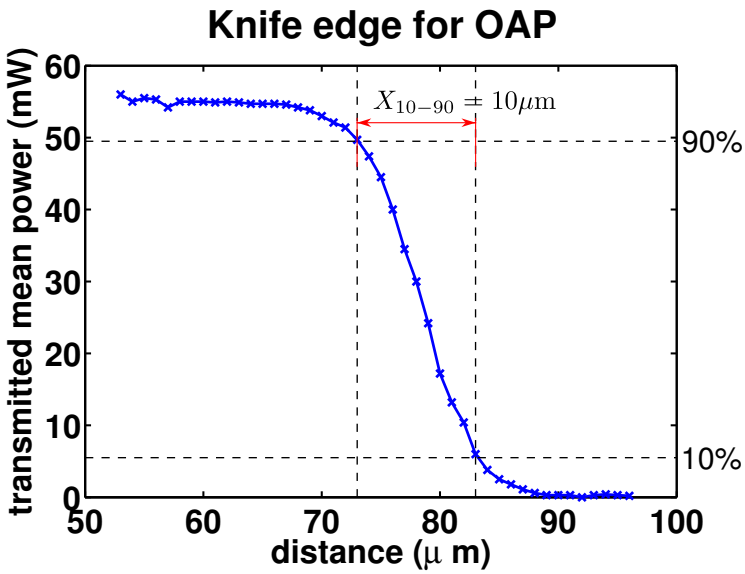

Figure 2.3 – Knife edge measurement for one dimension of the focus from an OAP. The X_{10-90} distance is 10 μm corresponding to $w_0 = 3.9$ μm.

We can calculate the $1/e^2$ radius of the beam using a simple conversion between the points at which the transmitted power is 10% and 90% maximum transmission, X_{10-90}. Fig. 2.3 shows a typical knife edge measurement from the OAP focusing element. Here the measured distance X_{10-90} is 10 μm. Relating the Gaussian function to Eq. 2.4, we have the relation that $X_{10-90} = 1.28 \cdot 2w_0$. From this we see that the measured radius of the OAP focus is $w_0 = 3.9$ μm. Such a small focus is needed to reach the peak laser intensities required for electron emission.

2.2.2 Pulse duration and phase

The measurement and characterization of an ultrafast laser pulse is essential for using them. This means measuring how long each pulse is as well as the spectral phase that may be on a pulse. A more in-depth analysis of spectral phase can be found in Sec. 1.1.2. The technique we use for 800 nm pulses is called Long Crystal Spectral Phase Interferometry for Direct Electrid-field Reconstruction (LX SPIDER) [Radunsky06] and is a method for mesuring a pulse entirely in the frequency domain from which via analysis of the fringe structure of a spectral interferogram, phase and pulse information can be retrieved [Iaconis98]. In a traditional SPIDER, the pulse that is to be analyzed is split into three. A known chirp is added to one pulse and a known delay separates the other two. Recombining the three pulses in a nonlinear crystal for Sum Frequency Generation of the whole spectrum allows the spectrogram to be collected in a spectrometer and then analyzed. In an LX SPIDER, the beam to be analyzed is spatially separated into two and passed at a slightly different angle through a nonlinear crystal with a known time separation and recombined on the entrance slit of a spectrometer. As the time delay and spectral shear is known, the spectrogram can be fit and the phase and pulse duration of the pulses can be retrieved. The layout of an LX SPIDER can be seen in Fig. 2.4.

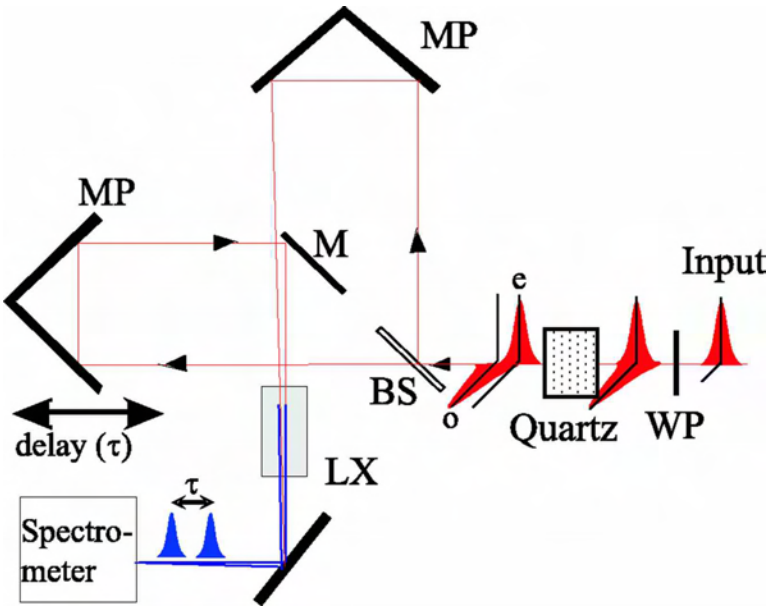

Figure 2.4 – This shows the layout of an LX SPIDER. Reprinted with permission from [Radunsky06]

We use a commercially available LX SPIDER pulse measurement system from APE[1]. An identical window to that of the laser incoupling window of chamber is placed in front of the the input to the SPIDER so that any induced chirp can be pre-compensated. The measurement is taken after the beam has passed through all dispersive elements (except for said incou-

[1] http://www.ape-berlin.de/en/products/spider/lx-spider

pling window) so that the exact characterization of the pulses that arrive on the nanotip is known.

2.2.3 Peak Intensity

In general when discussing ultrafast laser pulses, terms such as "pulse energy," and "peak intensity" are used, but the measurement of such is not evident. For low repetition lasers, such as the 1 kHz amplified pulses, the pulse energy can be directly measured using an energy meter. From this measurement, along with the spot size and pulse duration, the peak intensity for one pulse, can be calculated.

$$I_{\text{peak}} = \frac{2E}{\Delta t \pi w_0^2}, \tag{2.5}$$

where E is the pulse energy, Δt is the pulse duration and πw_0^2 is the spot size.

For high repetition lasers, such as those from the oscillator, direct measurement of the pulse energy is not possible because the pulses are too close temporally. Instead the average power is measured which includes the time between pulses when the energy is 0. Thus to calculate the peak intensity, and pulse energy one must also take into account the repetition rate of the laser as well as pulse duration and spot size.

$$I_{\text{peak}} = \frac{2P_{\text{mean}}}{R\Delta t \pi w_0^2}, \tag{2.6}$$

where R is the repetition rate of the laser.

2.3 Noncollinear Optical Parametric Amplifier (NOPA)

While the use of the traditional laser chain has great utility and flexibility in the types of experiments that can be done with our setup, further investigations into mean power and wavelength dependent effects were of interest to me during my thesis research. As such, we acquired an infrared fiber laser system which allows a variability in repetition rate, from single shot to several tens of MHz, while maintaining the same output peak power. The drawback of such a fiber system is long pulse duration, 300 fs. In order to have access to the short pulse duration needed, we built a Noncollinear Optical Parametric Amplification (NOPA) stage at the output [Cerullo03]. This laser source has both fine tuning capabilities in wavelength and repetition rate as well as a short output.

The high peak power of ultrafast laser systems has led to the use of Optical Parametric Amplification (OPA) which allows the fundamental wavelength to be transformed and amplified into any color from the visible to mid-infrared. In order to compare our results with those from the oscillator and regen interaction, as well as to use the same optical setup, we first center the output of the NOPA at 800 nm.

2.3.1 Optical parametric amplification

The amplification of a weak signal of frequency ω_s by an intense pump beam ω_p by the propagation of the two beams through a non-linear crystal can be achieved by difference frequency generation (DFG). In this case, a high energy photon, ω_p, is split into two lower energy photons: the signal ω_s, and idler ω_i. This is shown in Fig. 2.5. DFG must obey the conservation of momentum and energy relations so that $\hbar\omega_p = \hbar\omega_s + \hbar\omega_i$. When a sufficient intensity of high energy photons (the pump) is introduced to the nonlinear crystal, spontaneous amplification, or fluorescence, occurs for wavelengths that are phase matched. This is simply the parametric amplification of the vacuum or quantum fluctuations, or two-photon spontaneous emission from a virtually excited level [Cerullo03]. This forms a ring of multicolored light at the proper phase matching angle and is called parametric super fluorescence (SF.) This process is known as optical parametric amplification.

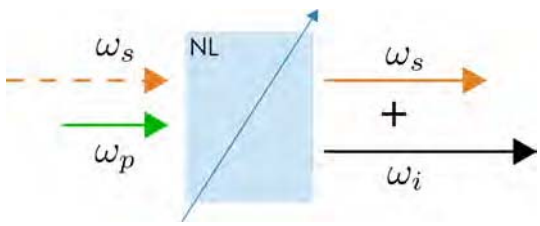

Figure 2.5 – This shows a schematic of the DFG process. A high energy photon ω_p, is split into two lower energy photons: the signal ω_s, and idler ω_i.

As part of the pump energy will be transfered to the seed wavelength, this parametric process is most efficient when the different interacting waves have a proper phase relationship in the propagation direction. This occurs when $\Delta\mathbf{k} = 0 = \mathbf{k}_p - \mathbf{k}_i - \mathbf{k}_s$. This is called phase matching. In order to achieve this phase matching, we use an anisotropic crystal, where the refractive index varies with the direction of propagation. The crystal is cut at a given angle θ such that the index seen by each wave is the same and

$$\mathbf{k}_p = \mathbf{k}_s + \mathbf{k}_i, \tag{2.7}$$

where $\mathbf{k}_j = \frac{\omega_j n_j}{c}$ is the wave vector of the beams and n_j is the relative index of refraction for each wavelength of ω_j, with $j = p, s, i$.

Simply tilting the crystal generally only allows phase matching for a narrow bandwidth of signal wavelengths. This is from the limitation of gain length in an OPA crystal due to spatial walkoff between the pump, signal and idler beams due to group velocity mismatch (GVM). To satisfy phase matching for a large bandwidth, we propagate the pump in the crystal with a noncollinear geometry from the signal with an angle α. This adds another degree of freedom to the system with which we can use to match the pump velocity to those of the signal and idler. To find the angle, α between the pump and signal angles we use the Sellmeier equations to play with the ordinary and extraordinary indices of the crystal. Satisfying the vector triangle given in Fig. 2.6, and Eq. 2.7 we have

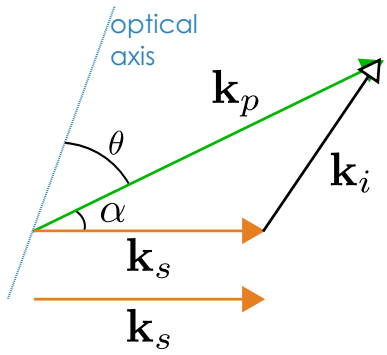

Figure 2.6 – Vector schematic of the 3 wave difference frequency mixing in a non-linear material. α is the angle between the pump and signal beams and θ is the angle between the pump and optical axis of the material. The phase matching is satisfied such that $\mathbf{k}_p = \mathbf{k}_i + \mathbf{k}_s$.

$$|k_i|^2 = |k_s|^2 + |k_p|^2 - 2|k_p||k_s|\cos(\alpha). \tag{2.8}$$

Since $\mathbf{k}_j$ is the wave vector, we know

$$(n_i\omega_i)^2 = (n_s\omega_s)^2 + (n_p\omega_p)^2 - 2n_p\omega_p n_s\omega_s\cos(\alpha). \tag{2.9}$$

This forms a solvable second order equation for n_p, given by

$$n_p^2 - 2n_p n_s \frac{\omega_s}{\omega_p}\cos(\alpha) + \frac{(n_s\omega_s)^2 - (n_p\omega_p)^2}{\omega_p^2} = 0. \tag{2.10}$$

We choose a solution for the extremes of the ordinary and extraordinary indices for the crystal for the pump, n_{po}, n_{pe}. These are given by the ellipsoid index which depends on the angle of the crystal,

$$\frac{1}{n_p(\theta)} = \frac{\sin^2(\theta)}{n_{pe}^2} + \frac{\cos^2(\theta)}{n_{pe}^2} \tag{2.11}$$

The ordinary and extraordinary indices are given by the Sellmeier equations. This allows us to solve for θ as a function of α and ω_s, the signal wavelength.

We consider our particular case using the second harmonic of our 1030 nm fiber laser at 515 nm. The amplification will be produced in the near-infrared regime. In order to shorten the pulse and study wavelength and repetition rate dependencies, the first step is to center the output wavelength at 800 nm in order to compare the results with those from the oscillator and regen interactions. Plotting the phase matching dependencies for various α, we find that the broadest bandwidth around 800 nm is found for $\alpha = 2.6°$, typically $\sim$150 nm, as seen in Fig. 2.7.

The biggest difficulty then becomes how to shorten the pulse and ensure the shot-to-shot stability of the NOPA output as the repetition rate changes. The NOPA output beam quality must not change in pulse energy, duration nor profile for different repetition rates.

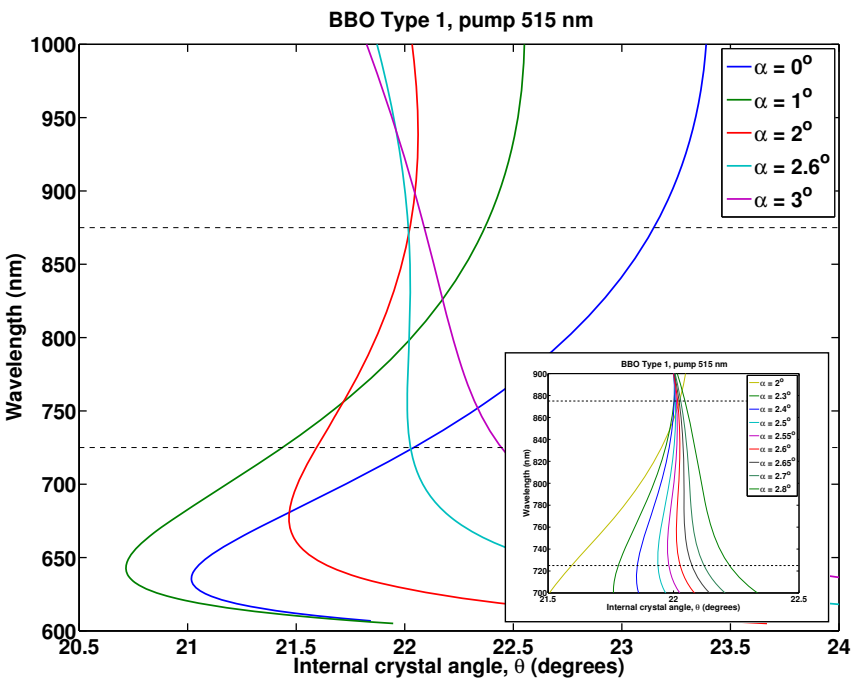

Figure 2.7 – Phase matching curves for a Type I BBO crystal for different pump tilt geometries for a pump of 515 nm. The figure plots the phase matched wavelength for a particular crystal angle. The largest band of phase matching is where a particular angle corresponds to many match wavelengths. Around 800 nm, the largest band of phase matching is for a pump angle of $\alpha = 2.6^\circ$ with an internal crystal angle of $\theta = 22^\circ$. The detail of these angles can be seen in the inset.

2.3.2 NOPA overview

The development of visible NOPAs using an 800 nm Ti:Sapphire source laser has been a very active field in the past 20 years [Cerullo97, Wilhelm97, Shirakawa98, Tan01, Degert02]. However, the repetition rate of such lasers is limited by the rate of the amplification laser. The scalability of OPAs in repetition rate is achievable as there is little energy storage in the nonlinear amplifying material [Rothhardt13]. The advent of pulsed, high repetition rate fiber lasers has driven the development of high repetition rate OPA systems [Rothhardt13, Rothhardt10, Hädrich08]. However, thermal effects will eventually limit the scaling of OPAs [Rothhardt13]. At high average power, thermal lensing will change the focusing of certain elements such as the pump into the OPA crystal as well as the white light continuum generation. Heating is caused by residual absorption of the pump and idler [Rothhardt13]. When scaling an OPA, one needs to take into account these thermal effects and aims to reduce these thermal gradients. One such method is to change the OPA crystal material to one with higher thermal conductivity; however, considerations of the phase-matching conditions must also be investigated. Another method is to cool the crystals and the elements that are absorbing heat. Finally, one can compensate for the thermal lensing by physical moving the focusing elements at higher average power.

2.3.3 NOPA setup

To construct a NOPA, first a chirped **white light continuum (WLC)** is generated in a material. A spectral portion of this WLC is used as a seed for the NOPA in a nonlinear crystal and amplified to by the **DFG process**. Finally this output is **compressed** using a prism compressor.

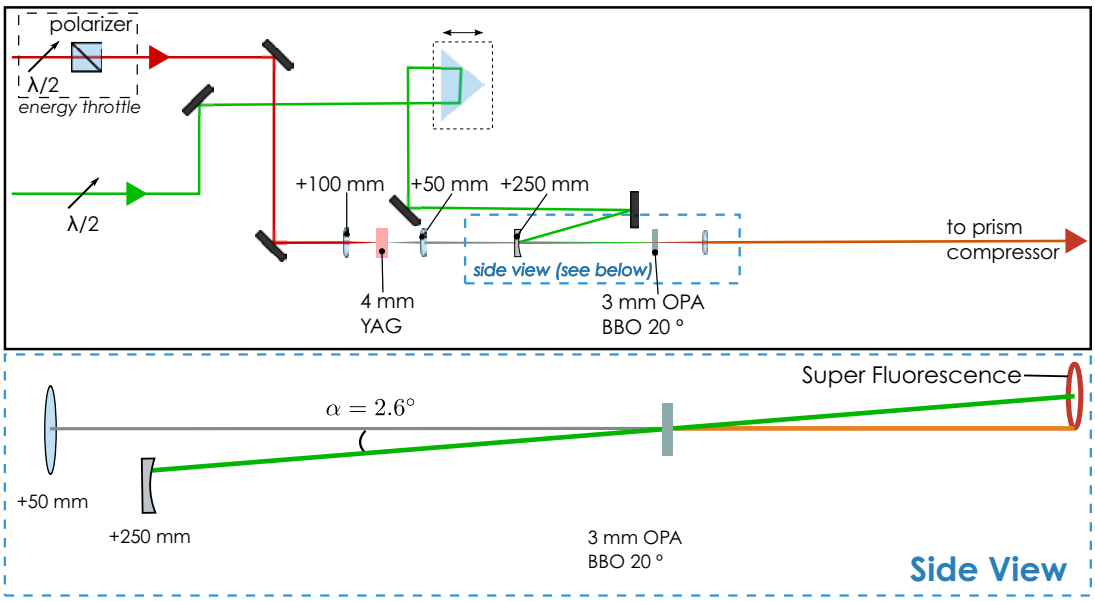

Figure 2.8 – Top: Photo of the IR NOPA with the schematic of the beam path overlaid. Bottom: Side view of the blue dashed box on top to illustrate the noncollinear angle of the pump and continuum within the crystal.

The basic design for our NOPA augments upon that of Bradler *et al.* in Ref. [Bradler13] who worked at 100 kHz. We wish to extend their results up to 1 MHz. The setup of the NOPA is seen in Figure 2.8. The Tangerine has two outputs: one at the fundamental, 1030 nm, used to create the WLC seed, and a second, frequency doubled output at 515 nm, used for the pump. $\sim$1.3 μJ of a 300 fs 1030 nm pulse is strongly focused into a 4 mm thick yttrium aluminum garnet (YAG, $Y_3Al_5O_{12}$). YAG is used instead of conventional sapphire due to its high thermal threshold and continuum stability over the IR wavelengths [Bradler09]. The thickness of the YAG and the focal length of the lens are chosen such that the thickness of the YAG is the same length as the Rayleigh range of the focus. Self-phase modulation in the YAG produces a $\sim$1000 nm super continuum centered around 1030 nm [Wegkamp11]. Due to the non-linearity of this process, the WLC is very sensitive to power density and focal profile. Therefore a power throttle consisting of a wave plate and polarizer is placed upstream to control the power. To characterize the WLC we used a spectrometer with a range from 340–1020 nm. To avoid saturation from residual 1030 nm fundamental, we only looked at a range from 450–950 nm. The continuum has a sharp cutoff at 515 nm, at the start of second harmonic generation. A short pass filter with a cut-off at 1000 nm is placed after the crystal to block any fundamental 1030 nm light that may not be amplified. This filter was not used when characterizing the WLC as it also cuts at 600 nm. An imaging lens is used after the WLC generation to focus the white light roughly in the center of the OPA crystal. The crystal is a 3 mm thick anisotropic

crystal β-barium borate (BBO) cut with an angle of $\theta = 20^\circ$ and used at $\theta = 22^\circ$. A thick crystal is chosen to help alleviate thermal effects and optimized for conversion efficiency and bandwidth [Bradler13].

Since the laser has a frequency doubling stage, this step is not incorporated into the NOPA setup. The time delay between the 515 nm pump and the chirped WLC determines what wavelength will be amplified as the signal because the WLC is strongly chirped during its generation. The pump light is then tilted upwards and focused using a spherical curved mirror with a focal length of +250 mm to focus slightly after the OPA crystal. The pump arrives in the crystal with an internal angle of $\alpha = 2.6^\circ$ for optimum phase matching conditions as seen in Fig. 2.7. The crystal is tilted such that the angle between signal and optical axis is 22° to allow phase matching between the signal and idler for a bandwidth of $\sim$150 nm as explained above and in Fig. 2.7. This angle is generally set by looking at the SF ring produced by the unseeded pump beam propagating in the crystal. In a visible NOPA, this looks like a multicolored ring whose width changes with respect to the crystal angle. The angle is correct when the ring width is minimized and all the colors arrive at the same place. As our NOPA amplifies in the IR, this ring is not visible to the naked eye, making it very tricky to set. The SF ring therefore must be observed using an IR viewer. The angle is set by minimizing the width of the ring as seen in the viewer and comparing that to the calculated angle.

As the WLC is heavily chirped, and the pump duration is $\sim$300 fs, the output of the NOPA will be very long temporally, on the order of $\sim$300 fs as well. The pulses can be compressed with a prism compressor. The derivation and physics behind these compressors can be found in the seminal paper by Fork, *et al.* in Ref. [Fork84].

Preliminary results are presented in the next section.

2.3.4 Characterization of the NOPA output

In this section, I present various figures and plots showing the characterization of the NOPA pulses. As one of the key features of a NOPA is the possibility to tune the wavelength by amplifying different portions of the signal white light continuum, while varying the repetition rate, this means that the beam quality must remain relatively uniform over these changing conditions. This NOPA is still under development at the time of the writing of this manuscript. Presented here are preliminary results.

WLC characterization:
Fig. 2.9 shows the white light continuum generated for different repetition rates, with an input energy of $\sim$1.3 μJ per pulse into the YAG. The spectral intensity has been normalized to account for the different repetition rates over the integration time. The input energy was chosen such that the continuum shape remained stable from shot-to-shot as well as over long periods time. At higher energies, multiple filamentation begins to occur in the YAG and spectral fringes and instabilities begin to appear in the spectra. At lower energies, thermal effect overtake the continuum generation and suppress the broadening of the spectra between 600 and 800 nm. The continuum remains stable in shape in the 550–850 nm bandwidth up between

1 – 200 kHz. An increase in temperature due the high repetition rate changes the focusing due to thermal lensing in the WLC generation [Rothhardt13]. At 500 kHz and 1 MHz the shape begins to change slightly due to thermal effects of the high repetition rate of the fundamental 1030 nm. However, there remains ample continuum for amplification at these wavelengths, and the spectrum and power remains as stable from shot-to-shot, with $< 3\%$ fluctuations (Tab. 2.1). The energy was measured by focusing the continuum onto a photodiode. The stability can be seen in Tab. 2.1.

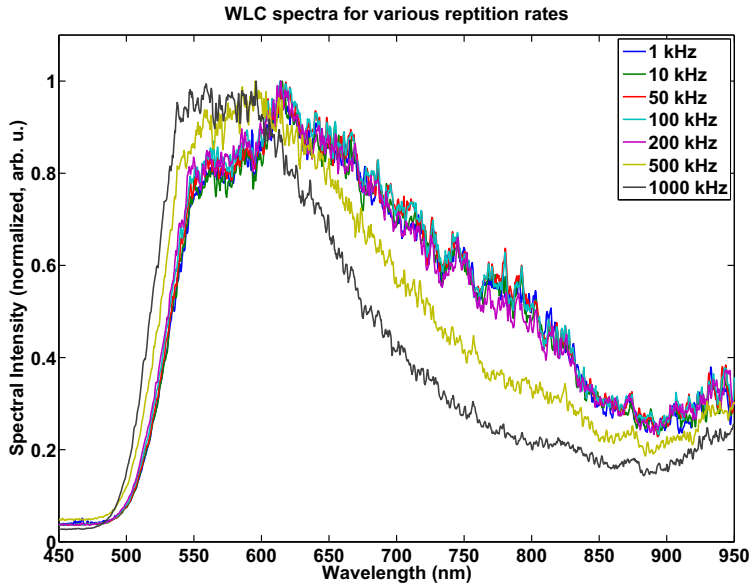

Figure 2.9 – WLC spectra for different repetition rates.

Table 2.1 – This shows a summary of the white light characterization. The bandwidth indicates the fwhm of the spectrum, and the power stability was measured by a photodiode.

Repetition Rate	Bandwidth	Power measure	Standard Deviation	% deviation
1 kHz	∼290 nm	34.3 V	0.875 V	2.55%
10 kHz	∼290 nm	34.3 V	0.750 V	2.18%
50 kHz	∼290 nm	33.9 V	0.805 V	2.27%
100 kHz	∼290 nm	34.0 V	0.900 V	2.67%
200 kHz	∼290 nm	34.3 V	0.800 V	2.35%
500 kHz	∼205 nm	33.6 V	0.820 V	2.44%
1000 kHz	∼160 nm	29.4 V	0.650 V	1.70%

NOPA output, 800 nm:

Because the WLC changes slightly as the repetition rate increases, the resulting amplified output spectrum changes as well. The shift can be due to thermal effects in metallic optics resulting from the high mean power creating some sort of thermal lens. For example, an output centered at 800 nm at 100 kHz shifts by ∼50 nm to 850 nm when the repetition rate is changed to 1000 kHz and nothing else is changed. However, the spectrum centered at 800 nm is easily recovered by simply changing the pump delay relative to the WLC. The shift in spectrum can be be seen in Fig. 2.10.

Fig. 2.11 shows the spectrum for 800 nm at different repetition rates. At 500 kHz and 1000 kHz,

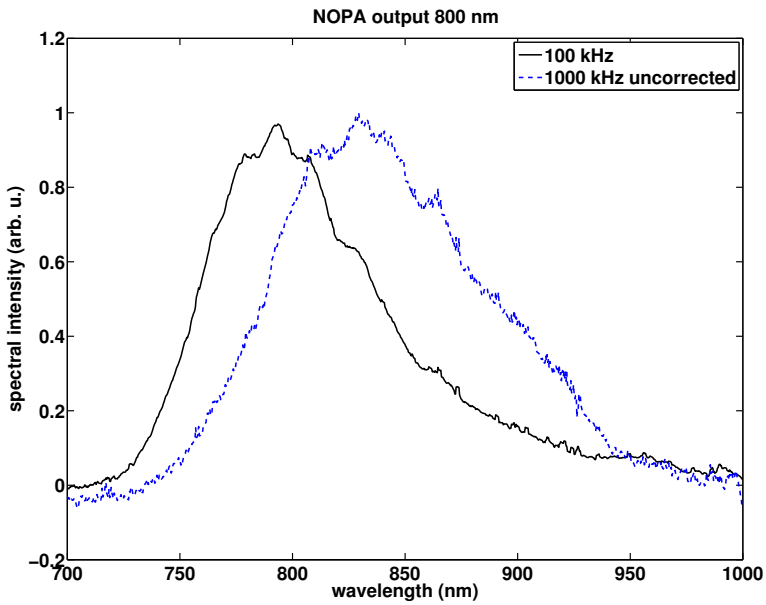

Figure 2.10 – The black solid line shows the output spectrum for the NOPA centered at 800 nm for100 kHz. At high repetition rates the WLC chirp changes, so the output shifts to 850 nm (blue dashed line). Simply by shifting the pump delay, the output is recovered back to nearly the same spectrum at 800 nm.

the WLC changed shape slightly, so the amplified spectrum changes shape as well. This is recovered by changing the pump delay. Aside from this shift in spectrum, the amplified spectrum does not change much for each repetition rate.

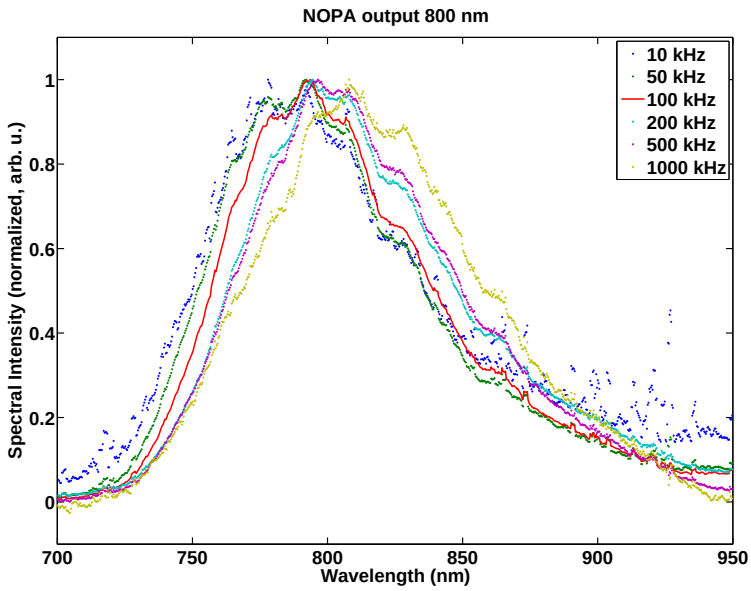

Figure 2.11 – NOPA output spectrum centered at 800 nm for different repetition rates, with adjusting the delay between the pump and WLC for high repetition rates.

Characterization of the NOPA output for several wavelengths:

Fig. 2.12 shows the amplified spectrum from the NOPA output centered at 700 nm, 750 nm

and 800 nm. The bandwidth of each output and corresponding Fourier limit can be found in Tab. 2.2.

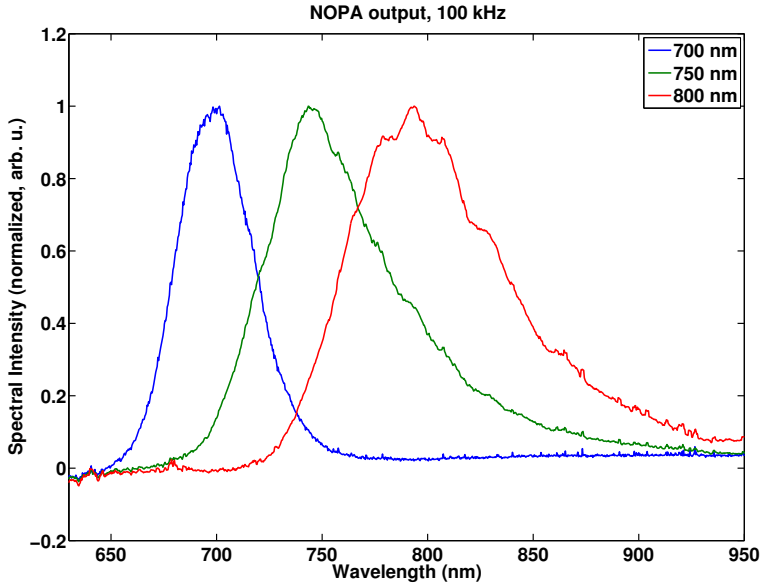

Figure 2.12 – Output NOPA spectra for different central wavelengths.

Table 2.2 – This shows a summary of the NOPA output spectra bandwidths and corresponding calculated Fourier limits.

Centered wavelength	Bandwidth (fwhm)	Fourier limit
700 nm	44 nm	17 fs
750 nm	67 nm	13 fs
800 nm	84 nm	11 fs

The peak-to-peak energy stability for the NOPA output is measured with a photodiode, after a 1000 nm short pass filter to eliminate any fundamental 1030 nm which is unconverted in the WLC generation process. Due to the efficiency of the white light generation and the phase matching conditions (Fig. 2.7 inset), the NOPA is much brighter at 750 nm compared to the other output wavelengths. At each repetition rate the energy fluctuation per pulse is less than 5% and generally around 2%. At high repetition rates, the efficiency begins to go down, and the output energy of the NOPA decreases. There are possible thermal effects as the crystal also is found to absorb heat mainly through pump absorption [Rothhardt13]. The fluctuations in energy, however, are still on the order of 5% at these rates. This is seen in of Fig. 2.13.

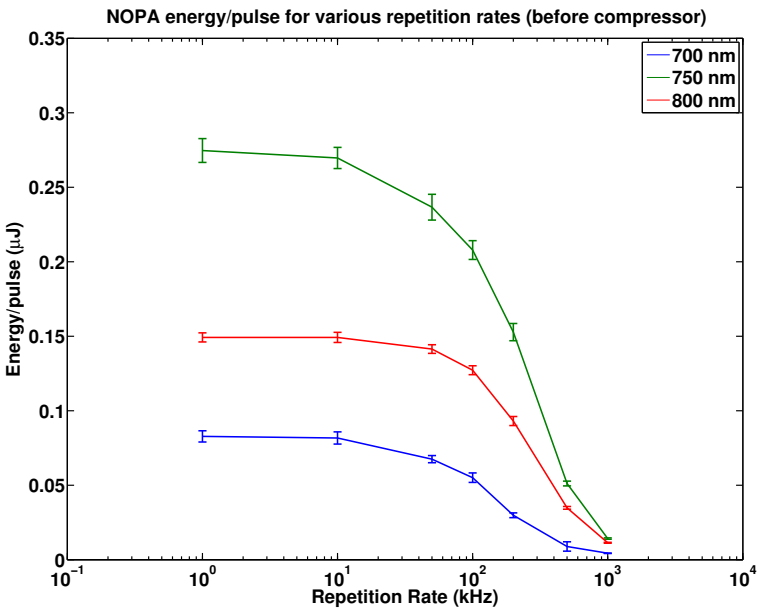

Figure 2.13 – NOPA energy measurements for different repetition rates at 700 nm, 750 nm and 800 nm.

NOPA parametric gain:

We investigated the parametric gain as a function of the power density of the pump for a given repetition rate (100 kHz) to see if there are any saturation or depletion effects in the amplification process. The 300 fs pump is focused to a spot size of $\sim$80 μm in diameter. The crystal is placed slightly before the focus, so the spot in the crystal is on the order of $\sim$150μm in diameter. The parametric gain remains linear and no saturation effects or depletion can be seen (Fig. 2.14).

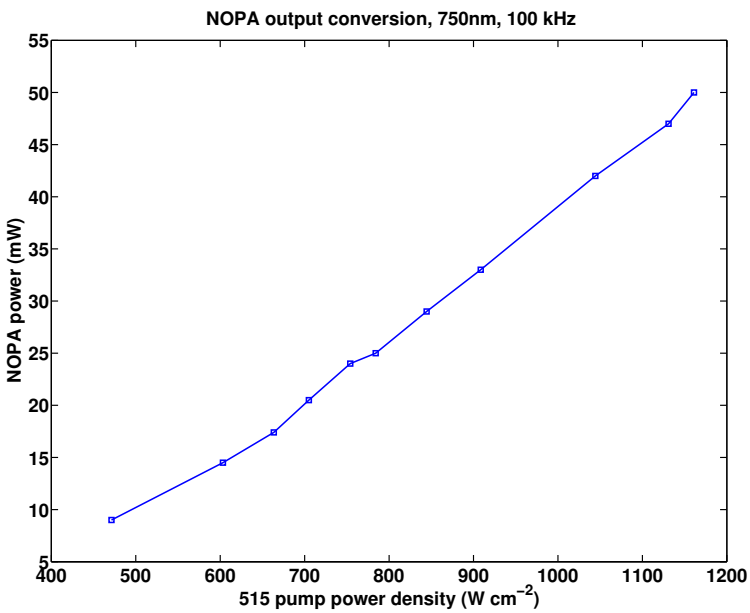

Figure 2.14 – Parametric gain for different pump powers.

Compression of the pulses:
The final pulse duration depends on both the final output bandwidth of the NOPA as well as the alignment of the prism compressor. A schematic of a prism compressor can be found in Fig. 2.15 The NOPA output at 750 nm has a spectral bandwidth of ∼67 nm, corresponding to a Fourier limit of 13 fs for a fully compressed pulse.

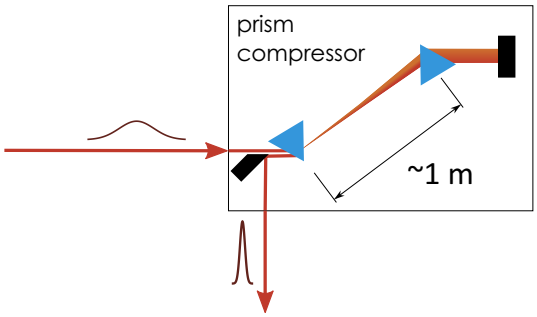

Figure 2.15 – This shows the schematic of the prism compressor we use.

Our compressor is made of equilateral prisms made of SiO_2 separated by a distance of 1 m. SiO_2 was chosen to minimize the amount of TOD added to the pulses. They are carefully aligned using the minimum deviation technique to avoid spatial chirp in the output beam. The output spectra are measured with an autocorrelator with a nonlinear crystal of 200 μm thick BBO. We cannot use the SPIDER for pulse characterization as SPIDER results are only valid for a central wavelength of 800 nm and a bandwidth of $\lesssim$65 nm. We find a compression of 35-40 fs fwhm. These measurements are probably greater than the actual pulse duration due to the thickness of the BBO crystal. For a more precise estimation, we would need to repeat these measurements with a thinner crystal (around ∼50 μm thick). The compression does not change much with repetition rate as seen in Fig. 2.16 with minor fluctuations possibly caused by slightly spectral differences in the non-linear amplification process from thermal effects or in the compression.

The beam quality of the output of the NOPA remained symmetrical and constant throughout the measurements presented. The NOPA is undergoing continual development. These are the current results at the time of the writing of this manuscript. By using high power mirrors, and compensating for thermal lensing effects, we can recuperate some of the energy lost at high repetition rates. These solutions and others are currently under investigation.

We hope to extend the current results to be able to use the full repetition range of the pump laser (single shot to 2 MHz), with tens of nJ of energy per pulse (after compression) for each repetition rate and wavelength. We also hope to compensate for the third order dispersion from the compressor to have fully compressed pulses.

2.4 Summary

We have implemented a flexible laser system that is fully characterizable and controllable. The first laser system is based on a conventional, 800 nm, Ti:sapphire laser oscillator and amplification chain. With this system, we have the ability to switch between a moderate mean

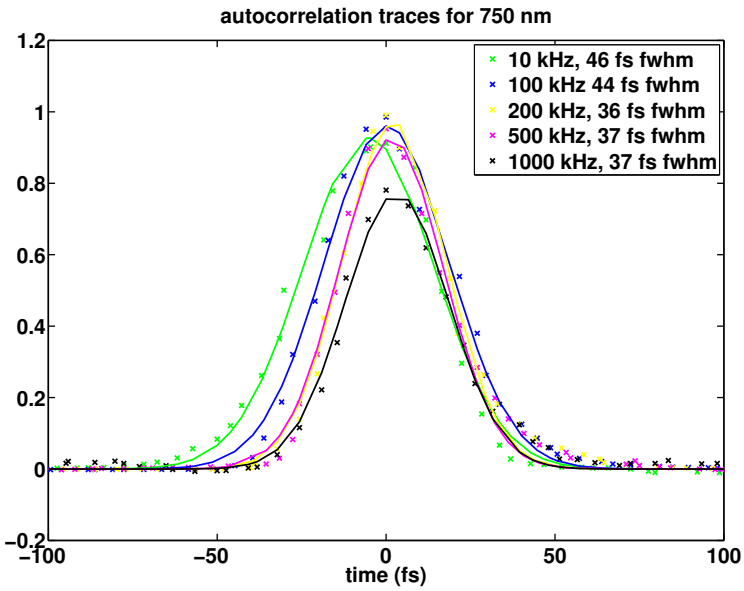

Figure 2.16 – This shows autocorrelation measurements for pulses at 750 nm for various repetition rates and their corresponding Gaussian fits.

power, high repetition rate mode at 62 MHz, as well as a low mean power, low repetition rate mode at 1 kHz, with the same pulse peak intensity in both modes. We also have the possibility of frequency doubling the laser output to produce 400 nm pulses.

To increase flexibility in both wavelength and repetition rate, we built a NOPA at the output of a fiber-based infrared laser. The source laser has a variable output repetition rate from single shot to 2 MHz. This means that the output of the NOPA will have variable repetition rate as well. We developed the NOPA to have a broad phase-matching bandwidth around 800 nm to allow comparisons with results taken with the Ti:sapphire laser chain, but at different mean powers. The effects of building a NOPA at high mean power and high repetition rate were characterized.

A summary of the laser characteristics for the various laser modes can be found in Tab. 2.3.

Table 2.3 – This shows a summary of the characteristics for the various laser modes used and accessible for the experiment.

	repetition rate (R)	**central wavelength**	**spectral bandwidth**	**pulse duration**	**pulse energy (before compressor)**	**max peak power (before chamber)**
oscillator	62 MHz	800 nm	70 nm	20 fs	5.8 nJ	1.9×10^5 W
Regen	1 kHz	800 nm	30 nm	40 fs	350 μJ	5.3×10^9 W
NOPA (now)	1 kHz – 1 MHz	700 nm	44 nm	45 fs	low R: 0.27 μJ high R: 14 nJ	1.7×10^6 W 8.8×10^5 W
		750 nm	67 nm	40 fs	low R: 0.15 μJ high R: 11 nJ	9.4×10^5 W 6.9×10^4 W
		800 nm	84 nm	35 fs	low R: 0.08 μJ high R: 4 nJ	5.0×10^5 W 2.5×10^4 W
NOPA (ideal)	single shot – 2 MHz	700-850 nm	$\sim$100 nm	$\sim$10 fs	10s nJ	$\sim 10^5$ W

3

Experimental setup and methods

This chapter describes the experimental setup used for my thesis research (Fig. 3.1). This setup was developed entirely during my Ph.D. research. Prior to my arrival, my group was involved in laser development for coherent control techniques. The aim of my thesis was able to combine their laser expertise with a new experimental setup to investigate the light-matter interaction at a sharp nanotip. As this is a brand new scientific direction for the group, the experimental setup went through much evolution during my Ph.D. with this group. In general, the setup is very versatile, involving many different elements from laser development to electron detection as well as vacuum technologies and home made data acquisition software.

For my Ph.D. research, I used 3 kinds of nanotips: tungsten nanotips which I made myself at CEMES; carbon cones which were made at CEMES by Aurélien Masseboeuf; and silver nanotips which were made by Ivan Blum at GPM in Rouen. I will first discuss the sample making procedure for the various nanotips we use. I will then discuss the experimental chamber, sample manipulators and detectors. Finally, I will discuss the alignment procedure for the various elements.

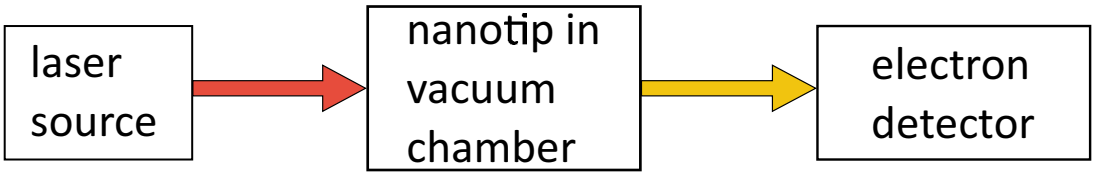

Figure 3.1 – This shows the basic flow of the experiment. A sharp nanotip placed in a vacuum chamber is illuminated by a laser source. The resulting electron emission is then detected by an electron spectrometer.

As shown in Fig. 3.1, the nanotip is placed in an ultra-high vacuum (UHV) chamber and illuminated by a tightly focused ultrafast laser source as described in Chap. 2. The emitted electrons are then detected with a field retarding electron spectrometer, with the possibility of spatially resolved detection.

3.1 Nanotip fabrication and characterization

Tungsten tips were first used as a benchmark tip to compare results from our new setup to established experiments and identify various emission mechanisms. We then investigate emission from novel new nanotips based on a single carbon nanotube and from silver.

3.1.1 Tungsten tips

Emission from tungsten nanotips were the first results investigated during my Ph.D. Their emission patterns provide a baseline for results with our new experimental setup that we can compare to other established experiments [Hommelhoff06b, Schenk10, Barwick07, Hommelhoff06a, Yanagisawa10]. Tungsten (W, atomic number 74) provides a robust material to study with its high melting point, 3695 K, and a work function of ∼4.5 eV. The high melting point makes tungsten tips ideal for field emission and microscopy. Tip formation methods via electrochemical etching are well known [Lucier04, Tsong90, Ekvall99].

The tips are made via electrochemical etching. As LCAR is not an electron microscopy laboratory, we turned to our collaboration with Aurélien Masseboeuf and the Nanomaterials group at the Centre d'Élaboration de Matériaux et d'Etudes Structurales (CEMES)[1] laboratory in Toulouse, France. This method of tip making is the most basic of creation of sharp nanotips. In electrochemical etching of sharp nanotips, a small diameter metal wire is dipped in an electrolyte solution. A small voltage is applied between the wire and the electrolyte until enough dissolution occurs that the wire has a sharp tip.

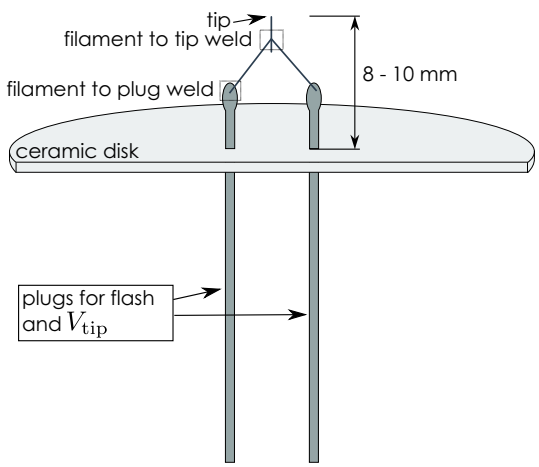

Figure 3.2 – This shows schematic of tip. A tungsten filament is welded onto metal plugs with a ceramic support. A straight tungsten wire is welded to this filament onto which the nanotip is electro-chemically etched. SEM images of the welded junctions (dashed boxes) can be seen in Fig. 3.3

The tip base is a FEI and Philips[2] Standard V Loop Filament. This base consists of a ceramic disk, 26 mm in diameter, that is cut in half. The disk is cut in half to allow the base to fit in a

[1] http://www.cemes.fr/
[2] http://www.fei.com/

Focused Ion Beam (FIB) environment for the eventual case of attaching a carbon cone to the end of the tungsten tip (see Sec. 3.1.2).

Usually the filament base for the tip is made from polycrystalline tungsten wire, and the tip is etched from single crystal tungsten oriented along the (310) direction. This means that the apex of the tip created will be oriented along the (310) axis. W(310) was chosen because it has the lowest work function, 4.35 eV [Mendenhall37], of all possible orientations and therefore is the brightest emitter [Yanagisawa09].

Since the bases are reused to make new tips, the first step to tip making is to make the filament. Tungsten wire 0.125 mm in diameter is bent into a 'V' shape, approximately ∼3 mm deep and the ends of the 'V' are the same distance apart as the plugs in the ceramic disk (5 mm). The filament is micro-welded on either end to the plugs of the tip base. The micro-welder is set to short current and 2 Ws and works by sending a short burst of current through the wires to be welded together. A small length of tungsten wire, ∼3-4 mm long, is welded to the point of the filament. This wire is to be etched into a tip. The height of the wire should be 9-11 mm from the top of the ceramic plate. Since the etching process shortens the wire by 1 mm, this corresponds to a final height of 8-10 mm from the top of the plate. A schematic of the tip base can be seen in Fig. 3.2 with SEM images of the welds seen in Fig. 3.3.

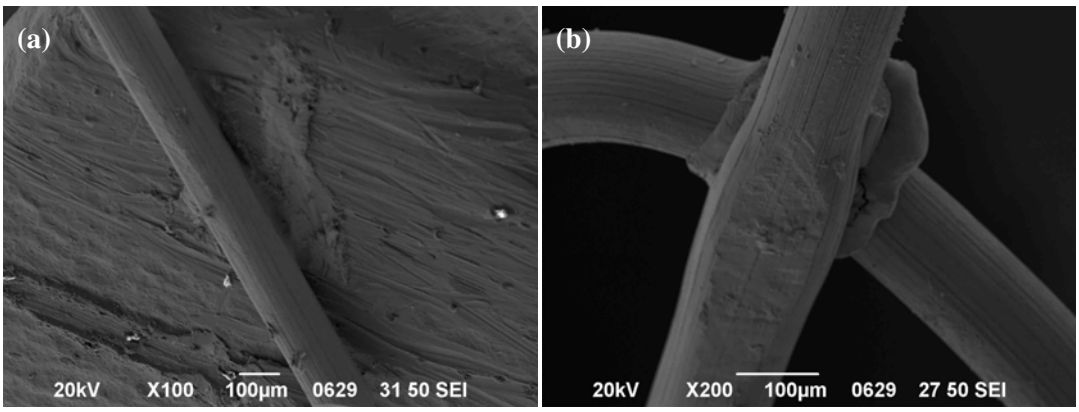

Figure 3.3 – This shows SEM images of the micro-weld of a filament to the ceramic tip base plugs. (a) This is a typical weld between the filament and a plug. (b) This is a typical weld between a filament and the to-be-etched tip wire.

The actual tip is formed via **electrochemical etching** in a 2 M NaOH solution. The electrochemical attack is performed by sending a voltage through the wire to be etched and the solution. The wire acts as the anode and is attached to the positive end of the voltage supplier, and the solution itself is used as the cathode and is connected to the negative end. The wire is then dipped 1.0 mm into the solution and lifted up 0.1 mm to form a meniscus. Due to the surface tension of the NaOH solution, a dip in surface of the solution is apparent when the wire enters the solution. An attack voltage of 4.2 V is applied to the tip with a base voltage of 0.5 V. A schematic of the setup is seen in Fig. 3.4.

The overall reaction [Ibe90] that occurs during the electrochemical etching process is given

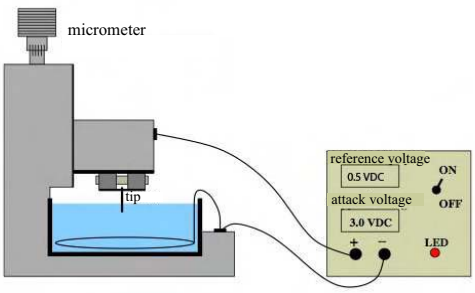

Figure 3.4 – This shows the setup developed at CEMES for electrochemical etching of the W tips. Adapted from [Bedel14].

by:

$$\begin{aligned} \text{cathode}: \quad & 6H_2O + 6e^- \rightarrow 3H_2(g) + 6OH^- \\ \text{anode}: \quad & \underline{W(s) + 8OH^- \rightarrow WO_4^{2-} + 4H_2O + 6e^-} \\ & W(s) + 2OH^- + 2H_2O \rightarrow WO_4^{2-} + 3H_2(g) \end{aligned}$$

As the etching occurs at the air/electrolyte interface, the shape of the meniscus is especially important in determining the tip shape. Due to a concentration gradient of OH^- along the axis of the tip, the etching rate is higher at the top of the meniscus. During the tip formation, the soluble tungsten flows towards the lower end of the wire forming a necking phenomenon which is observed at the meniscus interface. More details on the etching process can be found in [Ibe90, Lucier04, Bedel14].

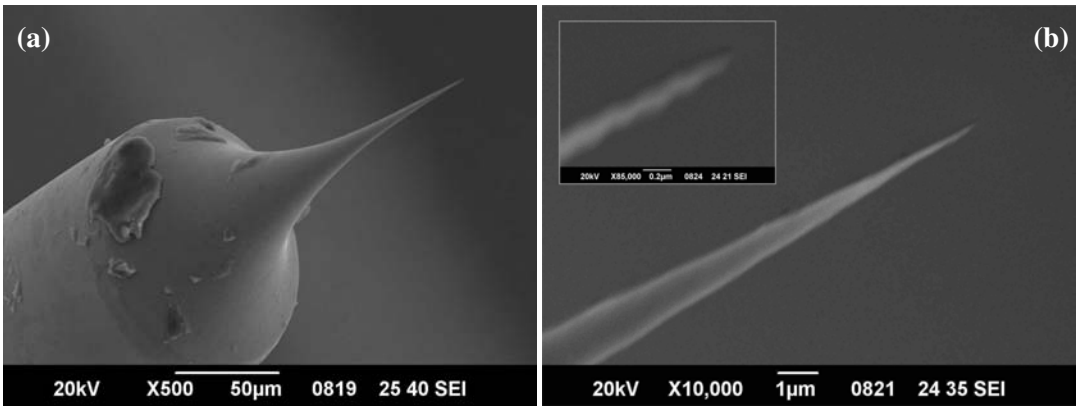

Figure 3.5 – (a) This shows SEM images of the final etched tungsten tip. Note the residual salt pollution leftover from the etching process. These are removed via current flash cleaning. (b) 10,000x magnification of the tip apex with 85,000x magnification in the inset.

As the neck of the wire becomes thinner, at some point the weight of the lower part of the wire is too much and the neck cannot support it. The lower part of the wire then breaks off forming the sharp tip. Afterwards the voltage must be immediately shut off as the etching process does not stop just because a tip has been formed. A circuit monitoring the current between the cathode and the anode provides the mechanism for shutting of the voltage quickly after the tip has been formed. The circuit design is based on that of Nakamura *et al.* [Nakamura99]

and yields a cutoff time of ∼0.5 μs. The tip is then characterized in a Scanning Electron Microscope (SEM) as seen in Fig. 3.5.

When the finished tip is mounted in the chamber, an AC current is passed through the filament to clean or "flash" the tip and remove residual salts from the etching process. The flash creates a burst of heat which cleans the surface of the tip. Typical current settings are ∼3.6 A, for 500 μs being sent across the tip. The current from the ion pump is closely monitored during this process for evidence of degassing from the tip. The ion pump current increases when salts are removed from the tip surface. The current stops changing once the surface is clean, typically after 1-3 flashes.

Many factors contribute to the success of the etching process, and a slight error can cause failure in the process. An example of an unsuccessful etch can be seen in Fig. 3.6. For this tip, the attack voltage stopped before the tip had finished etching; the lower part of the wire that has not been broken off can be seen as long blunt point at the end. In general, I find that the first few tips made per fresh batch of NaOH solution are discarded due to obvious gross flaws such as incomplete etching. Possibly this is due to the need of W ions already in the solution to aid in the etching process. The shape of the meniscus directly influences the tip shape. The wire to be etched must enter the solution as vertically as possible, and the meniscus height itself is fine-tuned using the micrometer screw. The etching is very sensitive to vibrations and disturbances, so much care is given not to bump the bench while etching is occurring [Lucier04].

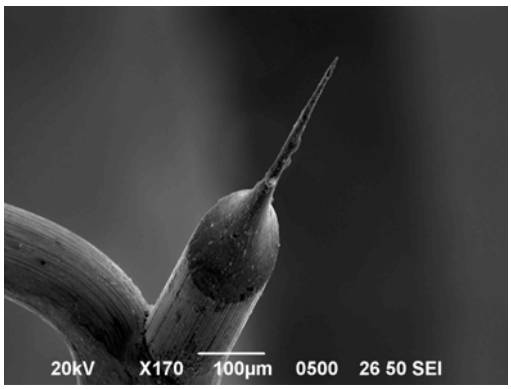

Figure 3.6 – This shows an example of a failed etch of W tip.

The etching is done at CEMES and the setup itself went through modifications [Bedel14]. In the original setup, a conducting beaker was used as the cathode; however, it was found that shaper tips are formed by using a submerged length of tungsten or gold wire as the cathode in a normal beaker. The ideal attack voltage for tungsten was found to be 4.2 V with a reference of 0.5 V for cutoff. With these conditions, the electrochemical etching process takes about 5 min.

The tungsten tip making procedure can be summarized as:

1. Filament:
    1.1 **bend** a length of tungsten wire such that it forms a 'V' shape ∼3 mm deep and is the same width as the plugs of the ceramic tip base

1.2 **micro-weld the ends** of the filament to the base plugs

1.3 **micro-weld a 4-5 mm length of tungsten wire** to the middle of the filament

2. Etch the tip:

2.1 fill a beaker with **2 M NaOH solution**

2.2 **attach** negative output of voltage tip attack box to a wire submerged in the solution and the positive output to one of the base plugs

2.3 **lower** the base until the tungsten wire is submerge 1.0 mm into the solution

2.4 **lift** the base up 0.1 mm to prepare the meniscus

2.5 use the tip attack box to **apply voltage** and start the etching process–the box will **automatically shutoff** once the process is finished

3.1.2 Carbon Cone nanoTips (CCnT)

Carbon cone nanotips (CCnT) [Jacobsen97, Houdellier12] are samples made in collaboration with CEMES. The CCnTs are synthesized by Mathieu Delmas and are mounted entirely at CEMES by Aurélien Masseboeuf.

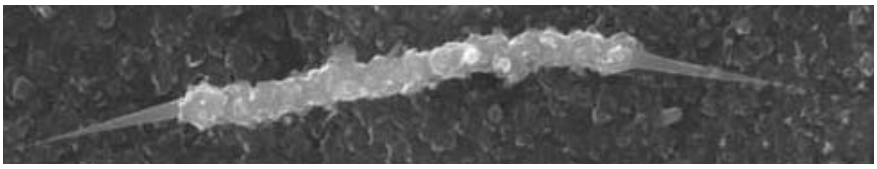

Figure 3.7 – This shows two carbon cone nanotips (CCnT) formed on either end of a short microfiber segment, which can be described as crumpled graphene sheets, that terminate with two opposed, smooth surfaced carbon cones. Adapted from Carbon, Vol 50, F. Houdellier *et al.*, "New carbon cone nanotip for use in a highly coherent cold field emission electron microscope," Pages No. 2037–2044, Copyright (2012), with permission from Elsevier. [Houdellier12].

CCnTs are based on a single multiwall carbon (C, atomic number 12) nanotube surrounded by concentric graphene sheets. The interior structure of the concentric graphene sheets can be seen in the Transmission electron microscopy (TEM) of Fig. 3.8. The structures are formed via a controllable time of flight chemical vapor deposition process [Allouche03, Allouche05, Monthioux06]. This recently developed nanotip raises high expectations for advances by implementation in electron microscopy [Houdellier12, Houdellier15]. The carbon cone is grown onto a single multi-wall carbon nanotube (CNT) with an apex diameter of a few nm, and mounted on a tungsten tip with a focused ion beam and a gas precursor injection system (FIB induced deposition, FIBID), as shown in Fig. 3.9. The use of this CNT-based nanotip (CCnT) has several advantages over W and Au nanotips. The mechanical and chemical strength of the carbon sp^2 bonds is larger, increasing robustness and stability. The aspect ratio of the carbon cone is sharper and the apex size can be smaller, which can lead to a higher field enhancement in the vicinity of the apex. The growth of the carbon cone can be completely controlled, which could allow modification of the electronic structure by doping or filling the CNT with

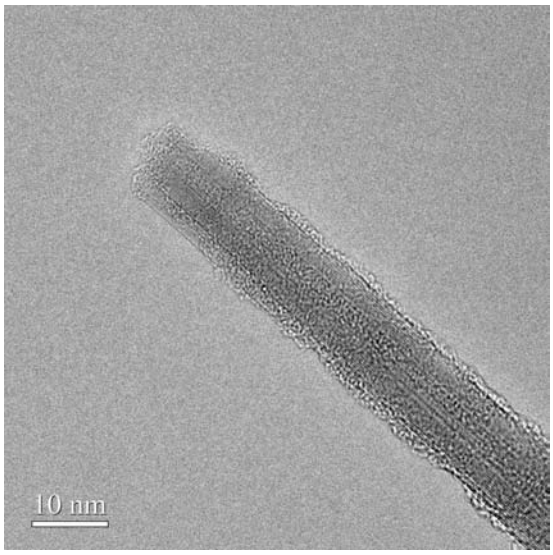

Figure 3.8 – This shows the interior structure of the concentric graphene sheets that make up the carbon cones via transmission electron microscopy (TEM).

other elements. A collaboration with CEMES and Raul Arenal at the University of Zaragoza is studying ways to grow CCnTs with doped CNTs. This is the research project of the Ph.D. student Rongrong Wang. The carefully controlled growth process allows the enhancement of properties important for cold field emission such as emission stability, life-time, and aspect ratio. They are formed on either end of a short microfiber segment, which can be described as crumpled graphene sheets, that terminate with two opposed, smooth surfaced carbon cones [Jacobsen97, Houdellier12]. This is seen in Fig. 3.7. A more detailed description of a CCnT can be found in [Houdellier12, deKnoop14].

Carbon tips are welded to the end of an already formed tungsten nanotip in a Focused Ion Beam (FIB) environment [Houdellier12]. The sharp end of an electrochemically etched tungsten is milled so that the end diameter is $\sim 1\ \mu$m, about the same diameter as the carbon onto which the CCnT is attached (Fig. 3.9 (B)). A suitable CCnT is located on the substrate onto which they have been dispersed. The CCnT must have proper alignment with the axis of the milled tip and be free from any visible defects (Fig. 3.9 (A)). Using micro-tweezers, the CCnT is then lifted from the substrate after being cut from its fiber base using the Ga^+ ion FIB (Fig. 3.9 (C)). The CCnT is then carefully placed in contact with the milled tungsten tip and welded into place via W ion beam induced-deposition from W precursor (Fig. 3.9 (D)). More details on this sample preparation process can be found in [Houdellier12] and [deKnoop14, Ch. 3].

The CCnT tip making process can be summarized as:

1. **fabricate** tungsten tip
2. **mill** the tip to end diameter of $\sim 1\ \mu$m
3. **locate** suitable CCnT on substrate
4. **excise** CCnT from carbon fiber base
5. using micro-tweezers, **lift** CCnT from substrate and **place in contact** with milled tungsten tip

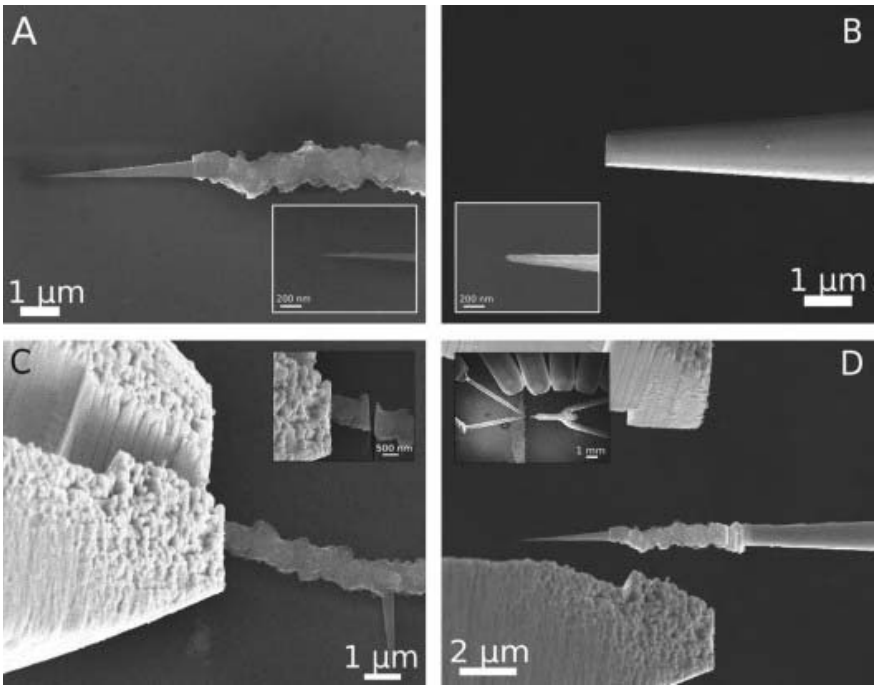

Figure 3.9 – The CCnT mounting process. (A) A suitable CCnT is chosen in alignment with the W tip axis and with sharp apex radius (inset). (B) The tungsten tip to the approximately the same diameter as the carbon fiber and original tip apex (inset). (C) Removal of the CCnT from the substrate using micro-tweezers after excision from the carbon fiber (inset). (D) The final mounted CCnT welded onto the tungsten tip. The inset shows the entire mounting setup with the micro-tweezers on the left, the tip on the right and the gas injection nozzles for welding on top. Reprinted from Carbon, Vol 50, F. Houdellier *et al.*, "New carbon cone nanotip for use in a highly coherent cold field emission electron microscope," Pages No. 2037–2044, Copyright (2012), with permission from Elsevier. [Houdellier12]

6. **weld** CCnT to tungsten tip

3.1.3 Silver Tips

Experiments on silver tips are made in collaboration with the Groupe de Physique des Matériaux (GPM)[1] in Rouen, France. The tips are fabricated entirely at GPM.

Silver (Ag, atomic number 47) provides an interesting noble material to investigate due to its strong plasmon resonance which in turn could yield to high electron emission and brightness. This is due to the small imaginary component of its dielectric constant as well as low optical damping. Generally gold is favored in air due to its inertness, but silver can be preferable in vacuum because it is less lossy in the relevant spectral ranges [Sasaki13]. Previous studies have demonstrated a high brightness and electron yields for silver emission an order of magnitude more than that of tungsten [Sasaki13, Zhang11]. The work function for polycrystalline silver is 4.26 eV [Haynes12], with a melting point of 1235 K. The melting point of silver is very low and could lead to potential thermal issues.

[1] `http://gpm.labos.univ-rouen.fr/`

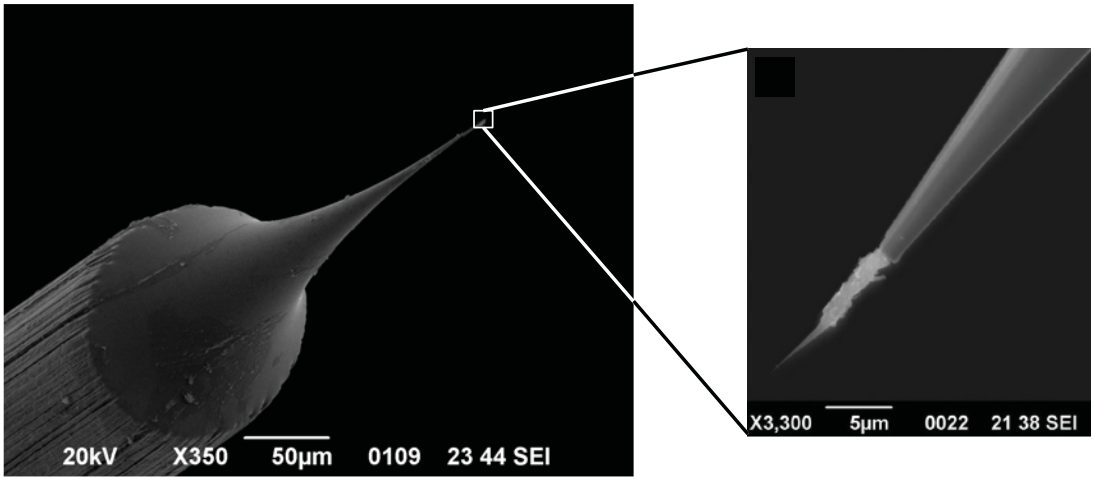

Figure 3.10 – SEM images showing a finished CCnT welded onto a tungsten tip.

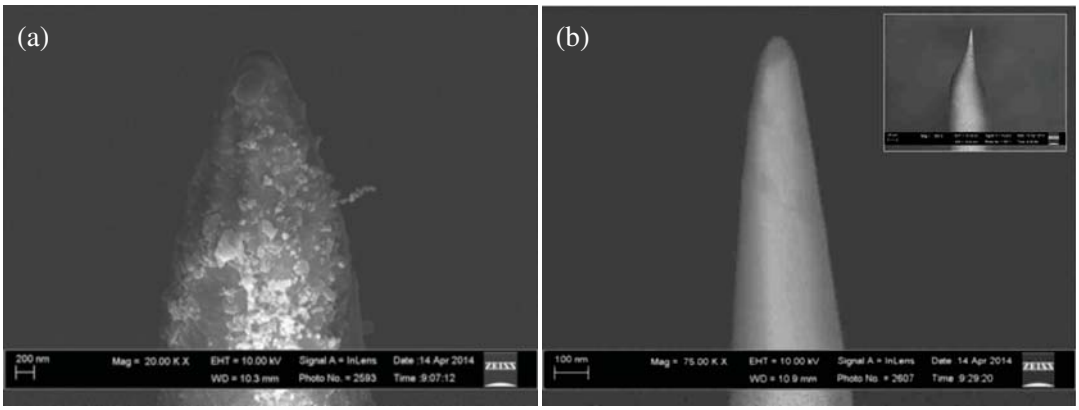

Figure 3.11 – (a) A silver tip after the electrochemical etching steps at 20,000x magnification. The scale bar is 200 nm. (b) The finished tip after the FIB milling at 75,000x magnification with a scale bar of 100 nm. The inset shows a the whole tip at 300x magnification, with a scale bar of 20 μm.

A sharp silver nanotip is formed in a three-step process at GPM by Ivan Blum. First the wire electrochemically etched to form the basic conical shape, then the tip is milled in with a FIB to form the final sharp nanotip. The tips are formed from a polycrystalline silver wire that is 99.99% pure and 125 μm in diameter. The wire is first electrochemically etched using the microloop technique (as described in [Sasaki13]), with a solution of 0.1% perchloric acid and 99.9% methanol and a voltage of 7 V. The concentration and voltage use are not very critical; however, it is important to obtain a surface with as little roughness as possible. The tips are then etched in the same solution using a beaker as described for tungsten tips using a device with an automatic cutoff time of 50 μs after the neck breaks. The tips are then dipped in isopropanol for cleaning. The tips after the electrochemical etching steps are seen in Fig. 3.11 (a).

The tips are then milled with a focused ion beam (FIB) to form the sharp shape of the nanotip. The tips are first milled with high energy Ga^+ ions at various currents, depending on the tip shape, to remove a lot of material to form the tip shape. The tip shape is obtained by annular milling [Miller07], where the ion beam is parallel to the tip axis. The annular milling

pattern is used with gradually reducing the inner radius until the correct end curvature radius is obtained. After the shape is formed, the tips are cleaned using low energy ions. The cleaning step removes ∼50 nm of material and excises the volume of material that was damaged by the high energy ions. In general, due to the nature of the milling process, ∼2 nm of Ga is implanted under the material surface. We do not believe this small amount of Ga affects the emission processes of the Ag. The tips have a final radius of ∼12-50 nm. A finished tip can be seen in Fig. 3.11 (b).

Due to the fact that these tips are made in the facilities at GPM, the tips are mounted very differently than those based on tungsten tips. Instead, the wire tip base is inserted into a small Ni capillary which is 4 mm in height, with an internal diameter of 0.8 mm and external diameter of 1 mm. This capillary can fit inside of a larger, 7 mm capillary, which is mounted directly onto the tip holder, as described in Sec. 3.3. This means that there is only one electrical connection on the tip, and therefore no possibility of cleaning via current flashing. However, due to the nature of tip fabrication (FIB milling versus electrochemical etching) there is no need to clean the tip in this manner as there is no contamination of the surface from the etching.

The silver tip making procedure can be summarized as:

1. **Micro-loop electrochemical etching** with a solution of 0.1% perchloric acid and 99.9% methanol and a voltage of 7 V
2. **Electrochemical etching** in a beaker with same solution and using a device with an automatic cutoff time of 50 μs after the neck breaks
3. **Cleaning** in isopropanol
4. **High energy FIB milling** to form tip shape and remove a lot of material
5. **Low energy FIB milling** to clean tip

3.2 Vacuum chamber

The experimental setup went through several generations. These will be described in the following sections and then summarized at the end.

The interaction region of the experimental setup is conducted inside an ultrahigh vacuum (UHV) in a stainless steel chamber. The chamber has a pressure on the order of $\sim 10^{-10}$ mbar. Good vacuum pressure is necessary to avoid fast surface contamination on the nanotip and prevent ionization of particles caught in the laser focus. We have found that a pressure greater than $\sim 10^{-9}$ mbar is not sufficient for stable emission.

Pressure is maintained with a turbomolecular pump and an ion pump. A passive Non-Evaporable Getter (NEG) from SAES Group[1] pump assists in pumping to the final base pressure. These are based on the principle of the absorption of molecules by a porous material. The chamber is baked for 24 - 72 hours at a temperature of 140° C each time it is opened. The chamber is

[1] http://www.saesgetters.com/it/products/capacitorr-pumps

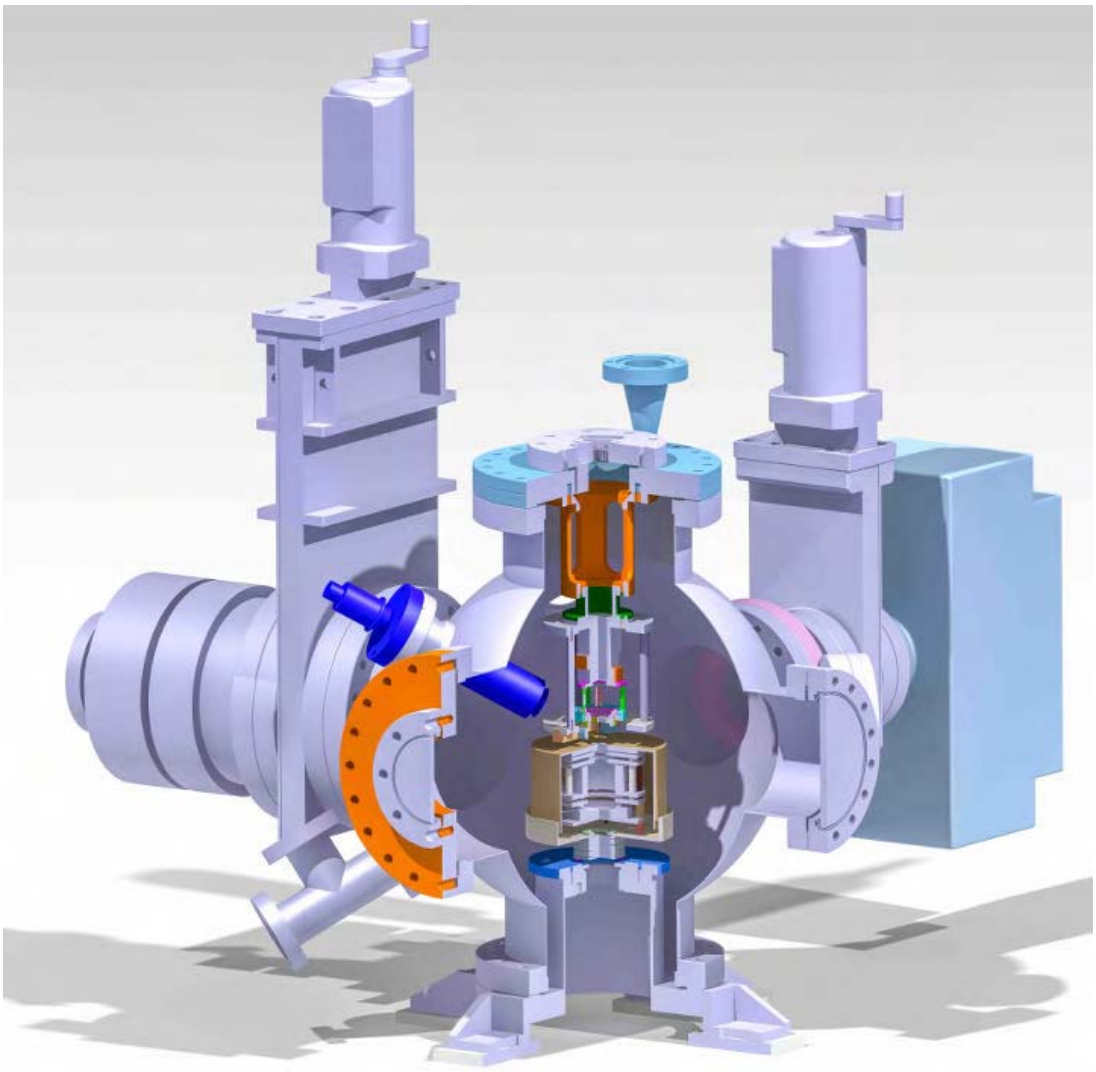

Figure 3.12 – Schematic of the UHV chamber and components used for our experiments.

then pumped and cooled for $\sim$ 24 hours. Once the minimum pressure achievable is reached, pressure is maintained only by the ion pump and NEG with the turbomolecular pump turned off to minimize vibrations. A schematic of the chamber can be seen in Fig. 3.12. A photo of the inside components is seen in Fig. 3.13.

The pressure is monitored in several ways. We have a full range gauge that can measure up to atmospheric pressure which is used when backfilling the chamber with N_2 whenever we need to open the chamber. We have a residual gas analyzer (RGA) which is a mass spectrometer used to check for contamination and leaks. For precise measurement of the UHV we use a Bayard-Alpert hot filament ionization gauge. As this is a heated filament, it must be turned off when the detectors are on or they will be influxed with electrons emitted from the gauge. For quick empirical measurements of sudden pressure fluctuations we look at the current from the ion pump. This is useful when flashing the tip to see when the pump needs to pump away material removed from the surface of the tip.

The windows into the chamber are made of UV fused silica and are 3–6 mm thick. The chirp

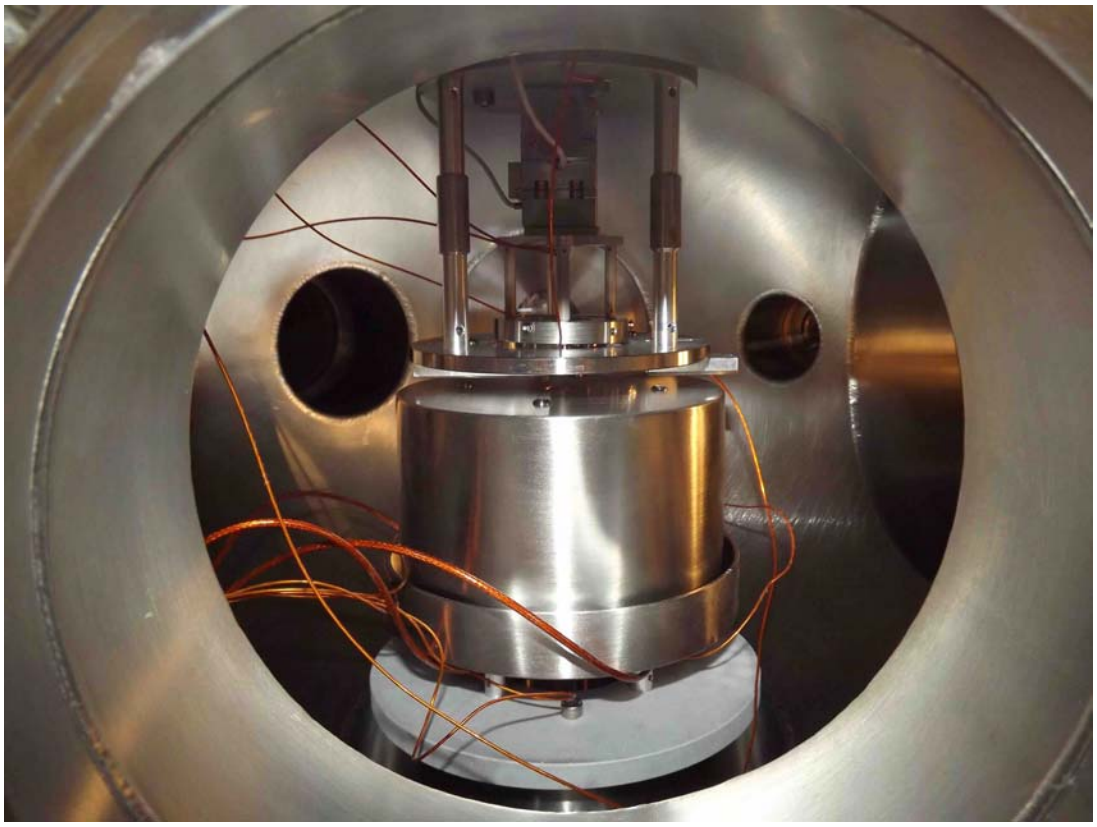

Figure 3.13 – photo of the tip holder (see Sec. 3.3) and spectrometer (see Sec. 3.5) geometry inside the chamber

induced by the windows on the laser pulses is pre-compensated for with either additive chirped mirrors or the laser compressor itself.

3.3 Tip holder and manipulator

The ensemble (Fig. 3.14) for holding and manipulating the tip samples is vital to the experiment. The purpose of the tip holder is twofold. The tip is placed on three dimensional nanopositioning translation stages (attocube model ANPx101num, and ANPz101num from Attocube systems AG[1]), each with nanometer resolution and a range of a few millimeters. These stages are used for precise positioning of the tip into the laser focus. The stages use a stick-slip motion with piezo stages allowing the piezo range of a few microns to be repeated many times to achieve the high level of performance for such a large range. The ANP series is made of titanium which eliminates potential magnetic fields caused by the positioners. The num series has an optical reader inside the device which allows for closed-loop positioning meaning that we can reproducibly return to the same position with precise accuracy. However, these attocube positioners can only carry a load of 100 g, so modifications to the standard electron gun tip holders must be made to minimize weight. The ensemble also includes the laser focusing elements.

[1] http://www.attocube.com/

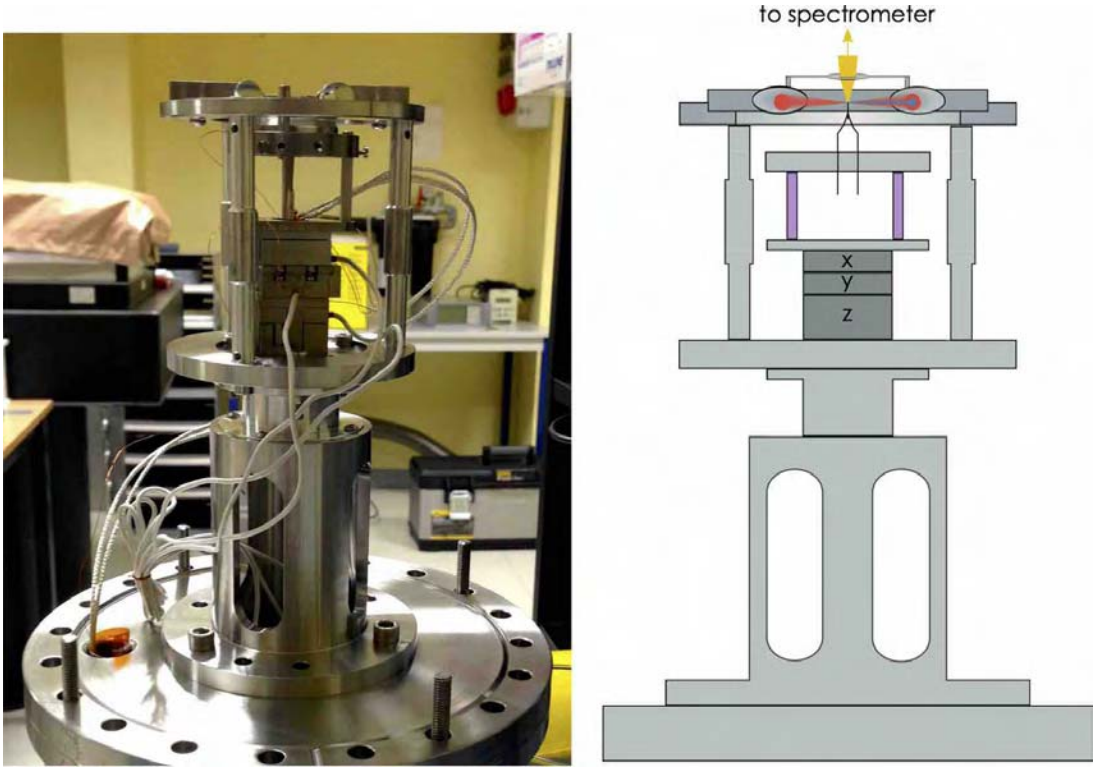

Figure 3.14 – Left: A photo of the tip manipulating ensemble. Right: schematic of the ensemble.

The tip holder is unique for each tip geometry.

3.3.1 Holder for tungsten based tips

The holder (Fig. 3.15 (a)) for tungsten based tips (single crystal W(310) and CCnT tips) provides a base for holding the tip. It is electrically separate from the rest of the setup to allow a voltage to be applied to the tip. Most importantly it allows both plugs to be electrically connected such that a current can pass through the filament, strongly heating the tip for cleaning purposes (flash, described in Sec. 3.1.1). There is the possibility of installing an anode. The anode is described in more detail below.

3.3.2 Holder for silver tips

The holder for silver tips (Fig. 3.15 (b)) centers the tips in the middle of the laser focus. This holder is different than that for tungsten based tips as the silver tips are made at GPM. The tips are electrically separated from the rest of the ensemble. A voltage can be applied to the tip. As there is only one connection to the tip, no current can be passed through the tip. However, due to the nature of fabrication of the silver tips, flash cleaning is not necessary.

3.3.3 Laser focus and intensity on the tip

The focusing of laser light and subsequent alignment went through several generations. In the first setup, as seen in Fig. 3.16 (a), the laser beam is focused with an on-axis silver mirror

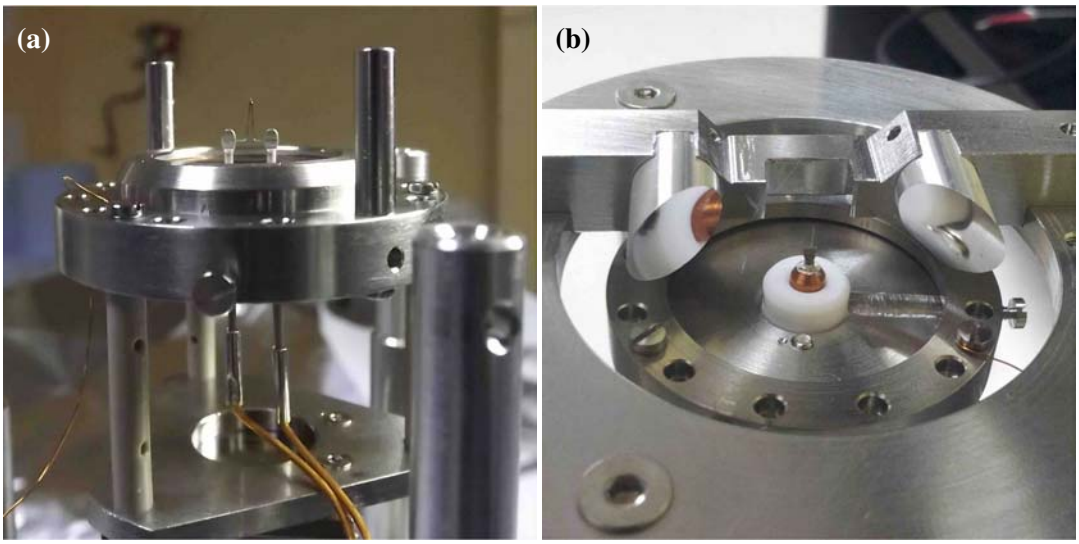

Figure 3.15 – (a) The tungsten-based tip holder. Note the possibility to pass a current through the tip via the plugs below. (b) The silver tip holder.

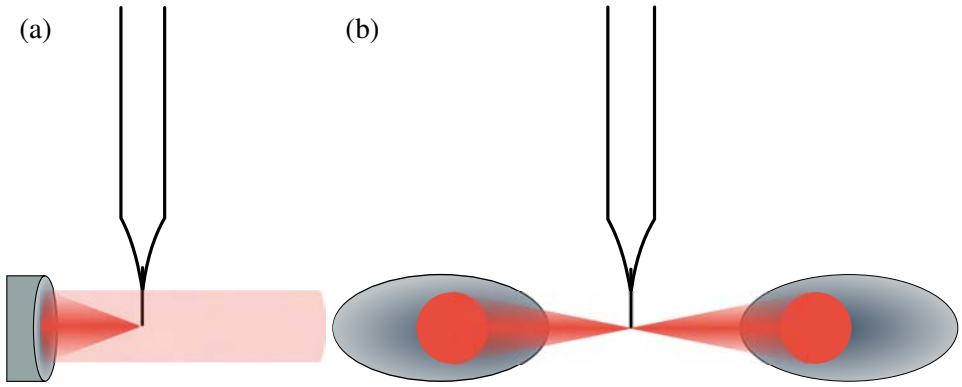

Figure 3.16 – (a) this panel shows the on-axis spherical mirror geometry, (b) shows off-axis parabola (OAP) geometry.

with a focal length of 4.5 mm to a beam waste of $\sim$2 μm in radius. The second focusing configuration, Fig 3.16 (b), uses 2 aluminum off-axis parabolas (OAP) with a focal length of 15 mm to focus the beam to $\sim$3 μm in radius. The off axis geometry allows us to collect the laser light after the experimental interaction for both analysis and alignment purposes, but has a slightly larger focus.

In all the experiments we performed, the optical intensity at the tip is a key parameter that needs to be carefully evaluated. The intensity is calculated as a function of laser spot size (measured via knife edge measurements as explained in Sec. 2.2.1) and the laser peak power (using the laser pulse energy and repetition rate as detailed in Sec. 2.2.3). We carefully measure the optical losses of the focusing mirror and vacuum window and from this can calculate the optical intensity illuminating the tip. However, these calculations do not take into account the optical field enhancement from the tip. The field enhancement could not always be precisely determined as we lack simulation tools. In Chap. 6, we will detail measurements which give us an estimation of the optical field enhancement from a silver nanotip.

3.3.4 Anode

The anode is a flat metal plate facing the tip with a hole centered at the tip (Fig. 3.17). In electron microscopy the anode serves three purposes. First, the anode is used in the traditional sense to collect electrons and measure the emitted current from the tip. Second, a small hole in the anode is used to select a portion of the electrons that are emitted. This allows a specific, coherent energy width of electrons to be used, and masks secondary electrons. Finally, the anode serves to define a ground potential around the electron trajectory. For our experiment, we use the anode for the second two purposes.

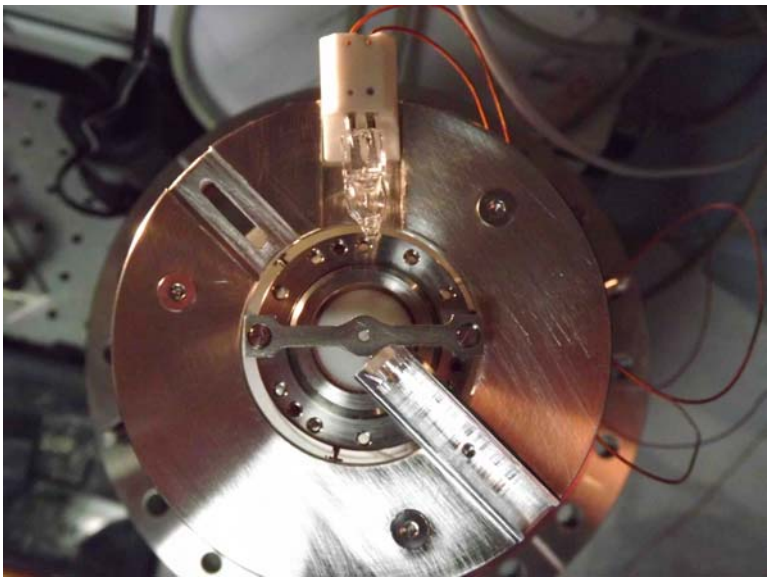

Figure 3.17 – Photo of the anode mounted on the tip holder ensemble centered facing the nanotip.

We fabricated several anodes with various diameter pinholes in the center. The anode is a circular disc made of titanium, 8 mm in diameter, 0.8 mm thick, with a central pinhole of 1-2 mm in diameter. It is positioned 3-5 mm from the tip, depending on the length of the tip. We use a microscope to align the tip in the center of the hole. Due to the slight inconsistencies from the home-made tip fabrication process, the tips are not perfectly centered on the filaments or slightly tilted from tip-to-tip. This makes it very difficult to align the small pinhole with the tip exactly facing the center of the hole. One solution is to enlarge the pinhole in the anode to allow for the variations of the tips. Unfortunately, this also diminishes the coherency and resolution of the electron energy selection. The anode also limits spatially resolved electron measurements as only electrons that are emitted in the range of the pinhole can be detected. Physical size can also be constricting as the anode extends out from the tip holder and is placed very close to the electron spectrometer.

The second generation anode is a copper pinhole on the entrance of the spectrometer. This pinhole, which is at ground, is used to both selection emitted electrons and define a potential at ground and has a diameter between 0.2 and 0.7 mm. Generally we used a diameter of

0.7 mm. Simulations performed by the Interactions Ion-Matiére (I^2M)[1] group at LCAR show that the electron trajectories within the spectrometer using just the pinhole are similar to those with the anode. Since the spectrometer is on 2D positioning stages, it can be aligned such that the centrally emitted electrons are counted by the spectrometer. It also can be scanned to form spatially resolved electron emission maps. More on this spectrometer functionality can be found in Secs. 3.5 and 3.6.2.

3.3.5 Voltage applied to the tip, V_{tip}

We apply a negative voltage (or bias) on the tip, called -V_{tip} (with V_{tip} is always taken to be $|-V_{\text{tip}}|$ for simplicity), generally between 0 and 600 V. The tip is facing a grounded electrode: either the grounded anode at a fixed position with respect to the tip (see Fig. 3.15), or the entrance pinhole of the spectrometer, that is grounded by construction (see Fig. 3.18).

This creates the static electric field near the tip.

It allows two things:

- with a high V_{tip} (typically 300-500V), we can reach detectable cold field emission.
- with a moderate V_{tip} (typically 15-50V), we extract laser-induced electrons to be detected by the spectrometer.

In both cases, emitted electrons reach the spectrometer with a kinetic energy equal to $e{\cdot}V_{\text{tip}}$.

3.4 Evolution of the setup

The experimental setup went through several generations.

1. In the first setup we used the anode to select electrons The laser was focused with an on-axis spherical mirror. The spectrometer was in a fixed location with respect to the tip. This setup was used for our tungsten results.
2. In the second setup we removed the anode and replaced it with the copper pinhole at the entrance of the spectrometer. This alleviates some of the geometrical constraints from the anode allowing us more flexibility with positioning the tip.
3. In the third generation of the setup, we removed the on-axis spherical mirror and replaced it with the OAPs (off-axis parabola). We also added nanopositioning stages underneath the spectrometer allowing for 2D position. This is described below in Sec. 3.5.

3.5 Electron emission and detection: the electron spectrometer

The electron emission is collected and measured in a field retarding spectrometer [Hori75], which gives us access to the kinetic energy distribution of the emitted electrons. Our spectrometer was designed and developed by the I^2M group at LCAR. Electrons are detected with

[1] http://www.lcar.ups-tlse.fr/spip.php?rubrique33

a microchannel plate (MCP). In our measurements with an MCP, the tip is negatively biased and acts as a cathode, the electron source. The MCP ensemble[1] from Hamamatsu has a 32 mm diameter active area with 2 stages. The front of the MCP is biased with +300 V, and the backside is biased with a high voltage of +2.08 kV with a final electrode as the anode. The field retarding spectrometer, with an entrance pinhole with a variable diameter of 0.2–0.7 mm (usually 0.7 mm), is placed between the tip and the MCP detector. The entire spectrometer ensemble is inside magnetic shield made of mu-metal to shield from external magnetic fields as low velocity electrons are very sensitive to residual magnetic fields.

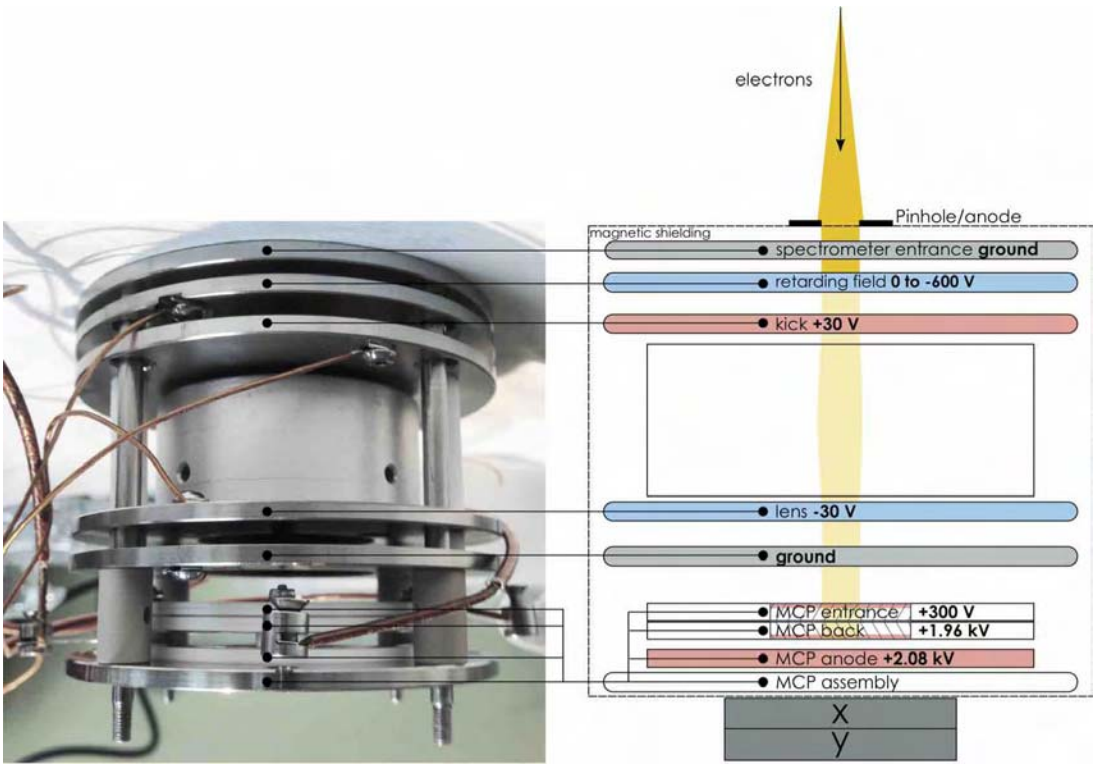

Figure 3.18 – left: A photo of the electron spectrometer without the magnetic shielding. Right: schematic of the spectrometer

The spectrometer is based on a double mesh tungsten grid with an adjustable retarding field (V_{retard}) combined with the MCP to record the integrated kinetic energy distribution of the emitted electrons. The grid acts as a high-pass energy filter for the emitted electrons. Only electrons with a minimum energy greater than that of the grid can pass and be collected. The electron energies measured are usually referenced to the Fermi energy, which in our experimental setup is equivalent to eV_{tip}. Since the electrons that pass have little residual energy, they are accelerated with a +30 V kick. The electrons then pass through an Einzel lens, which redistributes the electrons over the active area of the MCP. The entrance of the MCP is at +300 V to put the electrons which is the energy at which the MCP is most efficient. The back is at 2.8 kV, which is the point of saturation for the gain of electron collection (corresponding to a gain of $\sim 10^6$). A schematic of the spectrometer can be found in Fig. 3.18.

[1] http://www.hamamatsu.com/us/en/F2224.html

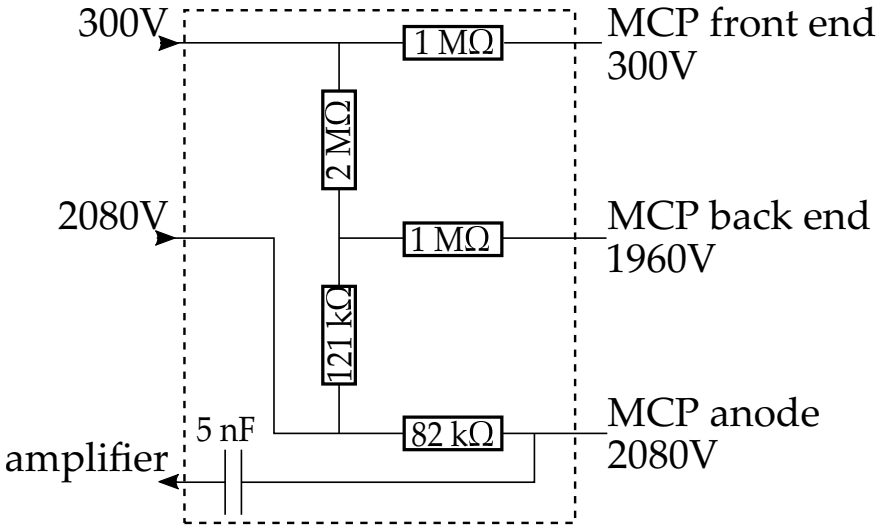

Figure 3.19 – This shows the schematic of the MCP signal amplifier.

The signal from the MCP is passed through an decoupler, Fig 3.19, which converts the tiny MCP signal into a signal that can be measured, a voltage of 100s of mVs. The amplified pulses are sent through a discriminator which converts them into a transistor-transistor logic (TTL) signal which can then be counted by the acquisition system of the computer. The discriminator only allows hits with a certain amplitude to be counted by the computer, therefore limiting the number of hits counted, but also lowering the noise that passes through and increasing the signal to noise ratio.

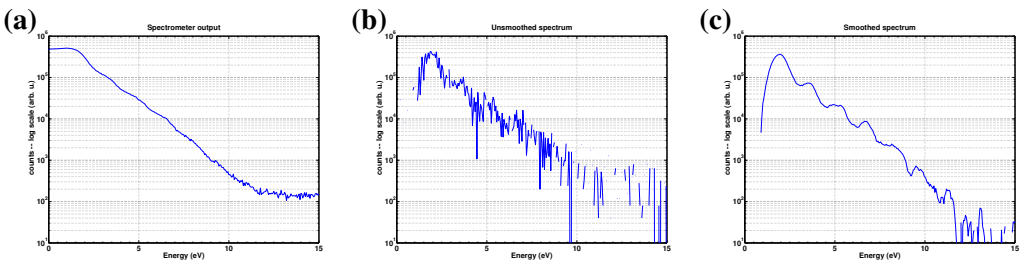

Figure 3.20 – (a) This shows the direct output of the spectrometer, an integrated spectrum. (b) This shows the differentiation of the output of the spectrometer, to get a kinetically resolved spectrum. (c) This is the spectrum after it has been smoothed with a Savitzky-Golay distribution over 11 points.

We scan V_{retard} around V_{tip}, with steps of 0.05 V to record the electron energy spectrum. The data collected by this type of spectrometer gives an integrated electron spectrum, Fig. 3.20 (a). The actual electron spectrum can be retrieved by the differentiation of the recorded curve, Fig 3.20 (b) and then smoothed with a Savitzky-Golay distribution, Fig. 3.20 (c).

This type of spectrometer has a resolution of $\Delta E/E \sim 4 \times 10^{-3}$ as evaluated by simulation from SIMION [1]. This means that we must keep the applied field (E) as low as possible to maximize resolution. By taking a static spectrum (a spectrum with a high enough V_{tip} to

[1] simion.com

induce cold field emission) we can measure the resolution (Fig. 3.21). As the configuration of the tips vary from tip to tip, so does the resolution of the spectrometer. We found the resolution to be from 5×10^{-3} (as in Fig. 3.21) to $\sim 10^{-2}$. We find that the typical transmission of the spectrometer, with no retarding field, to be on the order of 60 % (calculated from the grid fill factors).

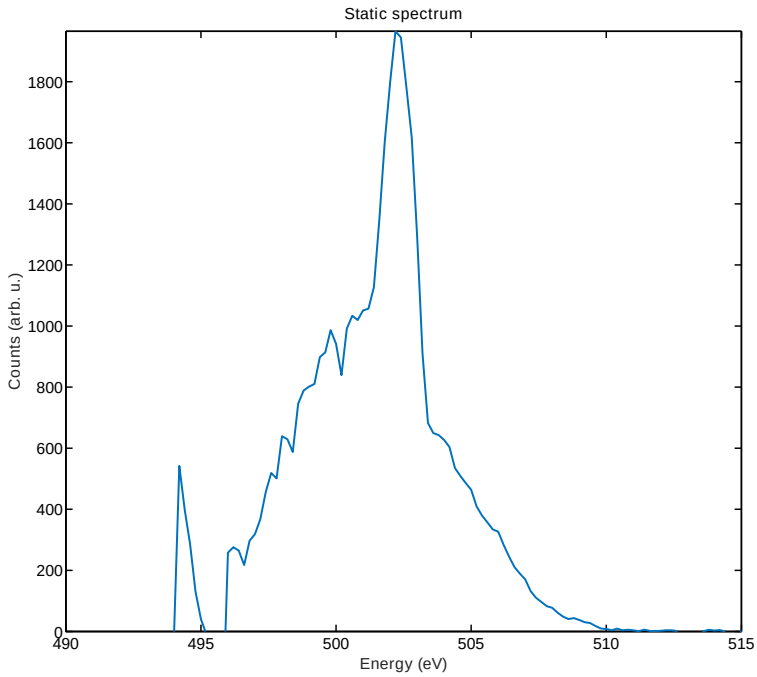

Figure 3.21 – This shows a typical static spectrum from a tungsten tip. The fwhm of the spectrum is $\sim$2.5 eV, and taking $E = 500$ eV, we find the resolution to be $\Delta E/E = 5 \times 10^{-3}$.

The MCPs can only detect one electron at a time. At high laser pulse energy, we are close to detecting one electron per pulse. With no retarding field and a 0.7 mm diameter pinhole at the entrance of the spectrometer, we detect $\sim$600 electrons per second for a 1 kHz repetition rate, indicating that there may have been one or more electron emitted per pulse; however, with the geometric constraints of the spectrometer, the number of electrons that are detected is less than one per pulse, avoiding space charge effects.

The second generation spectrometer ensemble is placed on two dimensional nanopositioning translation stages (ECS3030num, also from Attocube systems AG) with nanometer resolution and a range of several millimeters. These also have the num closed loop stabilization and can hold heavier loads; however, they are made from stainless steel so are not impervious to creating magnetic fields. They are placed outside the mu-metal shielding to prevent magnetic disturbances in the spectrometer.

As the samples are made in house, and from a variety of materials, the emission site and subsequent electron trajectories vary from sample to sample. For example, the tips may be mounted at an angle which not only changes the central bright spot location, but also the recorded maximum energy as seen in Fig. 3.22. This is because the spectrometer measures the kinetic energy

of the electron along its axis. If the electron enters with an angle θ this means that the spectrometer measured and energy of $E\cos^2\theta$. The spectrometer can then be positioned centered at the projected spot of highest electron yield, thus increasing the efficiency and resolution of the detector.

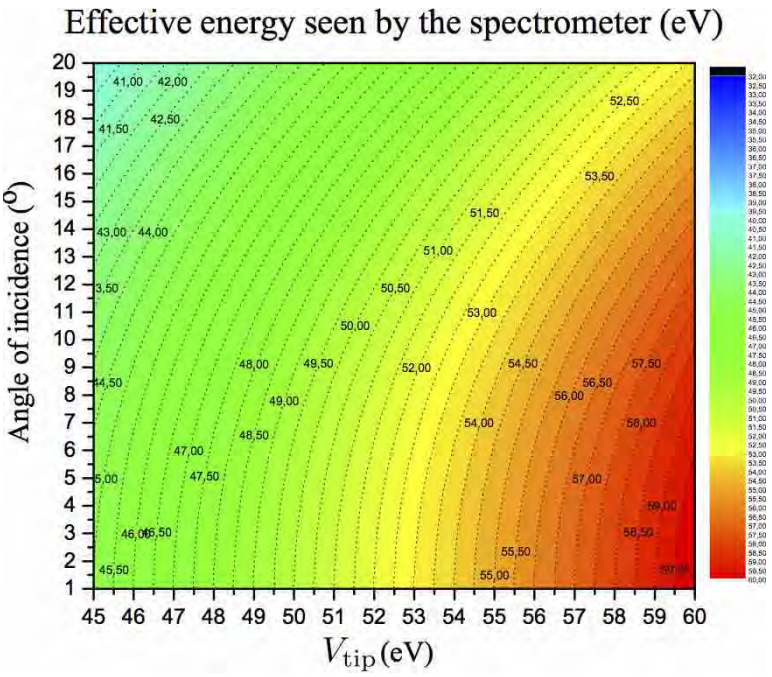

Figure 3.22 – This shows the calculated electron energy seen by the spectrometer for an angled tip.

The spectrometer can collect data in two ways. First the spectrometer is stationary and collects all the electrons from one position. In general when in counting mode, the retarding field is being scanned such that an integrated spectrum of the kinetic energy of the emitted electrons can be recorded.

This was further developed into a second mode. This is a 2D or position scanning mode. Here, the spectrometer can be scanned in both dimensions to study spatially resolved electron emission. With a small pinhole on the entrance of the spectrometer (0.2-0.7 mm in diameter) and 2D scanning, a Field Emission Microscopy (FEM)-like image is taken.

For static FEM, a high voltage is applied to the tip to induce cold field emission. The projection of the electron trajectories (Fig. 3.23) is then recorded as a function of number of electrons counted to the position of the spectrometer. The system works as a projection microscope with the magnification factor given by the ratio of tip-anode distance and tip radius.

The same spatially resolved data could be taken by replacing the MCP anode with a biased phosphor screen. The phosphor screen fluoresces when hit by an electron, and this can be recorded by a camera. While this detection scheme allows for single-shot recording of spatially resolved data, our chamber geometry and configuration does not allow for placement of a camera so we must resort to physically moving the spectrometer for spatial data collection. Generally these phosphor screen measurements do not have as much dynamics in data collection as our spectrometer.

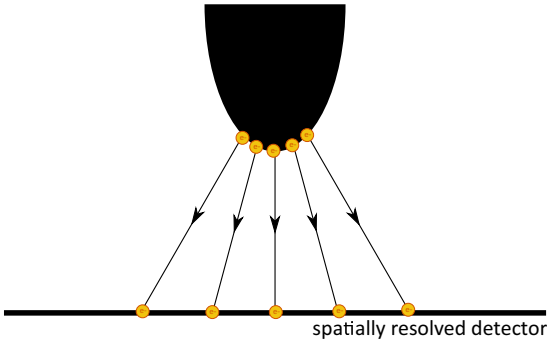

Figure 3.23 – This shows how the projection of the electron trajectories is recorded by a spatially resolved electron detector.

3.6 Alignment Procedure

3.6.1 Laser Alignment

The alignment of the laser through the chamber, and the alignment of the tip into the focus depends on the geometry of the focusing elements described in Sec. 3.3.

On-axis spherical mirror:
The alignment of the laser onto the focusing optic is done while the chamber is at atmospheric pressure, with no tip mounted in the chamber so that the focus can be checked with a card in the beam. This pre-alignment is checked through a side port of the chamber.

The position of the tip in the laser focus is first pre-aligned with no laser. First, a CCD camera with a long-distance microscope objective is places on axis with the laser propagation outside the chamber, using mirrors. The image of the nanotip in the mirror shows when the tip passes through the mirror focus along the laser propagation direction as the image of the nanotip in the flips direction in the focus. The tip apex is placed roughly in the focus plane also in reference to the reflection of the mirror. A schematic of this alignment outline is seen in Fig. 3.24 (a). This shows a schematic of the reflection of the tip in the mirror. The alignment is further checked and optimized using the diffraction from the laser seen by the camera when positioned perpendicular to the propagation direction. This can be seen in Fig. 3.24 (b). The left panel of the inset shows a schematic of the diffraction off of the tip, and the right panel shows a image of the tip in the focus. Fine tuning is achieved by maximizing electron emission from the laser and checking the emission polarization dependence. Polarization dependence will be explained more in Sec. 4.3.1.

Off-axis parabolic mirrors:
The alignment of the off-axis parabolas (OAPs) is first done outside the chamber in air, before mounting the mirrors onto the tip manipulator. This ensures the alignment and positioning of the OAPs themselves such that the beam is nicely focused by the first OAP and then properly recollimated by the second. Once the mirrors are in the chamber, the laser is pre-aligned off the OAPs with the tip not in the focus. An imaging lens is placed after the second OAP to image the focus onto a CCD camera.

The alignment of the tip into the focus is done while looking at the shadow of the tip in the

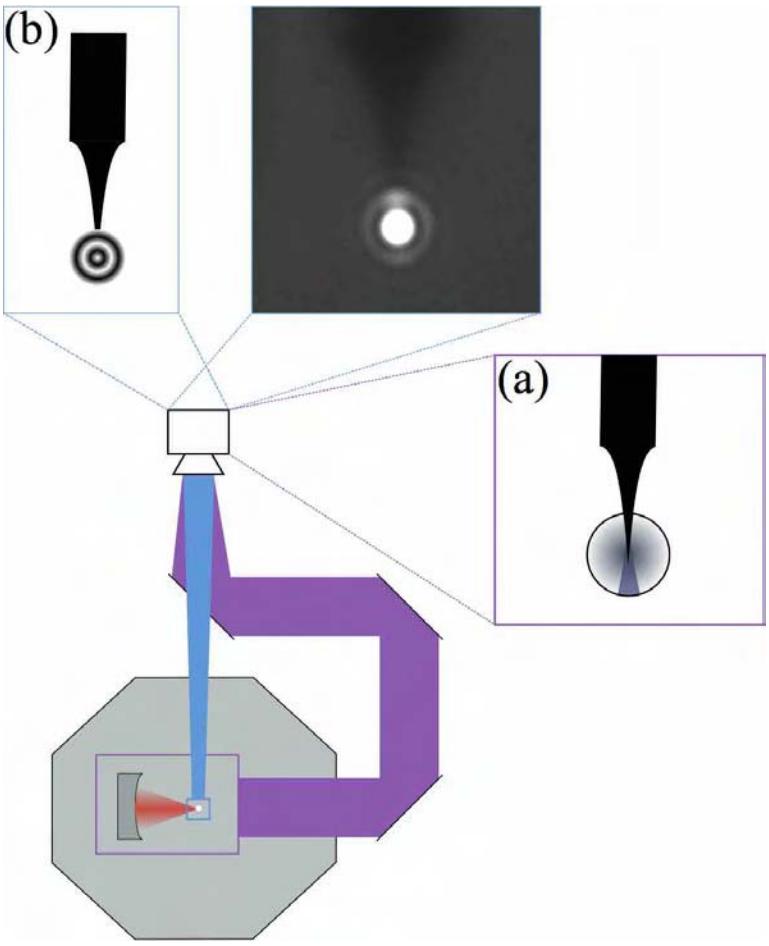

Figure 3.24 – This shows a schematic of the tip alignment into the laser focus using the on-axis spherical mirror.

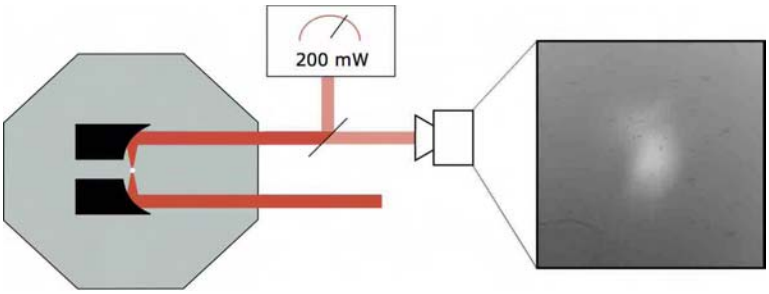

Figure 3.25 – This shows a schematic of the tip alignment into the laser focus using the OAP configuration. Alignment is checked by minimizing the transmission of the beam with the tip in the focus as well as looking at the shadow the tip makes while in the focus.

transmitted beam as well as the power of the transmitted beam. The tip is positioned such that the beam transmission is minimized. The tip is slowly lifted while continuing to minimize the transmitted power, thus ensuring that the tip is in the focus, until the tip only blocks $\sim$4% of the beam's output power. A schematic of this setup is seen in Fig. 3.25. Once again, fine tuning is reached by maximizing electron emission from the laser and by checking the polarization dependence of the emission.

3.6.2 Spectrometer Alignment

When the spectrometer is use in counting mode, it is typically positioned to collect the maximum number of electrons. A 2 dimensional map of the electron emission is made while the tip is emitting via cold field emission. This means that enough voltage is applied to the tip that a significant number of electrons can tunnel via cold field emission described in Sec. 1.2.2. The spectrometer is then moved to the position of maximum emission. This is done after the tip has already been placed in the laser focus

The position may vary due to inconsistencies in the tip geometry. For single emission site tips such as single crystal W(310) and CCnT tips, the tips might not be centered exactly in the same way from sample to sample. The tips might also have been welded or etched at a slight angle, changing the position of the emission. For polycrystalline tips, such as Ag, the emission site is not necessarily clear. The orientation of the crystals for each facet of the end of the nanotip changes for each tip, so this alignment step is important.

3.7 Summary

We have built a new experimental apparatus used to investigate electron emission from sharp nanotips. We also have access to a variety of materials from which make our tips: tungsten, silver and a carbon nanotube based tips. Each tip requires a slightly different mounting procedure into our ultrahigh vacuum chamber. The tips are positioned into the laser focus with three dimensional nanopositioning stages. The emitted electrons are detected in a homemade field retarding spectrometer with a resolution of $\sim 10^{-2}$ eV, and a transmission of ~ 60 %. This allows us to collect integrated electron spectra from which we can differentiate to kinetically resolve the energy of the electrons. The spectrometer can also move in two dimensions allowing for spatially resolved, FEM-like, measurements.

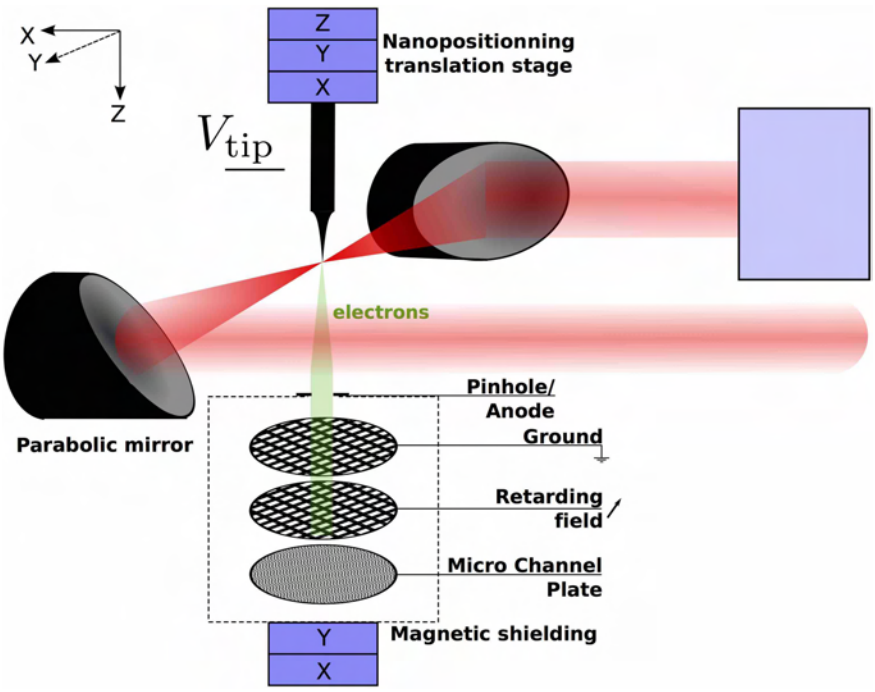

Figure 3.26 – This is a schematic of the final version of the experimental setup. Adapted from Ultramicroscopy, doi:10.1016/j.ultramic.2014.11.027, M. R. Bionta *et al.*, "First results on laser-induced field emission from a CNT-based nanotip", Copyright (2014), with permission from Elsevier. [Bionta14b]

The final version of experimental setup consists of:

- the laser is focused with an OAP
- the tip is moved with nanopositioning stages into the laser focus
- the spectrometer and copper pinhole can be moved together and aligned under the tip at location of maximum emission for integrated electron spectrum measurements
- the spectrometer and copper pinhole can be moved together to make a 2D map of the electron emission

This can be seen schematically in Fig. 3.26.

4

Results from tungsten nanotips

Tungsten (W, atomic number 74) is a robust material with a long history of usage as a field emitter for field emission and ionization systems due to its high melting point of 3695 K [Gomer61, Good Jr56]. Laser induced emission from sharp tungsten nanotips has been extensively studied [Hommelhoff06b, Schenk10, Barwick07, Hommelhoff06a, Yanagisawa10] and provides a baseline for which we can compare our new experimental setup.

I first detail the techniques used for *in-situ* tip characterization for new samples put into the chamber and show typical results. I will then discuss investigations into mechanical thermal effects the laser may have on the tips. Laser induced electron emission is discussed in two forms. First I describe non-kinetically resolved emission processes as a function of the laser. This includes the laser power and polarization dependence of the electron yield, and interferometric measurements. I then describe the kinetically resolved results. This involves kinetically resolved electron spectra and investigations on above threshold photoemission.

4.1 *In-situ* tip characterization

The characterization of the tips while they are in the chamber allows us a second method (after SEM images) for characterizing and confirming the sharpness of the tips as well as a means for checking if the tip end is still sharp. We also use *in-situ* characterization for understanding the unique emission patterns that arise from each tip.

4.1.1 Fowler-Nordheim plots

In order to determine the size of the tip, while it is in the chamber, we use the Fowler-Nordheim (FN) equations, which governs the emission of electrons induced by a large static field as a function of the field. This process is called cold field emission (explained in Sec. 1.2.2).

The FN equation (Eq 1.19) and resulting plots enable a simple method for relating the emission current to the radius of the apex of the tip as a function of the applied voltage. By applying the geometric field enhancement of a sharp nanotip ($F = \beta V$, Eq. 1.29), to Eq. 1.19 we see that the emitted current $J(V)$ has the following dependence on the tip bias V:

$$J(V) \propto \beta^2 V^2 \cdot \exp\left(-\frac{\alpha}{\beta V}\right), \tag{4.1}$$

where α is the constant in Eq. 1.20 involving the work function and taking into account the image force of the tunneling electron. Taking the natural log of both sides gives

$$\ln\left(\frac{J}{V^2}\right) = -\frac{\alpha}{\beta} \cdot \frac{1}{V} + \text{Constant}. \tag{4.2}$$

β can be determined from the slope of a curve (α/β) relating the total field emission current J as a function of applied voltage V by plotting $\ln\left(\frac{J}{V^2}\right)$ vs $\frac{1}{V}$. This plot is the FN plot. From β we can infer the radius of the tip. This means that the smaller the ratio of α/β, the sharper the tip.

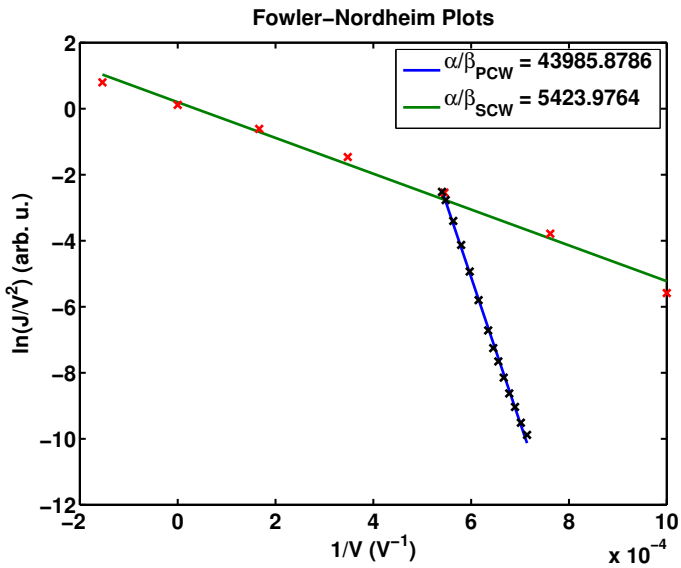

Figure 4.1 – The blue curve with black x's shows a FN plot for a polycrystalline tungsten tip. The green curve with red x's shows the FN plot for a single crystal W(310) tip. The single crystal tips are generally smaller in radius as is evidenced by their smaller α/β ratio and lower emission threshold (Tab. 1.1).

To determine the tip radius we can solve for β. From Eq. 1.20 we know that

$$\alpha = \frac{4\pi\sqrt{2m_e}\cdot}{3\hbar e} \cdot \phi^{3/2} \cdot v(w) = 6.83 \times 10^9 \cdot \phi^{3/2} \cdot v(w). \tag{4.3}$$

The derivation of $v(w)$, the Nordheim function, is discussed in Sec. 1.2.2. We use FN plots to ensure that the tip radius is maintained throughout our experiments. Curves are taken periodically throughout the lifetime of the tip to ensure that the ratio of α/β, the slope of the curve, is the same as laser has illuminated the tip. This helps certify that the tip has not been damaged during the experiments.

In Fig. 4.1, the blue curve shows the fit for FN plot taken for a polycrystalline tungsten (PCW) tip (black x's). The green curve shows the fit for a single crystal W(310) (SCW) tip emission (red x's). Typical voltages for detectable electron emission (called the emission threshold)

Table 4.1 – This table calculates the approximate tip radii for the FN plots given in Fig. 4.1. α is calculated without taking into account the image force (i.e. $v(w) = 1$) with α' assuming $v(w) = 0.6$ [Hommelhoff06b]. r is calculated using the relation $\beta = 1/kr$ with $k \sim 5$ (close to the apex) [Gomer61].

PCW (blue line)	SCW(310) (green line)
$\alpha/\beta = 43986$	$\alpha/\beta = 5424$
$\phi_{\mathrm{PCW}} = 4.5$ eV	$\phi_{\mathrm{W(310)}} = 4.34$ eV
$\alpha = 6.52 \times 10^{10}$ V/m	$\alpha = 6.20 \times 10^{10}$ V/m
$\alpha' = 3.91 \times 10^{10}$ V/m	$\alpha' = 3.72 \times 10^{10}$ V/m
$\beta = 0.89 \times 10^{6}$ m^{-1}	$\beta = 6.91 \times 10^{6}$ m^{-1}
$r = 230$ nm	$r = 30$ nm

are 750 V for a PCW tip of radius ~250 nm and 200 V for a SCW(310) tip with a radius of ~30 nm. The SCW tips are generally smaller in radius as is evidenced by their smaller α/β ratio. Using the relation $\beta = 1/kr$ we can calculate the tip radius. By assuming $v(w) = 0.6$ [Hommelhoff06b] and $k \sim 5$ (close to apex) [Gomer61], we can calculate the approximate radii for the FN plots in Fig. 4.1, as seen in Tab. 4.1. We find that for PCW, $r = 230$ nm, and for SCW(310) $r = 30$ nm. Indeed we confirm by SEM in Fig. 4.2 that the PCW tip apex is much larger than that of SCW(310).

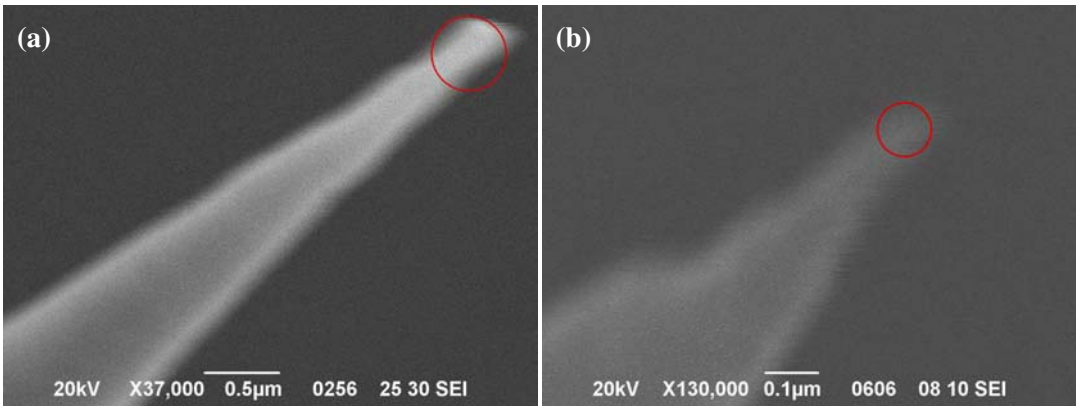

Figure 4.2 – This shows SEM images of the tips whose FN plots are given in Fig. 4.1 (a) This shows an SEM of a PCW nanotip. The tip apex is measured to be $r < 250$ nm (red circle) in agreement with the FN calculations. (b) This shows the SEM of the apex of a SCW(310) nanotip. The tip apex is measured to be $r < 50$ nm (red circle) as given by the FN calculations.

The FN plot is measured each time a new tip is put into the setup. We also periodically perform FN plots to ensure the tip is still sharp, for example, after illumination by an intense laser.

4.1.2 Field emission microscopy

To complete the characterization of the tip, we can perform spatially resolved electron detection. Field emission microscopy (FEM) [Gomer61, Müller36] is a simple method for investigating the electron emission patterns from a tip. In FEM, the nanotip emits towards a spatially resolved detector, in our case, the spectrometer in 2D position sensitive mode. This was only available in the latest generation of the experimental setup. Since these images are taken by

physically moving the spectrometer, they typically take a long time to record, on the order of 1-2 hours per image.

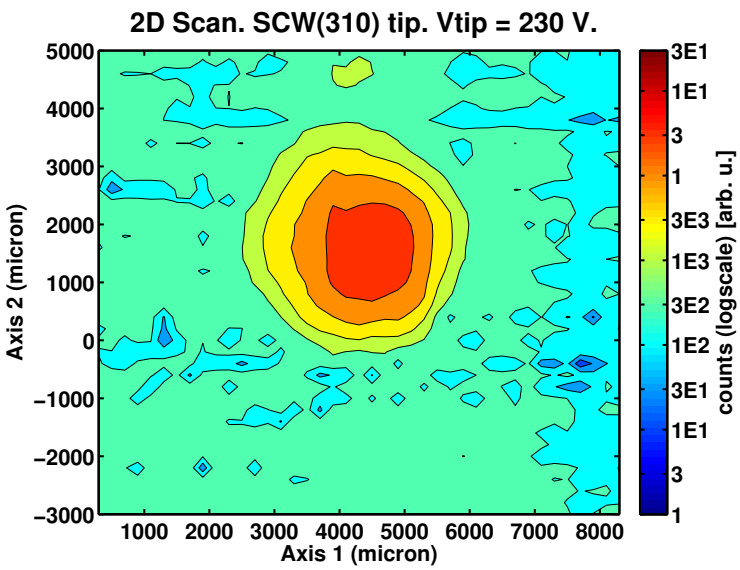

Figure 4.3 – This shows FEM (spatially resolved emission) for a single crystal tip, with $r = 50$ nm. The W(310) facet has the lowest work function of all so emits at the lowest threshold and has a higher electron yield than the other facets.

By comparing the FEM images from PCW to SCW we see that the PCW emits from the facets with the lowest emission thresholds (typically those of W(310)). We can see that by choosing W(310) allows the maximum number of electrons to be emitted and collected. Fig. 4.3 shows a FEM image for a (310) oriented tungsten tip. We can then position the spectrometer such that the highest brightness emission facet is oriented towards the entrance slit. We also can periodically take scans to confirm that the tip has not broken after strong laser illumination, forming new sharp edges where emission might occur.

4.2 Thermal damage studies

For high repetition rate, high mean power lasers, thermal effects are generally non-negligible which can lead to tip destruction. Evidence of damage to tips was sometimes observed after laser irradiation; however, it was unclear if this damage was thermal damage, or mechanical damage possibly from tip transportation. Because of this, we investigated the thermal effects of the oscillator laser on tungsten tips.

A tungsten "comb" was fabricated such that we could systematically look at the thermal effects in tungsten. The comb consisted of a silicon substrate onto which many tungsten tips were pasted. Each tip was then systematically irradiated in turn at a specific laser power and for a specific amount of time. We empirically looked for laser damage by comparing SEM images from before and after laser irradiation. The laser was focused with an on-axis spherical mirror with a focal length of either 7 mm or 50 mm to greatly vary the intensity. Due to the use of adhesive to attach the tips to the substrate, the application of a bias voltage was not possible. This means there was no way of extracting the emitted electrons from the irradiated tips. The

alignment of the tips was done at low laser intensity using the diffraction scattering seen by the CCD camera. For example, tip A4 was aligned with 250 μW of average power (4.11×10^7 W cm^{-2} peak intensity), a procedure which took $\sim$10 minutes before being illuminated with 10 mW (1.64×10^9 W cm^{-2}). The intensity of the illumination power is an order of magnitude less than the minimum laser intensity with which we tested. The long focal length also means that there was a long Rayleigh ranges and thus the tip was more likely in the focus of the laser. Two tips were not intentionally illuminated with the laser for control purposes.

Comparisons of SEM images before and after laser irradiation showed no significant modification in the nanotip structures. None of the tips illuminated with the longer focal length showed any signs of damage. Fig. 4.4 shows before and after SEM images of tip B1 after illumination with 200 mW of average power for 24 hours with a focal spot size of $\sim$25 μm, corresponding to a peak intensity of 3.29×10^9 W cm^{-2}. No visible damage is seen.

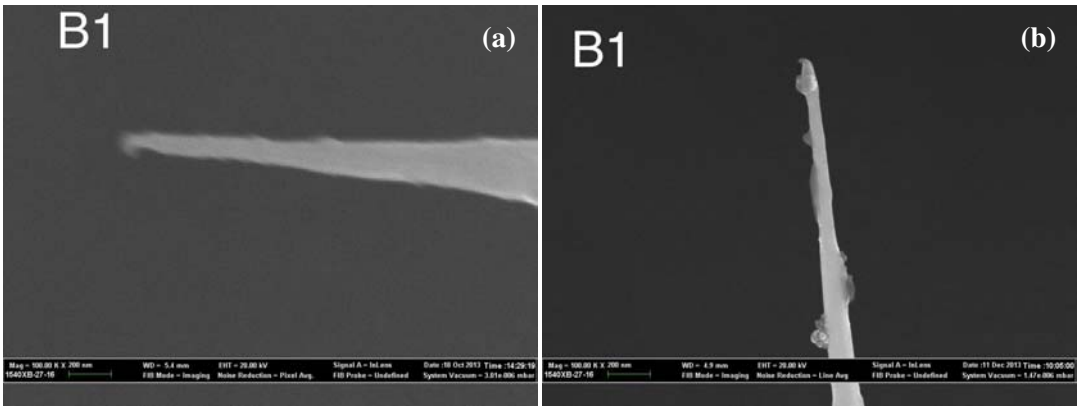

Figure 4.4 – (a) A SEM of tip B1 before laser irradiation. (b) SEM of the same tip after irradiation with 200 mW of average power for 24 hours with a focal spot size of $\sim$25 μm, corresponding to a peak intensity of 3.29×10^9 W cm^{-2}. No visible damage is seen.

C2 was illuminated with the highest laser intensity for the longest time, 8.38×10^{11} W cm^{-2} for 24 hours. This corresponds to 100 mW average power with a spot size of 3 μm due to the shorter focal length. A small drop appears on the side of the tip in after illumination with the laser. This could potentially be due to melting of the tungsten. The apex of the tip is also slightly bent, probably due to the laser irradiation.

Scans from a residual gas analyzer (RGA) were taken during each of the tests, however, no particular species were detected. As we could not detect emitted electrons by the tips due to the construction of the comb, we were not sure of the exact alignment of the tips into the focus. Apart form this, and even though the before and after SEM images were taking by two different people and thus the resolutions and areas investigated were not the same, we saw no evidence of laser induced thermal damage due to our tests. A complete data set of before and after SEM photos can be seen in App. B.

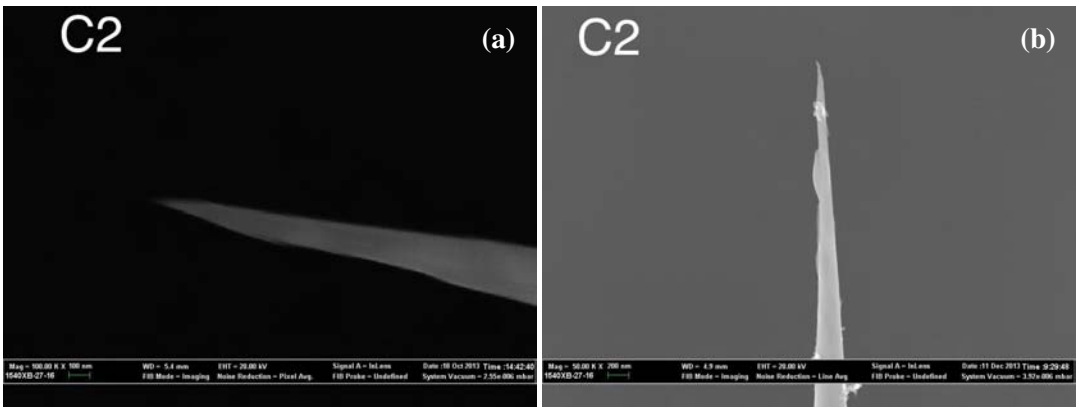

Figure 4.5 – (a) A SEM of tip C2 before laser irradiation. (b) SEM of after irradiation with 100 mW of average power for 24 hours with a focal spot size of $\sim$3 μm, corresponding to a peak intensity of 8.38×10^{11} W cm^{-2}. A small droplet is seen on the side of the tip and the apex is slightly bent after irradiation.

4.3 Laser induced emission

In order to test the validity of our setup, we investigate laser induced emission phenomenon in the Keldysh regime from the electron emission from the tip. Much of this discussion comes from and is augmented upon [Bionta14a].

To extract the electrons emitted from the tip, a small DC field, V_{tip}, typically between 20–50 V, is applied to the tip. After the laser is prealigned (Sec. 3.6.1) on the tip, it is carefully moved around in the focus to look for electron emission.

4.3.1 Laser polarization dependence

The electron emission induced by the laser is highly polarization dependent. This is because the photofield emission depends only on the component of the laser electric field which is normal to the surface [Venus83], which at the tip apex, is the component parallel to the tip axis. The optical field enhancement, due to the sub-wavelength size of the nanotip, is larger for polarizations parallel to the tip axis. By contrast, laser induced thermally enhanced field emission is most efficient at polarizations perpendicular to the tip axis [Barwick07, Hadley85].

When the tip is misaligned in the laser focus, the focus illuminates the shank of the tip. This strongly influences the heating of the tip, emphasizing thermally enhanced field emission. This provides a simple means of checking the alignment of the tip in the laser focus. If the tip is properly aligned, the focus will not heat the tip and there will not be any emission for polarizations perpendicular to the tip axis. By measuring the electron yield as a function of laser polarization, we can easily see if the tip is well aligned or not.

The polarization dependence of a well aligned tip is seen in Fig. 4.6 [Bionta14a]. The tip is illuminated with 150 mW (2.4 nJ/pulse, 8×10^{11} W cm^{-2}) from the output of the oscillator with V_{tip}= 50 V. The blue x's show the electron yield as a function of the laser polarization (θ) with respect to the tip axis. A polarization of 0° indicates that the laser field is parallel to the tip axis; likewise, a polarization of 90° means that the field is orthogonal to the tip

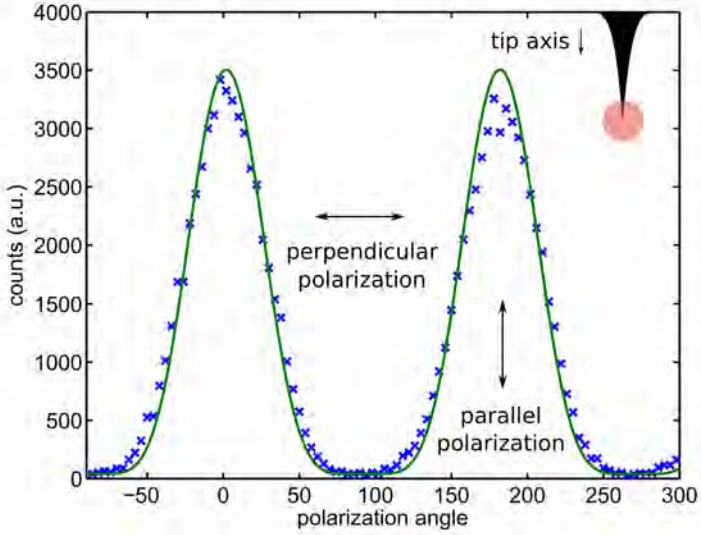

Figure 4.6 – Electron yield as a function of laser polarization (θ) with respect to the tip axis. Polarizations parallel to the tip axis (polarization angles of 0 and 90) have the highest electron emission, by contrast, perpendicular polarizations (angles of 180 and 270) have negligible emission. The experimental data (blue x's) are fit with the form $\cos^{2n}(\theta)$ (green line), where n is the number of photon absorbed by the system before emission. Figure adapted from [Bionta14a].

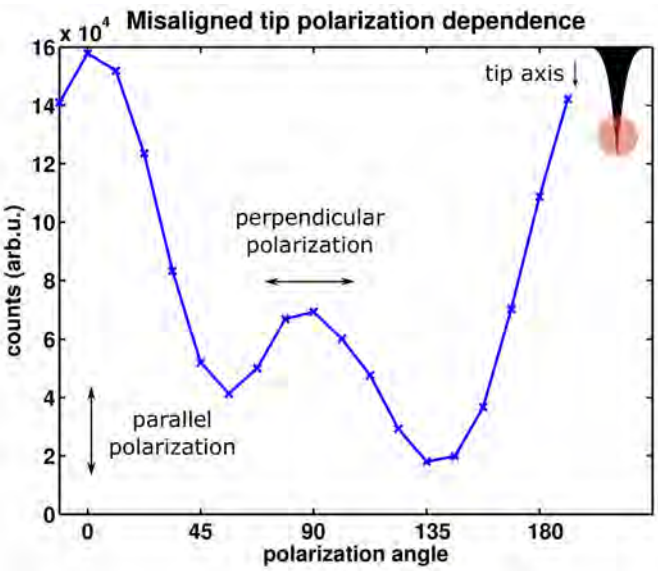

Figure 4.7 – This shows the electron yields as a function of polarization angle for a misaligned tip. As in Fig. 4.6, an angle of 0 corresponds to a polarization parallel to the tip axis, and an angle of 90 is perpendicular to the axis.

axis. As expected, maximum electron yield is found at polarization angles of 0 and 180, with a minimum at 90 and 270 and a contrast of ~3500:1. Fig. 4.7 shows the polarization dependence for a misaligned tip. Notice the counts that appear for orthogonal polarization. Maximizing the contrast demonstrates proper alignment. The polarization dependence is also very useful to check that the tip is still fully intact and not damaged.

4.3.2 Laser power dependence

Recall in Sec. 1.3.2, I derived the relation showing that for moderate laser fields, the current emitted is proportional to the intensity of the laser to an exponent η ($J \propto I^{\eta}$, Eq. 1.26). For emission from moderate laser intensity, including photofield emission and ATP, if the system absorbs n photons before an electron is emitted, we expect the exponent, η, to be equal to n, where n is the number of photons absorbed. The energy distribution of the electrons will average to η over all the contributions of the different number of absorbed photons for electrons of all energies emitted from the system. As we wish to study the Keldysh regime, we first investigate the laser power dependence for electron emission.

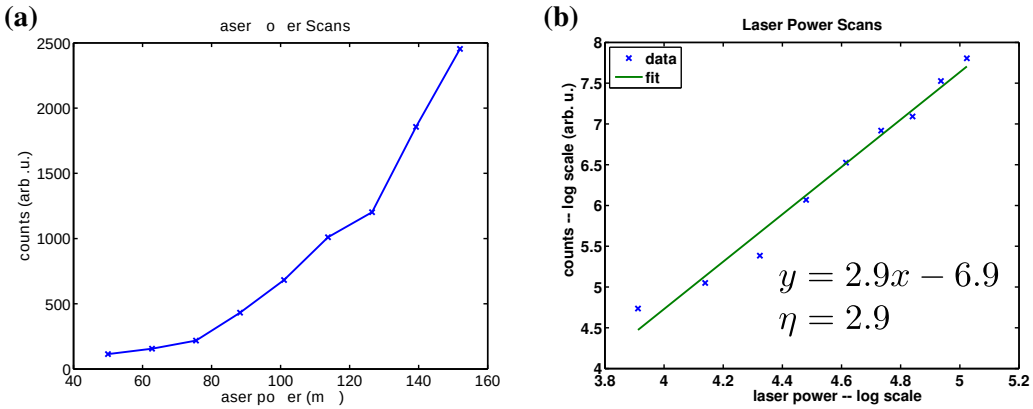

Figure 4.8 – (a) This shows the electron yield as a function of laser power for V_{tip} = 50 V. (b) This shows the same yield on a log-log scale. We can fit this curve to a linear equation from which the slope is the power exponent we wish to extract.

This relation is investigated on a polycrystalline tungsten nanotip for various V_{tip}. We measure the total number of electrons as a function of the laser power for different V_{tip}. To determine the power law for each V_{tip}, the number of electrons versus the laser power is fitted with a polynomial function of the form αI^{η}, where η can be non-integer. In practice, this is done by plotting the relation in log-log form. The slope of this resulting plot is the exponent η.

Fig. 4.8 shows an example of this. Here, the laser intensity was scanned from 3.8 to 11.4 $\times 10^{11}$ W cm^{-2} (50 to 150 mW) and V_{tip} = 50 V. Fig. 4.8 (a) shows the electron yield as a function of laser power. The exponential dependency is clearly seen. Plotting it in log-log scale, Fig. 4.8 (b), this becomes a linear relation from which we can fit a first order polynomial. The slope of this line shows us that $\eta = 2.9$. As PCW has a work function of $\phi = 4.5$ eV, and the photon energy of 800 nm light is 1.55 eV, we see that our extracted η is very close to $\phi/\hbar\omega = 2.9$, indicating over the threshold emission.

We perform the same study, now as a function of V_{tip}. This exponent η is plotted in Fig. 4.9 as a function of V_{tip}. For this figure, the laser intensity is scanned from 2.5 to 7.5 $\times$ 10^{11} W/cm^2 with the exponent retrieved from a polynomial fit of the data. The continuously decreasing behavior of this curve can be attributed to the Schottky effect (Sec. 1.1.1). As the applied voltage at the tip increases, the effective work function increases, decreasing the average number of absorbed photons needed to overcome the barrier. It is similar to that observed by Barwick *et al.*[Barwick07], however it is shifted by an offset which can be attributed to different exper-

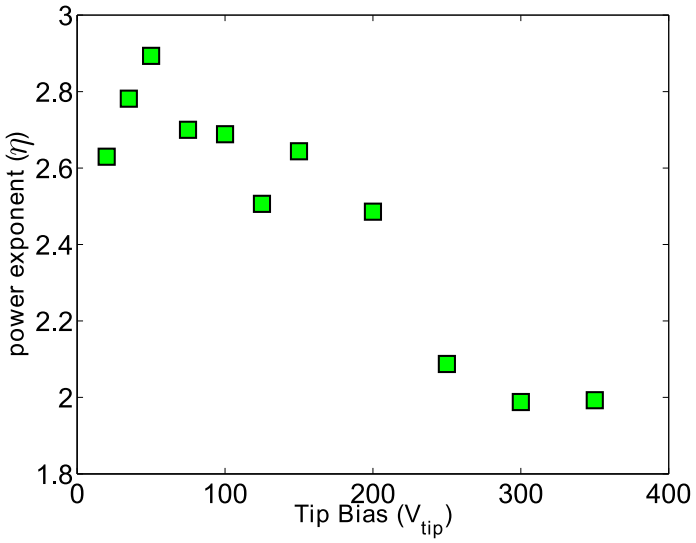

Figure 4.9 – Power law exponent η as a function of V_{tip}. The exponent is found by fitting the power dependence of the emitted current with respect to the laser intensity with a polynomial function of the form αI^{η}. The intensity is scanned from 2.5 to 7.5×10^{11} W cm^{-2}. Figure from [Bionta14a].

imental parameters. For example, if the vacuum is not sufficient, or if the tip is not properly cleaned, surface contamination of the tip can alter the metallic work function.

Polarization dependency curves corroborate the exponential proportionality of electron yield to laser intensity. As only the component of the polarization parallel to the tip axis contributes to the electron emission, this acts as a power dependency curve. We can fit the electron yield to $\cos^{2n}(\theta)$, where θ is the polarization angle with respect to the tip axis. For the polarization curve given in Fig. 4.6, with V_{tip}= 50 V, we find a fit (green line) for n = 2.8, which is in nice agreement of the exponential proportionality expression.

We find that indeed η is close to $\phi/\hbar\omega$ indication over the threshold emission. For photofield emission, we would find $\eta \sim 1$. We have sometimes found exponents much larger ($\eta \sim 7$ – 15), which we attributed to thermally enhanced field emission. However, it is difficult to relate these exponents to a theoretical model in this case as one would need to model the thermal dissipation in a tip. For our investigations V_{tip} is low, corresponding to an applied field F of $\sim 10^8$ V/m. For such a low tip bias, no thermal effects are expected. The investigations of thermally enhanced field emission performed by Kealhofer *et al* [Kealhofer12] demonstrate that for similar laser power, emission is mainly due to multiphoton absorption in HfC tips, which have lower thermal conductivity compared to tungsten, until the static electric field becomes on the order of 1×10^9 V/m. Only above this value does thermally enhanced field emission become dominant.

I will discuss the laser power dependence of the electron spectra in Sec. 4.4.

4.3.3 Two pulse interferometry

By adding a beam splitter and delay line to the beamline allows us to build a Michelson interferometer (Fig. 4.10), to send two pulses onto the tip separated by a time delay of τ. We investigate interferometric autocorrelations of the laser pulse using the non-linear response of the tip. This refers to an optical interferometer. The pulses interfere before interacting with the nanotip. The emitted electrons are then a function of the interference of the two laser pulses (i.e. delay between the two pulses). This type of autocorrelation trace can be used to verify the pulse duration at the interaction region of the experiment.

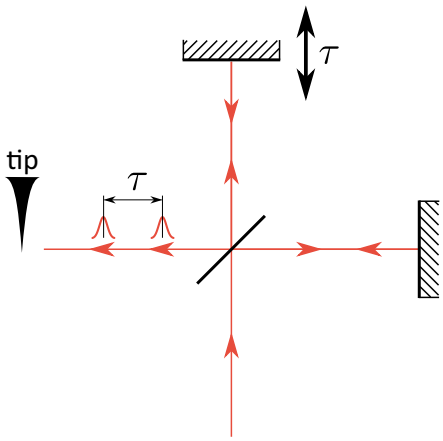

Figure 4.10 – This shows the schematic layout of a Michelson interferometer with a delay of τ between pulses.

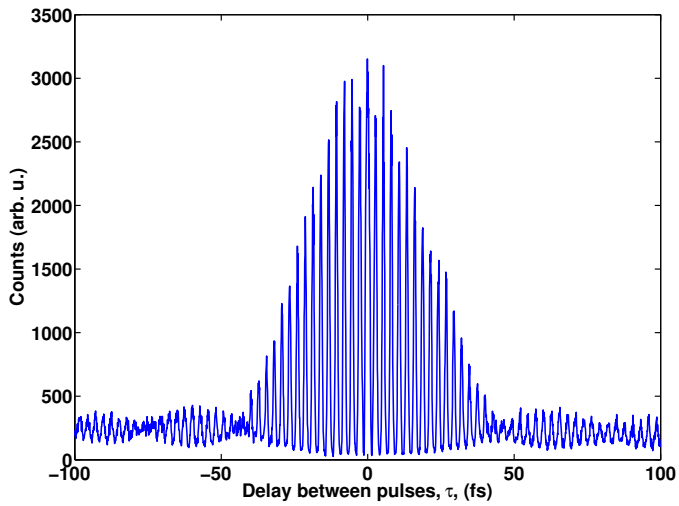

Figure 4.11 – Number of electrons as a function of delay between optical pulses, τ.

Fig. 4.11 shows the number of electrons as a function of the delay between the two laser pulses. The peak to base ratio is approximately equal to 17. This can be used to confirm the non linearity of the emission, and gives a power exponent $\eta \approx 2.6$. The width of the autocorrelation trace could be used to retrieve the optical pulse duration, knowing the power

exponent. While the trace confirms that the pulse is short, we preferred to use the complete pulse measurement provided by the LX Spider to characterize our laser pulses.

We can investigate that the electron emission is due to the electric field of the laser As thermally enhanced emission is long lasting (on the order of 100s of fs [Kealhofer13]), we would see emission from the tip long after the application of the first pulse onto the tip. The second pulse would simply enhance the emission from the first pulse. In our autocorrelation traces we see a flat baseline for delays greater than the pulse duration, thus indicating that there are no thermal effects in this case.

4.3.4 Photoelectron spectra

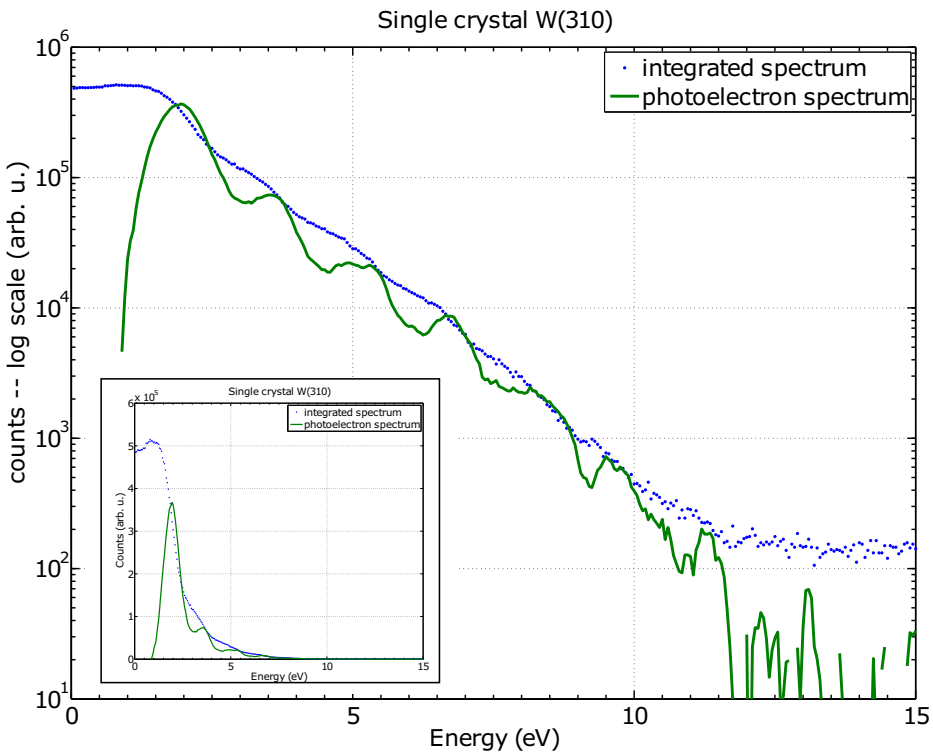

Figure 4.12 – This shows photoelectron spectra from a W(310) nanotip. For this spectrum an extraction voltage of V_{tip} = 20 V, and a laser power of 50 mW (0.8 nJ/pulse, 1.52×10^{12} W cm^{-2} peak intensity) was used. The direct spectrometer output, an integrated spectrum, is shown by blue dots. The kinetically resolved photoelectron spectrum is shown by the green line. Note ATP peaks up to order $n = 9$ are easily observable in the spectrum. The inset shows the spectra in linear scale. Only the first four ATP peaks are easily resolvable in this scale, thus it is beneficial to plot the spectra in log scale.

Fig. 4.12 shows a photoelectron spectrum from a W(310) nanotip. For this spectrum, an extraction voltage of V_{tip} = 20 V, and a laser power of 50 mW (0.8 nJ/pulse, 1.52×10^{12} W cm^{-2} peak intensity) was used. The kinetic energy acquired from the applied V_{tip} has been subtracted. The conditions are such that there is less than one electron emitted per laser pulse to avoid Coulomb space charge effects. The spectrometer records the number of electrons with a higher energy than the retarding field with a scan resolution of 0.05 V over 500 ms, thus makes an integrated

spectrum (blue dots). To find the number of electrons for each energy, the derivative of the spectrum is taken which are then smoothed with a Savitzky-Golay smoothing filter over 11 adjacent points (green line).

In the photoelectron spectrum, peaks are superimposed over the overall exponential decay of the electron emission. The peaks are separated by 1.55 eV corresponding to above threshold photoemission (ATP) peaks. The first peak corresponds to a photon order of 3, due to the fact that it takes 3 photons to overcome the potential barrier. The inset of Fig. 4.12 shows the spectra in linear scale. Only the first four ATP peaks are easily resolvable in this scale, thus it is beneficial to plot the spectra in log scale. With the y-axis in log scale, a photon order up to $n = 9$ is easily observable. The photon order is discussed more in Sec. 4.4.

4.4 Above Threshold Photoemission

Fig. 4.12 shows a photoelectron spectrum with above threshold photoemission (ATP) peaks up to order $n = 9$. As explained in Sec. 1.3.2, the emitted current density scales as I^n, where n is the number of photons absorbed by the system. We investigate the number of photons absorbed by each ATP peak to confirm the theory that each peak absorbs a certain integer number of photons. Much of this discussion comes from and is augmented upon [Bionta14a].

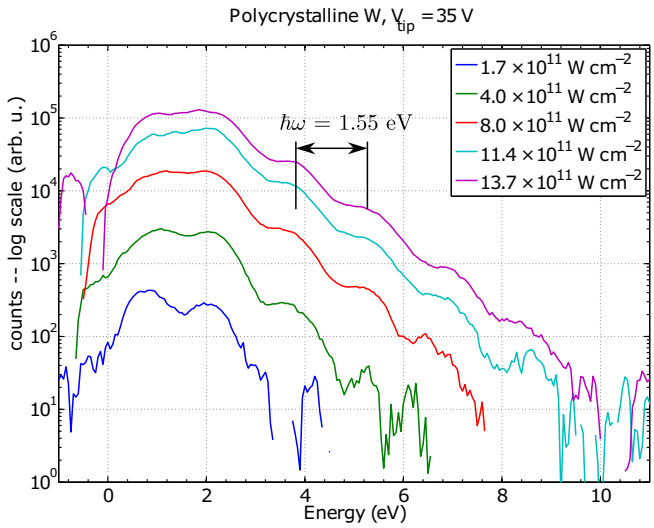

Figure 4.13 – This shows photoelectron spectra for nominal laser intensities {1.7, 4, 8, 11.4, 13.7} $\times$ 10^{11} W cm^{-2}. Note the presence of ATP peaks separated by the 1.55 eV photon energy.

Details of the laser-induced emission regime are studied via energy resolved measurements of the electrons using the field retarding spectrometer. Figure 4.13 presents photoelectron energy spectra as a function of laser intensity. Here the laser intensity is scanned from {1.7, 4, 8, 11.4, 13.7} $\times 10^{11}$ W cm^{-2}. Distinct peaks separated by the photon energy are visible, which are a clear signature of ATP, similar to what has been observed by Krüger *et al.* [Krüger11]. As the laser intensity increases, the system can absorb more and more photons before electrons are emitted. This broadens the spectra and allows us to observe higher and higher photon orders.

At low laser intensity (blue curve, Fig. 4.13), we can only see the distinguish the first two ATP peaks (up to $n = 4$); however, at high laser intensity (purple curve) we can easily see photon orders up to $n = 9$.

We confirm these emission mechanisms, and photon order, with an energy-selective, laser-power dependence measurement of these ATP peaks. Results are shown in Fig. 4.14 for an experiment with $V_{\text{tip}} = 30$ V and laser peak intensities from 1 to 3.6×10^{11} W/cm^2. Individual peaks are indicated by the same color throughout the figure. Fig. 4.14 (a) shows the energy spectrum recorded at 3.6×10^{11} W/cm^2, where different ATP peaks are identified with different colors. Fig. 4.14 (b) shows the electron count rate versus laser intensity plotted in log scale. Each line corresponds to one peak of the photoelectron spectra as defined in Fig. 4.14 (a). The electron yield is obtained by integrating over all of the energy window corresponding to each peak. We retrieve the exponent of each energy peak by extracting the slope of each fitted line. Fig. 4.14 (c) shows the retrieved power exponents of the four peaks from about 3 to 6, with corresponding error bars relative to the fit.

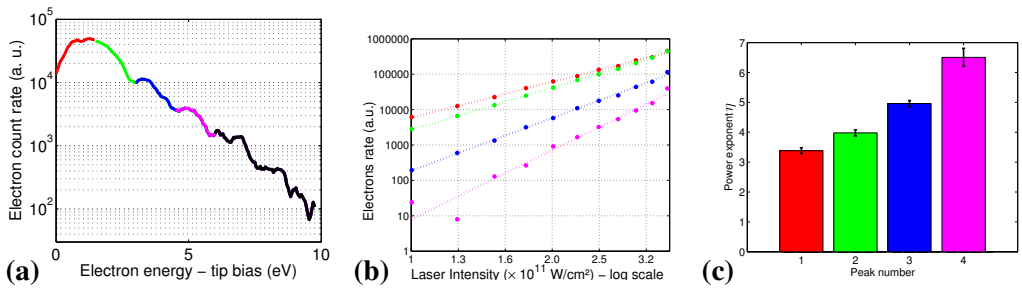

Figure 4.14 – (a) Electron energy spectrum obtained for a $V_{tip} = 30$ V and laser intensity of 3.6×10^{11} W cm^{-2}. The different ATP peaks are identified by the different colors. (b) Electron yield versus laser intensity plotted for each ATP peak. The dots are the experimental values, and the lines are the fit from which we retrieve the exponent. (c) Power exponents for each peak. As expected for ATP, we obtain exponents from 3 to 6. Reprinted with permission from [Bionta14a].

As expected for ATP, each peak corresponds to a different number of absorbed photons, therefore corresponding to a different exponent. The first peak is close to 3 (3.4 ± 0.1), since the work function of polycrystalline tungsten ($\phi = 4.5$ eV) is roughly equal to 3 times the photon energy (3×1.55 eV $= 4.65$ eV). The second, third and fourth peaks have respective exponents of 4.0 ± 0.1, 5.0 ± 0.1, and 6.5 ± 0.3, showing that in this part of the spectrum the system absorbs 4, 5 and 6 photons before electrons leave the laser focus. This confirms that in our case, the photoelectron emission is mainly due to multiphoton absorption, without any contribution of photofield emission. These experiments were reproduced for the two first peaks with various experimental conditions (different tips, different focusing), and with different energy selections–choosing electrons from within the entire peak, or just at the maximum of the peak. The values of the exponents are reproducible to within 10 % for several tips.

The Keldysh parameter can be calculated from Eq. 1.22. For PCW $\phi = 4.5$ eV and a laser wavelength of 800 nm of intensity 3.6×10^{11} W/cm^2, we find the Keldysh parameter to be $\gamma = 10$, before any enhancement from the tip. $\gamma > 1$ means that we should not be in the

optical tunneling regime, and indeed we do not see the spectral plateau signature of rescattering. However, for similar laser intensities (meaning a similar Keldysh parameter), Krüger *et al.* (group of P. Hommelhoff) observed spectral plateaus indicating optical tunneling and rescattering [Krüger12b]. The group reported a tip radius a factor of two smaller than ours, indicating there is more geometric field enhancement near the apex. They also have a pulse duration of their laser of only 6 fs. Our longer, 20 fs pulses may be suppressing the rescattering effect as the energy is spread out over a longer period of time. This may cause short-term thermal effects which overtake the emission mechanism for high energies.

4.5 Summary

We investigate electron emission from a tungsten nanotip in order to form a baseline to compare our new experimental setup to already existing experiments.

We have a variety of methods for *in-situ* characterization of the tip. Using FN plots we can calculate the tip radius. We use the slope of these plots to check that the tip radius stays the same throughout our investigations. Typical tip radii are on the order of 250 nm for PCW tips and 30 nm for SCW(310) tips. We also use FEM-like plots to investigate spatially resolved emission patterns from the tip. From these we see that there is indeed only one emission site from SCW(310) tips and that it is facing the detector.

The damage threshold due to laser irradiation was systematically and empirically studied. These test proved to be inconclusive, due to uncertainties in the laser alignment on the tips and the lack of visible damage to the tips.

Polarization dependence curves were used to check the alignment of the tip in the laser focus. A good contrast of $\sim$3500:1 was found for a well aligned tip. The laser power dependence gives us the average number of photons absorbed by the system before an electron was emitted. We find a decrease in this number as the applied voltage increases, due to the Schottky effect. Kinetically resolved power dependencies were also measured and for each individual ATP peak up to a photon order of $n = 6$. We confirmed that each peak corresponds to a different number of absorbed photons.

The experiments on tungsten allow us to validate our experimental setup in comparison to already established results. We were also able to familiarize ourselves with the new experimental setup as well as techniques for working with nanostructures. With a correct understanding of our results and experimental setup, we can turn to other samples for investigation.

5

Carbon Cone nanoTips (CCnT)

The investigation of electron emission from novel tip materials such as carbon nanotubes has yielded interesting properties for cold field emission. These new samples have a very different structure and electronic properties than conventional metallic nanotips. We believe that the mechanical and electrical properties the carbon tips present for cold field emission are a promising start towards the observation of strong field phenomenon resulting from the laser-tip interaction. Our collaboration with CEMES allows us access to a novel new nanotip type based on a central carbon nanotube, surrounded by concentric graphene sheets to form a conical shape. Extensive studies on cold field emission from these tips can be found in [deKnoop14, Houdellier12, Houdellier15] and show promising results. The mechanisms behind electron emission from these tips is unknown and we investigate the properties from laser-induced emission from these carbon based nanotips.

I first give a detailed description of the material and structural properties of the carbon nanotips. I then discuss the characterization of our tips using SEM, FN and FEM techniques. Laser induced electron emission is presented for polarization dependency curves as well as kinetically resolved photoelectron spectra. Damage to the samples was observed after laser irradiation, so systematic studies on the damage limits of the carbon tips are detailed. Some of the results presented in this chapter are published in [Bionta14b].

5.1 Description of a Carbon Cone nanoTip (CCnT)

We use Carbon Cone nanoTips (CCnT) in collaboration with CEMES. At CEMES, they focus on the synthesis of the tips as well as cold field emission properties for use as a field emitter for electron microscopy. My group aims to investigate the interaction of such a tip with an optical field to study the laser-induced emission properties from a CCnT.

The CCnT is a tip based on a conical form of carbon. These tips have a work function of $\phi = 5$ eV [Houdellier12], and an apex diameter of a few nm. The center of the cone is a single, multi-wall carbon nanotube (CNT) surrounded by concentric graphene sheets to form a conical shape. The interior structure of the sheets can be seen via transmission electron

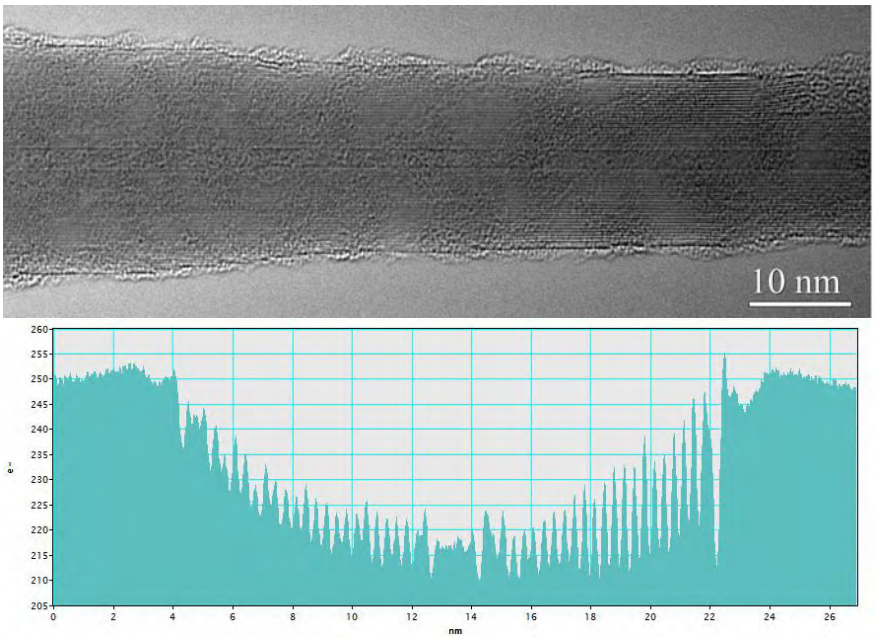

Figure 5.1 – Top: Transmission electron microscopy image of the cross section of a CCnT. The layers of graphene sheets are clearly visible. Bottom: a transverse profile at proper scale of the sheets. The CNT is located between 12 and 14 nm.

microscopy (TEM) as in Fig. 5.1 top panel. The bottom panel shows a transverse profile, at proper scale, of the sheets. We can see the central CNT has a diameter of ∼2 nm.

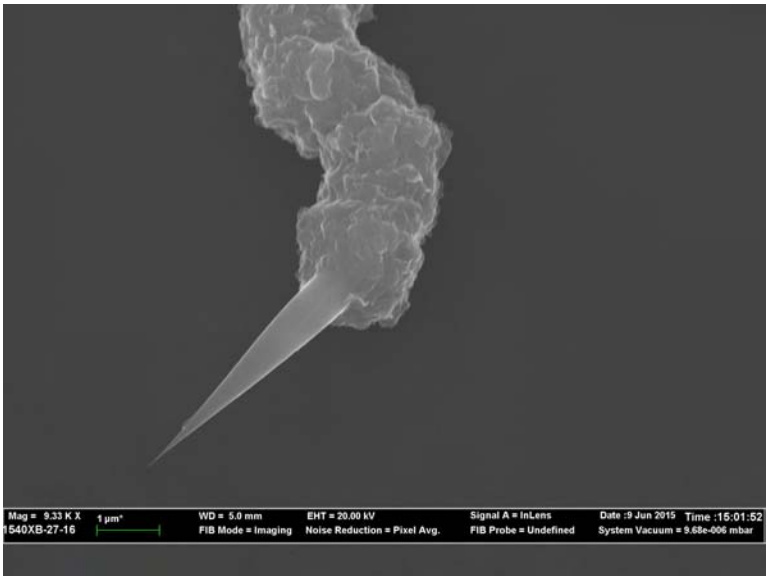

Figure 5.2 – SEM image of the final conical shape of a CCnT.

The final conical structure can be seen in Fig. 5.2. As described in Sec. 3.1.2, the cones are formed on either end of a short microfiber carbon segment via a controllable time of flight chemical vapor deposition process developed at CEMES. This unique growth process allows the CCnT to exhibit certain parameters that are important for our experiments. This includes a high aspect ratio of the CCnT, which can be sharper than conventional metallic tips such as

tungsten or gold, and has a smaller apex size leading to higher geometric field enhancement in the vicinity of the tip.

The static field emission properties of this tip have been extensively studied [Houdellier12, deKnoop14, Houdellier15]. Characterization of the cold field emission has shown high brightness and coherency in the emitted electrons, on the order of 3 times brighter than a standard tungsten emitter [Houdellier12]. The tip has demonstrated robustness in lifetime in current field emission gun installations [Houdellier12, Houdellier15].

Investigations into ways to grow CCnTs with doped CNTs is currently underway in collaboration with CEMES and the University of Zaragoza. There is theoretical evidence of changes in the emission properties of CNTs due to doping. These include a decreased work function promoting enhanced field emission [Qiao07, Ghosh10]. By tailoring the growth process of the CCnTs we hope to promote certain emission properties we wish to exhibit, such as enhanced directionality of electron emission.

5.2 CCnT characterization

5.2.1 Scanning electron microscopy

As the CCnTs are mounted onto tungsten tips in a FIB environment (Sec. 3.1.2), the tips are characterized as they are made. Fig. 5.3 shows the SEM of a finish mounted tip on a tungsten tip.

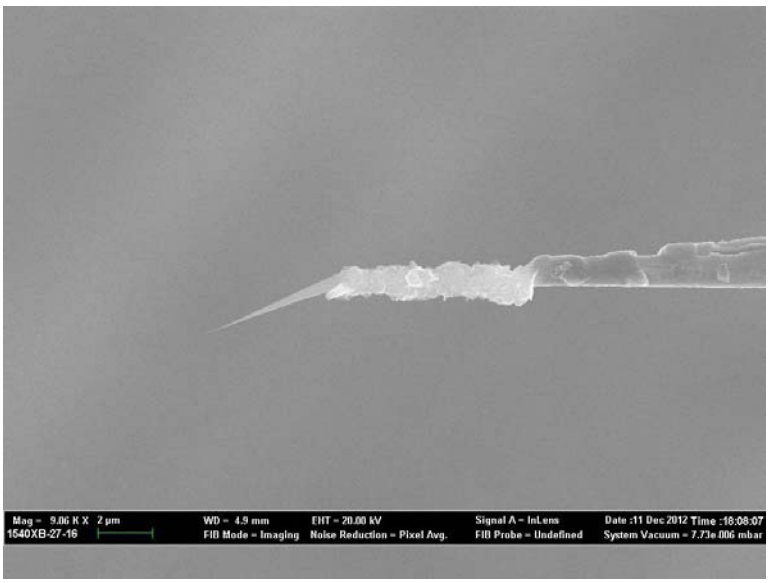

Figure 5.3 – This shows the SEM of a CCnT after it has been mounted onto a tungsten tip.

As the CCnTs are randomly formed and dispersed over the substrate, choosing a perfectly straight cone is not always evident. Fig. 5.3 shows an example of a CCnT with an highly angled cone with respect to the carbon fiber and tungsten tip. The placement of the fiber on the tungsten base also shows some of the irregularities that occur from tip to tip due to the in-house fabrication methods.

SEM inspection was also used for thermal damage studies. This is discussed in more detail in Sec. 5.4.

5.2.2 Fowler-Nordheim plots

Fig. 5.4 shows the Fowler-Nordheim (FN) plot for a CCnT as described in Sec. 1.2.2. Here we plot the emission of the tip as a function of applied voltage in the form of $\ln(\frac{J}{V^2})$ vs $\frac{1}{V}$. The slope of the line gives us α/β from the FN equation: $J(V) \propto \beta^2 V^2 \cdot \exp(-\frac{\alpha}{\beta V})$, Eq. 4.1. We see that $\alpha/\beta = 13069$. We can use this to approximate the radius of the tip.

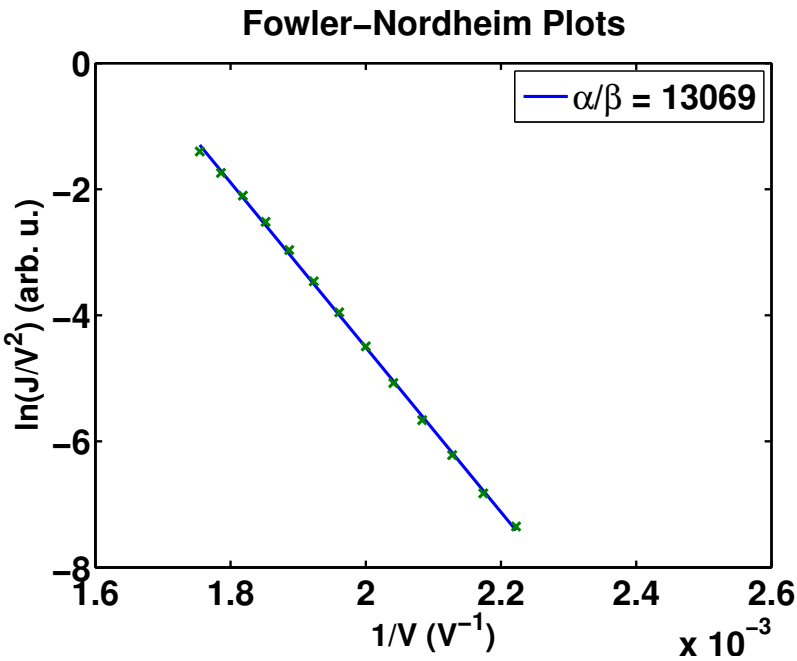

Figure 5.4 – Fowler-Nordheim (FN) curve for a CCnT, with an α/β slope of 13069.

Recall from Eq. 4.3 that $\alpha = 6.83 \times 10^9 \cdot \phi^{3/2} \cdot v(w)$, where $\phi = 5$ eV is the the work function of the CCnT and $v(w)$ is the Nordheim function. We use the same approximation for the Nordheim function $v(w) = 0.6$ as from Sec. 4.1.1 and [Hommelhoff06b]. Solving for β we find $\beta = 3.5 \times 10^{10}$ m^{-1}. Using the relation $\beta = 1/kr$ we can solve for the tip radius r. With the approximation $k \sim 5$ from [Gomer61], we find $r = 57$ nm. This is much larger than the reported radius of $r \approx 5$ nm by CEMES (also seen in Fig. 3.8). As we were able to correctly extract the radius of the tips in Sec. 4.1.1, this leads to doubts about the validity of a FN for a CCnT. However, the discrepancies may be because our approximations of k and $v(w)$ cannot be considered the same for both a CCnT and a tungsten nanotip.

According to [Gomer61], $k \sim 5$ near the tip apex and depends on the polar angle. The tip apex of a CCnT is no longer a half-sphere termination field emitter, as for a tungsten nanotip, but instead the base of a cylindrical CNT. As we no longer have the same type of conical tip shape, the value of k for a CCnT must be different. This would change the relation of β to r. The same can be assumed for the Nordheim function, $v(w)$. The value of $v(w)$ is dependent on the tip material and geometry. For an electrochemically etched tungsten nanotip, we take

$v(w) = 0.6$ [Hommelhoff06b], and Sec. 4.1.1. Since the geometry of a CCnT is different, as well as the material, we cannot use this approximation for the Nordheim function.

While we cannot necessarily extract each individual tip radius by using an FN plot, we can still use the ratio of α/β to periodically ensure that the same sharpness remains throughout our investigations.

5.2.3 Field emission microscopy

We take spatially resolved electron emission images to understand the emission patterns from a CCnT. The construction of the CCnTs indicates that emission should only come from the CNT apex, meaning we should see only one emission spot.

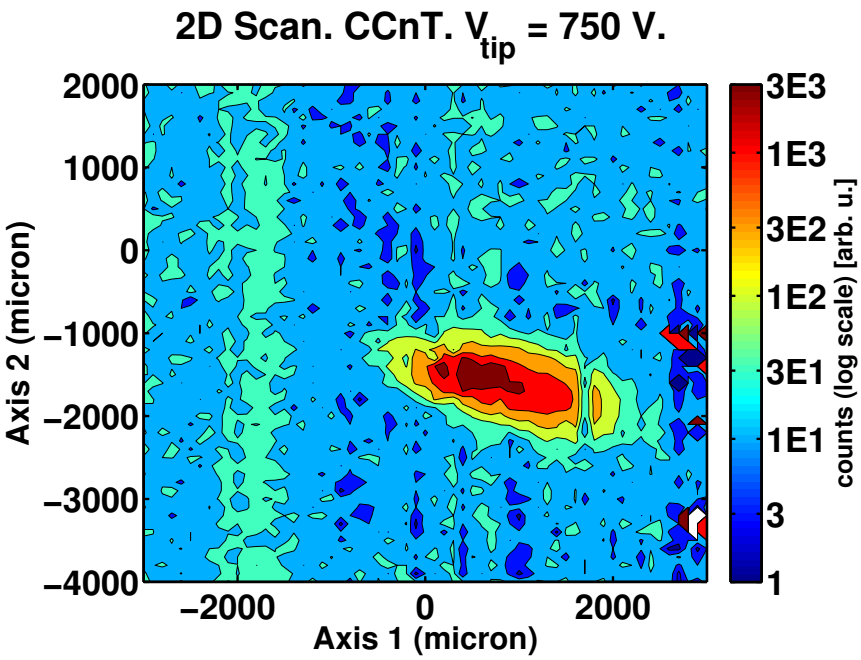

Figure 5.5 – This FEM image shows the single emission spot for a CCnT.

Fig. 5.5 shows an FEM image for a CCnT. We can see that there is only one bright spot of emission, confirming our assumption that emission originates from the apex of the central CNT. The spot is elliptical as the tip was angled and our spectrometer scans record the 2D projection of the electron emission. FEM images act as a projection microscope with a magnification factor given by the ratio of the tip-anode distance (in this case, the anode is the entrance pinhole of the spectrometer) and the radius of tip. In our case this is on the order of $\sim 10^6$. Indeed the spot seen in the FEM images is $\sim 1000 \times 2000\ \mu\text{m}^2$ corresponding to an emission spot size on the order of $\sim 1 \times 2$ nm, indicating that the emission area is less than the diameter of tip apex and in agreement with the measured size of the CNT. The tip has no reason to be asymmetrical, meaning this elliptical shape is due to the projection of the angle of the tip.

5.3 First CCnT results

Investigations of electron emission from CCnTs induced by a laser pulse were performed. Photoelectron emission from many CCnTs was investigated, but post-illumination examination revealed either the destruction or modification of the tips that had been irradiated. This lead to a set of systematic thermal studies to understand the thermal conduction and limits of the CCnTs. Much of the rest of this chapter comes from and is augmented upon [Bionta14b].

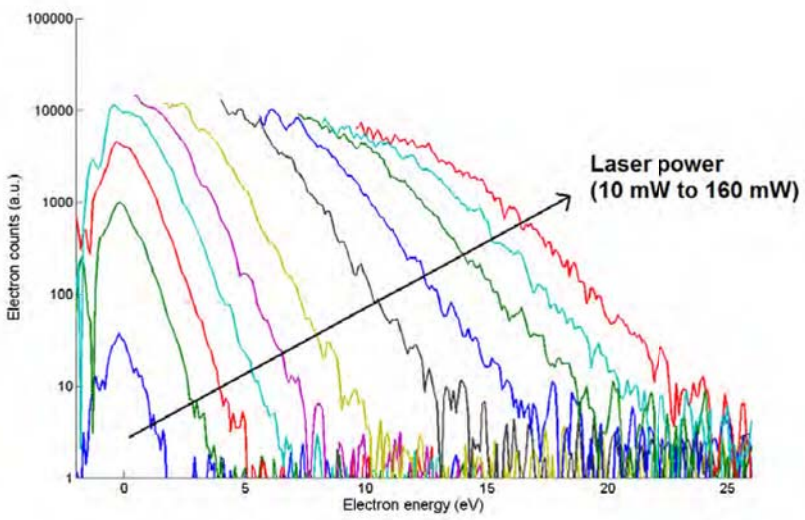

Figure 5.6 – Photoelectron spectra where the tip was illuminated with 2.7 to 41.1 $\times 10^{11}$ W cm^{-2} of laser intensity (0.16 to 2.6 nJ/pulse, 10 to 160 mW average power). Post-illumination SEM images show a destruction of the mounted CCnT so we cannot verify that the electrons collected were actually emitted from the CCnT.

We first tried to investigate laser power dependence curves from CCnTs to extract an exponent η, corresponding to the average number of absorbed electrons from the system before electron emission. However, emission from higher laser intensity led to damaged tips. Fig. 5.6 shows photoelectron spectra for the case of a CCnT for different laser power. Here the tip was illuminated with 2.7 to 41.1 $\times 10^{11}$ W cm^{-2} of laser intensity (0.16 to 2.6 nJ/pulse, 10 to 160 mW average power). An increase in the laser intensity shows a broadening of the spectrum. For large laser powers, the low energy part of the spectrum was not measurable due to too many counts on the MCPs leading to saturation effects. The corresponding saturated data has been removed from the spectra. However, with post-illumination SEM inspection of the tip, the remaining tip shows a bare tungsten tip with no remaining carbon structure post-illumination Fig. 5.7. Thus we were unable to verify that the electrons collected for the spectra in Fig. 5.6 were actually emitted from the CCnT.

The damage threshold was systematically studied and is discussed below in Sec. 5.4.

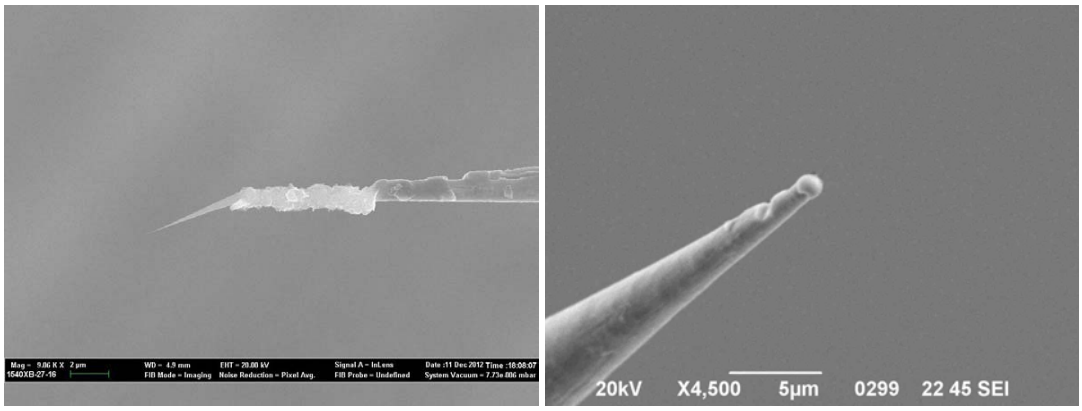

Figure 5.7 – The left panel shows the CCnT nanostructure (Fig. 5.3) before laser irradiation. The right panel shows the SEM inspection of the tip post-illumination revealing a bare tungsten tip with no remaining carbon structure.

5.4 Thermal damage studies

As mentioned above in Sec. 5.3, as we increased the intensity of the laser, we saw evidence of damage to the tips. This is seen in Fig. 5.7. After laser irradiation (Fig. 5.6) the attached CCnT was no longer observable, indicating laser damage.

Fig. 5.8 shows another example of a modified CCnT structure. The left panel shows the SEM of the CCnT as it was when it was mounted onto the tungsten tip base. The right panel shows the modification of the structure after it had been illuminated by 7.7×10^{11} W cm^{-2} laser intensity (0.48 nJ/pulse, 30 mW average power) for 30 minutes.

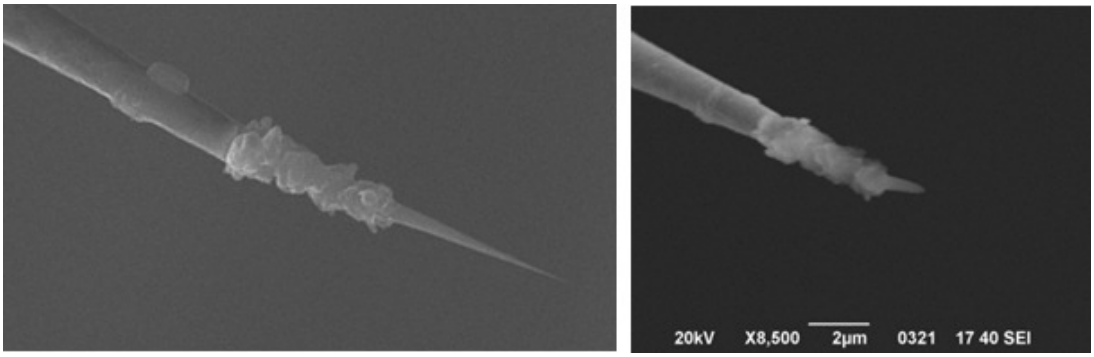

Figure 5.8 – The left panel shows the CCnT nanostructure before laser irradiation. The right panel shows the CCnT after it had been illuminated by 7.7×10^{11} W cm^{-2} laser intensity (0.48 nJ/pulse, 30 mW average power) for 30 minutes. Figure from Ultramicroscopy, doi:10.1016/j.ultramic.2014.11.027, M. R. Bionta *et al.*, "First results on laser-induced field emission from a CNT-based nanotip", Copyright (2014), with permission from Elsevier. [Bionta14b]

As explained in [Bionta14b], an understanding of the thermal damage as induced by the laser is necessary for evaluating the damage threshold of the material and to find ideal conditions for laser irradiation. As in Sec. 4.2, we systematically irradiated a carbon "comb", consisting of 4 different CCnTs mounted onto a conducting substrate, with varying intensities to look for visual as well as empirical evidence of damage. This was done with direct SEM imaging of the tips before and after irradiation as well as residual gas analyzer (RGA) scans performed

during each of the tests. Two sets of tests were performed: the first with an on-axis spherical mirror, whose focal alignment was checked using the camera method as explained in Sec. 3.6.1 for on-axis mirrors; the second used off-axis parabolic (OAP) mirrors whose alignment was verified by both checking the position of the shadow of the tip in the transmitted beam as well as by putting a small bias directly onto the comb and observing emitted electrons.

In the first set of tests, tips were illuminated with $\{0.084, 0.84, 4.2\} \times 10^{11}$ W cm^{-2} ($\{0.016, 0.16, 0.81\}$ nJ/pulse, $\{1, 10, 50\}$ mW average power) each for 1 hour, with one tip left not illuminated and no bias applied to any. No signs of damage are seen for any of the tips. Fig. 5.9 shows the SEM images of the tip illuminated with 4.2×10^{11} W cm^{-2} of laser intensity before and after irradiation. No visible signs of damage are seen. Note the tip shape was not a perfect conical CCnT initially.

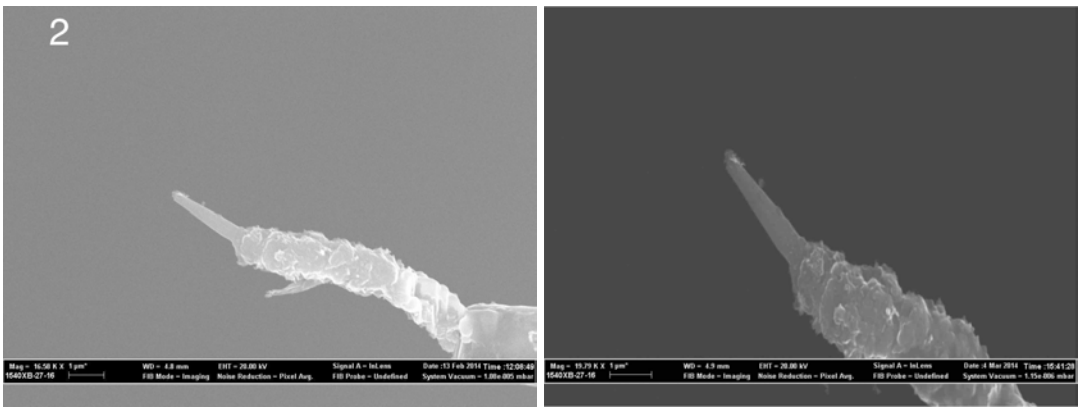

Figure 5.9 – The left panel shows the CCnT nanostructure before laser irradiation. The right panel shows the SEM inspection of the tip after illumination by 4.2×10^{11} W cm^{-2} of laser intensity for 1 hour. No visible signs of damage are seen.

In the second set of tests, the tips were illuminated with either 9.0×10^{11} W cm^{-2} (0.57 nJ/pulse, 35 mW average power), or 2.7×10^{11} W cm^{-2} (0.16 nJ/pulse, 10 mW average power), with either 50 V bias, or no bias applied, for an hour each. Only the tip irradiated with 2.7×10^{11} W cm^{-2} with a 50 V bias showed any indication of potential damage. Once again this tip was not a perfect CCnT initially. As seen in the left panel Fig. 5.10, the initial CCnT looks unfinished, but has a long central CNT protruding from the carbon cone structure. In the right panel we can see that this central CNT is no longer observable possibly due to irradiation by the laser.

While Figs. 5.7 and 5.8 clearly show signs of tip damage, the comparisons of our SEM images before and after laser irradiation from the carbon comb showed no significant signs of modification, and the RGA scans showed no indications of carbon atoms detected. This could be due to the quality of the CCnTs chosen for the tests. As some of the cones were not fully formed or were blunted, the enhanced field at the apex would be less than for a sharp CCnT. This might cause the damage threshold for these samples to be higher. Despite this, we find the damage threshold to be much lower than that for tungsten at high repetition rate lasers and therefore we limit the irradiation of our tips to be less than 7.7×10^{11} W cm^{-2}. A complete data set of before and after SEM photos for both tests can be seen in App. C.

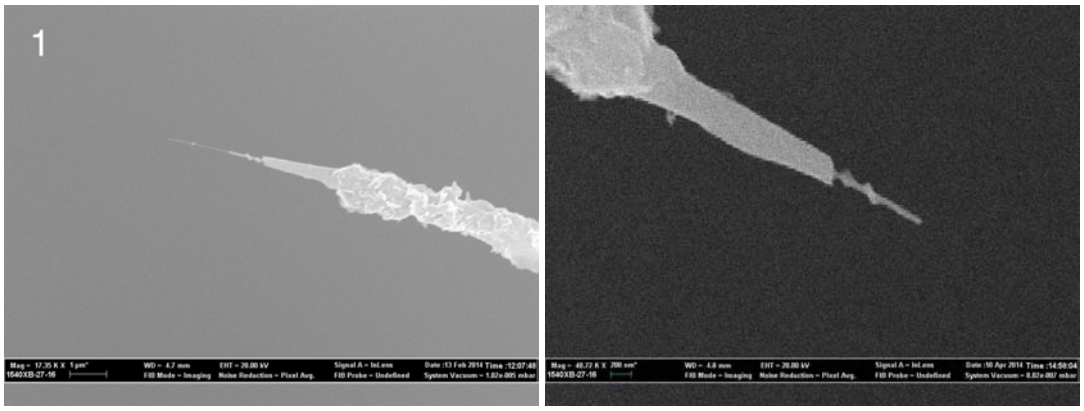

Figure 5.10 – The left panel shows the CCnT nanostructure before laser irradiation. The right panel shows the SEM inspection of the tip after 2.7×10^{11} W cm^{-2} with a 50 V bias. The protruding central CCnT is no longer observable possibly due to damage caused by irradiation of the laser.

5.5 Laser emission

Following the results of Sec. 5.4, we limited the laser intensity to avoid thermal damaging of the tips. The tip was verified with SEM images to ensure no damage resulted from the laser illumination.

5.5.1 Polarization studies

We verify alignment of the CCnT in the laser focus using the laser polarization as was done for W tips. This is seen in Fig. 5.11. The tip is illuminated with 5.13×10^{11} W cm^{-2} (0.3 nJ/pulse, 20 mW average power) with a V_{tip} of 50 V. We find decent alignment with maximum electron yield at polarization parallel to the tip axis and a contrast of ~4500:500. We think that the slight discrepancies in contrast are due to misalignments caused by the angled tip.

We fit the polarization to $\cos^{2n}(\theta)$ where n is the extracted exponent corresponding to non-linear laser exponent as discussed in Sec. 4.3.2 and therefore the average number of photons absorbed by the system and θ is the polarization of the laser field relative to the tip axis. We find a fit of $n = 3.52 \pm 0.13$, as seen in the red curve of Fig. 5.11. This corresponds to the minimum number of photons needed to overcome the work function for the CCnT. As $\phi = 5.0$ eV, we find that $n_{\text{min}} = \phi/\hbar\omega = 3.2$

5.5.2 Laser induced spectra

Fig. 5.12 shows a spectrum taken from a CCnT. This was taken with a moderate laser intensity of 5.13×10^{11} W cm^{-2} (0.3 nJ/pulse, 20 mW average power), and a V_{tip} of 50 V.

Even though the non-linear laser exponent indicates absorption of enough photons to overcome the work function barrier, this spectrum shows no signs of above threshold photoemission (ATP) peaks. The narrowness of the spectrum indicates the emission may be due to thermalization effects of the high repetition rate of the laser such as thermally assisted field emission,

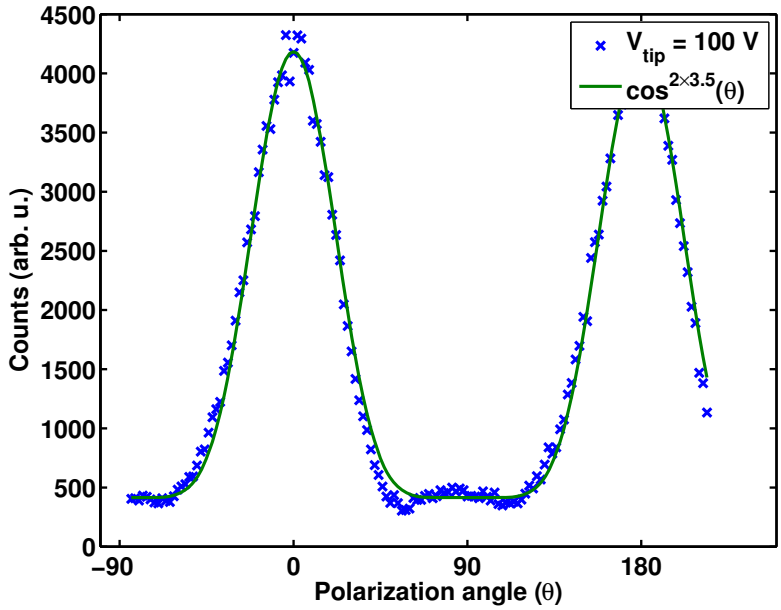

Figure 5.11 – Electron yield as a function of laser polarization. The experimental data (blue x's) is fit to the curve $\cos^{2n}(\theta)$ where $n = 3.52 \pm 0.13$.

or more complex mechanisms such as ATP from a thermally excited electron gas in which the temperature blurs the signature ATP peaks (i.e. if $k_B T \sim \hbar\omega$).

5.6 Perspectives on laser-induced CCnT emission

Contrary to our initial assumptions on the characteristics of CCnTs, it was difficult to observe strong field phenomenon from the laser interaction with a CCnT, despite their better mechanical and electrical properties in comparison to conventional metallic nanotips. At low mean laser power, the CCnTs emitted similarly to what we observed with tungsten tips; however, high mean power proved to be harmful to the tips. Possible explanations are considered. While the interface between the carbon fiber and the milled tungsten tip is a supposed tungsten "weld", not much is known about the actual interface between the carbon and the tungsten, and this might prove to be a fragile link, sensitive to thermal effects. As the cone itself is made of graphene sheets, the atomic structure of the carbon atoms that make up the CCnT means that there are less carbon atoms making up the tip than compared to atoms in a nanotip of the same dimensions made of bulk tungsten. This means there is more energy deposited per atom than compared to tungsten tips. Some other unknown property of the CCnT may also be a contributing factor to its apparent fragility.

Besides limiting the peak intensity of the applied laser, other solutions exist. Lowering the repetition rate of the laser would lower the mean power thus potentially reducing thermal effects. We tried illuminating a CCnT with the output of the regenerative amplifier at 1 kHz, however the data acquisition settings at the time did not allow us to retrieve a good signal to noise ratio. In the end, the tip that was illuminated was the one seen in Fig. 5.7 so even if counts had been recovered, it would not have been known if they were from the CCnT or the

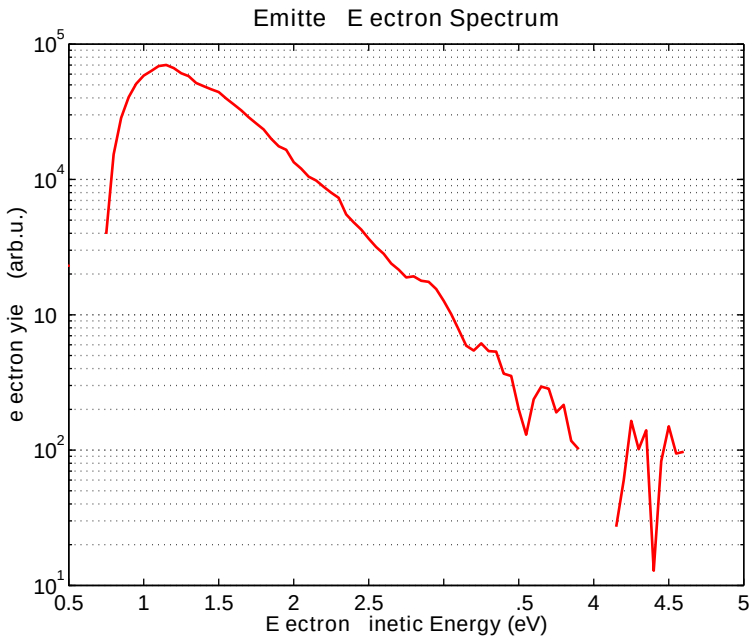

Figure 5.12 – Photoelectron spectra from a CCnT illuminated with a moderate laser intensity of 5.13×10^{11} W cm^{-2} (0.3 nJ/pulse, 20 mW average power), and a V_{tip} of 50 V. Figure from Ultramicroscopy, doi:10.1016/j.ultramic.2014.11.027, M. R. Bionta *et al.*, "First results on laser-induced field emission from a CNT-based nanotip", Copyright (2014), with permission from Elsevier. [Bionta14b]

bare tungsten tip base. The development of the NOPA (Sec. 2.3) allows for an intermediate repetition rate of the laser, so an intermediate mode between high and low repetition rate can be found. The NOPA also allows the possibility of using a longer wavelength, so we can apply the more ponderomotive energy from the laser without increasing the peak intensity.

5.7 Summary

We investigated electron emission from a CCnT in collaboration with CEMES. We observe the first laser-induced electron emission from an CCnT; however, our results were limited by thermal effects in the tips.

We tried to use FN plots to extract the apex radius of our CCnTs, but the number was not in agreement with the size observed in SEM and TEM images. This is possibly due to assumptions for the geometric enhancement and Nordheim function being no longer valid due to the tip geometry and material. However we could still use the α/β slope to ensure the tip was still sharp. FEM images confirmed the single emission site of the CCnTs.

We then studied laser irradiation effects. While electron emission effects were comprehensible for low mean power, at high mean power we saw destruction of the tip. Methodical studies on the damage threshold of CCnTs were performed. We observed damage for tips irradiated with 9.0×10^{11} W cm^{-2} for 30 minutes. However, many of our systematic studies seemed inconclusive. This is possibly due to the carbon structures used being not fully

formed or blunted, changing the enhancement. We limited our laser intensities to less than 7.7 $\times 10^{11}$ W cm^{-2}.

At low power, electron emission polarization dependency gave good contrast and a polarization fit of of $n = 3.4$. This is in good agreement of the minimum number of photons absorbed $n_{\text{min}} = 3.2$ to overcome the $\phi = 5$ eV work function of the CCnT. Photoelectron spectra for moderate intensity yielded a narrower spectra than those for similar intensities on tungsten, indicating possible thermal effects. However, attempts at increasing the laser intensity to measure the yield as a function of laser power to extract an η proved to be unsuccessful as we damaged the tip.

The development of a NOPA (Sec. 2.3) with variable repetition rate alongside our active collaboration with CEMES with the synthesis of CCnTs will hopefully lead to improved laser-induced results. In particular the shape of the tip seems to be crucial towards maximizing the emission process.

6

Silver nanotip results

You were born a child of light's wonderful secret— you return to the beauty you have always been.

– Aberjhani,
Visions of a Skylark Dressed in Black

In this chapter I detail results from silver nanotips. I was interested in using silver samples as bulk silver has a known surface plasmon resonance around ∼400 nm, which is easily reachable with our laser. I wanted to see how this resonance would affect electron emission and the optical field enhancement. The resonance will be shifted by the behavior of the tip, and we hope it will affect the electron emission in a measurable way. Studies on silver were done in collaboration with GPM in Rouen.

I first briefly describe plasmonics and silver itself as a material. I then discuss the characterization of our silver tips using SEM, FEM and FN techniques. Results taken at a high repetition rate from the output of the oscillator are detailed, including results from a tip that did not emit as expected. I describe results from low repetition rate which include the observance of a spectral plateau as well as enhancement factor calculations. Finally, I present preliminary results obtained with 400 nm laser irradiation.

6.1 Why silver?

Plasmonics describes a large field of physics which studies the interaction of electromagnetic radiation with the free electrons in a noble metal [Enoch12, Maier07, Shahbazyan13]. What happens is not evident, especially for sub-wavelength size metallic structures. At these sizes, the electric field interacts with the conduction electrons at the interface of the metal leading to an enhanced optical near field [Maier07]. This has brought the development of surface-enhanced spectroscopy and applications of metamaterials and optical antennae.

The plasmon response of a nano-object is highly size and geometry dependent [Lee06, Mock02, Vogel10, Ringe10]. In general sharp nanotips are used as local focusing elements for the plasmons [Babadjanyan00, Barthes12, Goncharenko07, Ma15, Vogelsang15]. In single material tips, the apex is connected to a seemingly infinitely long shaft which supports the focusing of the plasmons, however radiation effects reduce the enhancement factors in tips compared

to single nanoparticles. In single particles, the optical properties are governed by the dipolar modes of the surface plasmons, thus allowing greater enhancement. Much work has been done to characterize the plasmon resonances of noble metal nano-particles, in particular silver and gold [Juvé13, Baida11]. However these single particles are hard to individually manipulate and are generally studied in colloidal [Jain07, Link99, Mock02] or dispersed systems [Kim05]. Specific design of nano-particles to control this resonance is also studied [Weber15].

Silver (Ag, atomic number 47) has long been a metal of interest to study. It has a relatively low melting point of 1235 K and a work function of 4.25 eV [Haynes12] for its polycrystalline form. It is a noble metal with a completely filled *d* orbital and 1 electron in the *s* orbital. In general gold is preferred for studies in air due to its inertness, but silver can be preferable in vacuum because it is less lossy in the visible wavelengths [Sasaki13]. Silver has the highest electrical and thermal conductivity of all metals and a high reflectivity for wavelengths greater than 450 nm. However, this reflectivity quickly reduced off for shorter wavelengths and drops off to 0 for 310 nm. Silver is used for its strong plasmon response and field enhancement over a broad range of visible wavelengths [Schmid13] due to the small imaginary component of its dielectric constant [Zhang11, Johnson72]. It has a characteristic bright mode of the surface plasmon near ∼350 nm [Ma15, Chaturvedi09] which is not far from the second harmonic of the Ti:sapphire laser system (Sec. 2.1) and reachable with the second harmonic of the output of the NOPA (Sec. 2.3). Previous studies have shown a high brightness and electron yield for silver emission, an order of magnitude more than that of tungsten [Sasaki13, Zhang11]. However, the low melting point of silver may lead to potential thermal issues.

6.2 *In-situ* tip characterization

6.2.1 Scanning electron microscopy

Due to the nature of how the silver tips are made (Sec. 3.1.3), they are characterized as they are being formed. This means we know exactly the radius of the tips that we put into the chamber.

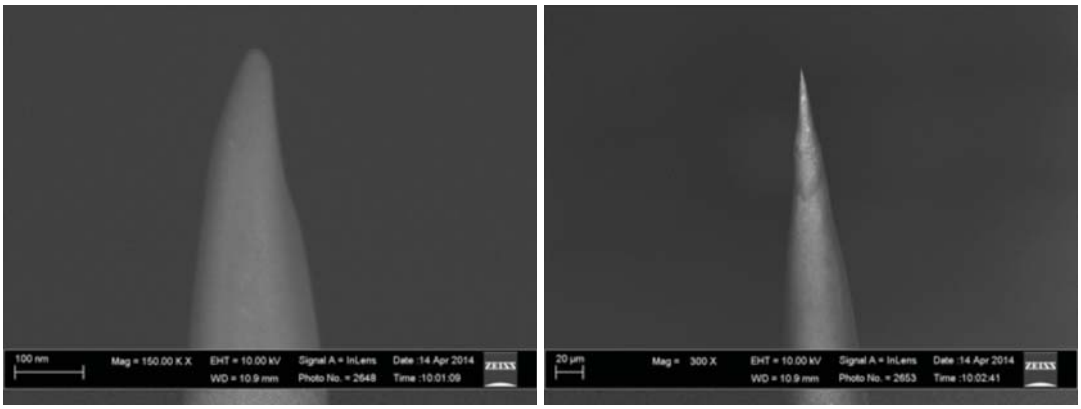

Figure 6.1 – SEM images of the first Ag tip put in the chamber. It has a radius of 20 nm.

The first tip we put in the experiment, Fig. 6.1, has a radius of 20 nm. However this tip emitted very unexpectedly with many low energy electrons and a polarization contrast with a high base

level, possibly indicating thermal effects. After laser irradiation, this tip was investigated in the SEM for evidence of thermal or mechanical damage from either the laser or the transportation methods and also for evidence of damage due to oxidation effects. No damage was seen, Fig. 6.2.

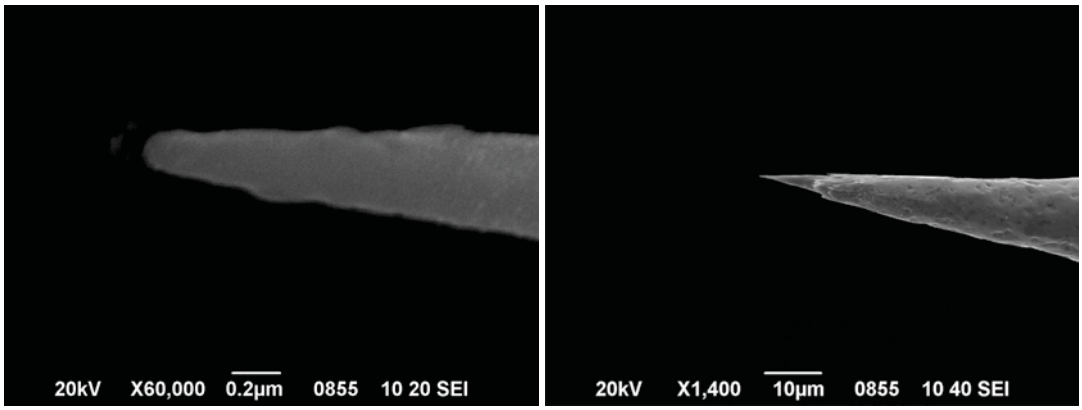

Figure 6.2 – SEM images of the first Ag tip after laser irradiation. No indications of damage or oxidation.

The second tip has a slightly larger radius of 50 nm. This tip gives comprehensible emission results. The following results presented in the rest of the chapter are from this tip unless otherwise indicated. SEM images of this tip can be seen in Fig. 6.3.

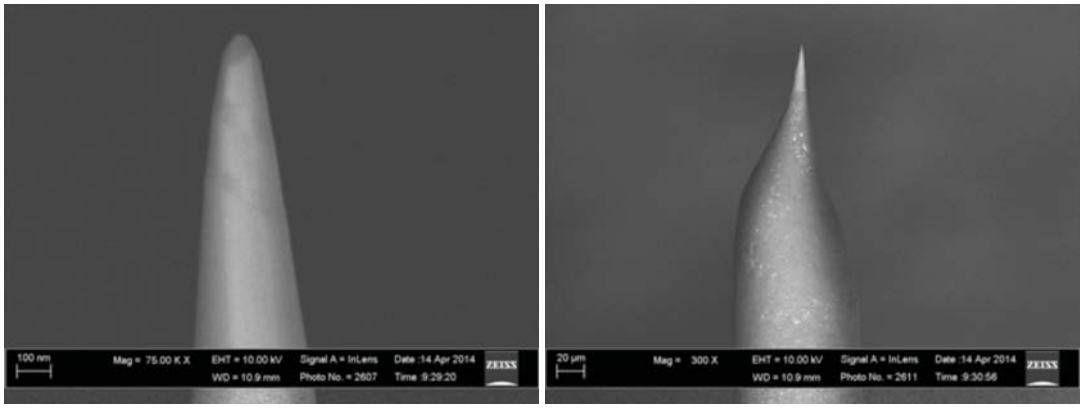

Figure 6.3 – SEM images of the second Ag tip after laser irradiation. It has a radius of 50 nm.

6.2.2 Field emission microscopy

Field emission microscopy (FEM)-like images were taken to characterize the polycrystalline silver tip. Since the tip is polycrystalline, this means there is no ordered structure to the orientation of the facets in the tip. This is evidenced in the resulting spatially resolved emission scan.

Fig. 6.4 shows the resulting FEM-like scans from the polycrystalline silver tip. The spectrometer is scanned with respect to the tip, recording the number of electrons emitted for a specific position. We can see from the image the non-ordered emission spots due to the polycrystalline nature of the wire from which the tip was formed. There are several bright spots corresponding

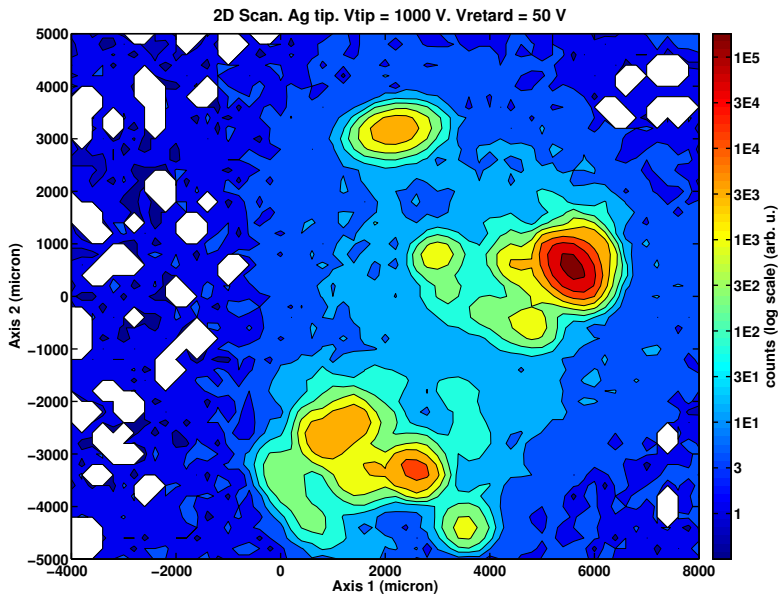

Figure 6.4 – FEM for a polycrystalline Ag tip. Since the wire from which the tip was formed is polycrystalline, there is no ordered structure to the facet orientation of the tip.

to the many facets with the lowest work function (or bigger field enhancement) that we found in our particular tip. These bright spots locations will change from tip to tip. We can position the spectrometer such that it collects the highest brightness of emission using the FEM image as a map.

The magnification of our FEM images is on the order of $\sim 10^6$. This means that the bright spot corresponds to an emission site size on the order of 1×1 nm^2 in correspondence with the emission site size seen in Sec. 5.2.3. The total emission area is on the order of 9×6 nm^2, which is less than the measured radius and in accordance with expected emission size.

6.2.3 Fowler-Nordheim plots

Since we already know the size of the nanotip, Fowler-Nordheim (FN) plots were used to periodically check the size of the tip to make sure that it is not destroyed.

Fig. 6.5 shows the $\ln\left(\frac{1}{V^2}\right)$ vs $\frac{1}{V}$ FN plot for the two brightly emitting facets seen in Fig. 6.4. Facet 1 is the bright spot seen at (500, 5500) and has a α/β slope of 24080. Facet 2 is the bright spot found at (-3500, 2000) and has an α/β slope of 23954. The slope of the two facets is about the same indicating that their facet orientation is probably the same and that the emission slope depends on the radius of the tip.

Since we have characterized the radius of the tip very well, we can use the FN equation to verify the value of the Nordheim function $v(w)$. We know α as a function of $v(w)$ and the work function ϕ from Eq. 1.20, and that $\beta = 1/kr$ with $k \sim 5$ and r given in Sec. 6.2.1. Using $r = 50$ nm, $\phi = 4.26$ eV, and the α/β slope given above, we find $v(w) = 0.6 \pm 0.02$. Even though the tip shape is not exactly the same, and material are different than in Sec. 4.1.1, our

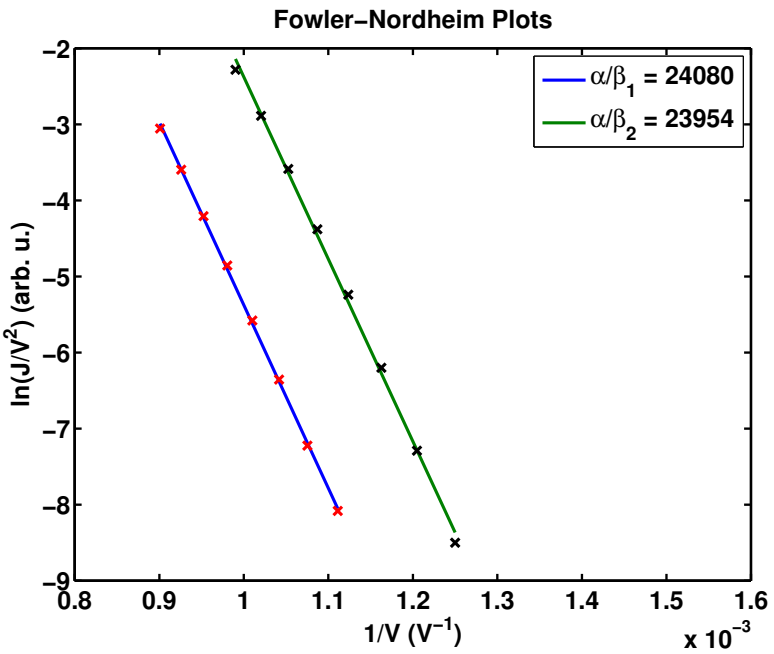

Figure 6.5 – This shows FN curves for two facets from polycrystalline silver.

value for $v(w)$ is in good agreement with the approximation we used ($v(w) = 0.6$, Sec. 4.1.1, [Hommelhoff06b]).

6.3 High repetition rate laser induced emission results

6.3.1 First Ag nanotip results

As mentioned in Sec. 6.2.1, the first tip we put in the experimental setup, Fig. 6.1, gave unexpected results. We tried to verify alignment using polarization scans, however we were unable to find good contrast at the correct polarizations. Fig. 6.6 shows two polarization scans for this tip. Scan 1 shows significant emission only for polarizations perpendicular to the tip axis (polarization angle $\theta = 90$). After realignment, scan 2 shows emission for both polarizations. We were unable to make the contrast any better than this. We attributed this to possible heating or oxidation of the new silver tip and attempted to proceed with irradiation at parallel polarization with the hopes that laser induced emission would dominate thermally assisted emission.

We irradiated the laser with 1.21×10^{12} W cm^{-2} (0.7 nJ/pulse, 47 mW average power) for various V_{tip}. This is seen in Fig. 6.7. We varied V_{tip} from 20 V, 50 V and 100 V to see if any features arise in the spectra. As there was not very much emission for low V_{tip}, and the spectral shape was not very similar to what we found in tungsten. Many low order electrons were emitted, mostly with energies below eV_{tip} (i.e. energies less than 0 in Fig. 6.7), seeming to indicate that the tip was not emitting properly or mostly because of thermal effects. We decided to check for thermal damage before continuing with experiments. None were found as discussed in Sec. 6.2.1.

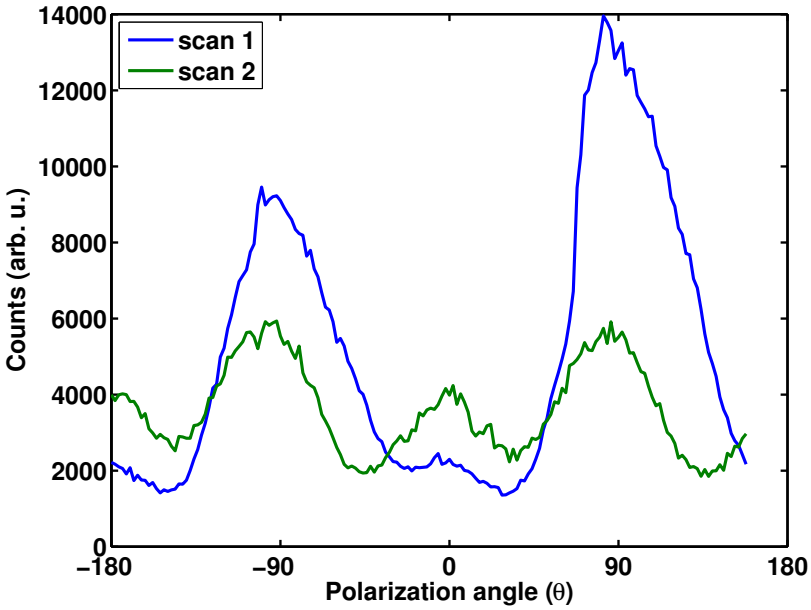

Figure 6.6 – Polarization scans for the first tip put in the experimental setup.

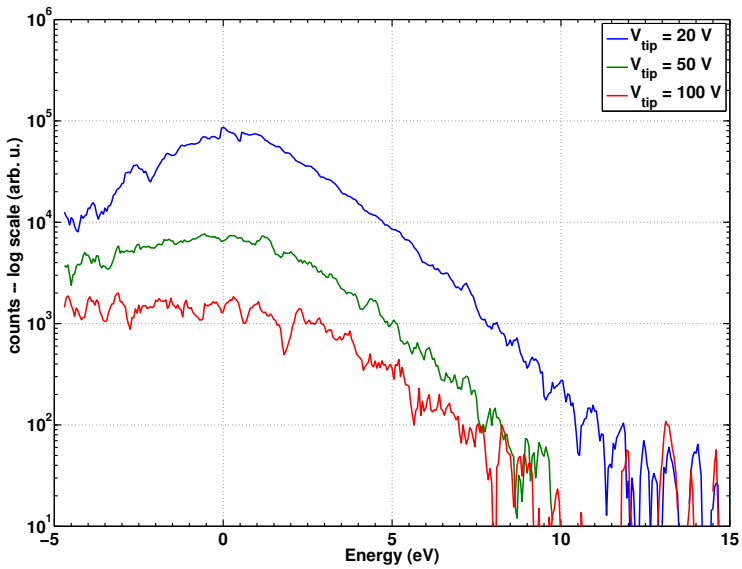

Figure 6.7 – Spectra from the first silver tip illuminated with 1.28 $\times 10^{12}$ W cm^{-2}, with V_{tip} =20 V, 50 V, and 100 V.

6.3.2 Second Ag tip results

The second silver tip we tried in our experimental setup had better results.

The polarization dependence of the electron emission can be seen in Fig. 6.8. The tip is illuminated with 1.28 $\times 10^{12}$ W cm^{-2} (0.6 nJ/pulse, 50 mW average power) from the output of the oscillator, with $V_{\text{tip}} = 20$ V. The blue x's show the electron yield as a function of the laser polarization θ with respect to the tip. As in Sec. 4.3.1, an angle of 0° corresponds to a polarization

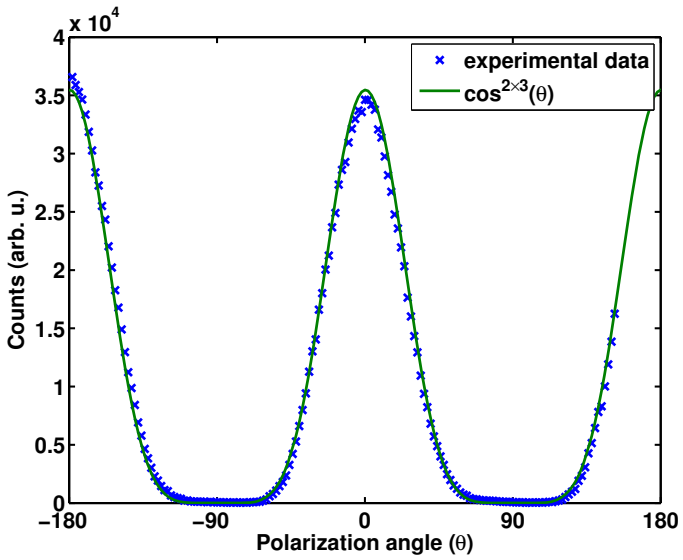

Figure 6.8 – Electron yield as a function of polarization for a laser intensity of 1.28 $\times 10^{12}$ W cm^{-2}. We can fit this to $\cos^{2n}(\theta)$, there $n = 3.0 \pm 0.6$.

parallel to the tip axis, and 90° is orthogonal. Fig. 6.8 shows good alignment with maximum electron yield for polarizations parallel to the tip axis with a contrast of ∼35000:1.

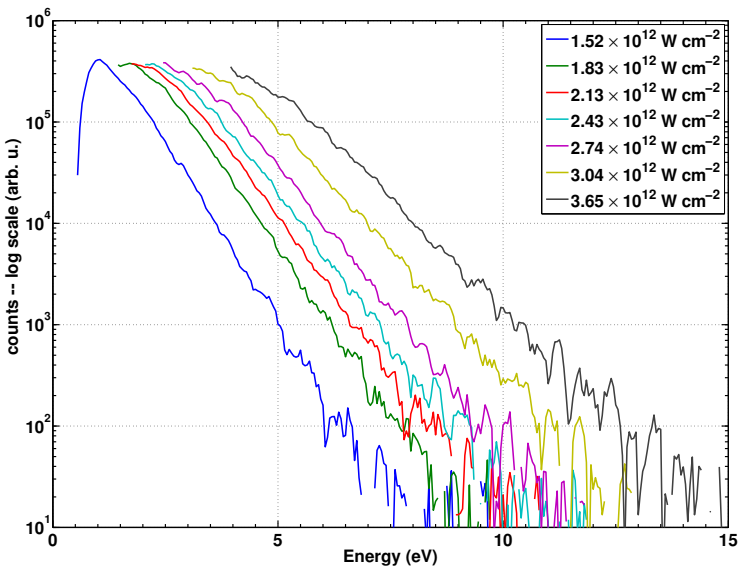

Figure 6.9 – Photoelectron spectra for laser intensities of {1.52, 1.83, 2.13, 2.43, 2.74, 3.04, 3.65} $\times 10^{12}$ W cm^{-2}, with V_{tip} = 20 V. The spectra are narrower than those from equivalent intensities from tungsten nanotips, but the electron yield reached saturation on the MCPs. These saturation effects have been removed from the spectra.

We fit the polarization to $\cos^{2n}(\theta)$, where n is the extracted exponent corresponding to the average number of photons absorbed by the system. We find a fit of $n = 3.0 \pm 0.6$. As $\phi = 4.26$, $n_{\text{min}} = \phi/\hbar\omega = 2.75$ meaning that the minimum number of photons needed to be absorbed to overcome the work function is 3.

Fig. 6.9 shows photoelectron spectra from a polycrystalline Ag tip. At higher intensities, we start to see saturation effects on the MCPs as too many low energy electrons are emitted to be counted. As the MCPs saturate at around 200,000 counts per second, but the repetition rate of the laser is 62 MHz, we are still in the regime of < 1 electron per pulse. These saturation effects have been removed. Fig. 6.9 shows spectra where the intensity is scanned from {1.52, 1.83, 2.13, 2.43, 2.74, 3.04, 3.65} $\times 10^{12}$ W cm^{-2}, with V_{tip} = 20 V. These spectra show no signs of above threshold photoemission (ATP) peaks and the spectra are narrower than those from equivalent intensities from tungsten nanotips. This may be due to thermally enhanced emission causing the tip to heat from absorption of energy from the laser allowing electron tunneling. As we found an extracted polarization fit of $n = 3$ corresponding to above threshold emission, perhaps the spectrum we see are a combination of thermal and above threshold effects which blur the characteristic ATP peaks from multiphoton emission. We tried changing the repetition rate of the laser to see if that alleviates the saturation effects.

6.4 Low repetition rate emission results

Due to the high count rate and saturation effects at high repetition rate, possibly due to thermal effects in silver, we lowered the repetition rate of the laser to 1 kHz, by using the regenerative amplifier (regen). The NOPA was not available at the time of this experiment. This allows the system more time to thermally recover between laser pulses. The change in repetition rate requires a few modifications to the experimental setup. Besides lowering the repetition rate, the use of the regen also greatly amplifies the pulse energy of the laser to about 350 μJ/pulse. Since we only need a few nJs of energy, we must greatly reduce the energy while maintaining clean polarization and a short pulse duration. This was done with several beamsplitters and carefully calibrated neutral density (ND) filters whose added chirp was precompensated for with the grating compressor of the amplifier. The low signal to noise ratio associated with the low repetition rate means changes to the acquisition system. To compensate for the long time between pulses, and to avoid noise counts on the MCPs, we gate the discriminator (described in Sec. 3.5) to only count during a short window of a few tens of ns around the arrival time of the laser pulses. This allows us to increase the signal to noise ratio by not counting during the time when there are no laser pulses. A high signal to noise ratio is crucial for maintaining a good dynamical range in signal counts.

6.4.1 Non kinetically resolved electron results at 1 kHz

The polarization dependency of the electron emission was checked to verify alignment. We find a good contrast of $\sim$210:1 indicating good alignment. The contrast is lower as we are working at low repetition rate and therefore have less signal. As in Sec. 4.3.2, the electron yield was fitted to the function $\cos^{2n}(\theta)$, where n corresponds to the average number of photons absorbed by the system before and electron is emitted and θ is the angle of polarization with respect to the tip axis. For the polarization curve given in Fig. 6.10, for V_{tip} = 100 V, we find $n = 1.48 \pm 0.08$. We increased V_{tip} to aid in electron extraction for the low repetition rate, but

kept it low enough as to not significantly reduce the resolution of the spectrometer and impact the effective work function of the tip. This number is much less than the n_{min}, the minimum number of photons needed to be absorbed to overcome the work function for polycrystalline silver. As discussed above, the work function $\phi = 4.26$ eV for polycrystalline silver, this means that for a photon energy of 1.55 eV for 800 nm light, $\phi/\hbar\omega = 2.75$ which is larger than the extracted n.

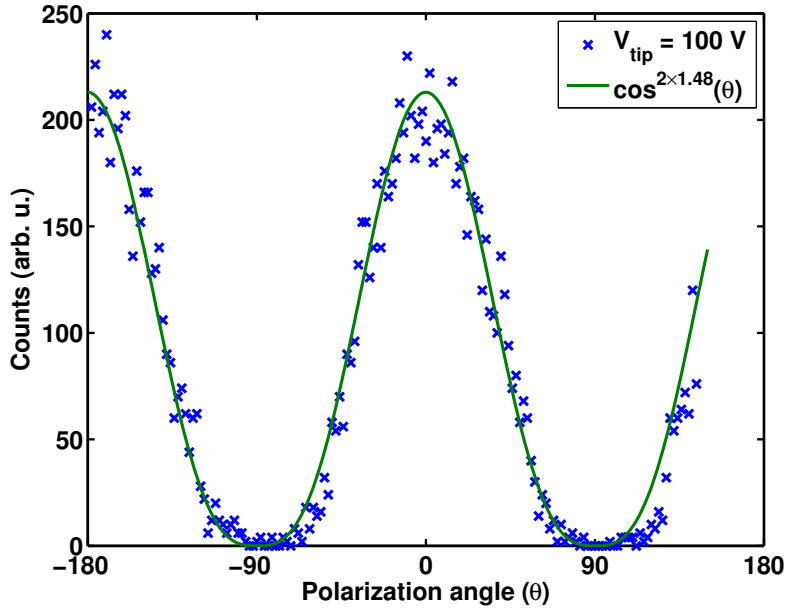

Figure 6.10 – Electron yield as a function of laser polarization (θ) with respect to the tip axis. The experimental data (blue x's) are fit with the form $\cos^{2n}$ where $n = 1.48 \pm 0.08$.

Laser power dependent curves, Fig 6.11, were also used to approximate η from $J \propto I^{\eta}$. Here, the laser intensity was scanned from 0.92 to 21.0 $\times$ 10^{12} W cm^{-2} (6.2 nJ to 14.8 nJ), for V_{tip} = 50 V. Fig 6.11 (a) shows the electron yield as a function of intensity. Plotting this yield in log-log scale, Fig 6.11 (b), we can fit a linear relation with a slope, and extracted exponent, of $\eta = 1.84 \pm 0.84$.

There could be many reasons for such a low extracted n and η. The laser intensity range is limited by experimental constraints, so the fit is done on a quite narrow range. Geometric effects would also skew the effects. As the repetition rate of the laser is 1 kHz, the maximum number of electrons we can count with the MCPs is 1000 per second. We count a high number of electrons detected by the MCPs (up to ~500 counts / second). Taking into account the transmission of the spectrometer, and the pinhole entrance to the spectrometer, there could have been more than one electron emitted per pulse. Space charge effects would cause Coulomb repulsion between the electrons meaning less electrons would be detected. This would cause the maximum of the polarization curve to be lower and the extracted exponent to be lower, but would not affect the resolution of kinetically resolved spectra. Photofield and thermally enhanced emission are all emission mechanisms that occur after absorption of less than n_{min}

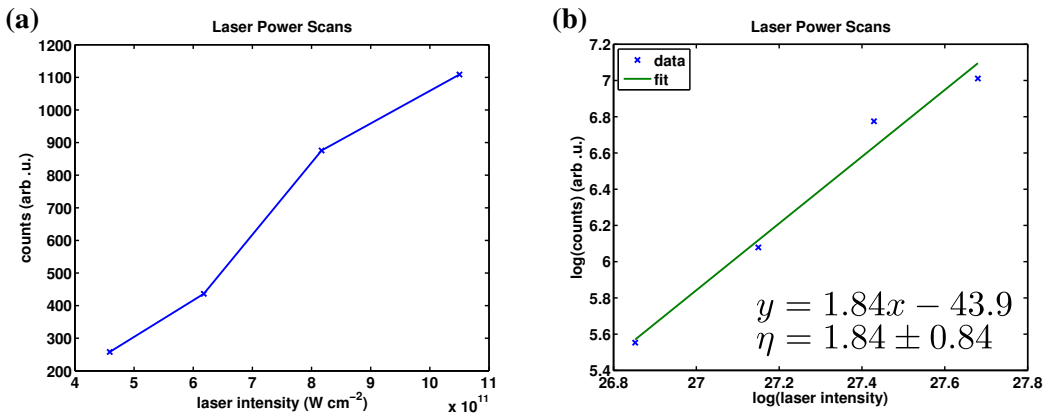

Figure 6.11 – (a) This shows the electron yield as a function of laser power for V_{tip} = 50 V. (b) This shows the same yield on a log-log scale. We can fit this curve to a linear equation from which the slope $\eta = 1.84 \pm 0.84$.

photons. In order to better understand the physical mechanisms behind the observed emission, we investigated the kinetically resolved photoelectron spectra.

6.4.2 Kinetically resolved analysis at 1 kHz

We take the kinetically resolved electron spectra to see if, by spectral shape, we can identify the regime of the electron emission. The spectra can be seen in Fig. 6.12 for a range of laser intensities.

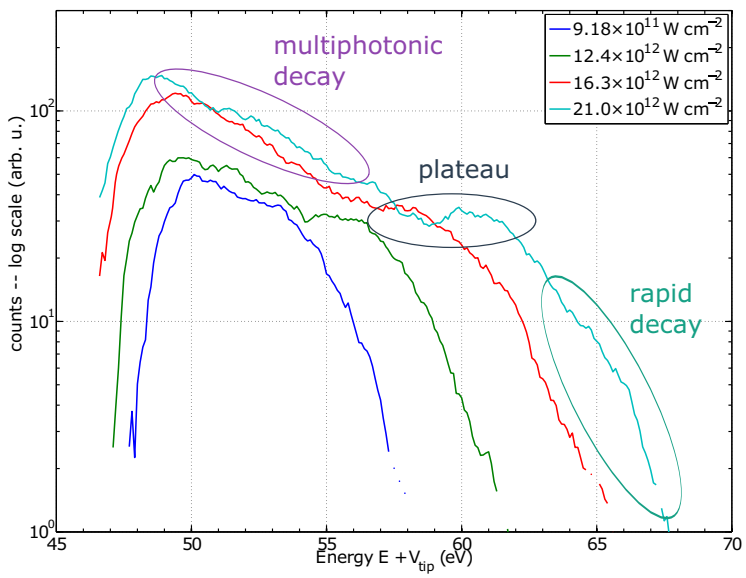

Figure 6.12 – Photoelectron spectra for laser intensities of {0.918, 12.4, 16.3, 21.0} $\times 10^{12}$ W cm^{-2}, V_{tip} = 50 V. Note the observance of a spectral plateau.

The spectra we record have distinct regions. The lower energy electrons show the characteristic exponential decay of above threshold photoemission. For higher intensities, a spectral plateau builds up for high energy electrons, where the count rate remains almost the same. This

spectral plateau is similar to that from electron recollision and rescattering explained by the three step model (Sec. 1.3.3). Beyond the plateau feature, we observe a rapid decay of the count rate. While the plateau becomes more and more pronounced at higher intensities, we do not illuminate the tip with more laser intensity to avoid damaging the tip. The spectra and plateau remain the same for each laser intensity for all the experiments that were performed. These regions are annotated in Fig. 6.12.

We can calculate the Keldysh parameter ($\gamma = \sqrt{\phi/2U_\mathrm{p}}$, Eq. 1.22) where U_p is the ponderomotive energy calculated using the applied intensity, I_app, without taking into account any enhancement, Tab. 6.1.

Table 6.1 – Calculated Keldysh parameter, γ, from the applied laser intensity, I_app, not taking into account any enhancement.

Pulse energy (nJ)	**Intensity (W cm^{-2})**	**Calculated U_p (eV)**	**Calculated γ**
6.2	0.918×10^{12}	0.0549	6.23
8.74	12.4×10^{12}	0.0739	5.37
11.55	16.3×10^{12}	0.0976	4.67
14.8	21.0×10^{12}	0.1255	4.12

From Tab 6.1 we can see that even for the highest intensities irradiating the tip, $\gamma > 1$, indicating that we should still be in the multiphotonic, above threshold regime. The observance of the spectral plateau in this regime is quite intriguing. However these calculations were done without taking into account the field enhancement from the tip. Assuming that these spectral features (the plateau) are due to rescattering and recollision of the electrons with the tip, we can calculate the field enhancement from the tip.

Field enhancement:

We can use the spectra to calculate the enhancement factor of our nanotip. By comparing the observed spectral features, such as the measured cutoff $10U_\mathrm{p}$, and peak shifting, to those expected via calculations from the applied intensity we can determine the enhancement.

The field enhancement factor is defined as

$$\xi = \frac{\mathscr{E}_{0,\mathrm{eff}}}{\mathscr{E}_{0,\mathrm{app}}}, \tag{6.1}$$

where $\mathscr{E}_{0,\mathrm{eff}}$ is the effective electric field of the laser at the apex of the tip, and $\mathscr{E}_{0,\mathrm{app}}$ is the applied electric field of the laser calculated from the applied intensity. The $10U_\mathrm{p}$ cutoff energy is a measurable feature of the spectra, where $U_\mathrm{p} = \frac{e^2\mathscr{E}_0^2}{4m_e\varepsilon_0\omega^2}$, Eq. 1.23, is the ponderomotive energy. Comparing the measured and applied U_p gives us the field enhancement

$$(\xi)^2 = \frac{U_\mathrm{p,meas}}{U_\mathrm{p,calc}}, \tag{6.2}$$

where $U_\mathrm{p,meas}$ is the measured ponderomotive energy from the observed $10U_\mathrm{p}$ cutoff and $U_\mathrm{p,calc}$ is the calculated ponderomotive energy from the applied intensity. Using the relation $I = \frac{1}{2}c\varepsilon_0\mathscr{E}_0^2$, Eq.1.16, we can find the effective intensity at the apex of the tip and the intensity enhancement ξ_I,

$$(\xi)^2 = \xi_I. \tag{6.3}$$

In practice, we use the measured and calculated ponderomotive energy to calculate the intensity enhancement which in turn is used to calculated the field enhancement.

Peak shifting:
We observe a peak shifting effect for the low-order spectral features which become more pronounced as the intensity increases. This causes the spectral features to shift to lower energy. This is attributed to the channel closing effect (Sec. 1.3.2). At high intensity, the ponderomotive energy, U_p, of the photoelectron is not negligible. This energy is added in addition to the energy difference of the final and initial states of the photoelectron. This means that there is an energy shift ΔE for all spectral features, where $\Delta E = -U_p$. We can use this to calculate U_p for the photoelectrons. As we add a potential V_{tip} to the tip to extract the electrons, the energy of the first peak should be,

$$E_{peak1} = n\hbar\omega - \phi - U_p - eV_{tip}, \tag{6.4}$$

where n is the minimum number of photons needed to be absorbed to overcome the work function, in this case 3. By comparing this measured U_p, to the U_p calculated from the applied laser intensity, we can extract an intensity enhancement factor: $\xi_I = U_{p,meas}/U_{p,calc}$, showin in Tab. 6.2.

Table 6.2 – Calculated U_p and intensity enhancement factor, ξ_I, using the measured U_p from peak shifting.

Pulse energy (nJ)	**Intensity (W cm^{-2})**	**Calculated U_p (eV)**	**First peak location (eV)**	**Measured U_p (eV)**	ξ_I
6.2	0.918×10^{12}	0.0549	50.1	0.29	5.28
8.74	12.4×10^{12}	0.0739	49.7	0.69	9.34
11.55	16.3×10^{12}	0.0976	49.3	1.09	11.2
14.8	21.0×10^{12}	0.1255	48.6	1.79	14.3

We can now correct the kinetic energy axis of Fig. 6.12 by shifting the spectra by $U_p + eV_{tip}$. This is seen in Fig. 6.13.

Cutoff energy:
As spectral shifting can also be cause by other effects apart from channel closing, such as geometric effects from angled tips, we compare our results to other methods of determining U_p. As discussed in Sec. 1.3.3, we assume that the maximum final energy an electron can gain through rescattering is $10U_p$. This assumption is a theoretical expansion upon calculations and observations from atomic systems [Krüger12b]. We determine the $10U_p$ cutoff from dropoff in the plateau in the spectra for higher energy electrons as in [Krüger12b], thus experimentally identifying the $10U_p$ cutoff energy, E_{cut}.

We fit a straight line to the plateau of the spectra and a straight line to the drop off in energy for higher energy electrons. The intersection of these two fits is considered the $10U_p$ cutoff, as

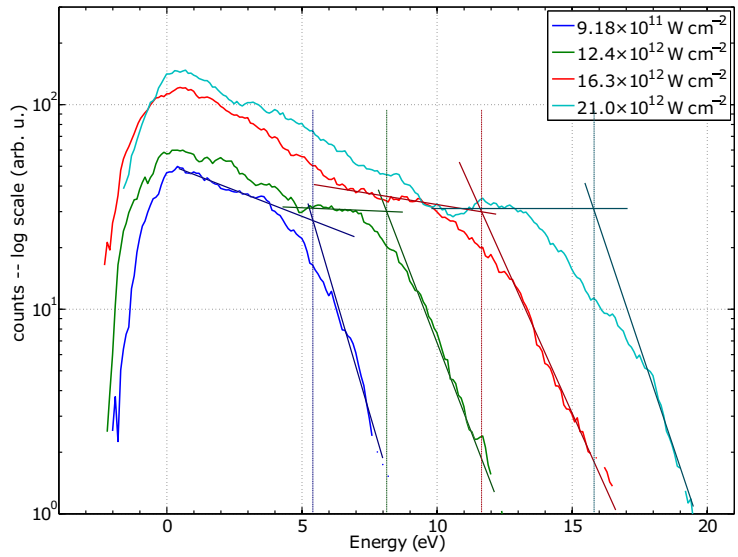

Figure 6.13 – Photoelectron spectra from Fig. 6.12 measured relative to the Fermi energy, $eV_{\text{tip}} + U_{\text{p}}$ (from Tab. 6.2). The energy cutoff energy can be determined by the dropoff from the plateau at the for the higher energy electrons.

seen in Fig. 6.13. This is a similar methodology as is done in [Krüger12b]. From the measured cutoff and therefore measured U_{p}, we can compare the values to the calculated U_{p} based on the applied intensity to find a value for the intensity and field enhancements which we can compare to the value from above. We can use the intensity enhancement factor to calculated the effective Keldysh parameter from the effective intensity, I_{eff}.

Table 6.3 – The measured cutoff energy from Fig. 6.12 and intensity enhancement ξ_I with corresponding effective intensity and Keldysh parameter γ.

Pulse energy (nJ)	**Applied intensity (W cm^{-2})**	**Calculated cutoff (eV)**	**Measured cutoff (eV)**	$\boldsymbol{\xi_I}$	**Effective intensity (W cm^{-2})**	**Effective $\boldsymbol{\gamma}$**
6.2	0.918×10^{12}	0.549	5.4	9.84	0.90×10^{13}	1.99
8.74	12.4×10^{12}	0.739	8.1	11.0	1.36×10^{13}	1.62
11.55	16.3×10^{12}	0.976	11.6	11.9	1.94×10^{13}	1.36
14.8	21.0×10^{12}	1.255	15.8	12.6	2.64×10^{13}	1.16

We see that with the calculated enhancement factor $\gamma \sim 1$ indicating a transition into the optical tunneling regime. This is in good agreement with the appearance of a spectral plateau.

The measured cutoff should scale linearly with the effective intensity. Indeed it does as seen in Fig. 6.14. The intensity dependence of the cutoff with the applied intensity yields a linear scaling with a slope of 8.81 ± 0.07 eV/(10^{12} W cm^{-2}) and an offset of 2.74 ± 0.52 eV seen in the blue line in Fig. 6.14. As $E_{\text{cut}} \propto I_{\text{eff}}$, there should not be an offset in the fit. This offset can be attributed to geometric factors in the experimental setup such as a tilted tip with respect to the spectrometer, thus shifting the effective Fermi level or a systematic error in our assumption of the Fermi level. We can correct for this error by shifting the spectra by the offset. The corrected spectra can be seen in Fig. 6.15. This yields a new measured

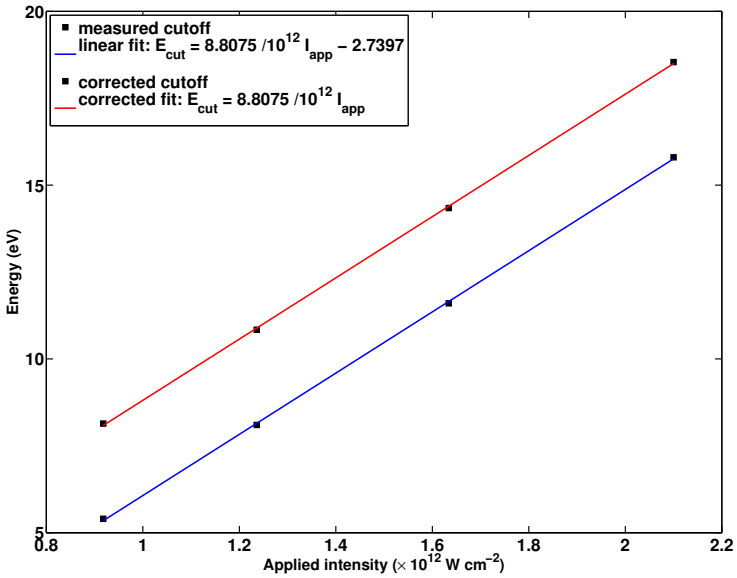

Figure 6.14 – This shows the measured cutoff scales linearly to the applied and effective intensities. The blue fit shows that E_{cut} = (8.81 $\pm$ 0.07) eV/(10^{12} W cm^{-2}) I_{app} − 2.74 $\pm$ 0.52 eV, for the applied intensity. Correcting for the offset due to geometric factors in the experimental setup, the corrected cutoff and fit can be seen by the red curve, with E_{cut} = 8.81 eV/(10^{12} W cm^{-2}) I_{app}.

cutoff and therefore new intensity enhancement as seen in Tab. 6.4. This indicates an intensity enhancement of 14.75 $\pm$ 0.05, and a field enhancement of 3.8 $\pm$ 0.05. We can see that with our field enhancement the Keldysh parameter $\gamma \sim 1$ indicating transition into the optical tunneling regime.

Table 6.4 – The corrected cutoff energy from Fig. 6.14 and 6.15 and corresponding intensity, ξ_I and field enhancements, ξ with the effective intensity and Keldysh Parameter, γ.

Pulse energy (nJ)	**Applied Intensity (W cm^{-2})**	**Calculated E_{cut} (eV)**	**Corrected measured E_{cut} (eV)**	ξ_I	ξ	**Effective intensity (W cm^{-2})**	**Corrected effective γ**
6.2	0.918×10^{12}	0.549	8.1	14.8	3.85	1.36×10^{13}	1.62
8.74	12.4×10^{12}	0.739	10.8	14.7	3.83	1.81×10^{13}	1.40
11.55	16.3×10^{12}	0.976	14.4	14.7	3.83	2.40×10^{13}	1.22
14.8	21.0×10^{12}	1.255	18.5	14.8	3.84	3.10×10^{13}	1.07

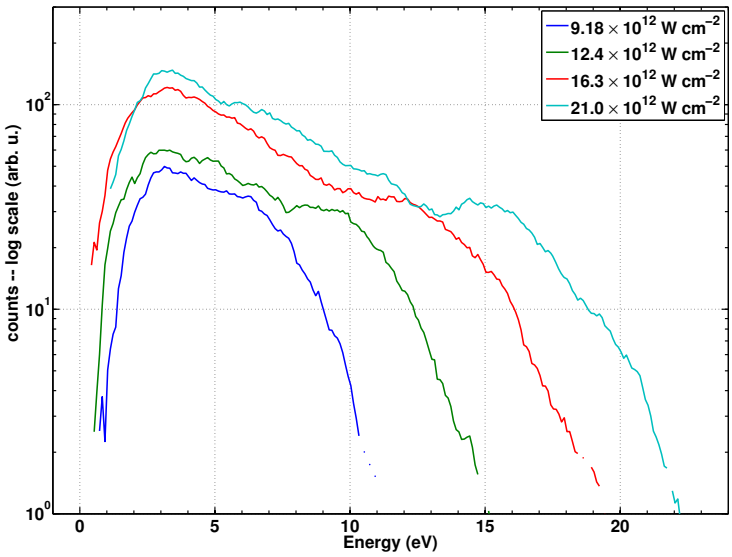

Figure 6.15 – Photoelectron spectra from Fig. 6.12 measured relative to the corrected Fermi energy, U_p (from Tab. 6.2) + eV_{tip}+ 2.59 eV.

Adiabaticity parameter δ:

To confirm that our cutoff analysis is correct, and that the electric field of the laser is not suppressing the normal electron propagation, we calculate the adiabaticity parameter, δ, described in Sec. 1.4.4. This parameter, given by Eq. 1.31, compares the (1/e) decay length of the optical field of the laser, $l_{\mathscr{E}_0}$, to the quiver excursion amplitude of a free electron in the laser field, l_q, yielding $\delta = \frac{l_{\mathscr{E}_0} m_e \omega^2}{e\mathscr{E}_0}$. δ determines how the electron motion propagates in the laser field, whether the electrons oscillate normally in the quasi homogeneous optical field of the laser, or if the field is intense enough to steer the electrons away from the tip.

Table 6.5 – Calculated and effective adiabaticity parameter, δ taking into account the enhancement calculated in Tab. 6.4.

Applied intensity (W cm^{-2})	**calculated δ**	**Effective intensity (W cm^{-2})**	**Effective δ**
0.918×10^{12}	240	1.36×10^{13}	62.3
12.4×10^{12}	207	1.81×10^{13}	54.0
16.3×10^{12}	180	2.40×10^{13}	46.9
21.0×10^{12}	159	3.10×10^{13}	41.3

As seen in Tab. 6.5, $\delta \gg 1$ which means that we are in the quiver regime and that the electron is not steered by the optical field and therefore its propagation and cutoff can be calculated normally (i.e. the quiver amplitude is less than the enhancement length).

Local value of the enhanced E-field:

We can use the cycle averaged intensity of the laser, $I = \frac{1}{2} c\varepsilon_0 \mathscr{E}_0^2$, Eq. 1.16, to find the amplitude of the electric field of the laser. Using the enhancement factors found above we can calculate the effective electric field at the apex of the tip due to the laser.

Table 6.6 – This gives the effective electric field, $\mathscr{E}_0$, of the laser taking into account the enhancement, ξ, from the tip.

Applied intensity (W cm^{-2})	**Applied $\mathcal{E}_0$ (GV/m)**	**Intensity enhancement ξ_I**	**Field enhancement ξ**	**Effective $\mathcal{E}_0$ (GV/m)**
0.918×10^{12}	2.7	14.8	3.85	10.4
12.4×10^{12}	3.1	14.7	3.83	11.9
16.3×10^{12}	3.5	14.7	3.83	13.4
21.0×10^{12}	4.0	14.8	3.84	15.4

Tab. 6.6 shows that the electric field of the laser is sufficiently enhanced to induce optical tunneling effects. Theoretical simulations for understanding exactly the enhancement effects we have and measured cutoff positions is under investigation with Thierry Auguste from CEA[1].

6.5 Preliminary 400 nm results

As silver has a very strong plasmon resonance, we investigated the response of the tip at 400 nm. 350 nm is a characteristic bright mode of the surface plasmon of bulk silver [Ma15, Chaturvedi09]. The second harmonic of the Ti:sapphire laser system, 400 nm provides an easy wavelength to convert to, which is not far from this resonance mode. Preliminary results are presented below.

A 250 μm BBO cut at an internal angle of 29.2° was used for second harmonic generation (SHG). The converted beam was reflected off three dichroich mirrors which reflect 400 nm light and pass 800 nm to eliminate any residual fundamental. As all our beam characterizing instruments are for 800 nm, and the focusing mirrors were at vacuum (making knife-edge measurements impossible), the characterization of the 400 nm pulses was not very precise. However, a few assumptions can be made. As SHG is a non-linear process which depends on the square of the spectral bandwidth of the fundamental beam, both the converted spectral bandwidth and spot-size are less than that of the fundamental. This means that the resulting focused spot-size for 400 nm will be larger than that for 800 nm. At the time, experimental constraints were such that we were not able to correctly characterize the 400 nm pulse durations. Recall from Eq. 1.12 that the Fourier limit of a pulse depends on both the bandwidth of the spectrum and the central wavelength. This means that we can have equally short pulses at 400 nm even with less bandwidth. However, 250 μm is a relatively thick non-linear crystal, so we assume that some linear chirp has been added to the pulse. For the results presented below, we assume the same spot size and pulse duration as those measured for 800 nm. This gives us an estimation for the applied intensity for the 400 nm, and therefore a possible enhancement factor.

Fig. 6.16 shows spectra for 400 nm and 800 nm with similar pulse energies. Since we are using the same values for the spot size and pulse duration for both wavelengths, this corresponds to

[1] `http://iramis.cea.fr/spam/en/Phocea/Vie_des_labos/Ast/index.php`

the same applied intensities. Without any analysis we can immediately see that the electron yield for the same pulse energy at 400 nm is much higher than the equivalent at 800 nm. We can also see that the spectral bandwidth for the 400 nm wavelength is much broader than those at 800 nm.

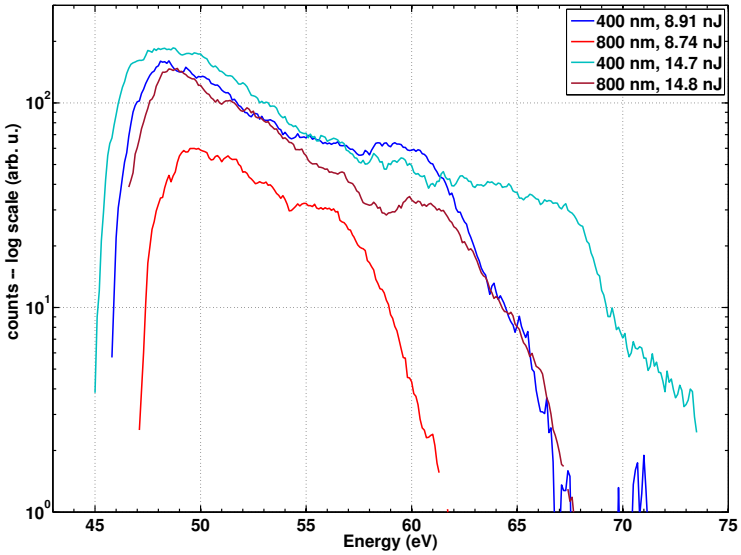

Figure 6.16 – Photoelectron spectra for irradiation by 400 nm and 800 nm laser light with the same pulse energies, ~8.8 nJ and 14.7 nJ. As we are assuming the rest of the laser parameters are the same (to maximize the possible intensity at 400 nm), this corresponds to intensities of $\sim\{6, 10\} \times 10^{11}$ W cm^{-2}.

We can apply the same analysis on the ponderomotive energy and enhancement factor as in Sec. 6.4. We use Eq. 6.4 and the location of the first peak to approximate the U_p of the system using the channel closing approximation. The photon energy for a pulse at 400 nm $\hbar\omega = 3.1$ eV, meaning that the minimum number of photons needed to overcome the work function is only 2. This also means that the excess energy an emitted electron has that absorbed 2 photons at 3.1 eV is more than would be for an emitted electron which absorbed 3 photons at 1.55 eV to overcome the barrier. We can compare this measured U_p based on peak shifting to the calculated U_p due to the applied intensity.

Table 6.7 – Calculated U_p from the peak shifting effect.

pulse energy (nJ)	Intensity (W cm^{-2})	calculated U_p (eV)	First peak location (eV)	Measured U_p (eV)	Intensity enhancement
8.91 @ 400 nm	12.6×10^{11}	0.0188	48.5	3.44	183
8.74 @ 800 nm	12.4×10^{12}	0.0739	49.7	0.69	9.34
14.7 @ 400 nm	20.8×10^{11}	0.031	48.2	3.74	121
14.8 @ 800 nm	21.0×10^{12}	0.1255	48.6	1.79	14.3

This first approximation and corrected Fermi energy from peak shifting is seen in Fig. 6.17. The intensity enhancement factors are much larger at 400 nm than those found for 800 nm. Recall our spot size and pulse duration assumptions meaning that the intensity we use for 400 nm is an estimation.

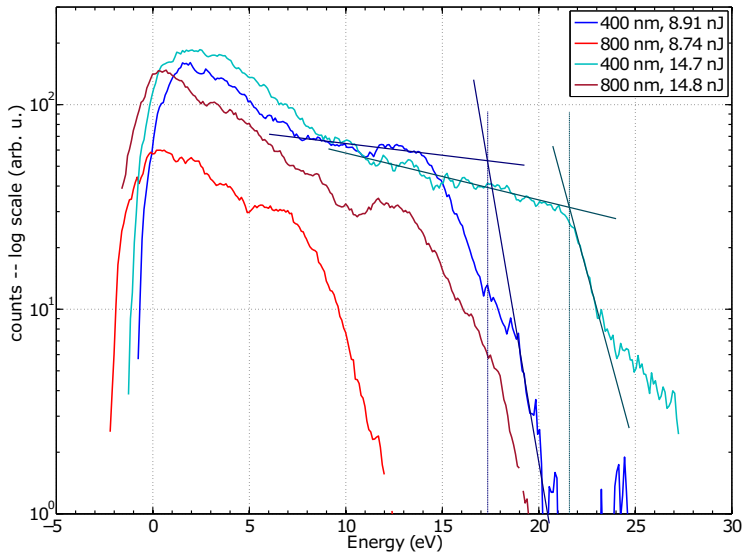

Figure 6.17 – This shows the photoelectron spectra from Fig. 6.16 measured relative to the Fermi energy $eV_{\text{tip}} + U_{\text{p}}$ measured from the peak shifting effect, Tab. 6.7. The $10U_{\text{p}}$ cutoff energy can be determined via the straight line method used in Sec. 6.4

We use Fig. 6.17 to calculate the $10U_{\text{p}}$ cutoff to see how these results compare. Using the straight line method described above in Sec. 6.4 we can find a measured cutoff and enhancement factors.

Table 6.8 – The measured cutoff energy from Fig. 6.17 for 400 nm and corresponding intensity and field enhancements.

pulse energy (nJ)	Intensity (W cm^{-2})	calculated cutoff (eV)	measured cutoff (eV)	Intensity enhancement	Field enhancement
8.91 @ 400 nm	12.6×10^{11}	0.188	17.3	92	9.6
8.74 @ 800 nm	12.4×10^{12}	0.739	8.1	11.0	3.3
14.7 @ 400 nm	20.8×10^{11}	0.31	21.6	70	8.4
14.8 @ 800 nm	21.0×10^{12}	1.2255	15.8	12.6	3.5

These preliminary results seem to indicate that we have an intensity enhancement of $\sim$100 with a corresponding field enhancement of $\sim$10. While it its unknown how much of this large field enhancement is due to plasmon resonance effects or due to other factors, it is promising for the pursuit of wavelength dependent effects. With the development of the NOPA (Sec. 2.3) more systematic investigations into wavelength dependent factors can be studied.

6.6 Summary

We investigated electron emission from a silver nanotip. Silver is of interest because of its strong plasmon resonance due the small imaginary component of its dielectric constant. These studies were performed in collaboration with GPM in Rouen.

We use FIB milled silver tips with known radii of 20-50 nm. The radius was used to corroborate the Nordheim function used in FN plots. We also used FEM images to observe the multi emission sites from the polycrystalline nature of the tips.

We irradiated the tip at a high repetition rate. Our first attempts had unexpected results which we could not account for. We imaged the tip after laser irradiation but found no evidence of thermal damage nor oxidation. Our second sample yielded results more consistent with our assumptions. This tip gave a good polarization contrast and fit with $n = 3 \pm 0.6$, however spectra yielded high emission to the point of detector saturation so no laser power dependent exponent could be extracted. We attributed the high emission to possible thermal effects and lowered the repetition rate of the laser to see if that alleviated the saturation.

At low repetition rate, our polarization scans gave good contrast; however, both laser power scans as wells as the polarization fit yielded a low extracted $\eta \sim 1.5$. Possible reasons for such a low η could be from photofield and thermally enhanced tunneling effects, or geometric effects such as an angled tip or space charge effects from high emission. Kinetically resolved spectra revealed a spectral plateau indicating electron recollision and rescattering. We can use the spectra to calculate the enhacement factor in two ways. First we can calculate U_p using the shift of the spectra from the channel closing peak shifting effect. We can compare these results to measuring the $10U_\mathrm{p}$ energy cutoff from the spectra. Comparing these measured values with the calculated U_p from the applied intensity we find an intensity enhancement factor of 14.75 ± 0.05 and a field enhancement of 3.8 ± 0.05.

Preliminary results at 400 nm indicate much higher electron emission and much broader energy spectrum for similar intensities at 400 nm than 800 nm. Again we use the two U_p measurement techniques to determine the enhancement and find and intensity enhancement of $\sim$100 with a corresponding field enhancement of $\sim$10. While we cannot make firm conclusions as to whether or not this high enhancement at 400 nm is due to plasmonic resonance effects, it is a promising start for further wavelength dependent investigations.

7

Re-examining emission mechanisms using spectral shape

Up until now we have been looking at spectra for an individual tip material and emission mechanism. In this chapter I compare the emitted spectra and mechanisms presented and discussed in the previous chapters. I first discuss the probability of photon absorption for an electron with an above threshold amount of energy. I then describe the expected shapes for each of the mechanisms and present a schematic of the spectra. I compare the photoelectron spectra from the previous chapters with the same applied intensities and compare the dominant emission mechanisms for the various spectra and discuss difficulties in simulating these tip-based systems.

7.1 ATP peaks: probability of free-free transitions

Recall above threshold photoemission (ATP) where the emitted spectra show characteristic peaks separated by the applied photon energy corresponding to the number of photons absorbed by an electron at a given energy. The above threshold absorption of photons is called the free-free transition [Agostini79]. From the ratio of the number of electrons emitted for a given peaks of ATP emission, we can determine the "probability" for an electron to absorb a photon before emission, after it has above threshold energy. An electron has a probability $\mathscr{P}_n$ of being emitted from the system after the absorption of n photons. This means that for an ATP peak of photon order n an electron has a probability of emission for that energy

$$\mathscr{P}_n = \mathscr{P}_{AT} \times (\mathscr{P}_1)^{n-n_{\min}}, \tag{7.1}$$

for $n > n_{\min}$, where $\mathscr{P}_{AT}$ is the probability of an electron to acquire above threshold energy. $\mathscr{P}_1$ is the probability for an electron to absorb 1 more photon. We find that

$$\mathscr{P}_1 = \frac{J_{n+1}}{J_n}, \tag{7.2}$$

where J_n is the number of electrons emitted at the ATP peak of photon order n (while $n > n_{\min}$). This relation is valid as long as the laser pulse is not depleted of photons and that $\mathscr{P}_1$ is not large ($\ll 1$), as in our case. We can extract the probability $\mathscr{P}_1$ of photon absorption by comparing the peak heights for ATP peaks, as the ratio between subsequent peaks is almost constant (corresponding to a straight line in log scale). This is seen in Fig. 7.1. The probability is proportional to the laser intensity, as seen in Fig. 7.2 and Tab. 7.1.

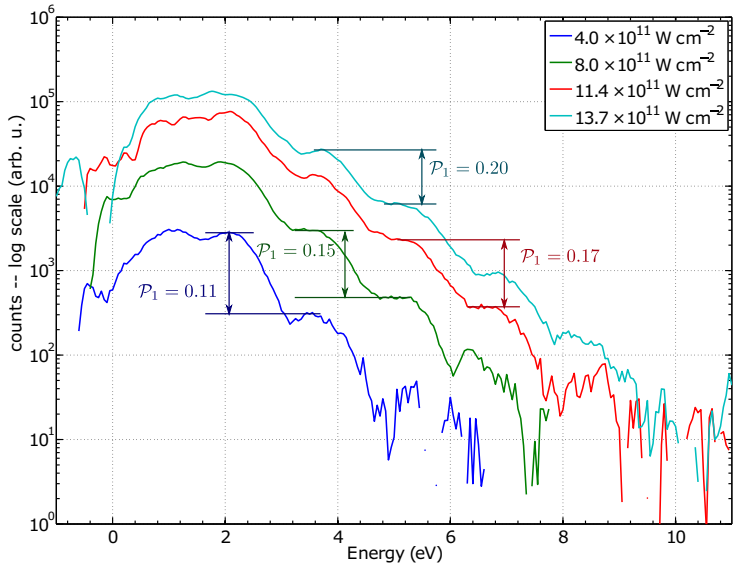

Figure 7.1 – Demonstration of $\mathscr{P}_1 = \frac{J_{n+1}}{J_n}$ as a function of applied laser intensity for a polycrystalline tungsten tip.

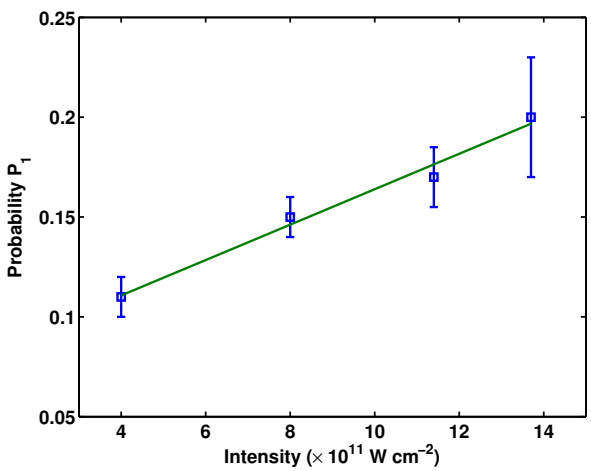

Figure 7.2 – The linearity of the probability of photon absorption with the applied intensity of the laser.

These probabilities give a roughly linear fit with respect to the applied intensity as seen in Fig. 7.2. As seen in Fig. 7.1 there are channel closing and peak shifting effects present in the spectrum causing shifts in the peaks and possible saturation effects or other detector efficiency effects to explain the slight non-linearity. This same probability can be compared to

Table 7.1 – A list of $\mathscr{P}_1$ probabilities extracted from Fig. 7.1 as a function of applied laser intensity.

Intensity (W cm^{-2})	$\mathcal{P}_1$
4.0×10^{11} W cm^{-2}	0.11
8.0×10^{11} W cm^{-2}	0.15
11.4×10^{11} W cm^{-2}	0.17
13.7×10^{11} W cm^{-2}	0.20

other examples of ATP peaks as well as above threshold ionization (ATI) peaks in atoms. For example, ionization in Xe atoms from [Agostini79] yields a free-free transition probability, $\mathscr{P}_1$, of ~0.15 for a laser intensity of 8×10^{12} W cm^{-2}. This is a much higher intensity than for equivalent probabilities we found for tungsten nanotips. This is possibly due to the higher ionization potential of a Xe atom compared to the work function of a tungsten nanotip, or due to the lack of field enhancement in atoms. For the tungsten tips found in [Schenk10], a $\mathscr{P}_1$ of ~0.3 was found for a laser intensity of 2.3×10^{11} W cm^{-2}. This is a much higher probability than we found for similar laser intensities. However, the tungsten tips used in [Schenk10] were a factor of two smaller than ours indicating a higher field enhancement and their laser pulses were much shorter possibly alleviating thermal effects which might have slightly surpressed the magnitude of our peaks.

7.2 Spectral shape

7.2.1 Different shapes for different mechanisms

We use the shape of the spectra to identify emission mechanisms. Fig. 7.3 shows a schematic of the different spectral shapes we identified.

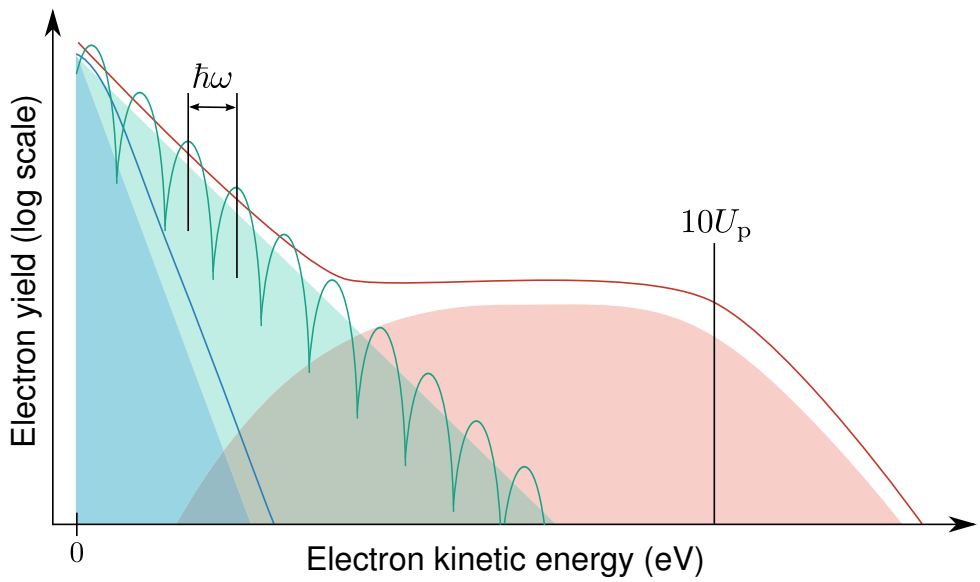

Figure 7.3 – This shows a schematic of the spectral shapes identified in this thesis. The blue portion represents thermally enhanced field emission (Sec. 1.2.3), the green represents above threshold photoemission (ATP, Sec. 1.3.2) and the red is from rescattering electrons (Sec. 1.3.3). The spectra we expect for each mechanism are represented by the solid lines.

In Fig. 7.3, the solid colors represent the spectral shapes we expect for each mechanism. The solid lines represent the spectrum. The blue portion represents thermally enhanced field emission (Sec. 1.2.3), the green represents above threshold photoemission (ATP, Sec. 1.3.2) and the red is from rescattering electrons (Sec. 1.3.3).

ATP emission is due to multiphoton absorption of a certain number photon energy packets to overcome the work function barrier. This type of emission is characterized by peaks separated by the photon energy $\hbar\omega$ of the photons absorbed, as shown by the green line. The electrons that have been rescattered by the laser field have gained high amounts of energy. These are shown in the red part of the spectrum. The resulting spectrum is the sum of low energy electrons who did not get rescattered and gained energy, and those who have been rescattered and gained energy up to $10U_\mathrm{p}$. This is shown in the red curve. The blue part of the spectrum represents thermally enhanced field emission. These are electrons which have been emitted by field emission after the system has been thermally heated, in our case by the laser. These spectra are much narrower, if the electron temperature is low enough, than those from other emission mechanisms and typically smooth and featureless, as seen by the blue line.

The spectra that we record are a sum of electrons emitted by various mechanisms. As the spectra are typically dominated by one emission mechanism, we can identify the physical process based on the overall spectral shape. Information on the specifics of each mechanism behind the electron emission can be identified for each type of spectral shape. As discussed in Sec. 6.4, the optical field enhancement of a tip can be measured from the observation of a spectral plateau by comparing the measured $10U_\mathrm{p}$ cutoff with the expected value from the applied intensity.

7.2.2 Comparisons of photoemission spectra

We compare the recorded photoelectron spectra for various tips to see if we can identify the dominant mechanism for electron emission.

Fig. 7.4 shows recorded photoelectron spectra for various tips with the same applied peak laser intensity. For each of the tips, the radius is about the same (the same order of magnitude), the work functions are similar ($\sim$ 5 eV), and the applied voltages are about the same (the same order of magnitude). This allows us to compare effects that occur because of the material properties of the tips, leading to the enhancement of certain emission processes.

The applied V_tip on for each spectra remains small enough to not affect the work function of the materials and to have no thermal effects on the system. The spectra taken at a lower repetition rate have been normalized to account for the low relative signal due to the repetition rate. The applied peak laser intensity does not take into account optical field enhancement from the tip.

From these spectra we can see that changing the different tip material, or modifying the laser parameters influences the dominant electron emission mechanism. The blue spectra are narrower without any identifiable features, indicating thermally assisted field emission, or a combination of ATP and thermal effects. The green spectra are wider with clearly observable ATP

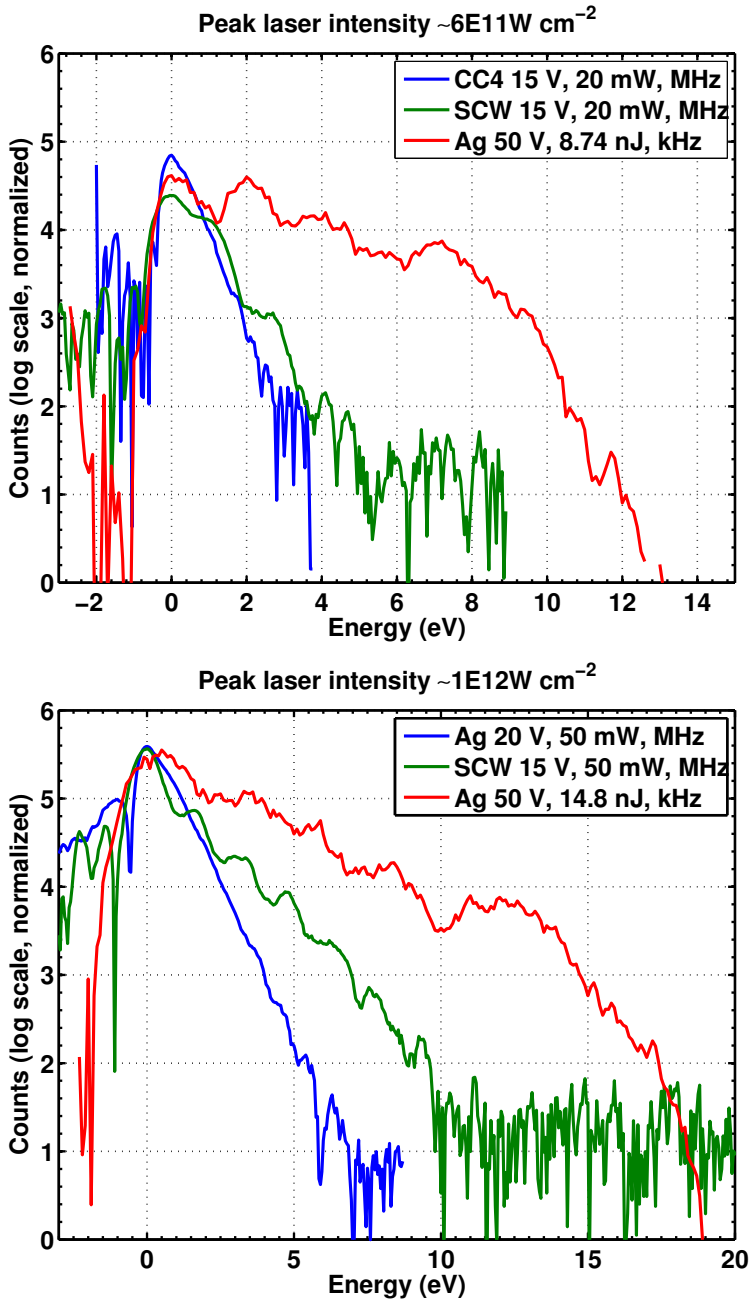

Figure 7.4 – Each set of spectrum were taken with the same applied peak laser intensity: top 6×10^{11} W cm^{-2}, bottom 1×10^{12} W cm^{-2}. Changing the tip material or laser repetition rate (mean power) changes the dominant emission mechanism. The blue spectra show narrower spectra indicating thermally enhanced field emission. The green spectra show multiphoton emission characterized by ATP peaks separated by the photon energy. The red spectra show much broader energies indicating a transition into the optical tunneling regime and the emergence of a spectral plateau for high intensity evidencing electron recollision and rescattering.

peaks indicating multiphotonic, over the barrier emission. The red spectra are much wider and show the emergence of the characteristic spectral plateau from optical tunneling and electron rescattering and recollision.

For top panel in Fig. 7.4, all spectra were taken with an applied intensity of 6×10^{11} W cm^{-2}.

The blue spectrum is from a CCnT at high repetition rate and has much narrower indicating thermal assisted field emission is the dominant mechanism. The green spectrum is from a SCW(310) nanotip at high repetition rate with a slightly broader spectrum than for the CCnT with visible ATP peaks up to a photon order of $n = 5$ (three visible peaks). The red spectrum is from a polycrystalline Ag nanotip taken at low repetition rate. The energies of these photoelectrons form a much broader spectrum possibly indicating a transition into the optical tunneling regime.

The bottom spectra in Fig. 7.4 were all taken with an applied intensity of 1×10^{12} W cm^{-2}. The green spectrum is from a SCW(310) nanotip. The wider spectrum and characteristic ATP peaks separated by the photon energy of the laser indicate multiphotonic emission up to a photon order of $n = 9$. The blue spectrum is from a polycrystalline AG nanotip taken at high repetition rate. The narrowness and featureless spectrum indicates the electrons were emitted with thermal assistance from the laser, possibly due to the high mean power. By reducing the repetition rate of the laser, the mean power of the laser becomes almost negligible. This alleviates thermal effects from the laser and the spectrum becomes much broader and a plateau forms indicating electron recollision and rescattering.

The indicated applied intensities do not take into account the field enhancement from the nanotips. The enhancement takes into account both the tip geometry and material. As seen by the various spectral shapes expressing the different emission mechanisms, the different enhancement factors of the tips augment the dominant emission mechanisms. Lowering the repetition rate of the laser alleviates the thermal effects of high mean power allowing other emission mechanism to dominate.

From this we see that the repetition rate of the laser has the largest effect on the dominant emission mechanism as it negates thermal effects from high mean power. For the same silver tip, we are able to observe thermal emission for high mean power laser and repetition rate irradiation, and electron recollision and rescattering for low mean powers. The intensity of the laser allows these spectral features to become more pronounced. The tip material also factors in as tungsten is the only material for which ATP emission was observable for high repetition rates, while the size of the tip affects the optical enhancement factors from the laser without adding thermal effects that come with higher mean power or intensity. Future investigations using the NOPA (Sec. 2.3) will allow further studies in wavelength and repetition rate dependencies.

7.2.3 Spectral simulations

Theoretical modeling of thermally assisted field emission is not as straight forward as there are many factors that must be taken into account [Kealhofer12]. All the contributions to the thermal balance of the system are not evident, and include parameters such as the thermal conductivity of the material, the transfer of heat energy to the electrons and from the electrons to the lattice ions, emission of electrons, the application of the tip bias, etc. Finite element modeling of the evolution of temperature within the tip has been done to assess the thermal

thresholds of tips [Houard11, Kealhofer12]. From these studies we can make first order approximations on the emitted spectra of thermally assisted field emission. We know that these spectra are generally narrower than those emitted by multiphonic absorption and the slope (and width) of the emitted spectra depends on the electron temperature and the static electric field from the tip bias.

Simulations on atomic and molecular systems on above threshold ionization (ATI) and rescattering electron emission effects have been extensively studied [Corkum93, Paulus94a, Ivanov05]. Expansion of these calculations to tip based systems is also under investigation [Krüger12b, Ciappina14a, Ciappina14b], but application of field enhancement effects is not evident as the field is not homogeneous. Tip based systems must also take into account other parameters which are not considered (or relevant) for atomic systems such as: the geometric shape of the system, the bulk energy band structure of the electron states (as opposed to discrete energy levels), the thermal effects of the system, the surface interface of the system with the vacuum and corresponding surface interaction effects, as well as the low work function for a metal ($\sim$5 eV) compared to the ionization potential of an atom ($\sim$15 eV).

7.3 Summary

In this chapter I present a comparison of the spectrum seen in this thesis. I first discuss the probability of free-free transitions where an above threshold electron can absorb another photon. This probability can be derived from the heights of the ATP peaks. I then discuss the expected spectral shapes for thermally assisted field emission, above threshold photoemission and electron recollision and rescattering. I present a schematic of each of the expected electron spectrum. I then compare spectra from different tips for the same applied laser intensity. We see the narrower spectra and lack of ATP peaks from thermally enhanced electron emission for a CCnT and Ag nanotip at high repetition rate. Multiphotonic photoemission is seen for SCW(310) with peaks in the spectrum indicate one more photon absorbed by the system and are separated by the photon energy. Finally we see signs of electron recollision and scattering in the photoemission spectrum for Ag. The laser repetition rate has been reduced, so that the mean power is almost negligible. The spectrum is much broader than emission from other mechanisms. A plateau forms at higher intensities indicating electron recollision. Finally I present some of the difficulties in simulating spectra from tips, as tip-based systems are not as straight forward as those on atoms and molecules.

Conclusion and Perspectives

In this thesis I present a novel experiment for investigating photoelectron emission induced by an ultrafast laser from a sharp nanotip. This new scientific direction for my group involved the complete design and development of a new experimental setup and apparatus incorporating existing electron spectroscopy techniques with laser development expertise. We expand upon previous results in conventional metallic nanotips of tungsten [Hommelhoff06b, Barwick07, Yanagisawa10] and gold [Ropers07, Bormann10, Park12] by using innovative new tips based on carbon nanotubes and silver.

The physical mechanisms behind electron emission induced by light have been studied since the discovery of the photoelectric effect by Einstein in 1905. Chapter 1 presents an overview of the physical processes for electron emission from a metal surface, and the peculiarities that arise from a sharp nanotip geometry. There are three main mechanisms behind electron emission from a system, depending on the field applied and the laser intensity illuminating the system. By changing the parameters applied to our system (applied voltage, nanotip material and radius, laser intensity, photon energy and repetition rate), we can change and control the dominant emission process observed. With no laser, the system can be heated up such that the electrons can obtain sufficient energy to overcome the work function of the material, or a strong enough external DC field can be applied so that the barrier becomes penetrable via quantum mechanical tunneling. With the addition of a low to moderate laser pulse, and an external electric field, an electron can be emitted via assisted tunneling by either the absorption of a photon or from the tail of the laser heated electron gas within the metal. With moderate to high laser intensities, the system can absorb enough energy from the laser to overcome the potential barrier of the system, and at high enough intensities, the optical field of the laser acts and modify the barrier itself to induce tunneling and possibly rescattering and recollision of the electron with the system.

All these mechanisms of electron emission are valid not just for nanotip systems. The sharp nanotip geometry adds factors to the system that must be taken into account. A simple geometric field enhancement is seen at the apex of the tip simply due to the nanometer sized tip, where the field at the end of the apex is given by $F = \beta V_{\text{tip}}$. A corresponding optical field enhancement is also considered when assessing nanotip geometries. This can lead to modifications in the electron propagation, steering the electrons away from their normal trajectories.

Chapters 2 and 3 describe in detail the experimental apparatus and methods for our investigations. We implement a fully characterized and controllable laser system based on a conventional 800 nm, Ti:sapphire laser oscillator and amplifier chain. This system can be used in a high repetition rate (62 MHz), moderate mean power mode, using the direct output from the oscillator, or a low repetition rate (1 kHz), low mean power mode using the regenerative amplifier, each mode with the same peak pulse intensity. We have also built a NOPA at the output of a fiber-based infrared laser which allows flexibility in wavelength and repetition rate, while maintaining short pulse duration and the same peak pulse intensity. This NOPA system has yet to be implemented in the experimental setup. Our new experimental apparatus is fully flexible to allow for the variety of parameters we can change. We have access to three types of nanotips, tungsten, silver and carbon nanotube based tips, each of which requires a slightly different mounting technique within our ultrahigh vacuum chamber. We use three dimensional nanopositioning stages to position the tips into the focus of the laser. The emitted electrons are detected in a homemade field retarding spectrometer, from which we record an integrated electron spectra. Later generations of the spectrometer can move in two dimensions allowing for spatially resolved, FEM-like measurements.

We compare our experimental setup to existing experiments using our results on tungsten nanotips in Chapter 4. We are able to confirm that our *in-situ* tip characterization techniques correspond with our assumptions on the size of the tip apex as well as the predicted emission sites. Using polarization dependence curves and the laser power dependence, we are able to extract the average number of photons, $\eta \sim 3$, the system absorbs before electron emission. This corresponds well with the minimum number of photons needed $n_{\min} = \phi/\hbar\omega = 2.9$ to overcome the work function barrier $\phi = 4.35$ eV of single crystal (310) tungsten. Kinetically resolved photoelectron spectra show easily observable ATP peaks. Power dependency for each peak confirm that each peak corresponds to a different number of absorbed photons. Our results on tungsten allow us to validate our experimental setup as well as familiarize us with this new setup.

Chapters 5 and 6 present results on novel nanotips. Studies on emission from CCnTs (Chapter 5) are performed in collaboration with CEMES in Toulouse. CCnTs provide an interesting sample from which to study electron emission. These samples are based on a single carbon nanotube surrounded by concentric graphene sheets to form a conical shape. As the formation and synthesis of these tips was fully developed in house, control parameters can be implemented to exhibit certain specifications in the CCnTs that are valued for our experiments. Electron emission polarization dependency result yields an average number of photons absorbed before emission of 3.4, consistent with the minimum number of photons needed to overcome the $\phi = 5.0$ eV work function of a CCnT. However, moderate laser intensity lead to the modification and destruction of samples due to laser irradiation. Systematic studies on the damage threshold of CCnTs due to laser illumination lead to a maximum applicable peak intensity of around $\sim 7.7 \times 10^{11}$ W cm^{-2} at high repetition rate. Using intensities less than this, we are able to record photoelectron spectra. These spectra show no signs of ATP phenomenon and the narrowness of their energy bandwidth compared to those of similar intensities taken from tungsten seems to indicate emission due to thermal effects on the system.

Investigations on silver nanotips (Chapter 6) are done in collaboration with GPM in Rouen. Silver is of interest due to its strong plasmonic response because of the small imaginary component of its dielectric component. This corresponds to a resonance near 400 nm, which is easily reachable with our laser system. At high repetition rate (moderate mean power), we extract an average of 3 absorbed photons of the system before emission of an electron, consistent with the $\phi = 4.26$ eV work function of polycrystalline silver. However, kinetically resolved spectra yield high emission, saturating the detectors, so no laser power dependent exponent can be extracted. These spectra are also very narrow in energy, indicating possible thermal effect aiding with the emission process. Low repetition rate yields a low extracted number of photons absorbed by the system. Possible reasons for such a low number could be from emission caused by tunneling effects or geometric factors such as space charge effects or angled nanotips. Kinetically resolved spectra demonstrate the first observance of a spectral plateau indicating electron recollision and rescattering. From the spectral features we can calculate an intensity enhancement of 14.75 ± 0.05 with corresponding field enhancement of 3.8 $\pm$ 0.05. Preliminary results from 400 nm irradiation indicate higher electron yield and broader spectrum for similar intensities at 400 nm than 800 nm.

We compare the spectra presented in Chapters 4, 5 and 6 in Chapter 7. Here we show that we are able to identify different dominant photoelectron emission mechanisms based on spectral shape. We compare spectra from various tips with the same applied laser intensities, not taking into account enhancement form the tips. Using the appearance of multiphotonic ATP peaks in tungsten emission as a baseline, we are able to see narrower spectra from high repetition rate result from CCnTs and silver nanotips indicating thermally assisted electron emission. Silver electron emission for low repetition gives broader electron spectra and the appearance of a spectral plateau, indicating the possibly the thermal effects from high repetition rate are suppressing the recollision effects of the laser field.

This thesis by no means presents an exhaustive study on the subject of electron emission from sharp nanotips, or even from these three materials. As we have been limited by thermal effects in our emission mechanisms, more investigation into these effects would be useful for future experiments. It would be interesting to see at what point emission from say, a silver nanotip switches from predominantly thermal emission to laser-induced and strong field effects. This would also give a time scale as to how long such elevated thermal states last. Such a study could be performed by investigating the emitted spectral shape as a function of repetition rate of the laser. The mechanisms of thermal emission are also not fully understood and thorough simulations are needed to corroborate our experimental results.

Investigations into the plasmonic response of materials would provide great insight into wavelength dependent emission mechanisms. Already preliminary results indicate there is higher electron yield and broader spectrum for laser irradiation close to the predicted plasmon resonance. Systematic studies on the electron yield as a function of wavelength close to the predicted resonance or even spectral shape could provide some insight to how these resonances affect the electron properties of these nanotips.

The flexibility of our experimental setup allows us the possibility to collect the laser light af-

ter it has interacted with the tip. As optical tunneling, electron rescattering and recollision are the same physical mechanisms behind high harmonic generation, perhaps slight modifications to our system would allow us to observe harmonics caused by the tips. Pump-probe experiments could provide insight to properties of the electron bunches themselves, and from pump-probe spectroscopy experiments we could extract optical properties of our nanostructures. The emission from tips can be used to study fundamental properties on electrons such as electron interference [Barwick08, Vidil] and for matter wave experiments.

The experiment presented in this thesis allows us flexibility to explore light-matter interactions in a unique regime between atomic and condensed states created by a sharp nanotips. We probe investigations into the electron emission from such a system and the parameters that influence the dominant physical mechanisms of emission. The combination of laser expertise and novel materials allows a push to strong field phenomenon and applications for these systems.

A

List of Symbols and Abbreviations

β	field amplification factor, $1/kr$
δ	adiabaticity parameter for electron propagation
η	extracted power exponent
γ	Keldysh parameter
$\hbar$	reduced Planck constant
λ	laser wavelength
$\mathscr{E}$	electric field of a laser pulse
e	Euler's number
μ	Fermi energy
ω	photon angular frequency
ϕ	work function
$\Phi(t)$	temporal phase of a laser pulse
$\mathbf{k}$	wave vector
$\varphi(\omega)$	spectral phase of a laser pulse
c	vacuum speed of light
e	electric charge
F	applied field
I	laser intensity
J	current density of emission
k	dimensionless factor depending on shape of tip and the extraction geometry
k_B	Boltzman constant
m_e	electron mass
n	number of photons absorbed by the system
r	radius of the nanotip
T	temperature
$U(x)$	potential barrier seen by an electron at position x
ε_0	permittivity of free space
U_p	ponderomotive energy
V_retard	retarding field of spectrometer
V_tip	nanotip bias
ATI	Above Threshold Ionization
ATP	Above Threshold Photoemission
BBO	β-barium borate crystal
CCD	charge-coupled device
CCnT	Carbon Cone nanoTip
CEMES	Centre d'Élaboration de Matériaux et d'Etudes Structurales, Toulouse, France
CEP	carrier envelope phase
cw	continuous wave
DC	direct current
DFG	difference frequency generation
FEM	field emission microscopy
FIB	Focused Ion Beam
FN	Fowler-Nordheim

fwhm	full width at half maximum
GDD	group delay dispersion
GPM	Groupe de Physique des Matériaux, Rouen, France
GVM	group velocity mismatch
HHG	high harmonic generation
IR	infrared
KLM	Kerr lens modelock
LOPT	lowest order perturbation theory
LX SPIDER	Long Crystal Spectral Phase Interferometry for Direct Electrid-field Reconstruction
MCP	microchannel plate
NEG	non-evaporable getter
NOPA	non-collinear optical parametric amplifier
OAP	off-axis parabola
OPA	optical parametric amplification
PCW	polycrystalline tungsten
regen	regenerative amplifier
RGA	residual gas analyzer
SCW	single crystal tungsten
SEM	Scanning Electron Microscope
SF	super fluorescence
SHG	second harmonic generation
TFP	thin film polarizer
Ti:sapphire	titanium doped sapphire
TOD	third order dispersion
TSM	Three Step Model
TTL	transistor-transistor logic
UHV	ultra-high vacuum
WLC	white light continuum
YAG	yttrium aluminum garnet, $Y_3Al_5O_{12}$

B

Thermal studies on W

This appendix shows the SEM images of the tungsten tips before and after laser irradiation. Macroscopic views of the comb before and after laser irradiation can be seen in Fig. B.1. The alignment of a tip into the laser focus is seen in Fig. B.2

Table B.1 – This shows the table of the systematic laser irradiation of the tungsten tips with various laser powers and intensities and times.

tip number	average power	time	focus	intensity
A1	10 mW	1 hr	50 mm	1.64×10^{9} W cm^{-2}
A2	1 mW	24 hr	50 mm	1.64×10^{8} W cm^{-2}
A4	10 mW	24 hr	50 mm	1.64×10^{9} W cm^{-2}
A5	100 mW	1 hr	50 mm	1.64×10^{10} W cm^{-2}
A6	100 mW	1 hr	50 mm	1.64×10^{10} W cm^{-2}
A7	200 mW	1 hr	50 mm	3.29×10^{10} W cm^{-2}
B1	200 mW	24 hr	50 mm	3.29×10^{10} W cm^{-2}
B2	–	–	–	–
B3	–	–	–	–
B4	10 mW	1 hr	7 mm	8.38×10^{10} W cm^{-2}
B5	1 mW	24 hr	7 mm	8.38×10^{9} W cm^{-2}
B6	50 mW	1 hr	7 mm	4.19×10^{11} W cm^{-2}
B7	10 mW	24 hr	7 mm	8.38×10^{10} W cm^{-2}
B8	50 mW	24 hr	7 mm	4.19×10^{11} W cm^{-2}
C1	100 mW	1 hr	7 mm	8.38×10^{11} W cm^{-2}
C2	100 mW	24 hr	7 mm	8.38×10^{11} W cm^{-2}

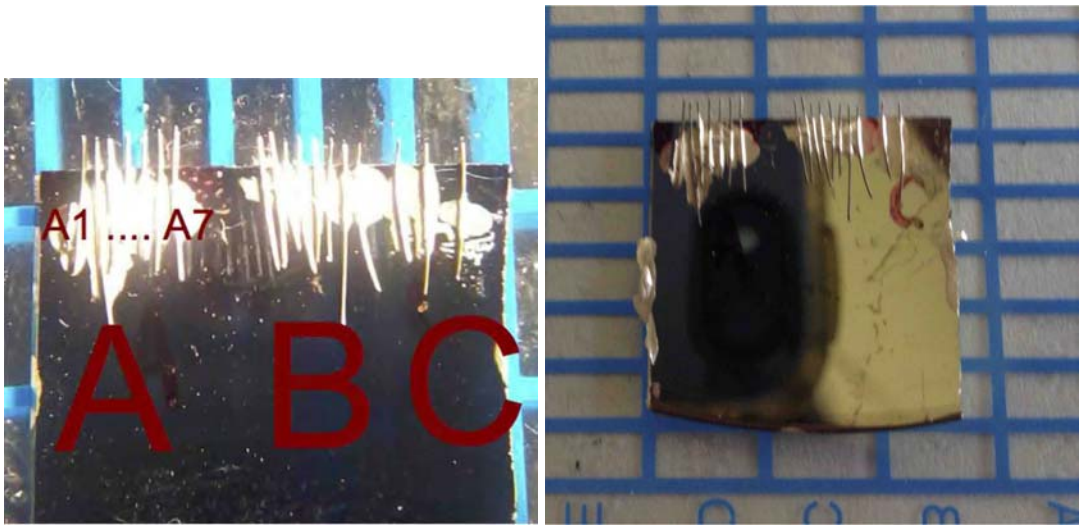

Figure B.1 – Left: Macroscopic view of the comb before the thermal tests. Right: Macroscopic view of the comb after the thermal tests, note the two end tips have fallen off.

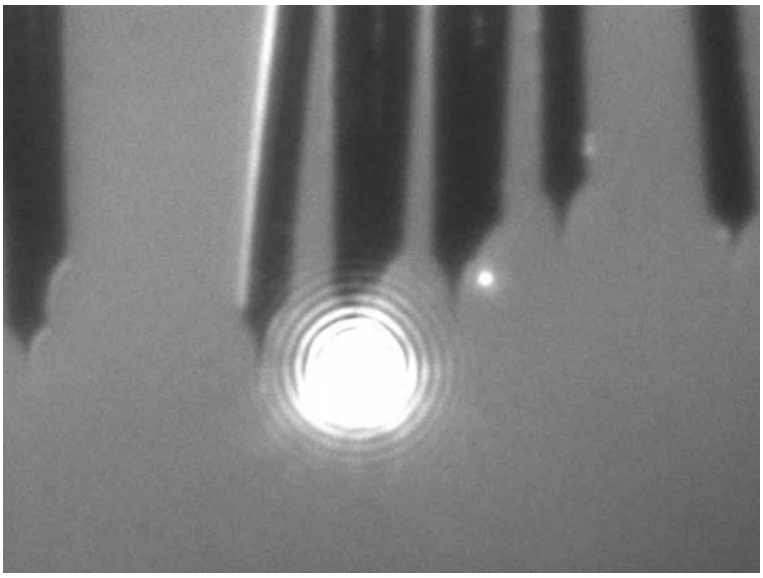

Figure B.2 – This shows the alignment of tip A4 in the focus of the laser with 250 μW of average power.

Tip A1: 10 mW for 1 hour. 50 mm focus (1.64×10^9 W cm^{-2})

Figure B.3 – SEM image of tip A1 before laser irradiation. No SEM image of tip A1 after laser irradiation. The sample kept charging up making imaging impossible.

Tip A2: 1 mW for 24 hour. 50 mm focus (1.64×10^8 W cm^{-2})

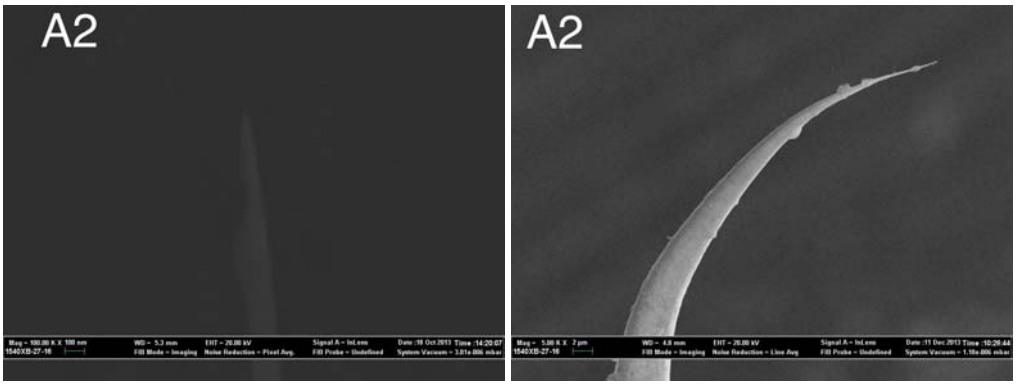

Figure B.4 – Left: SEM image of tip A2. As you can see this tip was curved before we irradiated it with laser. Right: SEM image of tip A2 after laser irradiation. Once again, the sample was charging up, so only one image was possible. However the tip is still curved.

Tip A4: 10 mW for 24 hour. 50 mm focus (1.64×10^9 W cm^{-2})

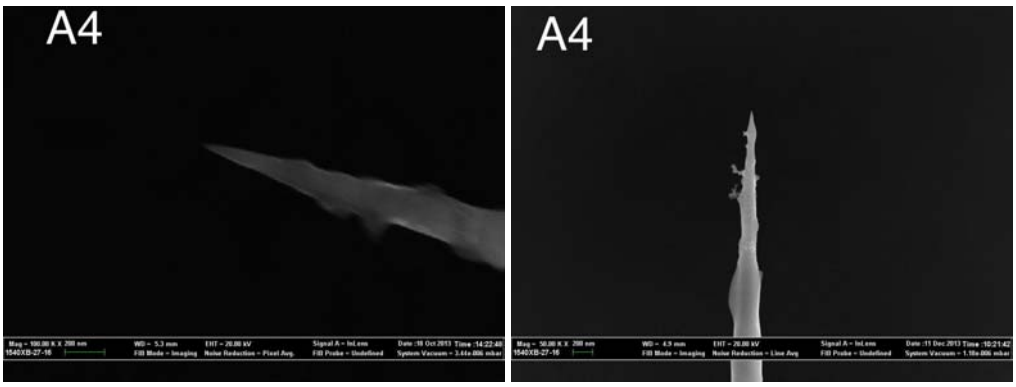

Figure B.5 – Left: SEM image of tip A4 before laser irradiation. Right: SEM image of tip A4 after laser irradiation.

Tip A5: 100 mW for 1 hour. 50 mm focus (1.64×10^{10} **W cm**$^{-2}$)

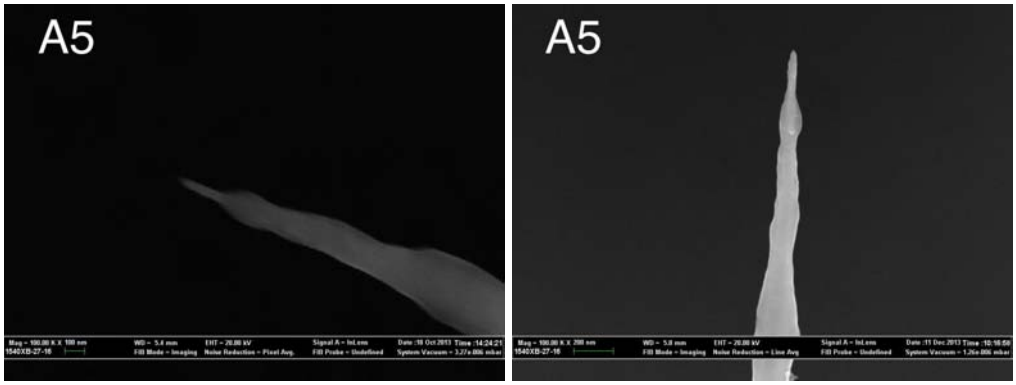

Figure B.6 – Left: SEM image of tip A5 before laser irradiation. Right:SEM image of tip A5 after laser irradiation. Lumpy looking due to salt deposition.

Tip A6: 100 mW for 24 hour. 50 mm focus (1.64×10^{10} **W cm**$^{-2}$)

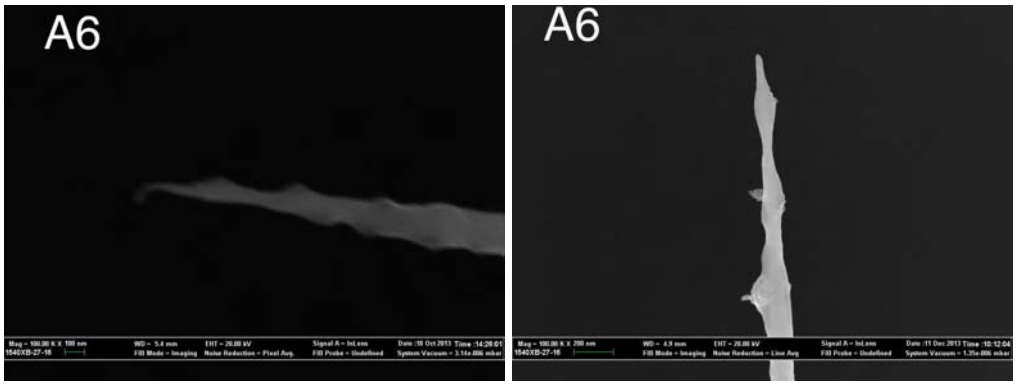

Figure B.7 – Left: SEM image of tip A6 before laser irradiation. Right: EM image of tip A6 after laser irradiation. Notice the new shape that is much blobbier than before.

Tip A7: 200 mW for 1 hour. 50 mm focus (3.29×10^{10} **W cm**$^{-2}$)

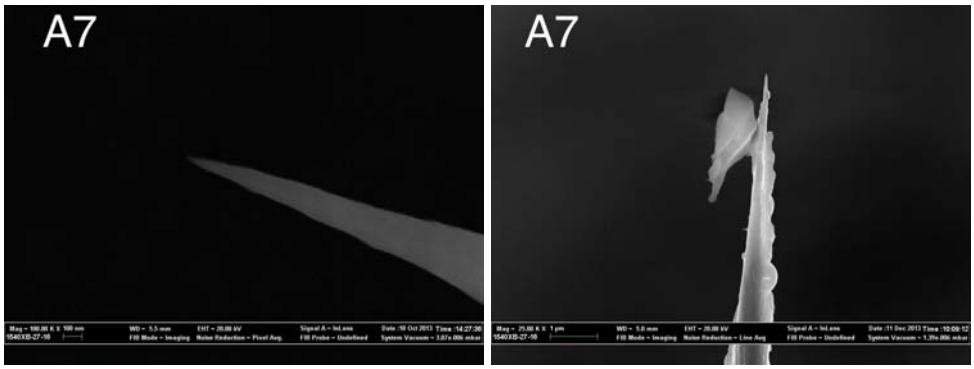

Figure B.8 – Left: SEM image of tip A7 before laser irradiation. Right: SEM image of tip A7 after laser irradiation. The tip is much saltier than before.

Tip B1: 200 mW for 24 hour. 50 mm focus (3.29×10^{10} W cm^{-2})

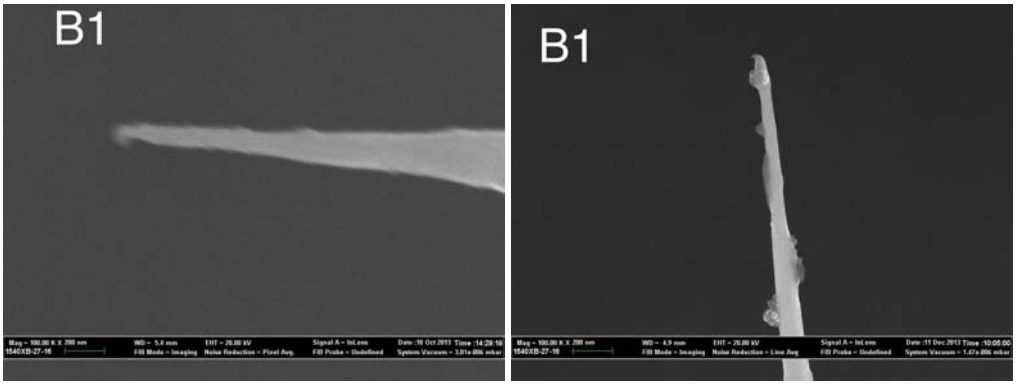

Figure B.9 – Left: SEM image of tip B1 before laser irradiation. Right: SEM image of tip B1 after laser irradiation.

Tip B2: no laser

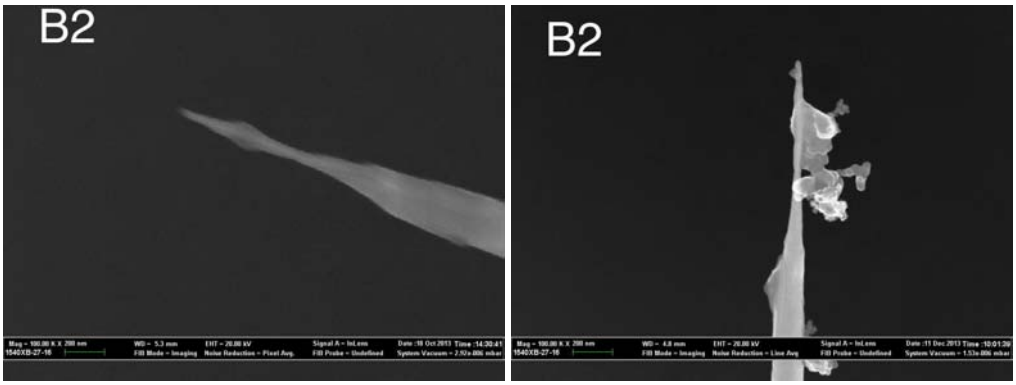

Figure B.10 – Left: SEM image of tip B2 before laser irradiation. Right: SEM image of tip B2 after laser irradiation.

Tip B3: no laser

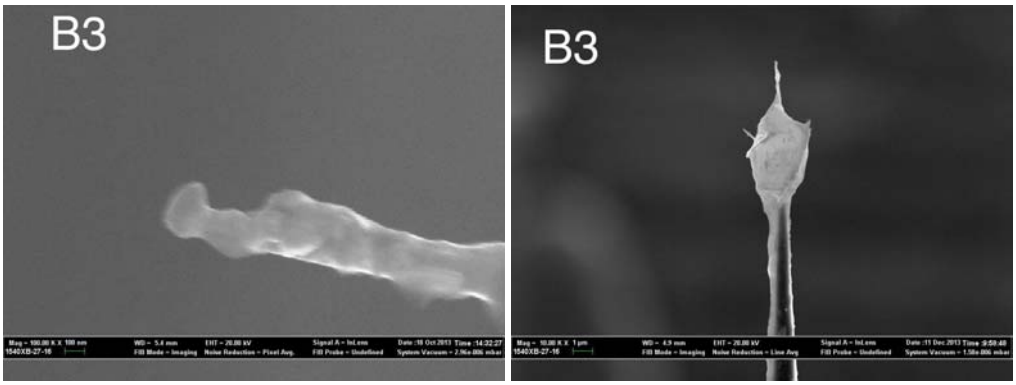

Figure B.11 – Left: SEM image of tip B3 before laser irradiation. Right: SEM image of tip 32 after laser irradiation.

Tip B4: 10 mW for 24 hour. 7 mm focus (8.38×10^{10} **W cm**$^{-2}$)

Figure B.12 – SEM image of tip B4 after laser irradiation. No SEM image of tip B4 before laser irradiation. Sample kept charging up making imaging impossible.

Tip B5: 1 mW for 24 hour. 7 mm focus (8.38×10^{9} **W cm**$^{-2}$)

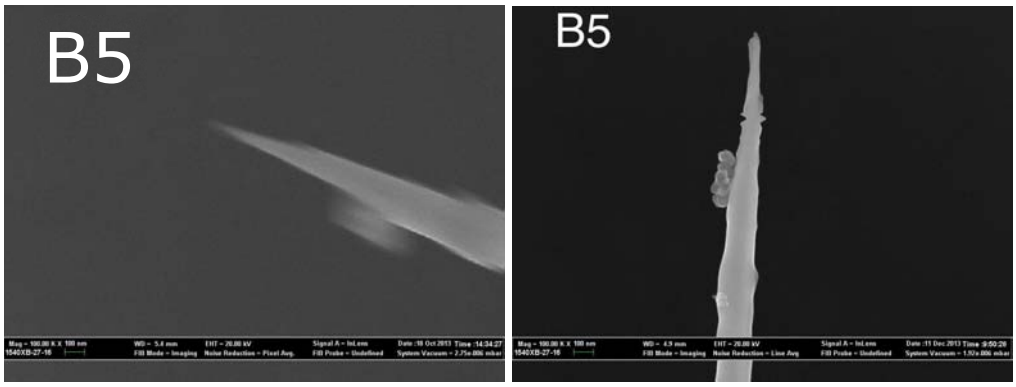

Figure B.13 – Left: SEM image of tip B5 before laser irradiation. Right: SEM image of tip B5 after laser irradiation.

Tip B6: 50 mW for 24 hour. 7 mm focus (4.19×10^{11} **W cm**$^{-2}$)

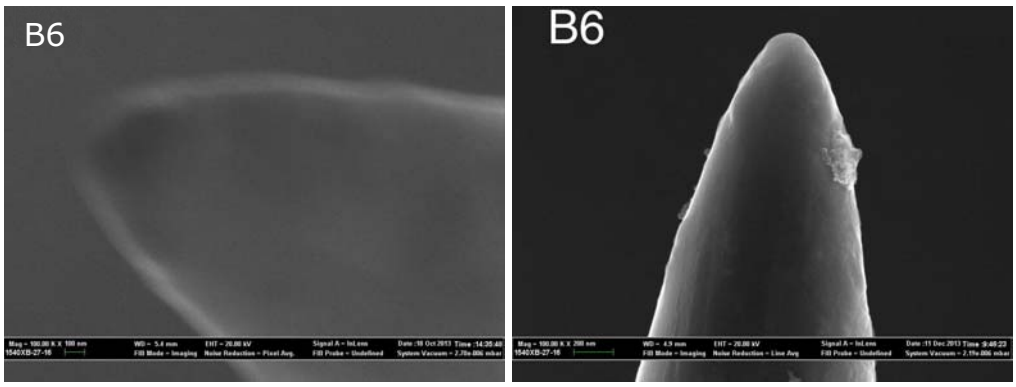

Figure B.14 – Left: SEM image of tip B6 before laser irradiation. Right: SEM image of tip B6 after laser irradiation.

Tip B7: 10 mW for 24 hour. 7 mm focus (8.38×10^{10} **W cm**$^{-2}$)

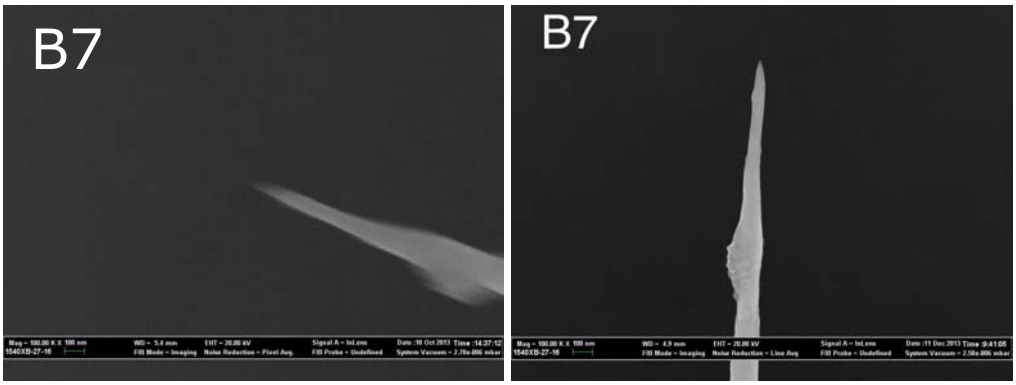

Figure B.15 – Left: SEM image of tip B7 before laser irradiation. Right: SEM image of tip B7 after laser irradiation.

Tip B8: 50 mW for 24 hour. 7 mm focus (4.19×10^{11} **W cm**$^{-2}$)

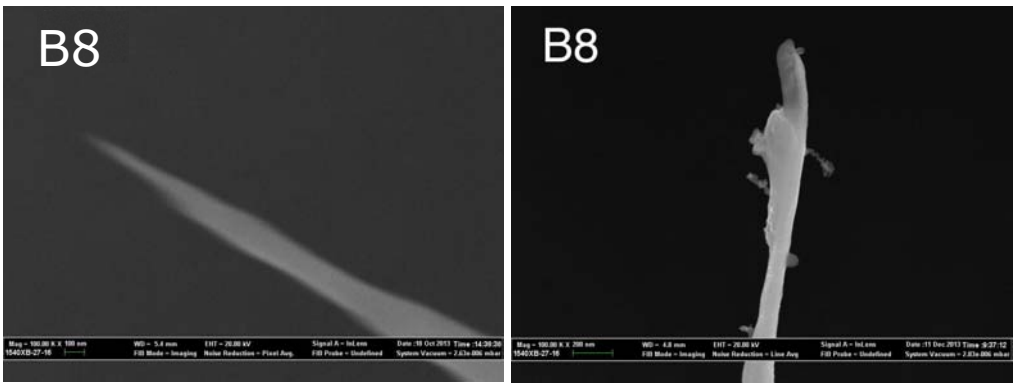

Figure B.16 – Left: SEM image of tip B8 before laser irradiation. Right: SEM image of tip B8 after laser irradiation. Possible laser damage.

Tip C1: 100 mW for 1 hour. 7 mm focus (8.38×10^{11} **W cm**$^{-2}$)

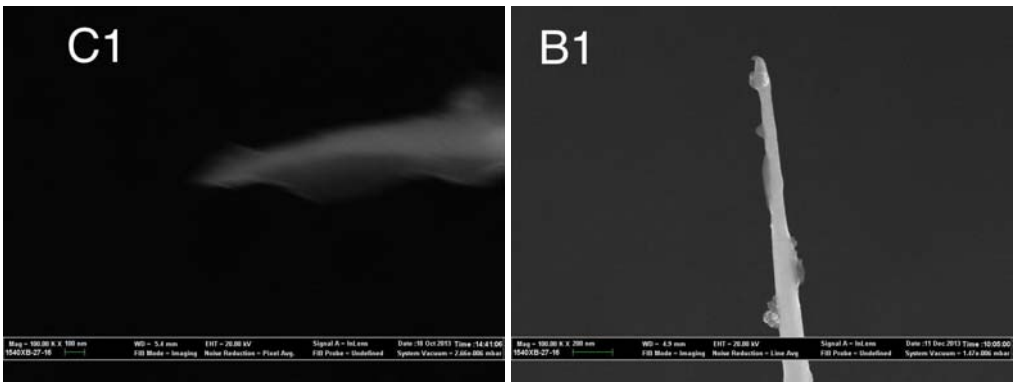

Figure B.17 – Left: SEM image of tip C1 before laser irradiation. Slight curve on end of tip. Right: SEM image of tip C1 after laser irradiation. Slight curve on end of tip.

Tip C2: 100 mW for 24 hour. 7 mm focus (8.38×10^{11} **W cm**$^{-2}$)

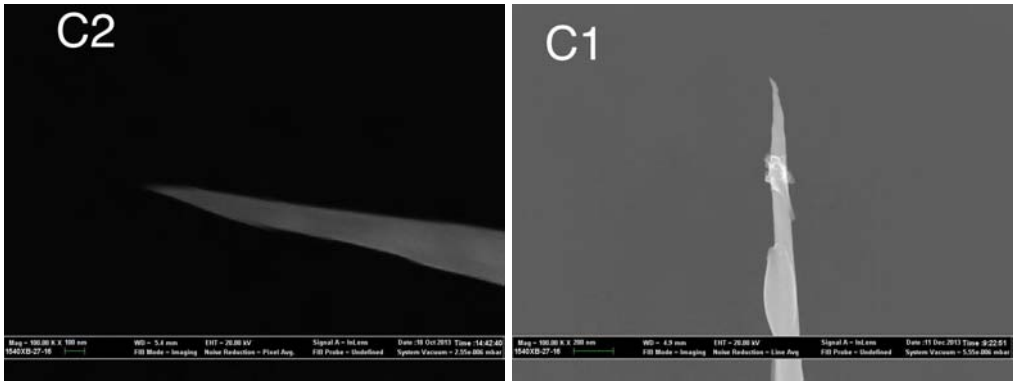

Figure B.18 – Left: SEM image of tip C2 before laser irradiation. Right: SEM image of tip C2 after laser irradiation. There is possible melted drop right below the tip, and the tip apex is slightly bent after irradiation. This is a potential indication of laser induced damage.

C

Thermal studies on CCnTs

This appendix shows the SEM images of the CCnTs before and after laser irradiation for thermal studies.

C.1 First tests: on-axis spherical focusing mirror

Table C.1 – The first set of CCnT thermal tests. Each tip was illuminated for 1 hour, with no tip bias.

tip number	average power	intensity	pulse energy
1	–	–	–
2	50 mW	4.2×10^{11} W cm^{-2}	0.8 nJ
3	10 mW	8.38×10^{10} W cm^{-2}	0.16 nJ
4	1 mW	8.38×10^{9} W cm^{-2}	0.016 nJ

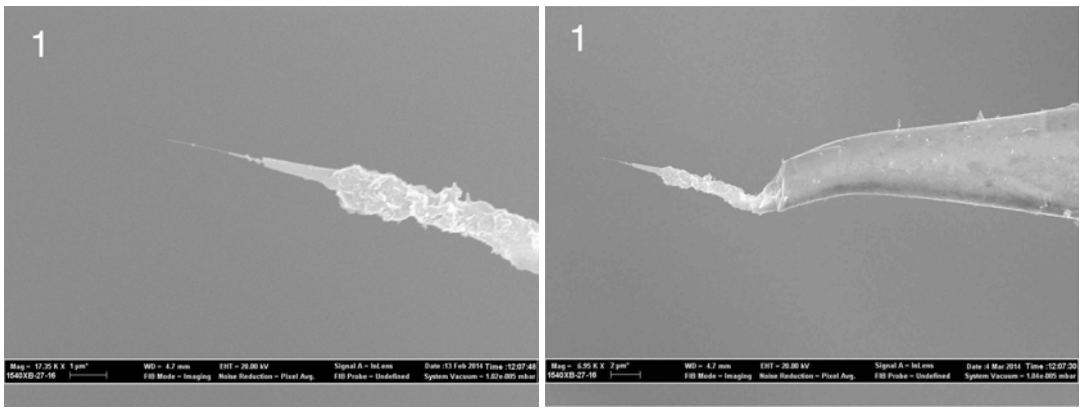

Figure C.1 – Tip 1 was not illuminated with any laser. Note the incomplete structure of the CCnT and the protruding central CNT. Left: Tip 1 before test. Right: after tests. No signs of damage

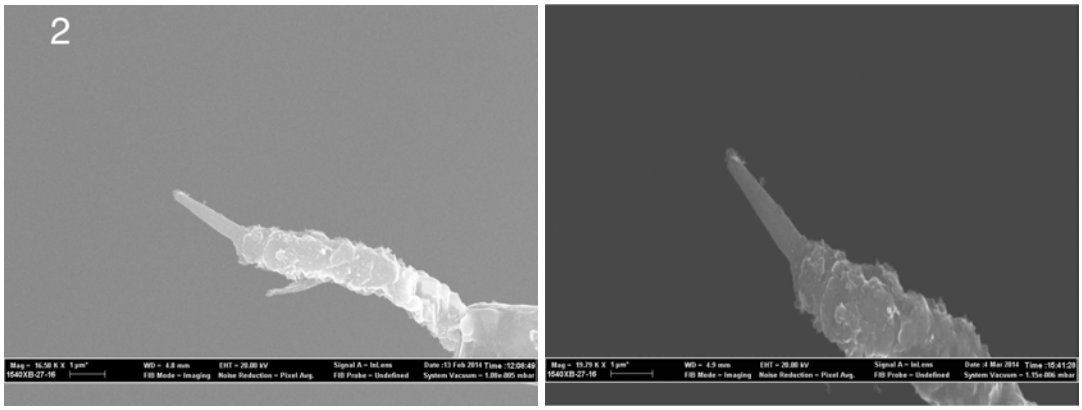

Figure C.2 – Tip 2 was illuminated with 4.2 $\times 10^{11}$ W cm^{-2} for 1 hour with no bias. Note blunted structure of the CCnT before irradiation. Left: Tip 2 before irradiation. Right: after irradiation. No signs of damage.

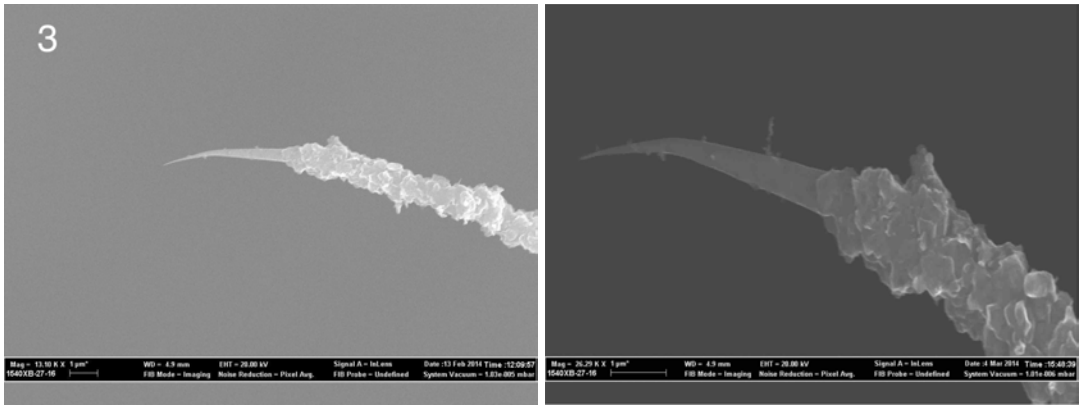

Figure C.3 – Tip 3 was illuminated with 8.38 $\times 10^{10}$ W cm^{-2} for 1 hour with no bias. Note the curved structure of the CCnT before irradiation. Left: Tip 3 before irradiation. Right: after irradiation. No signs of damage.

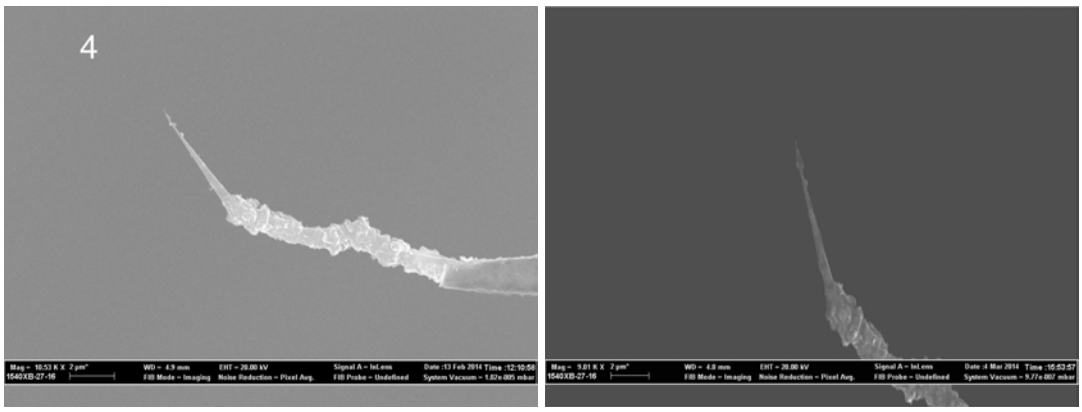

Figure C.4 – Tip 4 was illuminated with 8.38 $\times 10^{9}$ W cm^{-2} for 1 hour with no bias. Note the dust on the CCnT before and after irradiation. Left: Tip 4 before irradiation. Right: after irradiation. No signs of damage.

C.2 Second tests: off-axis parabolic focusing mirror

Table C.2 – The second set of CCnT thermal tests. Each tip was illuminated for 1 hour, with the possibility of a tip bias.

tip number	bias	average power	intensity	pulse energy
1	50 V	35 mW	9.0×10^{11} W cm^{-2}	0.57 nJ
2	50 V	10 mW	2.7×10^{11} W cm^{-2}	0.16 nJ
3	0 V	35 mW	9.0×10^{11} W cm^{-2}	0.57 nJ
4	0 V	10 mW	2.7×10^{11} W cm^{-2}	0.16 nJ

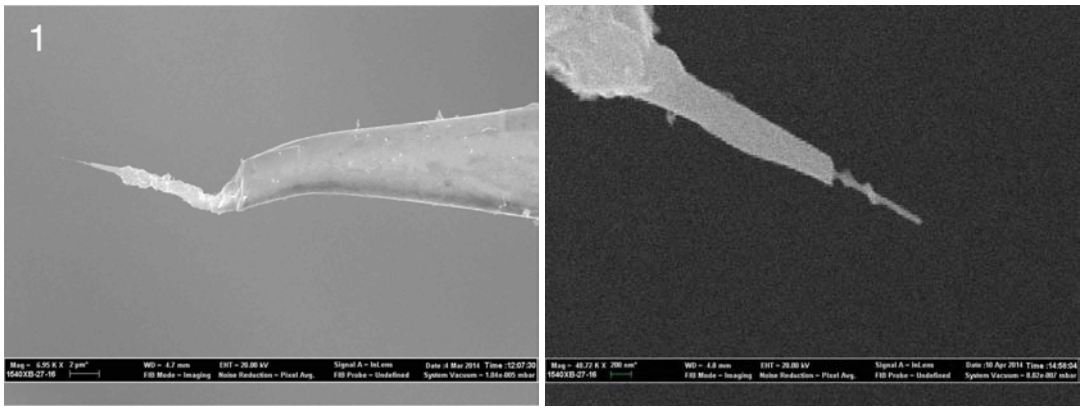

Figure C.5 – Tip 1 was illuminated with 9.0×10^{11} W cm^{-2}, with a bias of 50 V. Note the incomplete structure of the CCnT and the protruding central CNT. Left: Tip 1 before test. Right: after tests. the protruding CNT is no longer visible after irradiation.

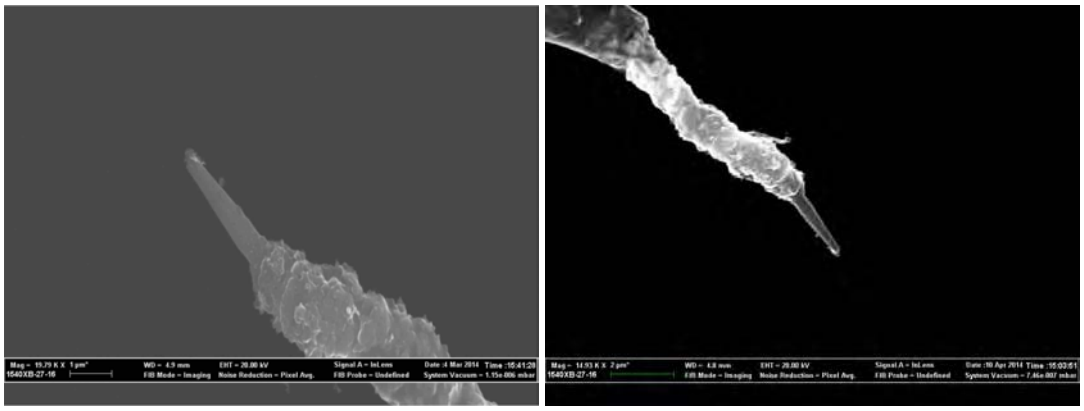

Figure C.6 – Tip 2 was illuminated with 2.7×10^{11} W cm^{-2} for 1 hour with 50 V. Note blunted structure of the CCnT before irradiation. Left: Tip 2 before irradiation. Right: after irradiation. No signs of damage.

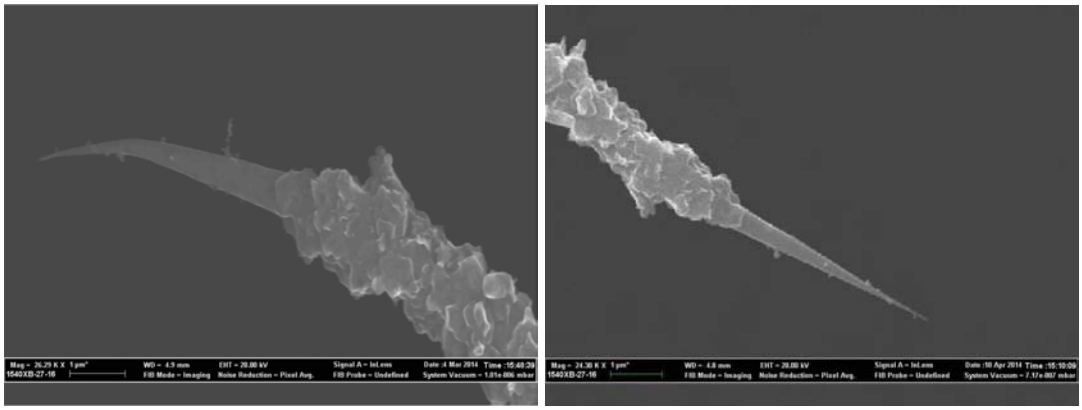

Figure C.7 – Tip 3 was illuminated with 9.0×10^{11} W cm^{-2} for 1 hour with no bias. Note the curved structure of the CCnT before irradiation. Left: Tip 3 before irradiation. Right: after irradiation. No signs of damage.

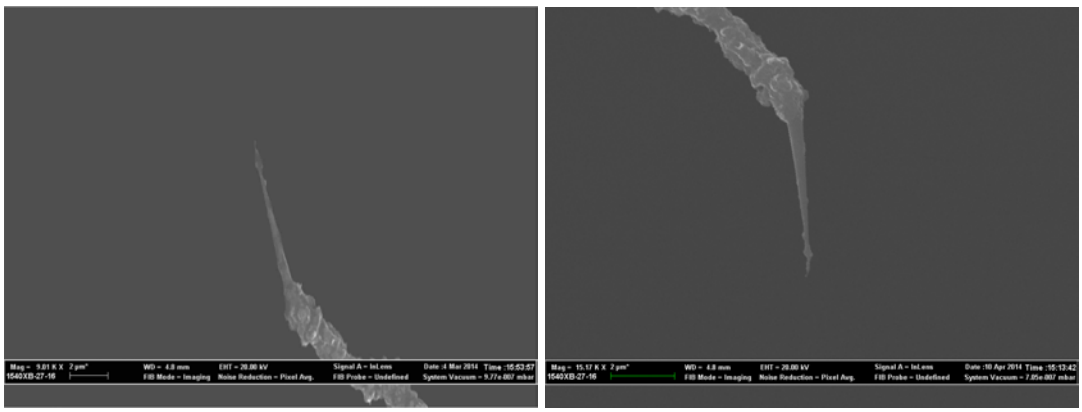

Figure C.8 – Tip 4 was illuminated with 2.7×10^{11} W cm^{-2} for 1 hour with no bias. Note the dust on the CCnT before and after irradiation. Left: Tip 4 before irradiation. Right: after irradiation. No signs of damage.

D

Résumé en français

Introduction

L'émission d'électrons d'un matériau est un problème fondamental de physique d'un grand intérêt. Comprendre les mécanismes induisant l'émission d'un électron est utile pour la compréhension des propriétés des matériaux mais aussi des processus d'interaction. Historiquement, le processus d'émission d'électrons par la lumière, l'effet photoélectrique [Einstein05], est intéressant grâce à ses applications potentielles. Avec l'arrivée des lasers, la photoémission d'électrons à partir d'une surface métallique a été systématiquement étudié [Lee73, Venus83]. Cela a conduit à l'étude de la physique des interactions entre la lumière et la matière et les phénomènes qui en découlent. Les applications potentielles comprennent des sources d'électrons pour la microscopie, des accélérateurs et des lasers à électrons libres.

Pour étendre les études de l'interaction lumière-matière en champ fort réalisées sur des systèmes en phase solide (macroscopique) ou gazeuse (microscopique), des nanopointes métalliques sont utilisées. Ces échantillons bénéficient de l'amplification locale du champ par effet de pointe. Cela signifie que le champ optique appliqué par le laser est amplifié en raison de la forme de l'échantillon, ce qui permet de diminuer la puissance laser nécessaire pour atteindre ce régime de champ fort. Les nanopointes peuvent être utilisées comme sources d'impulsions ultracourtes d'électrons avec une cohérence spatiale et temporelle élevée pour une utilisation dans des expériences d'onde de la matière [Barwick08]. Cela a des applications directes pour l'imagerie femtoseconde et sources de diffraction électronique aux temps courts.

Ma thèse concerne l'étude des mécanismes physiques qui conduisent à l'émission photo-assistée d'électrons par des impulsions laser ultracourtes à partir d'une nanopointe. Ceci est une nouvelle direction ' pour mon équipe et mon travail inclut donc le développement complet d'une nouvelle expérience pour observer et identifier ces mécanismes d'émission. Avant mon arrivée, la recherche de notre groupe était centrée sur des développements expérimentaux de protocoles de contrôle cohérent en utilisant des impulsions ultracourtes mises en forme [Monmayrant10] sur différents systèmes des atomes aux molécules aux boîtes quantiques, ainsi que dans les milieux diffusants [McCabe11]. Cette expertise dans le développement de source laser et des techniques de contrôle ajoute des paramètres que nous pouvons utiliser pour

étudier les mécanismes d'émission photo-assistée d'électron. J'ai travaillé à intégrer ces techniques à notre nouvelle expérience pour des études précises de l'interaction lumière-matière sur une nanopointe.

Les nanopointes métalliques ont une histoire longue d'utilisation comme émetteurs par effet de champ [Gomer61]. L'émission d'électrons à partir de surfaces, des atomes et des molécules a été largement étudiée depuis plus d'un siècle [Wood97, Joachain12, Agostini79, Luan89, Kupersztych01]. L'extraction d'électrons par effet de champ à partir d'un métal nécessite un champ électrique très élevé ; l'utilisation de nanopointes tire profit de leur forme pointue pour augmenter naturellement le champ appliqué. L'émission d'une nanopointe est influencée par plusieurs paramètres :

- Le rayon de la pointe et la tension appliquée déterminent le champ appliqué vu par le système [Gomer61].
- Une modification du matériau de la pointe change le travail de sortie.
- Une réponse plasmonique de certains matériaux, ou résonance de surface, qui peut être excitée quand la surface du matériau est irradié par des impulsions laser avec un longueur d'onde spécifique.

Pour étudier la physique du champ fort, des expériences d'émission de champ induite par laser à partir de nanopointes ont été réalisées depuis 2006 [Hommelhoff06b] par l'équipe de Kasevich à Stanford et indépendamment en 2007 [Ropers07] par le groupe de Ropers.

Les nanopointes sont à la frontière entre l'échelle microscopique et l'échelle macroscopique, et permettent d'observer la transition entre la physique du champ fort à l'échelle d'un atome, et celle pour une structure complexe en créant un régime unique pour l'étude des interactions lumière-matière. Ces études ont été réalisées avec des nanopointes de tungstène [Hommelhoff06b, Barwick07], d'or [Ropers07, Park12] et d'hafnium carbide (HfC) [Kealhofer12]. Les phénomènes de champ fort ont été mis en évidence par l'étude des spectres d'énergie cinétique des électrons. L'émission d'électrons multiphotonique et en particulier la photoémission au dessus du seuil (Above Threshold Photoemission ou ATP) a été observée dans plusieurs expériences [Barwick07, Ropers07, Schenk10, Krüger11, Krüger12a, Park12]. Un plateau dans le spectre d'énergie des électrons – une signature de la recollision et rediffusion des électrons sur la pointe – a été observée par [Krüger11, Krüger12b]. Une autre preuve de l'émission par effet de champ optique a été démontrée grâce aux déviations aux lois d'échelle en intensité multiphotonique du photocourant [Bormann10]. Au-delà de ces signatures de phénomènes champ fort, aucune génération d'harmoniques élevée (HHG) n'a encore été démontrée. En outre, un commentaire publié récemment dans Nature [Sivis12] conteste l'observation par Kim *et al.* [Sivis12] de la HHG assitée par une nanostructure. Jusqu'à présent, seulement des harmoniques d'ordre deux et trois ont été observées sur une nanopointe, et ce dans une configuration géométrique différente d'excitation [Bouhelier03].

Les applications utilisant les électrons émis par une nanopointe sont nombreuses. Les électrons émis ont une durée temporelle ultracourte [Hommelhoff06b, Barwick07] avec une cohérence spatiale et temporelle élevée, mesurée par la brillance de la source. Cela signifie que les nan-

pointes sont idéales comme sources pour la diffraction électronique ultra-rapide [Baum13]. Jusqu'à présent, la microscopie électronique résolue en temps [Aidelsburger10, Sciaini11, Zewail10] est basée sur l'utilisation de photocathodes avec un processus d'émission photoélectrique sur une grande surface (i.e. associée à une faible brillance). Par conséquent, il y a une demande pour des sources d'électrons de haute brillance et de durée ultracourte [Arbouet12] qui serait aussi avantageuses pour les lasers à électrons libres [Ganter08]. Ces idées commencent à être mise en pratique avec la création récente de techniques de microscopie ultrarapide assitée par une nanopointe comme un canon à électrons pulsé [Gulde14, Quinonez13, Yang10]. Les paquets d'électrons qui sont émis peuvent être accélérés [Breuer13] et peuvent être optimisé pour utilisation dans les lasers à l'électrons libres libre [Hoffrogge14] contrairement à ceux des cathodes d'une surface de cuivre de surface utilisés dans ces installations [Emma10].

Cette nouvelle expérience a pour objectif de combiner les techniques de spectroscopie électronique existantes et l'expertise de développement du laser avec des nanopointes fabriquées avec de nouveaux matériaux pour comprendre et identifier les mécanismes différents d'émission des électrons. Notre collaboration avec le groupe nanomatériaux du Centre d'Élaboration de Matériaux et d'Etudes Structurales (CEMES) nous donne accès à des nanopointes de carbone. Ces nanocône de carbone (CCnT)[Houdellier12] sont formés autour d'un nanotube de carbone unique entourée par des feuilles de graphène concentriques. Nous avons aussi étudié des nanopointes d'argent [Sasaki13, Zhang11], qui nous permettent de sonder les régimes d'émissions et les facteurs d'amplification qui sont différents de celui des émetteurs de tungstène classiques. En changeant les paramètres expérimentaux — paramètres du laser, tension appliquée, composition des pointes, etc. — nous explorons les différents régimes d'émission d'électrons.

D.1 Théorie des mécanismes d'émission d'électrons

Dans cette section, je décris les processus physiques et la théorie de l'émission d'électrons à partir d'un système métallique en général puis dans le cas particulier d'une nanopointe. L'émission est induite par plusieurs paramètres, tels que : la température, le champ électrique statique appliquée, et l'illumination du laser. L'émission des électrons a été étudiée pour comprendre les processus électroniques fondamentaux.

Nous examinons les mécanismes d'émission en fonction des paramètres suivants : la température locale du système (T [K]), le champ électrique du laser ($\mathscr{E}$ [V/m]), et le champ électrique statique (F [V/m]). Ce dernier est lié à la tension appliquée à la pointe (V_{tip} [V]) et à sa taille par la relation $F = \beta V_{\text{tip}}$ [Gomer61], avec β [m^{-1}] un facteur géométrique tenant compte de la forme de la pointe et la distance à l'anode.

Le remplissage des états d'énergie des électrons dans un système métallique peut être décrit selon la distribution de Fermi-Dirac. L'énergie de Fermi, μ, est le maximum d'énergie qu'un électron peut avoir dans un métal lorsque le système est à $T = 0$ K. On considère la barrière de potentiel $U(x)$ vue par un électron à l'interface métal-vide à la position $x = 0$, avec le métal dans le demi-espace $x < 0$ et le vide pour $x > 0$. Le travail de sortie, ϕ, est l'énergie minimum

nécessaire pour arracher un électron d'un système métallique. Ceci est équivalent a l'énergie d'ionisation nécessaire pour arracher un électron d'un système atomique ou moléculaire. Si les états électroniques sont pleins jusqu'à l'énergie de Fermi, ϕ représente l'énergie minimale que le système doit absorber pour qu'un électron puisse être arraché du métal. Le travail de sortie dépend du matériau et de son orientation (les différentes facettes d'une structure cristalline ont chacune un travail de sortie différent) ainsi que l'état de surface (des molécules adsorbées et la propreté de la surface).

Les processus d'émission sont résumés sous forme graphique dans la figure Fig. D.1. Quand on modifie les paramètres appliqués à notre système (tension appliquée V_{tip}, intensité du laser I, énergie des photons $\hbar\omega$, composition et rayon r de la nanopointe), on peut changer le processus d'émission dominant qu'on observe.

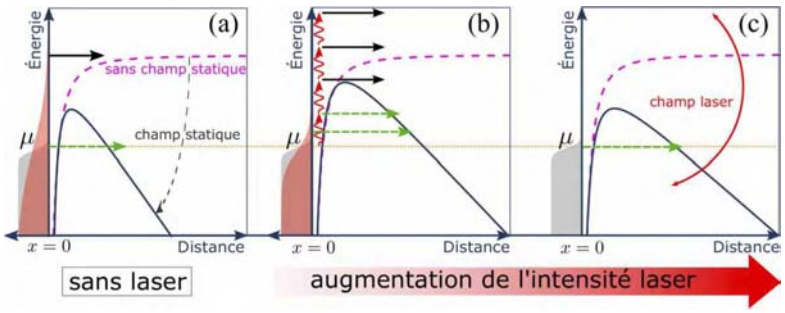

Figure D.1 – Schéma montrant les mécanismes pour l'émission d'un électron induite par laser à partir d'une interface métal-vide. Le niveau d'énergie de Fermi est μ, et la distribution de Fermi-Dirac est représentée schématiquement en gris à basse température et en rouge à température plus élevée. L'interface métal/vide est située à $x = 0$ et le potentiel $U(x)$ vu par les électrons pour $x > 0$ est représenté en bleu. (a) Émission par effet de champ (flèche verte en pointillés) et émission thermique ou thermoionique (flèche noire). Ces mécanismes ne nécessitent pas d'illumination laser. (b) Processus d'émission à faible illumination laser. Les impulsions laser peuvent être considérés du point de vue photonique. Si un nombre suffisant de photons sont absorbés, un électron peut s'échapper au-dessus de la barrière de potentiel (flèches noires), sinon un électron peut être émis par l'intermédiaire d'effet tunnel assisté par absorption d'un photon ou d'absorption thermique de l'énergie d'un photon (flèche verte en pointillés). (b) Aux intensités laser élevées, le champ laser modifie la barrière de potentiel lui-même et peut émettre des électrons par effet tunnel optique.

Il existe plusieurs mécanismes à l'origine de l'émission d'électrons à partir de nanopointe, en fonction du champ appliqué et l'intensité induite par laser sur le système. Fig. D.1 montre ces mécanismes d'émission. La distribution en énergie des électrons à basse température est représentée en gris, avec le niveau de Fermi, μ, marqué par une ligne jaune. La redistribution des énergies de Fermi due aux effets thermiques est représenté en rouge. L'interface métal/vide est située à $x = 0$. La Fig. D.1 (a) représente le cas sans laser. Le système peut être chauffé tel que les électrons peuvent obtenir une énergie suffisante pour surmonter la barrière de potentiel (flèche noire). C'est l'émission thermo-ionique décrite par l'équation de Dushman-Richardson. En appliquant un champ électrique externe suffisant, la barrière est modifié donc un électron peut passer à travers par effet tunnel (flèche verte en pointillés). C'est l'émission de champ décrite par l'équation de Fowler Norheim. Dans Fig. D.1 (b), les impulsions laser peuvent être considérées à partir de point de vue photonique. Ici, le laser a une intensité modérée et un champ externe faible à modéré peut être appliqué au système. Si un nombre suffisant

de photons sont absorbés, un électron peut s'échapper au dessus de la barrière de potentiel (émission au dessus du seuil, flèche noire). Sinon, un électron peut être émis par l'intermédiaire de l'effet tunnel assisté par l'absorption d'un photon (que nous appelons ici émission de champ photonique) ou à partir d'un niveau d'énergie plus élevé peuplé par chauffage laser du gaz d'électrons (émission de champ thermique). Aux intensités laser suffisamment élevées, le champ laser lui-même modifie la barrière de potentiel permettant l'émission d'un électron par effet tunnel pendant une fraction de cycle optique (Fig. D.1 (c)).

Les phénomènes d'émission laser décrits jusqu'à présent sont valables pour les systèmes atomiques et les surfaces métalliques [Joachain12], mais on doit considère le fait que dans cette thèse, on regarde le photoémission à partie des systèmes d'une nanopointe. En tant que tel, la géométrie de ces systèmes doit être prise en compte quand on considère le champ statique appliqué ainsi que le champ optique du laser.

Le champ optique d'un laser est fortement affecté par les nanostructures. En particulier, on parle de champ proche optique lorsque la longueur d'onde de la lumière est supérieure à la taille de l'objet. Une localisation forte des champs se produit à proximité des structures et en particulier de leurs extrémités. Typiquement nos nanopointes ont un rayon de l'ordre de $\sim$10-100 nm de diamètre, beaucoup plus petit que la longueur d'onde du laser (800 nm) qui est généralement utilisé.

Il y a trois raisons principales pour l'augmentation d'un champ optique [Thomas13] :

1. Une **augmentation du champ géométrique** provoquée par le discontinuité du constante diélectrique à l'interface métal/vide. Cela conduit à une accumulation de charge sous la surface qui crée un champ fort local en raison de la petite taille de la structure du nanoobjet. Ceci est analogue à l'effet de paratonnerre électrostatique.

2. Une **résonance d'antenne** qui se produit dans des structures dont la taille est un multiple impair de la moitié de la longueur d'onde [Thomas13, Krüger13].

3. Des **effets plasmoniques** dans des matériaux comme l'argent ou l'or. qui peuvent avoir une résonance des électrons de surface lorsque la fréquence optique est proche de la fréquence de résonance du plasmon [Sasaki13, Stockman11]. Ces résonances sont très dépendantes du matériau, de la forme du nanoobjet et de la longueur d'onde appliquée.

Cela signifie que les intensités laser typiquement nécessaires pour atteindre le régime de champ fort peuvent être réduites grâce à l'amplification du champ optique, ce qui ne rend plus nécessaire l'utilisation d'une chaine laser amplifiée.

D.2 Dispositifs optiques et développement d'un NOPA

Dans cette section, je décris le système optique développé et utilisé pendant ma thèse. Pour étudier l'émission d'électrons à partir de nanopointe induite par un champ laser, ce système doit remplir certaines conditions. On a besoin d'une durée d'impulsion courte pour obtenir une puissance crête associée élevée mais sans avoir une puissance moyenne élevée, et ainsi éviter les effets thermiques créés par le laser. On voudrait également une haute cadence du laser pour

avoir le meilleur rapport signal sur bruit possible car l'utilisation d'un objet unique ne permet pas de détecter plus d'un électron par impulsion laser. Le système laser que nous avons utilisé est passé par beaucoup évolution au cours de ma thèse : oscillateur femtoseconde, chaine laser amplifiée, et développement d'une nouvelle source à partir d'un laser femtoseconde fibré.

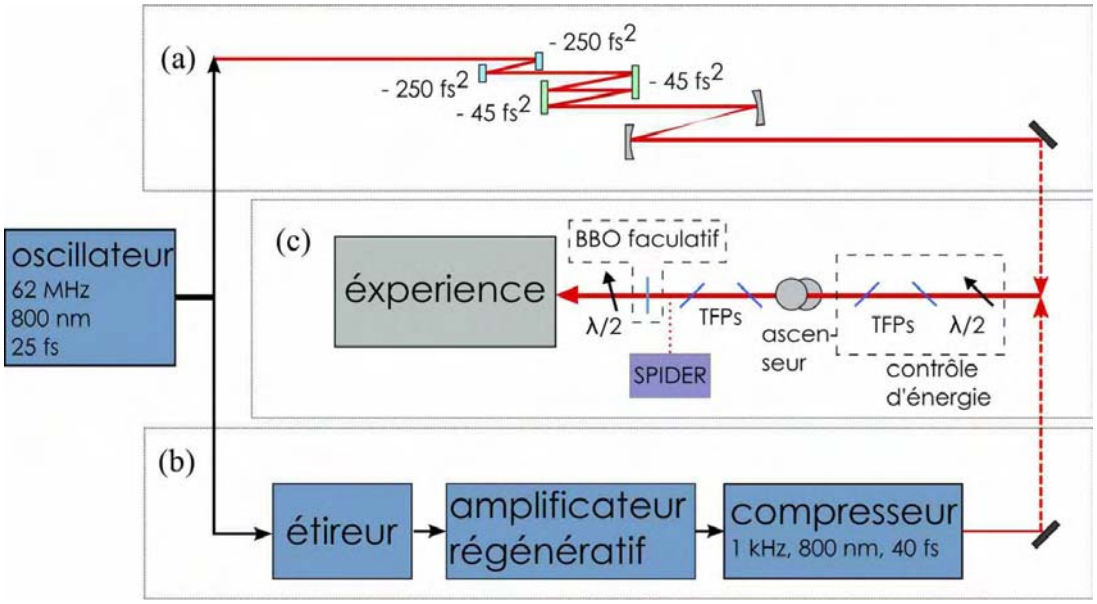

Figure D.2 – (a) La sortie directe de l'oscillateur peut être précisément contrôlée et envoyée vers l'expérience (b) ou peut être amplifiée en énergie et avec un taux de répétition réduit. (c) Le contrôle précis de la polarisation et de l'énergie déposée sur la pointe est crucial pour l'expérience. Un cristal non-linéaire facultatif peut être inséré dans le faisceau pour le doublage de fréquence la lumière. TFP : polariseur de couche mince, SPIDER : dispositif de mesure de la durée des impulsions décrit dans Sec 2.2

Nous avons mis en place un système laser flexible complètement caractérisable et contrôlable. Le premier système de laser est basé sur un oscillateur Ti :saphir classique de 800 nm qui peut aussi être utilisé dans une chaîne d'ampflication. Avec ce système, nous avons la possibilité de basculer entre un mode du puissance moyenne modérée, avec une haute cadence à 62 MHz, ainsi que un mode du puissance moyenne faible, avec une basse cadence de 1 kHz, avec la même intensité crête pour les deux modes. On a aussi la possibilité de doubler la fréquence de la sortie du laser pour produire des impulsions à 400 nm.

Un oscillateur femtoseconde commercial standard de Titane-saphir, "Femtolaser femotsource synergy", est la source de laser primaire pour les expériences à haute cadence. L'oscillateur a un taux de répétition de 62 MHz, avec une longueur d'onde centrale de 800 nm et une bande passante spectrale de largeur environ 70 nm à mi-hauteur (fwhm) correspondant à une durée d'impulsion de $\sim$20 fs. La puissance moyenne totale disponible à la sortie de l'oscillateur est $\sim$ 360 mW ce qui correspond à une énergie par impulsion de 5,8 nJ.

Quand on utilise le faisceau de l'oscillateur (Fig. D.2 (a)), l'énergie d'impulsion (ou puissance moyenne), la polarisation, la durée et la dispersion (chirp) sont attentivement réglées et contrôlées pendant toute l'expérience. La dispersion inhérente de l'oscillateur ainsi que toute dispersion supplémentaire ajoutée par les matériaux optiques et le hublot de la chambre expé-

rimentale sont mesurées avec un SPIDER (décrit dans Sec. 2.2) et pré-compensées avec des paires de miroirs à dispersion négative. La puissance est réglée avec une lame demi-onde et un polariseur de couche mince (TFP) avec un taux d'extinction de $\sim$ 200 :1. La polarisation du faisceau est nettoyée avec un autre polariseur TFP et ensuite choisie avec une lame demi-onde avant que les impulsions laser ne soient envoyées vers l'expérience. Pour minimiser la dispersion et maintenir la durée courte des impulsions, toutes les optiques utilisées sont réfléchissantes quand cela était possible (miroirs plans et sphériques, etc.), et sinon, le plus mince possible (polariseurs TFP, lame demi-onde d'ordre 0 (femtolaser), etc.).

Alternativement, la sortie de l'oscillateur peut être envoyée vers la chaine d'amplification (amplificateur régénératif ou regen) (Fig. D.2 (b)). Un regen marche d'une manière similaire à une cavité laser [Barty96, Wynne94]. Pendant l'étape d'amplification, les impulsions de quelques femtosecondes générées à partir de l'oscillateur sont étirées temporellement jusqu'à quelques centaines de picosecondes. L'impulsion étirée de faible énergie, est injectée dans la cavité en utilisant une cellule de Pockels et fait plusieurs allers-retours à travers le milieu à gain (généralement Ti :saphir). Enfin, elle sort de la cavité par une autre cellule de Pockels. L'impulsion de haute énergie est ensuite recomprimée jusqu'à sa durée limitée par transformée de Fourier. Cela nous permet d'avoir des impulsions avec une énergie de l'ordre de 350 μJ, avec un taux de répétition de 1 kHz, et une durée des impulsions autour de 40 fs, avec une limite de Fourier de 35 fs. Bien que seuls quelques nJ d'énergie soient nécessaires pour l'émission d'électrons à partir de nanopointe, les impulsions de plus haute énergie pourraient nous permettre de manipuler les impulsions avec des dispositifs de mise en forme temporelle et de conversion en longueur d'onde. Le taux de répétition relativement bas permet de s'affranchir des effets thermiques potentiels dans la nanopointe, dus au dépôt de puissance moyenne modérée.

Table D.1 – Résumé des caractéristiques des différents modes defonctionnement du laser utilisés et accessibles pour l'expérience.

	taux de répétition (R)	**longueur d'onde centrale**	**bande passante spectrale**	**durée impulsion**	**énergie d'impulsion (avant compresseur)**	**puissance crête (avant la chambre)**
oscillateur	62 MHz	800 nm	70 nm	20 fs	5.8 nJ	1.9×10^5 W
Regen	1 kHz	800 nm	30 nm	40 fs	350 μJ	5.3×10^9 W
NOPA (now)	1 kHz – 1 MHz	700 nm	44 nm	45 fs	low R : 0.27 μJ	1.7×10^6 W
					high R : 14 nJ	8.8×10^5 W
		750 nm	67 nm	40 fs	low R : 0.15 μJ	9.4×10^5 W
					high R : 11 nJ	6.9×10^4 W
		800 nm	84 nm	35 fs	low R : 0.08 μJ	5.0×10^5 W
					high R : 4 nJ	2.5×10^4 W
NOPA (ideal)	single shot – 2 MHz	700-850 nm	$\sim$100 nm	$\sim$10 f	10s nJ	$\sim 10^5$ W

Pour pouvoir étudier plus précisément les effets du taux de répétition et de la longueur d'onde sur l'émission d'électrons dans la nanopointes, nous avons acquis un système laser fibré infrarouge (1030 nm) qui permet une variabilité des taux de répétition, du tir unique à plusieurs dizaines de MHz, tout en conservant la même puissance crête (Tangerine, Amplitude Systèmes). L'inconvénient d'un tel système est la longue durée d'impulsion, de 300 fs. Pour avoir

accès à la courte durée d'impulsion nécessaire, nous avons construit un étage d'amplification paramétrique optique non colinéaire (NOPA) à la sortie [Cerullo03]. Cette source laser a deux possibilités de réglage fin en longueur d'onde et en taux de répétition, ainsi qu'une sortie de puissance suffisante de de courte durée.

Un résumé des caractéristiques des impulsions pour les différents modes laser se trouve dans Tab. D.1.

D.3 Dispositif expérimental

La nanopointe est montée dans une chambre à ultra-vide (UHV) et éclairée par une source laser ultracourte très focalisée décrite dans la section précédente et dans le chapitre 2. Les électrons émis sont ensuite détectés avec un spectromètre d'électrons à champ retardé, avec la possibilité d'une détection résolue spatialement. Cette configuration a été entièrement développée au cours de mon travail de thèse. Le dispositif expérimental a subi plusieurs évolutions pendant ma thèse. D'une manière générale, la configuration est très polyvalente, et utilise de nombreux éléments différents : lasers, manipulation nanométrique de la nanopointe détection d'électrons, technologies sous vide et logiciels fait maison pour l'acquisition de données.

Pour la recherche de ma thèse, j'ai utilisé 3 types de nanopointes : nanopointes de tungstène que j'ai fabriquée au CEMES ; cônes de carbone qui ont été faites au CEMES par Aurélien Masseboeuf ; nanopointes et d'argent qui ont été faites par Ivan Blum au GPM de Rouen.

Chaque pointe nécessite une procédure de montage différente dans notre chambre à ultravide. Les pointes sont positionnées dans la focalisation du laser avec des platines de translation nanométriques dans les trois dimensions. Les électrons émis sont détectés dans un spectromètre à champ retardé fabriqué au laboratoire avec une résolution relative de $\sim 5 \times 10^{-2}$, et une transmission de ~ 60 %. Cet appareil nous permet de récupérer des spectres d'électrons intégrés à partir desquels nous pouvons résoudre l'énergie cinétique des électrons. Le spectromètre peut aussi se déplacer dans les deux dimensions transverses grâce à des platines de translation. Ceci permet des mesures résolues spatialement (similaires au « field emission microscopy » FEM).

La version finale du montage expérimental est composée de :

- une paire de miroirs paraboliques pour focaliser le laser et le recollimater.
- des platines de nanopositionnement pour positionner la nanopointe dans le foyer du laser.
- un spectrométre et diaphragme en cuivre à l'entrée. Ces éléments bougent ensemble pour être alignés sous la pointe à l'emplacement d'émission maximale pour des mesures de spectre d'électrons intégrée, et peuvent également être translatés pour faire une carte 2D d'émission des électrons

On peux voir un schéma du montage expérimental dans la figure D.3.

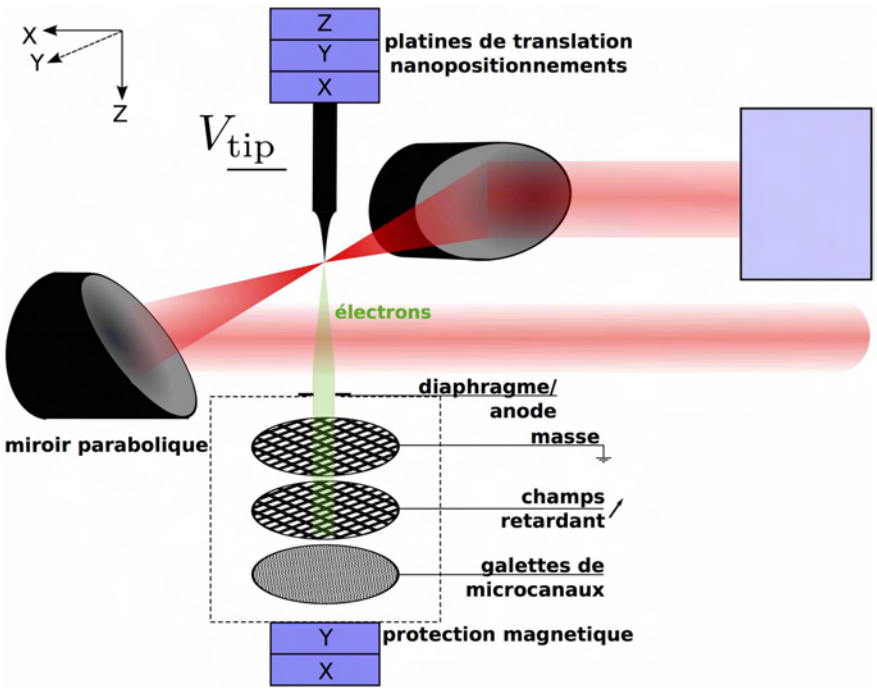

Figure D.3 – Schéma de la version finale du montage expérimental. Adapted from Ultramicroscopy, doi :10.1016/j.ultramic.2014.11.027, M. R. Bionta *et al.*, "First results on laser-induced field emission from a CNT-based nanotip", Copyright (2014), with permission from Elsevier. [Bionta14b]

D.4 Résultats avec une nanopointe de tungstène

Le tungstène (W, numéro atomique 74) est un matériau robuste avec une longue histoire d'utilisation comme un émetteur pour les systèmes d'émission par effet de champ et d'ionisation due à son point de fusion élevé de 3695 K [Gomer61, Good Jr56]. L'émission induite par laser d'une nanopointe de tungstène a été étudiée depuis une dizaine d'année[Hommelhoff06b, Schenk10, Barwick07, Hommelhoff06a, Yanagisawa10] et fournit une base de référence que nous pouvons comparer à notre nouveau dispositif expérimental.

Nous avons plusieurs de méthodes de caractérisation *in situ* de la pointe. En utilisant des graphes de Fowler-Nordheim (FN), nous pouvons calculer le rayon de la pointe. L'équation FN (Eq 1.19) et les graphes résultant nous permettent une méthode simple pour relier le courant d'émission au rayon de l'apex de la pointe en fonction de la tension appliquée. En appliquant le facteur d'amplification du champ statique d'une nanopointe ($F = \beta V$, Eq. 1.29), à l'Eq. 1.19, nous voyons que le courant émis $J(V)$ est dépendante de la tension appliquée à la pointe V. Nous utilisons la pente de ces graphes de vérifier que le rayon de la pointe reste le même au cours de nos expériences. Les rayons typiques des pointes que nous fabriquons sont de l'ordre de 250 nm pour les pointes de tungstène polycristalline (PCW) et 30 nm pour les pointes monocristalline (SCW(310)).

Nous utilisons également des cartes "FEM" pour étudier les cartographie de l'émission de champ de la pointe, en repérant les différents sites d'émission. Nous comparons ces sites d'émission pour les pointes de polycristallines et monocristallines. Pour ces dernières, il n'y a effectivement qu'un seul site d'émission, qui est dirigé vers le détecteur.

Le seuil de dommages des nanopointes à partir de l'irradiation du laser ont été empiriquement étudié. Ces tests n'ont pas été concluants.

L'émission d'électrons induite par le laser est très dépendante de la polarisation. Nous avons utilisé des courbes de dépendance de l'émission d'électrons en fonction de la polarisation pour vérifier l'alignement de la pointe dans le foyer de focalisation du laser. En effet, l'émission par effet de champ photonique dépend uniquement de la composante du champ électrique de laser qui est perpendiculaire de la surface [Venus83]. À l'apex de la pointe, il s'agit de la composante parallèle à l'axe de la pointe. Par ailleurs, l'amplification du champ optique, en raison de la taille du sous-longueur d'onde de la nanopointe, est plus grande pour des polarisations parallèles à l'axe de la pointe. Par contre, l'émission d'électrons thermiques induite par laser est plus efficace pour la polarisation perpendiculaire à l'axe de la pointe [Barwick07, Hadley85].

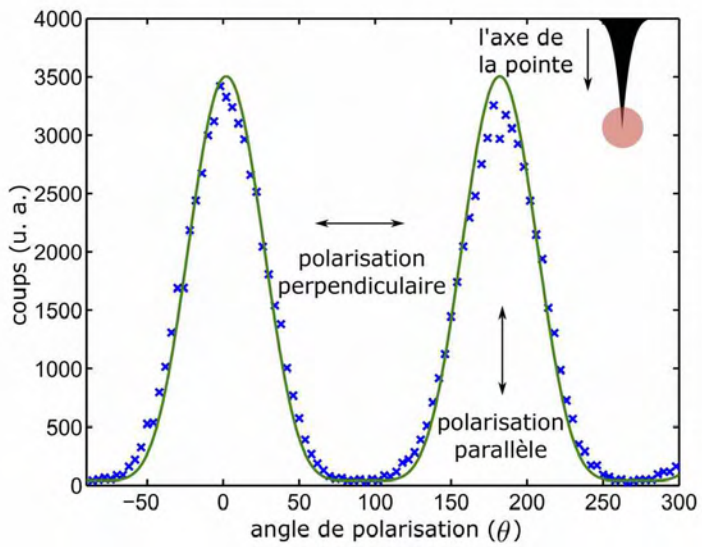

Figure D.4 – Nombre d'électrons en fonction de la polarisation du laser (θ) par rapport de l'axe de la pointe. Les polarisations parallèles à l'axe de pointe (angles de polarisation de 0 et 90) conduisent à l'émission d'électrons la plus forte. Par contre, des polarisations perpendiculaires (angles de 180 et 270) ont des émissions négligeables. Les données expérimentales (x bleus) sont ajustées à une courbe de la forme $\cos^{2n}(\theta)$ (ligne verte). Adapted with permission from [Bionta14a].

La dépendance en polarisation d'une pointe bien alignée est décrite dans la dans la figure 4.6 [Bionta14a]. La production d'électrons maximale a lieu pour des angles de polarisation de 0 et 180, et est minimale à 90 et 270 et un contraste de ∼3500 : 1.

Pour des champs laser modérés, le courant d'électrons émis est proportionnel à l'intensité du laser avec un exposant η ($J \propto I^{\eta}$, Eq. 1.26). Cela signifie que pour les régimes multiphotoniques (l'émission par effet de champ photonique et la photoémission au dessus du seuil ou ATP), si le système absorbe n photons avant qu'un électron ne soit émis, nous nous attendons à l'exposant η soit égale à n, où n est le nombre de photons absorbés. La moyenne d'énergie des électrons sera alors $\eta\hbar\omega - \phi$. η est la moyenne des photons absorbé pour l'ensemble des contributions des différents nombre de photons absorbés pour les électrons qui sont émis

par le système. La dépendance en puissance du laser nous donne donc le nombre moyen de photons absorbés par le système avant l'émission d'électrons. Pour mesurer ce facteur η, on fait varier l'intensité du laser de 3,8 à 11,4 $\times 10^{11}$ W cm^{-2} (puissance moyenne de 50 à 150 mW) avec V_{tip} = 50 V. Une dépendance exponentielle est clairement visible. En traçant en échelle logarithmique, cela devient une relation linéaire à partir de laquelle nous pouvons faire un ajustement linéaire. La pente de cette droite nous montre que $\eta = 2,9$. Comme le tungstène polycristallin (PCW) a un travail de sortie de $\phi = 4,5$ eV, et que l'énergie des photons à 800 nm est 1,55 eV, nous voyons que le facteur η extrait est très proche de $\phi/\hbar\omega = 2,9$, en indiquant l'émission sur le seuil. Nous trouvons une diminution de ce nombre quand la tension appliquée augmente, en raison de l'effet Schottky (réduction du travail de sortie du au potentiel image en présence d'un champ statique appliqué). Nous pouvons également utiliser les courbes de dépendance en polarisation pour déterminer ce facteur η à l'aide d'une courbe d'ajustement du type $\cos^{2\eta}\theta$. Dans la courbe de la figure 4.6, on trouve une valeur de 2,8 pour cet exposant.

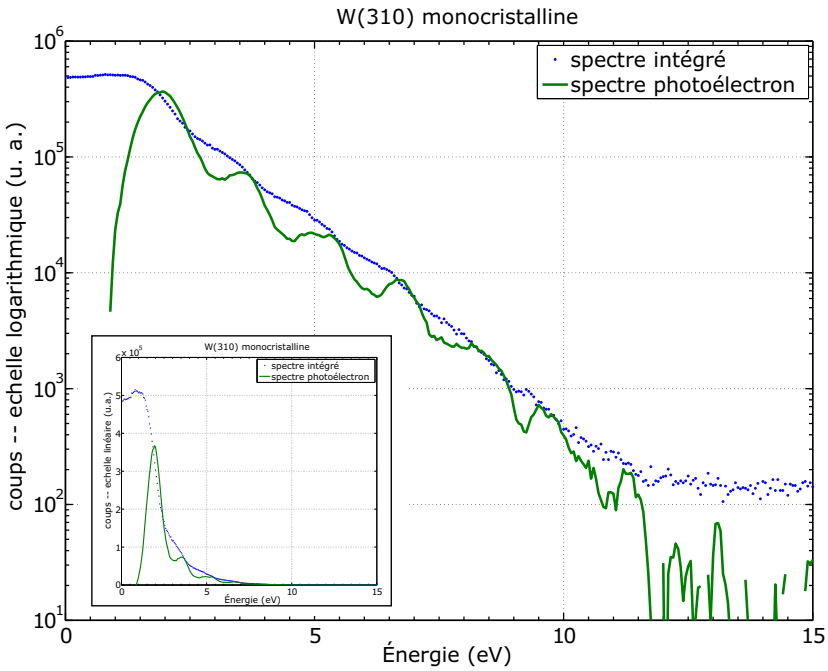

Figure D.5 – Cela montre les spectres de photoélectrons à partir de nanopointe de W(310). Pour ce spectre une tension d'extraction de V_{tip} = 20 V, et une puissance laser de 50 mW (0,8 nJ/pulse, $1,52 \times 10^{12}$ W cm^{-2} puissance crête) a été utilisé. La sortie du spectromètre directe, une spectre intégré, est représentée par des points bleus. Le spectre de photoélectrons résolu cinétiquement et représenté par la ligne verte. Remarquez que les pics d'ATP jusqu'à l'ordre $n = 9$ sont facilement observables dans le spectres/ L'insert montre les spectres en échelle linéaire. Seuls les quatre premiers pics d'ATP sont facilement résoluble dans cette échelle ; il est donc bénéfique pour tracer les spectres en échelle logarithmique.

Fig. D.5 montre un spectre de photoélectrons à partir de nanopointe W(310). Pour ce spectre une tension d'extraction de V_{tip} = 20 V, et une puissance laser de 50 mW (0,8 nJ/pulse, $1,52 \times 10^{12}$ W cm^{-2} puissance crête) ont été utilisées. L'énergie cinétique ajoutait de la V_{tip} appliqué a été soustraite. L'insert de Fig. D.5 montre les spectres en échelle linéaire. Dans le spectre de photoélectrons, les pics sont superposées sur la décroissance exponentielle glo-

bale de l'émission d'électrons. Les pics sont séparés par 1,55 V correspondant à des pics de la photoémission au dessus du seuil (ATP).

Le dépendances en puissance résolues cinétiquement ont été mesurées pour chaque pic ATP individuellement jusqu'à un ordre de photons de $n = 6$. Le premier pic correspond à un ordre de photons de 3, parce qu'il faut trois photons pour surmonter la barrière de potentiel.

Nous avons confirmé que chaque pic correspond à un nombre différent de photons absorbés. Les résultats sont présentés dans la Fig. D.6 pour une expérience avec $V_{\text{tip}} = 30$ V et les puissances crêtes laser de 1 à 3,6 $\times$ 10^{11} W/cm^2. Chaque pic est indiqué par la même couleur sur les trois graphes. Fig. D.6 (a) montre le spectre d'énergie enregistrée à 3,6 $\times$ 10^{11} W/cm^2, où les pics différents d'ATP sont identifiés par des couleurs différentes. Fig. D.6 (b) montre le taux de comptage d'électrons par rapport à l'intensité du laser tracé en échelle logarithmique. Chaque droite correspond à la totalité des électrons d'un pic du spectre tel que défini dans Fig. D.6 (a). Nous calculons l'exposant de chaque pic d'énergie comme la pente de la courbe d'ajustement pour chaque droite. Fig. D.6 (c) montre les exposants de puissance extraits pour les quatre pics, avec des barres d'erreur.

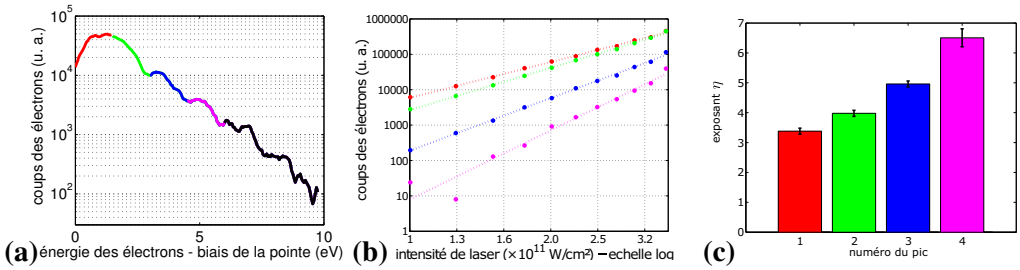

Figure D.6 – (a) Un spectre d'énergie électronique obtenue pour V_{tip} = 30 V et une intensité laser de $3,6 \times 10^{11}$ W cm^{-2}. Les différents pics ATP sont identifés par des couleurs différentes. (b) Nombre d'électrons en fonction de l'intensité laser tracée pour chaque pic ATP. Les points sont les données expérimentales et les lignes sont les courbes d'ajustement desquelles nous calculons l'exposant. (c) Les exposants de puissance pour chaque pic du spectre. Comme prévue pour l'ATP, on obtient des exposants 3–6. Adapted with permission from [Bionta14a].

Comme prévu pour l'ATP, chaque pic correspond à un nombre différent de photons absorbés, c'est-à-dire un exposant différent. Le premier pic est proche de 3 (3,4 $\pm$ 0,1), car le travail de sortie du tungstène polycristallin ($\phi = 4,5$ eV) est presque égale à 3 fois l'énergie des photons ($3 \times 1,55$ eV $= 4,65$ eV). Les deuxième, troisième et quatrième pics ont des exposants respectifs de 4,0 $\pm$ 0,1, 5,0 $\pm$ 0,1, and 6,5 $\pm$ 0,3, ce qui montre que, dans cette partie du spectre, le système absorbe 4, 5 et 6 photons avant que l'électron soit émis. Cela confirme que dans notre cas, l'émission de photoélectrons est principalement due à l'absorption multiphotonique, sans aucune contribution de l'émission par effet de champ photonique.

Les expériences sur le tungstène nous permettent de valider notre dispositif expérimental en comparaison des résultats qui sont déjà établis par d'autres groupes. Nous avons également pu nous familiariser avec le nouveau dispositif expérimental ainsi que les techniques pour travailler avec des nanoobjets. Avec une compréhension correcte de nos résultats et de la configuration expérimentale, nous pouvons commencer à étudier des nouvelles nanopointes.

D.5 Résultats avec un nanocône de carbone

L'investigation de l'émission d'électrons à partir de nouveaux matériaux comme les nanotubes de carbone a donné des propriétés intéressantes pour l'émission par effet de champ. Ces nouveaux échantillons ont une structure et des propriétés électroniques très différentes des nanopointes métalliques classiques. Nous avons utilisé ces nanopointes car elles ont démontré des propriétés mécaniques et électriques excellentes pour l'émission par effet de champ. Elles sont donc prometteuses pour l'observation du phénomène de champ fort en résultant de l'interaction laser-pointe.

Notre collaboration avec CEMES nous permet d'accéder à ce nouveau type de nanopointe formée autour d'un nanotube de carbone unique, entouré de feuilles de graphène concentriques pour former une forme conique. Ces pointes sont appelées nanocônes de carbone (Carbon Cone nanoTip, CCnT). Des études vastes sur les émission par effet de champ à partir de ces pointes peuvent être trouvés dans [deKnoop14, Houdellier12, Houdellier15]. Les mécanismes à l'origine de l'émission d'électrons à partir de ces pointes sont inconnus et nous étudions les propriétés de l'émission induite par laser de ces nanopointes à base de carbone.

Nos collaborateurs du CEMES se concentrent sur la synthèse des pointes ainsi que l'étude des propriétés d'émission par effet de champ dans l'objectif d'utiliser ces pointes comme une source d'électrons pour la microscopie électronique. Notre groupe vise à étudier l'interaction d'une telle pointe avec un champ laser pour étudier les propriétés des émissions induites par laser à partir d'une CCnT.

Le CCnT est une pointe basée sur une forme conique de carbone. Ces pointes ont un travail de sortie de $\phi = 5$ eV [Houdellier12], et un diamètre d'apex de quelques nm. Le centre du cône est un nanotube de carbone multifeuilles (CNT) unique, entourée par des feuilles de graphène concentriques pour donner une forme conique. Le CNT central a un diamètre de $\sim$2 nm.

L'image de gauche de la figure D.7 montre la structure du nanocône. Comme décrit dans les Secs. 3.1.2 et 5.1, les cônes sont initialement formés à chaque extrémité d'un court segment de microfibre de carbone. Cette microfibre est fabriquée par un procédé de dépôt chimique en phase vapeur développé au CEMES. Après avoir été coupée, la microfibre de carbone est soudée sur une pointe de tungstène dans un FIB (Focused Ion Beam). Ce processus de développement unique permet aux CCnT d'exposer certains paramètres qui sont importants pour nos expériences. Cela comprend un ratio d'aspect élevé du CCnT, qui peut être plus pointu que des pointes métalliques classiques tels que le tungstène ou l'or, et une taille d'apex plus petite qui donne une amélioration de champ plus élevée au voisinage de la pointe.

Nous avons essayé d'utiliser des courbes de FN pour extraire le rayon de l'apex de nos CCnTs, mais lla valeur obtenue n'était pas en accord avec la taille observée dans les images de SEM et TEM. Ceci est probablement parce que les hypothèses utilisées pour l'amplification géométrique et la fonction de Nordheim ne sont plus valables. Néanmois, nous pouvons toujours utiliser la pente α/β des courbes de FN pour s'assurer que la pointe garde le même diamètre. Les images FEM ont confirmé un site d'émission unique des CCnTs.

Nous avons donc étudié les effets de l'irradiation laser sur les CCnTs. Alors que les effets de

l'émission d'électrons étaient compréhensibles pour une faible puissance moyenne, nous avons observé la destruction de la pointe à puissance moyenne modérée. Des études méthodiques sur le seuil de dommage de CCnTs ont été effectuées. Nous avons observé des dommages pour des pointes irradiées avec $9,0 \times 10^{11}$ W cm^{-2} pendant 30 minutes comme on le voit dans le Fig. D.7. Mais, beaucoup de nos études systématiques ont été peu concluantes. Par la suite, nous avons limité nos intensités laser à moins de 7,7 $\times$ 10^{11} W cm^{-2}.

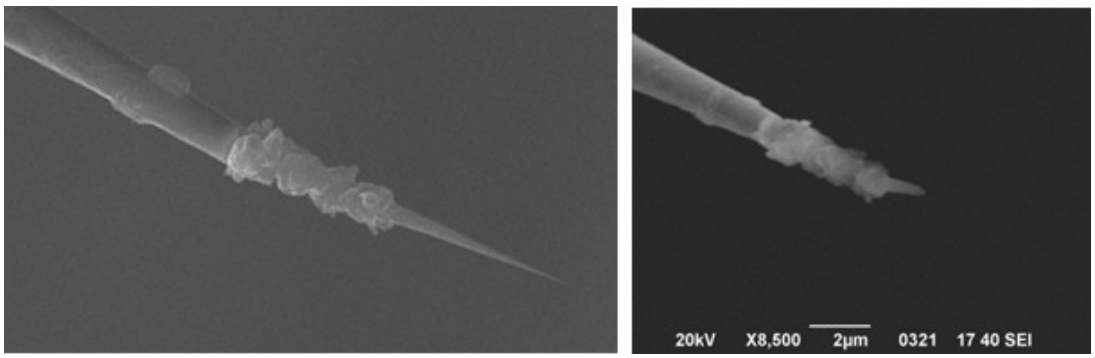

Figure D.7 – L'image de gauche montre le CCnT avant l'irradiation du laser. L'image de droite montre le même CCnT après avoir été éclairé par $7,7 \times 10^{11}$ W cm^{-2} d'intensité laser (0,48 nJ/impulsion, 30 mW puissance moyenne) pendant 30 minutes. Adapted from Ultramicroscopy, doi :10.1016/j.ultramic.2014.11.027, M. R. Bionta *et al.*, "First results on laser-induced field emission from a CNT-based nanotip", Copyright (2014), with permission from Elsevier [Bionta14b].

À faible puissance laser, la dépendance de l'émission d'électrons par rapport à la polarisation laser a donné un bon contraste et une courbe d'ajustement avec un exposant n = $3,4$. Ceci est en bon accord du nombre minimum de photons absorbés $n_{\text{min}} = 3,2$ pour surmonter le travail de sortie $\phi = 5$ eV du CCNT. Les spectres de photoélectrons pour des intensités laser modérées ont des formes plus étroites que celles pour des intensités similaire sur le tungstène, indiquant des effets thermiques possibles.

La figure D.8 montre un spectre d'électrons émis à partir d'un CCnT. Le CCnT était éclairé avec une intensité laser modérée de 5,13 $\times 10^{11}$ W cm^{-2} (0,3 nJ/impulsion, 20 mW puissance moyenne), et une tensions appliquée sur la pointe V_{tip} de 50 V.

Même si l'exposant laser non linéaire indique une absorption de photons suffisamment pour surmonter la fonction barrière de travail, ce spectre ne montre aucun signe de des pics de photoémission au dessus du seuil. L'étroitesse du spectre indique que l'émission peut être causée par des effets thermiques à haute cadence du laser comme l'émission par effet de champ assistée thermiquement, ou des mécanismes plus complexes comme l'ATP à partir d'un gaz d'électrons excités thermiquement dans lequel la température brouille la signature des pics ATP (i.e. si $k_B T \sim \hbar\omega$).

Nos essais d'augmenter l'intensité du laser pour mesurer la production des électrons en fonction de la puissance du laser pour extraire un η ont été infructueuses comme nous avons endommagé la pointe.

Contrairement à nos hypothèses initiales sur les caractéristiques des CCnTs, il a donc été difficile d'observer des phénomènes de champ fort à partir d'une interaction du laser avec

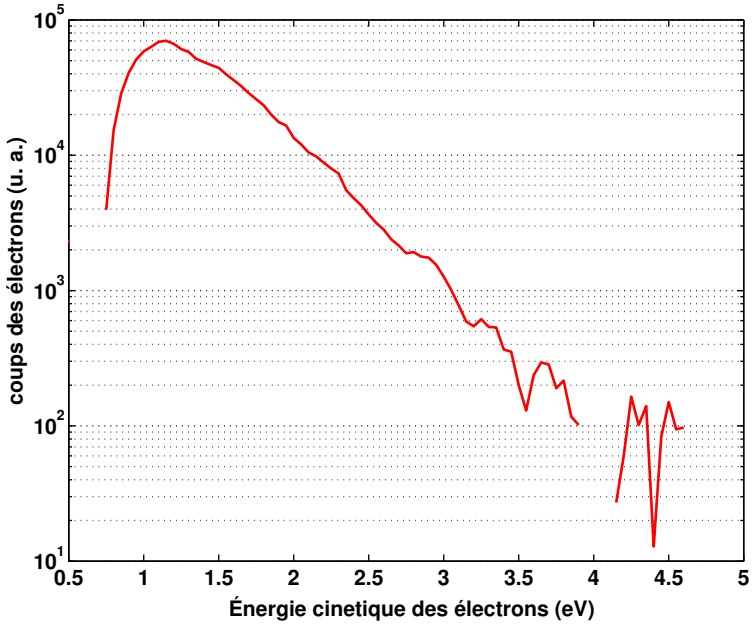

Figure D.8 – Spectre d'énergie des photoélectrons émis d'un CCnT éclairé avec une intensité laser modérée de 5,13 $\times 10^{11}$ W cm^{-2} (0,3 nJ/impulsion, 20 mW puissance moyenne), et une tension V_{tip} de 50 V. Adapted from Ultramicroscopy, doi :10.1016/j.ultramic.2014.11.027, M. R. Bionta *et al.*, "First results on laser-induced field emission from a CNT-based nanotip", Copyright (2014), with permission from Elsevier [Bionta14b].

un CCnT, en dépit de leurs meilleures propriétés mécaniques et électriques par rapport aux nanopointes métalliques classiques. À faible puissance laser moyenne, les CCnTs émettent de façon similaire à ce que nous avons observé avec des pointes de tungstène ; toutefois, les hautes puissances moyennes ont conduit à une destruction des pointes. Nous avons envisagé les explications suivantes sans être certains de leur validité. Bien que l'interface entre la fibre de carbone et de la pointe de tungstène est supposée être une "soudure" tungstène, on ne connait pas l'interface réelle entre le carbone et le tungstène, et cela pourrait se révéler un lien fragile et sensible aux effets thermiques. Comme le cône lui-même est composé de feuilles de graphène, la structure atomique des atomes de carbone qui forment la CCnT signifie qu'il y a moins d'atomes de carbone constituant la pointe que dans une nanopointe de mêmes dimensions fait en tungstène. Cela signifie qu'il y a plus d'énergie déposée par atome que par rapport à des pointes tungstène. Une autre propriété inconnue de la CCnT peut aussi être un facteur contribuant à son apparente fragilité.

Grâce au développement d'un NOPA (Sec. 2.3) avec une cadence variable et notre collaboration active avec le CEMES vers la synthèse de nouveaux types de CCnTs, nous espérons améliorer nos études sur l'émission laser d'électrons à partir des CCnTs. En particulier, la forme de la pointe semble être cruciale pour la maximisation du processus d'émission.

D.6 Résultats avec une nanopointe d'argent

Nous avons étudié l'émission d'électrons à partir d'une nanopointe d'argent. L'argent (Ag, numéro atomique 47) a une résonance connue de plasmon de surface autour de ∼400 nm, qui est facilement accessible avec notre système de laser par doublage de fréquence. L'argent a un point de fusion relativement faible de 1235 K et un travail de sortie de 4,25 eV [Haynes12] pour sa forme polycristalline. C'est un métal noble avec une orbitale *d* complètement rempli et 1 électron dans l'orbitale *s*. En général l'or est préféré pour des études dans l'air en raison de son inertie vis à vis de l'oxydation, mais l'argent peut être préférable dans le vide car il a moins de pertes pour les longueurs d'onde visibles [Sasaki13]. L'argent est utilisé pour sa réponse plasmonique forte et l'amplification de champ sur une large gamme de longueurs d'onde visibles [Schmid13] en raison de la petite composante imaginaire de sa constante diélectrique [Zhang11, Johnson72]. Nous voulons voir comment cette résonance affecte l'émission d'électrons et l'amélioration de champ optique.

Nous avons réalisé ces études en collaboration avec le GPM de Rouen.

Nous utilisons des pointes fabriquées dans un FIB avec un rayon connu de 20-50 nm. Le rayon a été utilisé pour corroborer la fonction Nordheim utilisé avec les courbes de FN. Nous avons également utilisé des images FEM pour observer les sites d'émission multiples dus à la nature polycristalline des pointes.

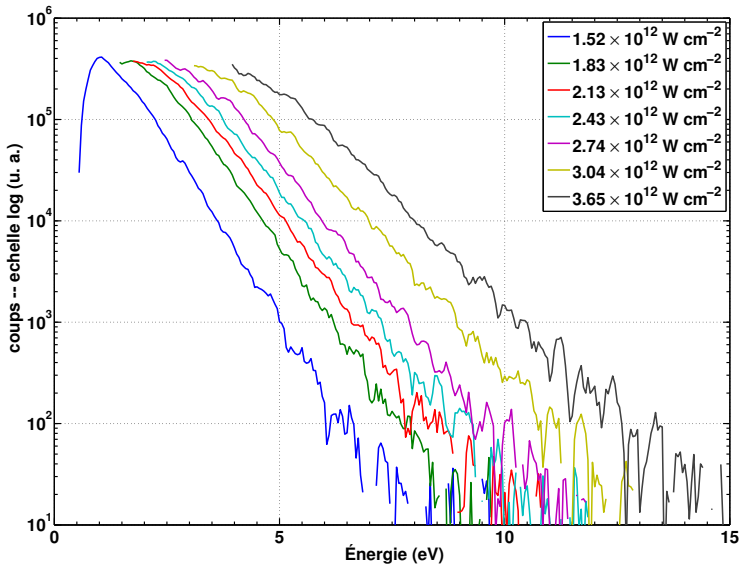

Figure D.9 – Spectres de photoélectrons pour des intensités laser de {1,52, 1,83, 2,13, 2,43, 2,74, 3,04, 3,65 } × 10^{12} W cm^{-2}, avec V_{tip} = 20 V. Les spectres sont plus étroits que ceux obtenus à partir de nanopointes de tungstène avec des intensités équivalentes, mais avec une émission beaucoup plus intense qui sature les MCPs. Ces effets de saturation ont été supprimé des spectres.

Nous avons commencer par irradier la pointe avec une haute cadence. Nos premiers essais ont eu des résultats imprévus que nous ne pouvions pas expliquer. Nous avons imagé la pointe

après l'irradiation du laser, mais nous n'avons trouvé aucune indication de dommages thermiques, ni oxydation.

Notre deuxième échantillon a donné des résultats plus cohérents avec nos hypothèses. À des intensités plus élevées, nous commençons à voir les effets de saturation sur les MCPs car trop d'électrons de faible énergie sont émis pour être comptés. Comme les MCPs saturent à environ 200 000 coups par seconde, mais le taux de répétition du laser est de 62 MHz, nous sommes toujours dans le régime de < 1 électron par impulsion. Ces effets de saturation ont été supprimés dans les données enregistrées. La figure D.9 montre des spectres de photoélectrons où l'intensité vaut $\{1{,}52,\ 1{,}83,\ 2{,}13,\ 2{,}43,\ 2{,}74,\ 3{,}04,\ 3{,}65\} \times 10^{12}$ W cm^{-2}, avec $V_{\text{tip}} = 20$ V. Ces spectres ne montrent aucun signe de pics d'ATP et les spectres sont plus étroits que ceux avec des intensités équivalentes pour les nanopointes de tungstène. Cela peut être causé par l'émission de champ thermique : l'absorption de photons chauffe le gaz d'électrons et permet aux électrons de plus grande énergie de tunneler. Cependant, les courbes de de dépendance en polarisation donnent un exposant $n = 3 \pm 0.6$ ce qui semble indiquer une émission au dessus du seuil. Peut-être le spectre que nous voyons est une combinaison d'effets thermiques et d'émission au dessus du seuil qui brouillent les pics d'ATP caractéristiques d'émission multiphotonique. Nous avons attribué le taux d'émission élevé aux effets thermiques et avons baissé le taux de répétition du laser.

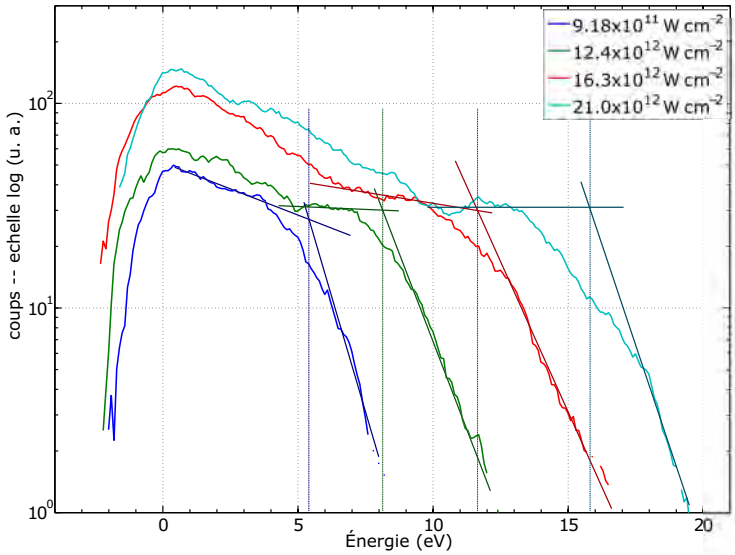

Figure D.10 – Spectres de photoélectrons mesure par rapport à l'énergie de Fermi, $eV_{\text{tip}} + U_{\text{p}}$. L'énergie de coupure peut être déterminée par la décroissance du plateau les électrons de haut énergie

Au taux de répétition faible, nos analyses de polarisation ont donné un bon contraste pour les polarisations orthogonales. Cependant, les variations de puissance laser et de polarisation ont donné un faible exposant de puissance $\eta \sim 1.5$. Les raisons possibles pour un exposant η aussi bas pourraient être l'émission par effet de champ photonique et thermique, ou les effets géométriques comme une pointe angulaire ou des effets de charge d'espace de haute émission.

Des spectres d'énergie des électrons (figure D.10) révèlent un plateau dans le spectre d'énergie, ce qui est la signature de la recollision et rediffusion des électrons sur la pointe. Les spectres que nous enregistrons ont des régions distinctes. Les électrons de basse énergie montrent une décroissance exponentielle caractéristique de la photoémission au dessus du seuil. Aux intensités laser plus élevées, on observe un plateau des électrons de haute énergie, où le taux de comptage reste presque le même. Ce plateau dans le spectre d'énergie est la signature de la recollision et rediffusion des électrons sur la pointe et s'explique par le modèle de trois étapes (Sec. 1.3.3). Après le plateau, nous observons une décroissance rapide du taux de comptage.

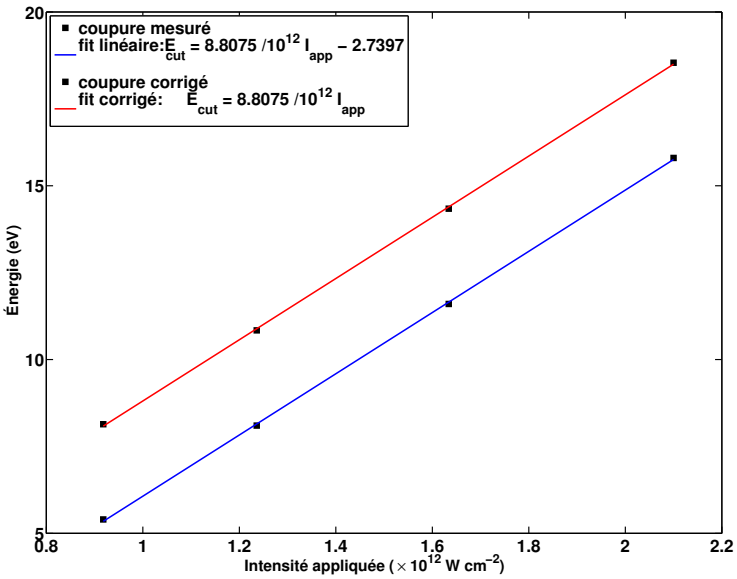

Figure D.11 – Ce graphe montre que l'énergie de coupure mesurée varie linéairement en fonction de l'intensité laser. La courbe bleue montre que E_{cut} = (8,81 $\pm$ 0.07) eV/(10^{12} W cm^{-2}) $I_{\text{app}} = 2,74 \pm$ 0.52 eV. En corrigeant pour le décalage dû à des facteurs géométriques dans le montage expérimental, on voit l'énergie de coupure corrigée dans la courbe rouge avec E_{cut} = 8,81 eV/(10^{12} W cm^{-2}) I_{app}.

Nous pouvons utiliser les spectres pour calculer l'énergie pondéromotrice U_{p}de deux façons. D'abord nous pouvons calculer U_{p} en utilisant le décalage du spectre qui vient de l'effet de Stark. On compare ces résultats à la mesure de l'énergie de coupure du plateau dans le spectre. Comme discuté dans Sec. 1.3.3, nous savons que l'énergie finale maximale qu'un électron peut gagner grâce à rediffusion est $10U_{\text{p}}$. Donc nous pouvons identifier expérimentalement $10U_{\text{p}}$ à l'énergie de coupure E_{cut}. Nous déterminons cette énergie de coupure à partir de la décroissance du plateau dans les spectres pour les électrons d'énergie plus élevés en utilisant la technique décrite dans [Krüger12b]. On ajuste une droite au plateau dans le spectre et une droite à la décroissance d'énergie pour les électrons de haute énergie. L'intersection de ces deux droites est considérée être l'énergie de coupure à $10U_{\text{p}}$, comme on le voit sur la figure. D.10. Grâce à cette mesure, nous pouvons comparer les valeurs à U_{p} calculé à partir de l'intensité appliquée pour trouver une valeur pour l'amplification de l'intensité et champ.

La coupure mesurée doit évoluer linéairement avec l'intensité comme on le voit dans la fi-

gure D.11. La pente de cette dépendance est de 8,81 $\pm$ 0,07 eV/(10^{12} W cm^{-2}) avec un décalage de 2,74 $\pm$ 0,52 eV (courbe bleue). Comme E_{cut}=$10U_{\text{p}} \propto I_{\text{eff}}$, il ne devrait pas y avoir de décalage dans l'ajustement. Ce décalage peut être attribué à des facteurs géométriques dans le montage expérimental tel que une pointe inclinée par rapport au spectromètre, ou une erreur systématique dans notre hypothèse du niveau de Fermi. Nous pouvons corriger cette erreur en déplaçant les spectres par le décalage calculé dans la courbe bleue. Cela donne une nouvelle coupure d'énergie mesurée et donc nouvelle amplification de l'intensité comme on le voit dans le Tab. D.2. On obtient alors une mesure de l'amplification de l'intensité laser de 14,74 $\pm$ 0,05, et une amplification du champ de 3,8 $\pm$ 0,05.

Table D.2 – Table donnant l'énergie de coupure de la figure D.11, l'intensité laser correspondante, l'amplification d'intensité ξ_I, l'amplification de champ ξ et le paramètre de Keldysh, γ correspondant.

Énergie d'impulsion (nJ)	**Intensité appliquée (W cm^{-2})**	E_{cut} **calculé (eV)**	E_{cut} **corrigé mesuré (eV)**	ξ_I	ξ	**Intensité réelle (W cm^{-2})**	γ **corrigé réel**
6.2	0.918×10^{12}	0.549	8.1	14.8	3.85	1.36×10^{13}	1.62
8.74	12.4×10^{12}	0.739	10.8	14.7	3.83	1.81×10^{13}	1.40
11.55	16.3×10^{12}	0.976	14.4	14.7	3.83	2.40×10^{13}	1.22
14.8	21.0×10^{12}	1.255	18.5	14.8	3.84	3.10×10^{13}	1.07

Des résultats préliminaires à 400 nm indiquent que l'émission d'électrons est plus efficace et le spectre d'énergie est beaucoup plus large pour des intensités similaire à celles utilisées à 800 nm. Comme avant, nous utilisons les deux techniques de mesure de U_{p} pour déterminer l'amplification et nous trouvons une amélioration de l'intensité de $\sim$ 100 avec une amplification de champ correspondant de $\sim$ 10. Bien que nous ne pouvons pas faire des conclusions fermes quant à savoir si oui ou non cette haute amplification à 400 nm est due à des effets de résonance plasmonique, il est un début prometteur pour les investigations des effets dépendant en longueur d'onde.

D.7 Re-examen des mécanismes d'émission en utilisant la forme spectrale

Dans cette dernière section, nous comparons les différents spectres obtenus pour les différentes pointes.

La photoémission au dessus du seuil correspond à une transition libre-libre des électrons dans le continuum avant qu'ils n'aient quitté le potentiel atomique[Agostini79]. À partir du ratio du nombre d'électrons émis pour les différents pics ATP, on peut déterminer la "probabilité" pour le système d'absorber un photon avant émission, après qu'il ait acquis une énergie suffisante pour passer au dessus du seuil. Cette probabilité peut être dérivée à partir des hauteurs des pics d'ATP. Pour les résultats dans le tungstène, nous trouvons des valeurs de l'ordre de 0,1.

Par ailleurs, nous utilisons la forme des spectres d'identifier les différents mécanismes d'émission. Les spectres que nous enregistrons sont une somme d'électrons émis par divers mécanismes. Comme les spectres sont généralement dominés par un mécanisme d'émission, nous

pouvons identifier le processus physique basé sur la forme spectrale globale. Des informations sur les spécificités de chaque mécanisme derrière l'émission d'électrons peuvent être obtenues pour chaque type de forme spectrale. Comme discuté dans les sections 6.4 et D.6, l'augmentation de champ optique d'une pointe peut être mesurée à partir de l'observation d'un plateau spectrale avec une comparaison de la mesure $10U_{\mathrm{p}}$ coupure avec la valeur attendue de l'intensité appliquée.

Nous comparons les spectres de photoélectrons enregistrés pour diverses pointes avec la même intensité crête du laser appliquée comme voir en Fig. D.12. Pour chaque pointe, le rayon est environ le même (même ordre de grandeur, $\sim$ 30 nm), les travails de sortie sont similaires ($\sim$ 5 eV), et les tensions appliquées sont du même ordre de grandeur ($\sim$ 50 eV). Cela nous permet de comparer les effets qui se produisent en raison des propriétés matériaux des pointes, guidant à l'amplification de processus d'émission spécifique. Nous voyons un spectre plus étroit et le manque de pics d'ATP pour une pointe d'argent et un CCnT à haute cadence (Fig. D.12, les spectres bleus). On observe la photoémission multiphotonique pour SCW(310) avec des pics dans le spectre (Fig. D.12, les spectres verts). Finalement, nous voyons des signes la recollision et rediffusion des électrons sur la pointe dans le spectre de photoémission pour une pointe d'argent à bas taux de répétition (Fig. D.12, les spectres rouges). Le taux de répétition du laser a été baissé, donc la puissance moyenne est presque négligeable dans ce cas. Le spectre est beaucoup plus large que ceux pour l'émission d'autres mécanismes. Il se forme un plateau à des intensités plus élevées indiquant la recollision d'électrons.

Conclusion et perspectives

Dans cette thèse, j'ai présenté une nouvelle expérience pour étudier de l'émission des photoélectrons induite par des impulsions laser ultracourtes à partir d'une nanopointe. Cette nouvelle direction ' pour mon groupe impliquait la conception complète et développement d'un nouveau dispositif expérimental incorporant des techniques de spectroscopie électronique existantes avec un expertise en développement du laser. Nous avons élargit les résultats existants dans les nanopointes métalliques classiques de tungstène [Hommelhoff06b, Barwick07, Yanagisawa10] et or [Ropers07, Bormann10, Park12] en utilisant de nouvelles pointes innovantes basées sur les nanotubes de carbone et de l'argent.

Cette thèse ne présente nullement une étude exhaustive sur le sujet de l'émission d'électrons à partir nanopointe, ou même à partir de ces trois matériaux. Comme nous avons été limités par des effets thermiques dans nos mécanismes d'émission, des investigations sur ces effets serait utile pour des expériences de l'avenir. Il serait intéressant de voir à quel point les émissions d'une nanopointe d'argent changent en fonction de la cadence des impulsions laser, de l'émission thermique à haute cadence aux effets de champ fort à cadence réduite. Cela permettrait également de donner une échelle de temps pour la durée de états thermiques. Cet étude pourrait être réalisée en examinant la forme spectrale émise en fonction de la cadence du laser ce qui devient possible avec le développement du NOPA. Les mécanismes d'émission thermique ne sont pas compris entièrement et des simulations sont nécessaires pour corroborer nos résultats expérimentaux.

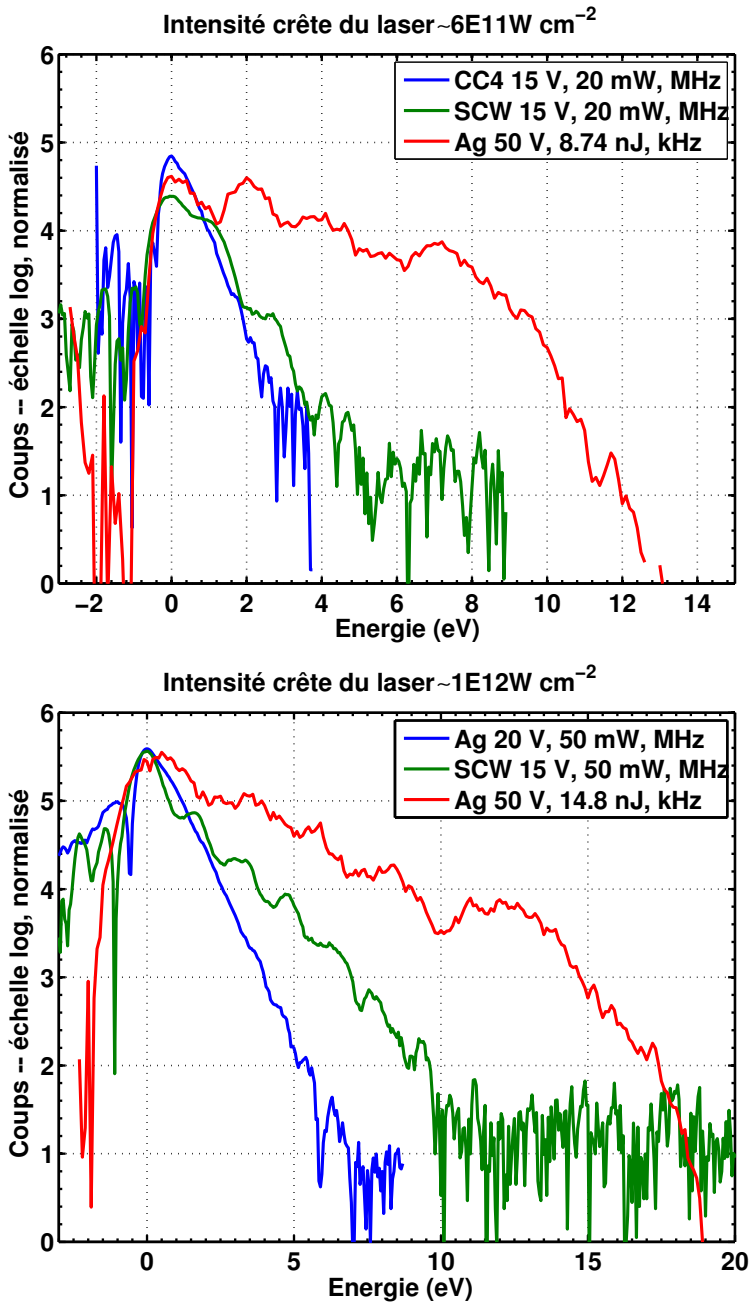

Figure D.12 – Chaque ensemble de spectres a été enregistré avec la même intensité crête du laser : en haut 6×10^{11} W cm^{-2}, en bas : 1×10^{12} W cm^{-2}. En changeant le matériau de la pointe ou le taux de répétition du laser (puissance moyenne), on change le mécanisme d'émission dominant. Les spectres bleus montrent des spectres plus étroits sans pics d'ATP, indiquant des effets thermiques possibles. Les spectres verts montrent la photoémission multiphotonique caractérisée par des pics d'ATP séparé par l'énergie d'un photon. Les spectres rouges montrent une transition dans le régime de l'effet tunnel optique avec un spectre plus large et l'émergence un plateau, indiquant la recollision et rediffusion des électrons sur la pointe.

Les investigations sur la réponse plasmonique d'un matériau pourraient conduire à des mécanismes d'émission dépendant de la longueur d'onde. Déjà des résultats préliminaires indiquent qu'il y a une production d'électrons plus élevée et un spectre plus large pour un éclairage du

laser à proximité de la résonance de plasmon prédite théoriquement (pointe d'argent autour de 400nm). Des études systématiques sur la productions d'électrons en fonction de la longueur d'onde proche de la résonance ou même la forme spectrale pourraient donner une vision de la façon dont ces résonances affectent les propriétés électroniques de ces nanopointes.

La flexibilité de notre dispositif expérimental permet la possibilité de collecter la lumière laser après son interaction avec la pointe. Comme effet tunnel optique, recollision et rediffusion des électrons sont les mécanismes physiques à l'origine de la génération d'harmoniques élevée, il est possible qu'avec quelques modifications de notre système, nous serions à même d'observer des harmoniques provoquées par les pointes. Des expériences pompe-sonde pourraient permettre de mesurer les propriétés des photoélectrons, et à l'aide de spectroscopie pompe-sonde nous pourrions extraire les propriétés optiques de nos nanostructures. Enfin, l'émission de pointes assistée par laser peut être utilisée pour étudier les propriétés fondamentales sur les électrons tels que l'interférence électronique [Barwick08, Vidil] et pour des expériences d'onde de matière.

L'expérience présentée dans cette thèse permet d'explorer les interactions lumière-matière dans un régime unique entre la phase gazeuse de la physique atomique et la matière condensée grâce à l'utilisation des nanopointes. L'émission d'électrons à partir d'une nanopointe exhibe déjà des comportements de ces deux régimes, et la combinaison des expertises en physique des lasers et en nanomatériaux pourra permettre d'étendre la physique du champ fort à ces nouveaux systèmes au fort potentiel d'application.

References

[Agostini79] Agostini P, Fabre F, Mainfray G, Petite G and Rahman NK. *Free-Free Transitions Following Six-Photon Ionization of Xenon Atoms*. Physical Review Letters, **42** (17): 1127 (1979).

[Aidelsburger10] Aidelsburger M, Kirchner FO, Krausz F and Baum P. *Single-electron pulses for ultrafast diffraction*. Proceedings of the National Academy of Sciences of the United States of America, **107** (46): 19714–19719 (2010).

[Allouche03] Allouche H, Monthioux M and Jacobsen RL. *Chemical vapor deposition of pyrolytic carbon on carbon nanotubes Part 1. Synthesis and morphology*. Carbon, **41** (15): 2897–2912 (2003).

[Allouche05] Allouche H and Monthioux M. *Chemical vapor deposition of pyrolytic carbon on carbon nanotubes. Part 2. Texture and structure*. Carbon, **43** (6): 1265–1278 (2005).

[Arbouet12] Arbouet A, Houdellier F, Marty R and Girard C. *Interaction of an ultrashort optical pulse with a metallic nanotip: A Green dyadic approach*. Journal of Applied Physics, **112** (5): 053103 (2012).

[Babadjanyan00] Babadjanyan AJ, Margaryan NL and Nerkararyan KV. *Superfocusing of surface polaritons in the conical structure*. Journal of Applied Physics, **87** (8): 3785 (2000).

[Baida11] Baida H, Christofilos D, Maioli P, Crut A, Del Fatti N and Vallée F. *Surface plasmon resonance spectroscopy of single surfactant-stabilized gold nanoparticles*. The European Physical Journal D, **63** (2): 293–299 (2011).

[Barthes12] Barthes J, Colas des Francs G, Bouhelier A and Dereux A. *A coupled lossy local-mode theory description of a plasmonic tip*. New Journal of Physics, **14** (8): 083041 (2012).

[Barty96] Barty CP, Korn G, Raksi F, Rose-Petruck C, Squier J, Tien AC, Wilson KR, Yakovlev VV and Yamakawa K. *Regenerative pulse shaping and amplification of ultrabroadband optical pulses*. Optics letters, **21**: 219 (1996).

[Barwick07] Barwick B, Corder C, Strohaber J, Chandler-Smith N, Uiterwaal C and Batelaan H. *Laser-induced ultrafast electron emission from a field emission tip*. New Journal of Physics, **9** (5): 142–142 (2007).

[Barwick08] Barwick B and Batelaan H. *Aharonov-bohm phase shifts induced by laser pulses*. New Journal of Physics, **10** (8): 083036 (2008).

[Baum13] Baum P. *On the physics of ultrashort single-electron pulses for time-resolved microscopy and diffraction*. Chemical Physics, **423**: 55–61 (2013).

[Bedel14] Bedel V. *Emission de champ de pointes métalliques*. Rapport de stage M1, Université Toulouse III – Paul Sabatier (2014).

[Bionta14a] Bionta M, Chalopin B, Champeaux J, Faure S, Masseboeuf A, Moretto-Capelle P and Chatel B. *Laser-induced electron emission from a tungsten nanotip: identifying above threshold photoemission using energy-resolved laser power dependencies*. Journal of Modern Optics, **61** (10): 833 (2014).

[Bionta14b] Bionta MR, Chalopin B, Masseboeuf A and Chatel B. *First results on laser-induced field emission from a CNT-based nanotip*. Ultramicroscopy: doi:10.1016/j.ultramic.2014.11.027 (2014).

[Bormann10] Bormann R, Gulde M, Weismann A, Yalunin SV and Ropers C. *Tip-Enhanced Strong-Field Photoemission*. Physical Review Letters, **105** (14): 147601 (2010).

[Bouhelier03] Bouhelier a, Beversluis M, Hartschuh a and Novotny L. *Near-field second-harmonic generation induced by local field enhancement*. Physical Review Letters, **90** (1): 013903 (2003).

[Brabec92] Brabec T, Spielmann C, Curley PF and Krausz F. *Kerr lens mode locking*. Optics Letters, **17** (18): 1292 (1992).

[Bradler09] Bradler M, Baum P and Riedle E. *Femtosecond continuum generation in bulk laser host materials with sub-μJ pump pulses*. Applied Physics B: Lasers and Optics, **97** (3): 561–574 (2009).

[Bradler13] Bradler M, Homann C and Riedle E. *Broadband difference frequency mixing between visible and near-infrared pulses for few-cycle pulse generation with stable carrier-envelope phase*. Applied Physics B, **113** (1): 19 (2013).

[Breuer13] Breuer J and Hommelhoff P. *Laser-based acceleration of nonrelativistic electrons at a dielectric structure*. Physical Review Letters, **111**: 134803 (2013).

[Bunkin65] Bunkin FV and Fedorov MV. *Cold Emission of Electrons from Surface of a Metal in a Strong Radiation Field*. Soviet Physics JETP, **21** (5): 896 (1965).

[Burnett77] Burnett NH, Baldis HA, Richardson MC and Enright GD. *Harmonic generation in CO2 laser target interaction*. Applied Physics Letters, **31** (3): 172 (1977).

[Cerullo97] Cerullo G, Nisoli M and De Silvestri S. *Generation of 11 fs pulses tunable across the visible by optical parametric amplification*. Applied Physics Letters, **71** (25): 3616 (1997).

[Cerullo03] Cerullo G and De Silvestri S. *Ultrafast optical parametric amplifiers*. Review of Scientific Instruments, **74** (1): 1 (2003).

[Chaturvedi09] Chaturvedi P, Hsu KH, Kumar A, Fung KH, Mabon JC and Fang NX. *Imaging of plasmonic modes of silver nanoparticles using high-resolution cathodoluminescence spectroscopy*. ACS Nano, **3** (10): 2965–2974. PMID: 19739603 (2009).

[Ciappina14a] Ciappina M, Pérez-Hernández JA, Shaaran T and Lewenstein M. *Coherent XUV generation driven by sharp metal tips photoemission*. The European Physical Journal D, **68** (6): 172 (2014).

[Ciappina14b] Ciappina MF, Pérez-Hernández JA, Shaaran T, Lewenstein M, Krüger M and Hommelhoff P. *High-order-harmonic generation driven by metal nanotip photoemission: Theory and simulations*. Physical Review A, **89** (1): 013409 (2014).

[Corkum93] Corkum PB. *Plasma Perspective on Strong-Field Multiphoton Ionization*. Physical Review Letters, **71** (13): 1994 (1993).

[Degert02] Degert J. *Manipulation cohérente d'atoms et de molécules diatomiques avec des impulsions mises en forme*. Ph.D. thesis, Université Toulouse III – Paul Sabatier (2002).

[deKnoop14] de Knoop L. *Development of Quantitative In-Situ Transmission Electron Microscopy for Nanoindentation and Cold-Field Emission*. Ph.D. thesis, Université Toulouse III – Paul Sabatier (2014).

[Einstein05] Einstein A. *Über einen die Erzeugung und Verwandlung des Lichtes betreffenden heuristischen Gesichtspunkt*. Annalen der Physik, **322** (6): 132–148 (1905).

[Ekvall99] Ekvall I, Wahlstrom E, Claesson D, Olin H and Olsson E. *Preparation and characterization of electrochemically etched W tips for STM*. Measurment and Science Technology, **10**: 11–18 (1999).

[Emma10] Emma P, Akre R, Arthur J, Bionta R, Bostedt C, Bozek J, Brachmann a, Bucksbaum P, Coffee R, Decker FJ, Ding Y, Dowell D, Edstrom S, Fisher a, Frisch J, Gilevich S, Hastings J, Hays G, Hering P, Huang Z, Iverson R, Loos H, Messerschmidt M, Miahnahri a, Moeller S, Nuhn HD, Pile G, Ratner D, Rzepiela J, Schultz D, Smith T, Stefan P, Tompkins H, Turner

J, Welch J, White W, Wu J, Yocky G and Galayda J. *First lasing and operation of an ångstrom-wavelength free-electron laser*. Nature Photonics, **4** (9): 641–647 (2010).

[Enoch12] Enoch S and Bonod N (Eds.). *Plasmonics: From Basics to Advanced Topics*. Springer-Verlag, Berlin (2012).

[Ferray88] Ferray M, L'Huillier A, Li XF, Lompre LA, Mainfray G and Manus C. *Multiple-harmonic conversion of 1064 nm radiation in rare gases*. Journal of Physics B: Atomic, Molecular and Optical Physics, **21** (3): L31 (1988).

[Fork84] Fork RL, Martinez OE and Gordon JP. *Negative dispersion using pairs of prisms*. Optics Letters, **9** (5): 150 (1984).

[Fowler28] Fowler RH and Nordheim L. *Electron Emission in Intense Electric Fields*. Royal Society of London Proceedings Series A, **119**: 173 (1928).

[Ganter08] Ganter R, Bakker R, Gough C, Leemann SC, Paraliev M, Pedrozzi M, Le Pimpec F, Schlott V, Rivkin L and Wrulich A. *Laser-photofield emission from needle cathodes for low-emittance electron beams*. Physical Review Letters, **100**: 064801 (2008).

[Ghosh10] Ghosh K, Kumar M, Maruyama T and Ando Y. *Tailoring the field emission property of nitrogen-doped carbon nanotubes by controlling the graphitic/pyridinic substitution*. Carbon, **48** (1): 191–200 (2010).

[Gomer61] Gomer R. *Field emission and field ionization*, vol. 34. Harvard University Press Cambridge, MA (1961).

[Goncharenko07] Goncharenko AV, Chang HC and Wang JK. *Electric near-field enhancing properties of a finite-size metal conical nano-tip*. Ultramicroscopy, **107**: 151 (2007).

[Good Jr56] Good Jr RH and Müller EW. *Field Emission*. Handbuch der Physik, **4** (21): 1956 (1956).

[Gulde14] Gulde M, Schweda S, Storeck G, Maiti M, Yu HK, Wodtke AM, Schäfer S and Ropers C. *Ultrafast low-energy electron diffraction in transmission resolves polymer/graphene superstructure dynamics*. Science, **345** (6193): 200–204 (2014).

[Hadley85] Hadley KW, Donders PJ and Lee MJG. *Influence of shank profile on laser heating of a field emitter*. Journal of Applied Physics, **57** (7): 2617 (1985).

[Hädrich08] Hädrich S, Rothhardt J, Röser F, Gottschall T, Limpert J and Tünnermann A. *Degenerate optical parametric amplifier delivering sub 30 fs pulses with 2GW peak power*. Optics Express, **16** (24): 19812 (2008).

[Haynes12] Haynes W. *CRC Handbook of Chemistry and Physics, 93rd Edition*. CRC Handbook of Chemistry and Physics. Taylor & Francis (2012).

[Herink12] Herink G, Solli DR, Gulde M and Ropers C. *Field-driven photoemission from nanostructures quenches the quiver motion*. Nature, **483** (7388): 190–193 (2012).

[Herring49] Herring C and Nichols MH. *Thermionic emission*. Reviews of Modern Physics, **21** (2): 185 (1949).

[Hoffrogge14] Hoffrogge J, Paul Stein J, Krüger M, Förster M, Hammer J, Ehberger D, Baum P and Hommelhoff P. *Tip-based source of femtosecond electron pulses at 30 keV*. Journal of Applied Physics, **115** (9): 094506 (2014).

[Hommelhoff06a] Hommelhoff P, Kealhofer C and Kasevich MA. *Ultrafast Electron Pulses from a Tungsten Tip Triggered by Low-Power Femtosecond Laser Pulses*. Physical Review Letters, **97** (24): 247402 (2006).

[Hommelhoff06b] Hommelhoff P, Sortais Y, Aghajani-Talesh A and Kasevich MA. *Field Emission Tip as a Nanometer Source of Free Electron Femtosecond Pulses*. Physical Review Letters, **96** (7): 077401 (2006).

[Hori75] Hori H, Maeda N, Kobayashi N and Sakisaka M. *Electron energy spectrometer of retarding field type*. Nuclear Instruments and Methods, **130** (1): 135–141 (1975).

[Houard11] Houard J, Vella A, Vurpillot F and Deconihout B. *Three-dimensional thermal response of a metal subwavelength tip under femtosecond laser illumination*. Physical Review B, **84** (3): 033405 (2011).

[Houdellier12] Houdellier F, Masseboeuf A, Monthioux M and Hÿtch MJ. *New carbon cone nanotip for use in a highly coherent cold field emission electron microscope*. Carbon, **50** (5): 2037–2044 (2012).

[Houdellier15] Houdellier F, de Knoop L, Gatel C, Masseboeuf A, Mamishin S, Taniguchi Y, Delmas M, Monthioux M, Hÿtch M and Snoeck E. *Development of tem and sem high brightness electron guns using cold-field emission from a carbon nanotip*. Ultramicroscopy, **151** (0): 107 – 115. Special Issue: 80th Birthday of Harald Rose; PICO 2015 — Third Conference on Frontiers of Aberration Corrected Electron Microscopy (2015).

[Iaconis98] Iaconis C and Walmsley I. *Spectral phase interferometry for direct electric-field reconstruction of ultrashort optical pulses*. Optics Letters, **23** (10): 792 (1998).

[Ibe90] Ibe JP. *On the electrochemical etching of tips for scanning tunneling microscopy*. Journal of Vacuum Science & Technology A: Vacuum, Surfaces, and Films, **8** (1990): 3570 (1990).

[Itatani02] Itatani J, Quéré F, Yudin GL, Ivanov MY, Krausz F and Corkum PB. *Attosecond streak camera*. Phys. Rev. Lett., **88**: 173903 (2002).

[Itatani04] Itatani J, Levesque J, Zeidler D, Niikura H, Pepin H, Kieffer JC, Corkum PB and Villeneuve DM. *Tomographic imaging of molecular orbitals*. Nature, **432** (7019): 867–871 (2004).

[Ivanov05] Ivanov MY, Spanner M and Smirnova O. *Anatomy of strong field ionization*. Journal of Modern Optics, **52** (2-3): 165–184 (2005).

[Jacobsen97] Jacobsen RL and Monthioux M. *Carbon beads with protruding cones*. Nature, **385**: 211 (1997).

[Jain07] Jain PK, Huang X, El-Sayed IH and El-Sayed MA. *Review of Some Interesting Surface Plasmon Resonance-enhanced Properties of Noble Metal Nanoparticles and Their Applications to Biosystems*. Plasmonics, **2** (3): 107–118 (2007).

[Joachain12] Joachain C, Kylstra N and Potvliege R. *Atoms in Intense Laser Fields*. Cambridge University Press, Cambridge (2012).

[Johnson72] Johnson PB and Christy RW. *Optical Constants of the Noble Metals*. Physical Review B, **6** (12): 4370 (1972).

[Juvé13] Juvé V, Cardinal MF, Lombardi A, Crut A, Maioli P, Pérez-Juste J, Liz-Marzén LM, Del Fatti N and Vallée F Fe. *Size-dependent surface plasmon resonance broadening in nonspherical nanoparticles: Single gold nanorods*. Nano Letters, **13** (5): 2234–2240. PMID: 23611370 (2013).

[Kealhofer12] Kealhofer C, Foreman SM, Gerlich S and Kasevich MA. *Ultrafast laser-triggered emission from hafnium carbide tips*. Physical Review B, **86** (3): 035405 (2012).

[Kealhofer13] Kealhofer C. *Nanometer tip-based ultrafast electron sources: emission processes and direct pulse characterization techniques*. Ph.D. thesis, Stanford University (2013).

[Keldysh65] Keldysh L. *Ionization in a field of a strong electromagnetic wave*. Soviet Physics JETP, **20** (5): 1307 (1965).

[Kim05] Kim EM, Elovikov SS, Murzina TV, Nikulin aa, Aktsipetrov Oa, Bader Ma and Marowsky G. *Surface-enhanced optical third-harmonic generation in Ag Island films*. Physical Review Letters, **95** (22): 1–4 (2005).

[Kim08] Kim S, Jin J, Kim YJ, Park IY, Kim Y and Kim SW. *High-harmonic generation by resonant plasmon field enhancement*. Nature, **453** (7196): 757–760 (2008).

[Krüger11] Krüger M, Schenk M and Hommelhoff P. *Attosecond control of electrons emitted from a nanoscale metal tip*. Nature, **475** (7354): 78–81 (2011).

[Krüger12a] Krüger M, Schenk M, Förster M and Hommelhoff P. *Attosecond physics in photoemission from a metal nanotip*. Journal of Physics B: Atomic, Molecular and Optical Physics, **45** (7): 074006 (2012).

[Krüger12b] Krüger M, Schenk M, Hommelhoff P, Wachter G, Lemell C and Burgdörfer J. *Interaction of ultrashort laser pulses with metal nanotips: a model system for strong-field phenomena*. New Journal of Physics, **14** (8): 085019 (2012).

[Krüger13] Krüger M. *Attosecond Physics in Strong-Field Photoemission from Metal Nanotips*. Ph.D. thesis, Ludwig-Maximilians-Universität (2013).

[Kupersztych01] Kupersztych J, Monchicourt P and Raynaud M. *Ponderomotive Acceleration of Photoelectrons in Surface-Plasmon-Assisted Multiphoton Photoelectric Emission*. Physical Review Letters, **86** (22): 5180–5183 (2001).

[Lee73] Lee MJG. *Field emission of hot electrons from tungsten*. Physical Review Letters, **30** (24): 1193 (1973).

[Lee06] Lee KS and El-Sayed Ma. *Gold and silver nanoparticles in sensing and imaging: sensitivity of plasmon response to size, shape, and metal composition*. The Journal of Physical Chemistry B, **110** (39): 19220–5 (2006).

[L'Huillier93] L'Huillier A and Balcou P. *High-order harmonic generation in rare gases with a 1-ps 1053-nm laser*. Physical Review Letters, **70**: 774–777 (1993).

[Link99] Link S and El-Sayed Ma. *Size and Temperature Dependence of the Plasmon Absorption of Colloidal Gold Nanoparticles*. The Journal of Physical Chemistry B, **103** (21): 4212–4217 (1999).

[Luan89] Luan S, Hippler R, Schwier H and Lutz HO. *Electron Emission from Polycrystalline Copper Surfaces by Multi-Photon Absorption*. Europhysics Letters (EPL), **9** (5): 489 (1989).

[Lucier04] Lucier As. *Preparation and Characterization of Tungsten Tips Suitable for Molecular Electronics Studies*. Master's thesis, McGill University (2004).

[Ma15] Ma X, Grüß er M and Schuster R. *Plasmonic nanospheres with a handle—Local electrochemical deposition of Au or Ag at the apex of optically inactive W- or C-tips*. Applied Physics Letters, **106** (24): 241103 (2015).

[Maier07] Maier SA (Ed.). *Plasmonics: Fundamentals and Appliations*. Springer Science+Business Media, LLC, New York, NY (2007).

[McCabe11] McCabe DJ, Tajalli A, Austin DR, Bondareff P, Walmsley IA, Gigan S and Chatel B. *Spatio-temporal focusing of an ultrafast pulse through a multiply scattering medium*. Nature Communications, **2**: 447 (2011).

[McPherson87] McPherson A, Gibson G, Jara H, Johann U, Luk TS, McIntyre IA, Boyer K and Rhodes CK. *Studies of multiphoton production of vacuum-ultraviolet radiation in the rare gases*. Journal of the Optical Society of America B, **4** (4): 595 (1987).

[Mendenhall37] Mendenhall CE and DeVoe CF. *The Photoelectric Work Functions of the 211 and 310 Planes of Tungsten*. Physical Review, **51** (5): 346 (1937).

[Miller07] Miller M and Russell K. *Atom probe specimen preparation with a dual beam sem/fib miller*. Ultramicroscopy, **107** (9): 761 – 766 (2007).

[Mock02] Mock JJ, Barbic M, Smith DR, Schultz DA and Schultz S. *Shape effects in plasmon resonance of individual colloidal silver nanoparticles*. The Journal of Chemical Physics, **116** (15): 6755 (2002).

[Monmayrant10] Monmayrant A, Weber S and Chatel B. *A newcomer's guide to ultrashort pulse shaping and characterization*. Journal of Physics B: Atomic, Molecular and Optical Physics, **43** (10): 103001 (2010).

[Monthioux06] Monthioux M, Allouche H and Jacobsen RL. *Chemical vapour deposition of pyrolytic carbon on carbon nanotubes Part 3: Growth mechanisms*. Carbon, **44** (15): 3183–3194 (2006).

[Moulton86] Moulton PF. *Spectroscopic and laser characteristics of Ti:Al_2O_3*. Journal of the Optical Society of America B, **3** (1): 125 (1986).

[Müller36] Müller EW. *Versuche zur Theorie der Elektronenemission unter der Einwirkung hoher Feldstärken*. Zeitschrift für technische Physik, **37**: 838 (1936).

[Muller83] Muller HG, Tip A and van der Wiel MJ. *Ponderomotive force and AC Stark shift in multiphoton ionisation*. Journal of Physics B: Atomic, Molecular and Optical Physics, **16** (22): L679 (1983).

[Muller88] Muller HG, van Linden van den Heuvell HB, Agostini P, Petite G, Antonetti A, Franco M and Migus A. *Multiphoton ionization of xenon with 100-fs laser pulses*. Physical Review Letters, **60** (7): 565 (1988).

[Mulser93] Mulser P, Uryupin S, Sauerbrey R and Wellegehausen B. *Ponderomotive potential and dynamical Stark shift in multiphoton ionization*. Physical Review A, **48** (6): 4547 (1993).

[Murphy56] Murphy EL and Good Jr RH. *Thermonic Emission, Field Emission, and the Transition Region*. Physical Review, **102** (6): 1464 (1956).

[Nakamura99] Nakamura Y, Mera Y and Maeda K. *A reproducible method to fabricate atomically sharp tips for scanning tunneling microscopy*. Review of Scientific Instruments, **70** (8): 3373 (1999).

[Park12] Park DJ, Piglosiewicz B, Schmidt S, Kollmann H, Mascheck M and Lienau C. *Strong Field Acceleration and Steering of Ultrafast Electron Pulses from a Sharp Metallic Nanotip*. Physical Review Letters, **109** (24): 244803 (2012).

[Paulus94a] Paulus GG, Becker W, Nicklich W and Walther H. *Rescattering effects in above-threshold ionization: a classical model*. Journal of Physics B: Atomic, Molecular and Optical Physics, **27** (21): L703 (1994).

[Paulus94b] Paulus GG, Nicklich W, Xu HL, Lambropoulos P and Walther H. *Plateau in above-Threshold Ionization Spectra*. Physical Review Letters, **72**: 2851 (1994).

[Paulus04] Paulus GG, Lindner F, Milošević DB and Becker W. *Phase-Controlled Single-Cycle Strong-Field Photoionization*. Physica Scripta, **T110**: 120 (2004).

[Qiao07] Qiao L, Zheng WT, Xu H, Zhang L and Jiang Q. *Field emission properties of N-doped capped single-walled carbon nanotubes: a first-principles density-functional study*. The Journal of Chemical Physics, **126** (16): 164702 (2007).

[Quinonez13] Quinonez E, Handali J and Barwick B. *Femtosecond photoelectron point projection microscope*. Review of Scientific Instruments, **84** (10): 103710 (2013).

[Radunsky06] Radunsky AS, Kosik Williams EM, Walmsley IA, Wasylczyk P, Wasilewski W, U'Ren AB and Anderson ME. *Simplified spectral phase interferometry for direct electric-field reconstruction by using a thick nonlinear crystal*. Optics Letters, **31** (7): 1008 (2006).

[Ringe10] Ringe E, McMahon JM, Sohn K, Cobley C, Xia Y, Huang J, Schatz GC, Marks LD and Van Duyne RP. *Unraveling the Effects of Size, Composition, and Substrate on the Localized Surface Plasmon Resonance Frequencies of Gold and Silver Nanocubes: A Systematic Single-Particle Approach*. The Journal of Physical Chemistry C, **114** (29): 12511–12516 (2010).

[Ropers07] Ropers C, Solli DR, Schulz CP, Lienau C and Elsaesser T. *Localized Multiphoton Emission of Femtosecond Electron Pulses from Metal Nanotips*. Physical Review Letters, **98** (4): 043907 (2007).

[Rothhardt10] Rothhardt J, Hädrich S, Seise E, Krebs M, Tavella F, Willner A, Düsterer S, Schlarb H, Feldhaus J, Limpert J, Rossbach J and Tünnermann A. *High average and peak power few-cycle laser pulses delivered by fiber pumped OPCPA system*. Optics express, **18** (12): 12719 (2010).

[Rothhardt13] Rothhardt J, Demmler S, Hädrich S, Peschel T, Limpert J and Tünnermann A. *Thermal effects in high average power optical parametric amplifiers*. Optics letters, **38** (5): 763 (2013).

[Saleh07] Saleh BEA and Teich MC. *Fundamentals of Photonics*. Wiley-Interscience, Hoboken, NJ, 2nd edn. (2007).

[Sasaki13] Sasaki SS, Perdue SM, Rodriguez Perez A, Tallarida N, Majors JH, Apkarian VA and Lee J. *Note: Automated electrochemical etching and polishing of silver scanning tunneling microscope tips*. Review of Scientific Instruments, **84** (9): 096109 (2013).

[Schenk10] Schenk M, Krüger M and Hommelhoff P. *Strong-Field Above-Threshold Photoemission from Sharp Metal Tips*. Physical Review Letters, **105** (25): 257601 (2010).

[Schertz12] Schertz F, Schmelzeisen M, Kreiter M, Elmers HJ and Schönhense G. *Field emission of electrons generated by the near field of strongly coupled plasmons*. Physical Review Letters, **108**: 237602 (2012).

[Schmid13] Schmid T, Opilik L, Blum C and Zenobi R. *Nanoscale chemical imaging using tip-enhanced raman spectroscopy: A critical review*. Angewandte Chemie International Edition, **52** (23): 5940–5954 (2013).

[Schottky23] Schottky WH. Z. tech. Physik, **14**: 63 (1923).

[Sciaini11] Sciaini G and Miller RJD. *Femtosecond electron diffraction: heralding the era of atomically resolved dynamics*. Reports on Progress in Physics, **74** (9): 096101 (2011).

[Shahbazyan13] Shahbazyan TV and Stockman MI (Eds.). *Plasmonics : Theory and Applications*. Springer Science+Business Media, LLC, Dordrecht (2013).

[Shirakawa98] Shirakawa A and Kobayashi T. *Noncollinearly phase-matched femtosecond optical parametric amplification with a 2000 cm^{-1} bandwidth*. Applied Physics Letters, **72** (2): 147 (1998).

[Sivis12] Sivis M, Duwe M, Abel B and Ropers C. *Nanostructure-enhanced atomic line emission*. Nature, **485** (7397): E1–E3 (2012).

[Stockman11] Stockman MI. *Nanoplasmonics: past, present, and glimpse into future*. Optics Express, **10** (22): 22029 (2011).

[Tan01] Tan HS, Warren WS and Schreiber E. *Generation and amplification of ultrashort shaped pulses in the visible by a two-stage noncollinear optical parametric process*. Optics letters, **26** (22): 1812–1814 (2001).

[Thomas13] Thomas S, Krüger M, Förster M, Schenk M and Hommelhoff P. *Probing of optical near-fields by electron rescattering on the 1 nm scale*. Nano Letters, **13** (10): 4790 (2013).

[Thomas14] Thomas S, Wachter G, Lemell C, Burgdörfer J and Hommelhoff P. *Large optical field enhancement for nanotips with large opening angles*. ArXiv:1412.8172 (2014).

[Tóth91] Tóth C, Farkas G and Vodopyanov KL. *Laser-induced electron emission from an Au surface irradiated by single picosecond pulses at λ=2.94 μm. The intermediate region between multiphoton and tunneling effects*. Applied Physics B Photophysics and Laser Chemistry, **53** (4): 221 (1991).

[Träger07] Träger F (Ed.). *Springer handbook of lasers and optics*. Springer Berlin Heidelberg, Berlin, Heidelberg, 2nd edn. (2007).

[Tsong90] Tsong TT. *Atom-Probe Field Ion Microscopy*. Cambridge University Press, New York, NY (1990).

[Venus83] Venus D and Lee M. *Polarization dependence of photoexcitation in photofield emission*. Surface Science, **125** (2): 452–472 (1983).

[Vidil] Vidil P and Chalopin B. *A blazed grating for electrons using kapitza-dirac diffraction with multiple-harmonic standing-waves*. To be submitted.

[Vogel10] Vogel MW and Gramotnev DK. *Shape effects in tapered metal rods during adiabatic nanofocusing of plasmons*. Journal of Applied Physics, **107** (4): 044303 (2010).

[Vogelsang15] Vogelsang J, Robin J, Nagy BJ, Dombi P, Rosenkranz D, Schiek M, Groß P and Lienau C. *Ultrafast electron emission from a sharp metal nanotaper driven by adiabatic nanofocusing of surface plasmons*. Nano Letters. Doi: 10.1021/acs.nanolett.5b01513 (2015).

[Weber15] Weber SJ, Colas des Francs G and Girard C. *Spatiotemporal properties of nanoshell plasmonic response for strong-field experiments*. Physical Review B, **91**: 205419 (2015).

[Wegkamp11] Wegkamp D, Brida D, Bonora S, Cerullo G, Stähler J, Wolf M and Wall S. *Phase retrieval and compression of low-power white-light pulses*. Applied Physics Letters, **99** (10): 101101 (2011).

[Wilhelm97] Wilhelm T, Piel J and Riedle E. *Sub-20-fs pulses tunable across the visible from a blue-pumped single-pass noncollinear parametric converter*. Optics Letters, **22** (19): 1494 (1997).

[Wood97] Wood RW. *A new form of cathode discharge and the production of x-rays, together with some notes on diffraction. preliminary communication*. Physical Review (Series I), **5**: 1–10 (1897).

[Wynne94] Wynne K, Reid GD and Hochstrasser RM. *Regenerative amplification of 30-fs pulses in Ti:sapphire at 5 kHz*. Optics Letters, **19**: 895 (1994).

[Yanagisawa09] Yanagisawa H, Hafner C, Doná P, Klöckner M, Leuenberger D, Greber T, Hengsberger M and Osterwalder J. *Optical Control of Field-Emission Sites by Femtosecond Laser Pulses*. Physical Review Letters, **103** (25): 257603 (2009).

[Yanagisawa10] Yanagisawa H, Hafner C and Doná P. *Laser-induced field emission from a tungsten tip: Optical control of emission sites and the emission process*. Physical Review B, **81** (11): 115429 (2010).

[Yanagisawa11] Yanagisawa H, Hengsberger M, Leuenberger D, Klöckner M, Hafner C, Greber T and Osterwalder J. *Energy Distribution Curves of Ultrafast Laser-Induced Field Emission and Their Implications for Electron Dynamics*. Physical Review Letters, **107** (8): 087601 (2011).

[Yang10] Yang DS, Mohammed OF and Zewail AH. *Scanning ultrafast electron microscopy*. Proceedings of the National Academy of Sciences of the United States of America, **107** (34): 14993–8 (2010).

[Zewail10] Zewail AH. *Four-Dimensional Electron Microscopy*. Science, **328** (April): 187 (2010).

[Zhang11] Zhang C, Gao B, Chen LG, Meng QS, Yang H, Zhang R, Tao X, Gao HY, Liao Y and Dong ZC. *Fabrication of silver tips for scanning tunneling microscope induced luminescence*. Review of Scientific Instruments, **82** (8): 083101 (2011).

[Zherebtsov11] Zherebtsov S, Fennel T, Plenge J, Antonsson E, Znakovskaya I, Wirth A, Herrwerth O, Süß mann F, Peltz C, Ahmad I, Trushin SA, Pervak V, Karsch S, Vrakking MJJ, Langer B, Graf C, Stockman MI, Krausz F, Rühl E and Kling MF. *Controlled near-field enhanced electron acceleration from dielectric nanospheres with intense few-cycle laser fields*. Nature Physics, **7** (8): 656–662 (2011).

TITRE DE LA THÈSE EN FRANÇAIS :

Nouvelle expérience pour l'émission photo-assistée d'électrons avec des impulsions laser ultracourtes à partir de nanopointes métalliques.

TITRE DE LA THÈSE EN ANGLAIS :

New experiment for understanding the physical mechanisms of ultrafast laser-induced electron emission from novel metallic nanotips

RESUMÉ DE LA THÈSE EN FRANÇAIS

Cette thèse étudie l'interaction de nanopointes avec des impulsions laser ultracourtes pour observer l'émission photo-assistée d'électrons. Plusieurs mécanismes physiques entrent en jeu, chacun ayant une signature unique identifiable dans le spectre d'énergie des électrons.

Nous avons développé une nouvelle expérience pour observer et identifier ces mécanismes d'émission. Ceci inclut le développement complet d'un système laser flexible (notamment un amplificateur optique non colinéaire (NOPA) haute cadence), une chambre ultra-vide avec détecteur d'électrons (mesure de spectre d'électrons et carte 2D de l'émission) et un dispositif de nanopositionnement de la pointe dans le foyer du laser, et enfin la fabrication et caractérisation de pointes diverses (en collaboration avec les laboratoires CEMES (Toulouse) et GPM (Rouen)).

Nous avons observé l'émission photo-induite d'électrons à partir de nanopointes de différents matériaux (tungstène, argent, et une nouvelle pointe formée autour d'un nanotube de carbone unique). Nous avons confirmé l'observation de pics ATP (signature de la photoémission au dessus du seuil) sur une pointe de tungstène. Nous avons détecté la première émission induite par laser à partir de nanocône de carbone unique. Enfin, nous avons observé un plateau dans le spectre d'énergie des électrons d'une pointe d'argent, signature de la recollision et rediffusion des électrons sur la pointe. Pour identifier et caractériser ces mécanismes, des études variées ont été faites en fonction de la tension appliquée sur la pointe, du taux de répétition du laser, de sa polarisation, de sa puissance et de sa longueur d'onde. En étudiant la forme du spectre des photoélectrons, nous avons pu extraire des informations sur l'interaction: le facteur d'amplification du champ laser proche de la nanopointe et la probabilité d'absorption d'un photon au dessus du seuil.

RESUMÉ DE LA THÈSE EN ANGLAIS

This thesis concerns the interaction of a sharp nanotip with an ultrashort laser pulse for the observation of emission of photoelectrons. An electron can be emitted from a sharp nanotip system by many different mechanisms. Each mechanism gives a unique signature that can be identified by the photoelectron energy spectrum.

We developed a new experiment to observe and identify these emission mechanisms. This consists of a flexible laser system (including the development of a high repetition rate, variable repetition rate noncollinear optical parametric amplifier (NOPA)), ultra high vacuum chamber, electron detector (electron spectrometer with 2D resolution), nanopositioning of a sharp nanotip in the focus of the laser, and fabrication of these nanotip samples in a variety of materials (in collaboration with CEMES (Toulouse) and GPM (Rouen)).

We observed the emission of photoelectrons from various nanotips based on different materials: tungsten, silver, and a new type of carbon-based nanotip formed around a single carbon nanotube. We confirm the observation of above threshold photoemission (ATP) peaks from a tungsten nanotip. We detected the first laser induced electron emission from a carbon cone based on a single carbon nanotube. We observed a plateau in the electron spectra from a silver nanotip, the signature of electron recollision and rescattering in the tip. Various studies were performed in function of the voltage applied, repetition rate of the laser, laser polarization, energy and wavelength of the laser in order to understand these phenomena. From spectral features we were able to extract information about the system such as the enhancement factor of the laser electric field near the nanotip and the probability of above threshold photon absorption. Comparisons of the various spectra observed allowed us to spectrally identify the mechanisms for photoemission for tip based systems.

PROPOSITION DE MOTS-CLÉS :
Nanopointe, photoémission, laser femtoseconde, nanotechnologie.
Nanotip, photoemission, femtosecond laser, nanotechnology.